UNIVERSITÉ DE STRASBOURG

ÉCOLE DOCTORALE des Sciences Chimiques

[UMR 7006]

THÈSE présentée par :

[Ye WANG]

soutenue le : **10 Juin 2021**

pour obtenir le grade de : **Docteur de l'université de Strasbourg**

Discipline/ Spécialité : Chimie Physique

Science moléculaire et matériaux bi-dimensionnels : Système hybride pour opto-électroniques

THÈSE dirigée par :

Prof. SAMORI Paolo	Professeur, Université de Strasbourg, Strasbourg ; France

RAPPORTEURS :

Prof. PALERMO Vincenzo	Professeur, Institute for Organic Synthesis and Photoreactivity, CNR Italie, Bologne, Italie
Prof. BRATINA Gvido	Professeur, University of Nova Gorica, Ajdovščina, Slovenia

---

AUTRES MEMBRES DU JURY :

Prof. ERSEN Ovidiu	Professeur, Institut de Physique et Chimie des Matériaux de Strasbourg (IPCMS), Strasbourg, France

“Be less curious about people

and more curious about ideas.”

--- Marie Sklodowska Curie

To my parents

Résumé de Thèse

Les matériaux bidimensionnels (2D) ont attiré une grande attention au cours de la dernière décennie, bénéficiant de leur riche variété de structures chimiques et cristallines définissant des propriétés physiques et chimiques uniques qui surpassent généralement les nanomatériaux traditionnels. [1,2] Plus précisément, les propriétés électroniques et optiques pourraient être ajustées soit en variant les combinaisons atomiques et le motif structurel, soit en modifiant le nombre de couches dans le même type de matériau.[3,4] La réduction de l'épaisseur à une échelle inférieure au nanomètre dans le canal des transistors à effet de champ (FET) avec des matériaux 2D permet d'éviter l'effet de canal court de l'industrie traditionnelle à base de silicium et améliore l'efficacité du contrôle de grille, offrant des solutions alternatives pour la fabrication de semi-conducteurs à l'ère de l'après-loi de Moore.[5] Leur surface ultra-plate permet aux matériaux 2D de s'empiler facilement les uns avec les autres, formant des hétérostructures de Van der Waals qui pourraient servir de matériaux actifs d'unités élémentaires dans des dispositifs électroniques tels que les FET et les jonctions p-n. [6,7]

Outre les hautes performances intrinsèques des matériaux 2D en tant que semi-conducteurs, leur grand rapport de surface-volume et leurs surfaces plates leur permettent d'interagir activement avec l'environnement local, y compris les molécules organiques en voisinage. [8,9] Ces molécules, physisorbées ou chimisorbées à la surface des semi-conducteurs 2D, sont capables d'influencer nettement les propriétés de ce dernier composant. [10-12] À cet égard, cette thèse couvre l'étude des interactions entre les molécules organiques et les matériaux semi-conducteurs 2D du point de vue physico-chimique fondamental et aussi des aspects d'application dans les dispositifs électroniques. Les sujets de cette thèse comprennent une large sélection de molécules et de matériaux 2D, notamment :

i. Réglage des propriétés optiques de monocouches de dichalcogénures de métaux de transition (TMD) avec de petites molécules aromatiques.

ii. Dopage de quelques couches de phosphore noir (BP) avec des molécules de solvant organique communes et démonstration de son influence au niveau des FET.

iii. Réglage des propriétés structurelles et électroniques du séléniure d'indium (InSe) à quelques couches avec des molécules de surfactants auto-assemblées et application en photodétecteurs à ultra-hautes performances

iv. Construction de potentiels périodiques supramoléculaires à la surface de MoS_2 par des ligands coordonnés axialement sur la phtalocyanine métallique.

Le 1er projet se concentre sur l'étude de l'effet des petites molécules aromatiques sur les TMDs, en particulier le bisulfure de molybdène (MoS_2) et le diséléniure de tungstène (WSe_2). Nous avons choisi 5 molécules à cycle benzénique unique en faisant varier la position et les propriétés électro-attracteur /donneur du groupe fonctionnel (Figure 1). En déposant à la tournette chaque molécule sur une monocouche de MoS_2 et WSe_2 exfoliée mécaniquement, un transfert de charge est observé entre les molécules aromatiques et les matériaux 2D dans des spectres de photoluminescence (PL) à basse température. Les calculs DFT ont révélé que les molécules riches en électrons (benzène, m-xylène et p-xylène) induisent un dopage n sur les matériaux 2D alors que les molécules déficientes en électrons (1,3-TFMB et 1,4-TFMB) sont des dopants p. Cela peut être traduit expérimentalement en calculant le changement de densité de porteurs de charge par la loi d'action de masse, qui est obtenue à partir des intensités de pic d'exciton neutre et chargé. Il en résulte que la densité moléculaire physisorbée sur la monocouche de MoS_2 est estimée à environ $10^{13}/cm^2$. Les résultats globaux ont démontré que les groupes fonctionnels sur les molécules aromatiques ont des rôles clés pour régir le processus de transfert de charge vers / depuis les TMD monocouches 2D, et que l'effet d'un tel dopage ne peut être négligé lors de la manipulation des matériaux.

Le 2ème projet aborde les effets des solvants organiques courants sur le BP. En tant que semi-conducteur anisotrope à bande interdite étroite (~ 0,3 eV pour quelques couches), le BP présente des caractéristiques ambipolaires à haute mobilité dans les FET contactés au chrome/or (Cr/Au). Nous avons sélectionné 9 molécules de solvant courants, à savoir l'acétone, le benzène, le chloroforme, l'éthanol, l'hexane, l'isopropanol (IPA), le m-xylène, le p-xylène et le toluène. En déposant à la tournette les molécules de solvant dans une boîte à gants remplie d'azote, les

courbes de transfert des FET montrent des déplacements distincts vers différentes molécules. La tension de seuil (V_{th}) des FET, étant un facteur critique pour évaluer le changement de densité des porteurs de charge par dopage (Δn), est considérée comme décalée négativement avec le benzène et le toluène, et positivement décalée avec l'hexane, le chloroforme, l'acétone, l'IPA et l'éthanol, en moyenne. Le Δn atteint $10^{12}/cm^2$, soit une magnitude de dopage similaire aux dopants moléculaires traditionnels forts. L'erreur du dopage évolue aussi largement avec la constante diélectrique, ε_r, où les molécules de solvant avec un grand ε_r montrent de grandes barres d'erreur à partir d'un ensemble répété de mesures. Pour enquêter sur l'origine d'une telle dégénérescence, un calcul DFT a été effectué et a identifié deux mécanismes majeurs du dopage : 1) Transfert de charge entre les molécules et BP ; 2) Dopage induit par dipôle moléculaire. Le changement de fonction de travail des systèmes BP / molécule a révélé une grande dépendance au transfert de charge pour chaque molécule, tandis que pour les solvants à ε_r élevé, les dipôles moléculaires fournissent un effet de criblage important allant jusqu'à +0,157 eV pour l'éthanol. Considérant que les molécules sont distribuées aléatoirement sur la surface, les grands dipôles moléculaires distribueraient un désordre plus élevé dans le dopage que les petits. Cela pourrait donc expliquer l'observation de la variation de la barre d'erreur au sein de différentes molécules de solvant. Le dopage induit également le décalage vers le rouge et le décalage vers le bleu du mode Raman hors plan (A_{1g}) sur BP, provenant également du changement de densité électronique dans le matériau.

Le 3ème projet révèle une première démonstration de dopage moléculaire sur InSe. Nos travaux ont d'abord porté sur l'ingénierie diélectrique de FET d'InSe en utilisant le polymère BCB sans pièges, augmentant la mobilité par effet de champ de 0,01 cm^2/Vs à plus de 688 cm^2/Vs. En fonctionnalisant avec une molécule de surfactant ionique, le bromure de didodécyldiméthylammonium (DDAB), un dopage n évident et une amélioration supplémentaire de la mobilité à effet de champ ont été observés. L'amélioration de la mobilité à effet de champ à quatre sondes jusqu'à 2875 cm^2 /Vs à température ambiante, est principalement attribuable à l'augmentation de la concentration d'électrons dans le canal et à l'occupation des défauts de sélénium par l'ion brome. La fonctionnalisation moléculaire s'avère bénéfique non seulement pour les dispositifs FET standard normaux mais aussi pour les propriétés photoréactives de InSe car c'est l'un des meilleurs matériaux 2D pour les applications photoréactives. Dans ce travail, le dopage moléculaire d'InSe a été appliqué dans trois prototypes distincts de photodétecteurs : les phototransistors InSe, la jonction p-n asymétrique latérale InSe et les jonctions p-n Van der Waals (VdW) verticales de BP et InSe. Dans le premier prototype d'appareil, les photoréponses d'InSe sur SiO_2, InSe sur BCB et InSe / DDAB sur BCB sont comparées. En appliquant l'éclairage de 300 nm à

690 nm, une réponse sélective de la gamme de longueurs d'onde ultraviolette (UV) est observée. Un raccourcissement du temps de réponse de >300 ms à 16 ms est présent après la fonctionnalisation de l'InSe avec DDAB sur BCB tandis que le photocourant est bonifié de l'ordre de 10^7. Ceci est attribué à la réduction de la diffusion des porteurs photogénérés tant par la modification du diélectrique sous l'InSe, que par l'effet de réparation des défauts avec la molécule auto-assemblée sur le dessus. Cet effet apporte une réactivité ultra élevée atteignant 10^6 A /W à 365 nm avec une puissance lumineuse à 50 mW/cm^2. Le facteur de linéarité α qui est calculé par $I_{ph} \propto P^{\alpha}$ montre également une augmentation de 0,448 pour InSe à 0,658 pour InSe / DDAB, indiquant une réduction des pièges de charge. Le deuxième prototype de dispositif implique la fabrication d'une jonction P-N latérale d'InSe en utilisant une électrode asymétrique, plus précisément, Palladium (Pd, fonction de travail ~ 5,6 eV) et Chrome (Cr, fonction de travail ~ 4,4 eV)). La diode Schottky montre un redressement à une tension de grille nulle dans le cas vierge. En couvrant la moitié du canal avec h-BN et en dopant le côté en contact avec le Cr avec DDAB, un potentiel intégré plus élevé est formé avec une augmentation évidente du rapport de rectification de 198 à 716. Le temps de photodétection apparaît à l'échelle inférieure à la milliseconde après la fonctionnalisation moléculaire. De plus, une haute sensibilité (R) et une efficacité quantique externe (EQE) sont observées dans la jonction PN dopée dépassant 10^3 A / W et 3 × 10^5% avec une haute détectivité (D *) atteignant 4 × 10^{11} Jones. Le dernier prototype de dispositif est réalisé en superposant InSe sur BP, où les deux matériaux forment un alignement de bande de type Ⅱ. Une stratégie de fonctionnalisation moléculaire similaire a été employée, obtenant ainsi un temps de montée / décroissance de la photoresponse réduit à 0,96 / 2,97 ms, ce qui est 20 fois plus petit que les non fonctionnalisés. De façon analogue à la jonction latérale P-N, le R et l'EQE ont connu une augmentation exponentielle à 10^3 A / W et 3,5 × 10^5% respectivement, dépassant largement les valeurs actuellement rapportées dans la littérature. Il est à noter que dans toutes les formes de dispositifs photodétecteurs, la tension de fonctionnement est V_g = 0 V et V_d = 1 V, ce qui est bien inférieur à la plupart des dispositifs haute performance rapportés dans la littérature. La faible consommation d'énergie et les caractéristiques de réactivité élevée des dispositifs font de la fonctionnalisation moléculaire une approche économique et pratique pour réaliser l'optoélectronique intelligente de nouvelle génération.

Le 4ème projet concerne la formation d'une hétérostructure organique-inorganique à l'aide de métal-phtalocyanine et de monocouche de MoS_2. Il est bien connu que les phtalocyanines métalliques forment des monocouches auto-assemblées sur des matériaux 2D. Bénéficiant de la structure périodique sur la surface MoS_2, la coordination axiale à l'aide de ligands pyridiniques a été appliquée pour créer des dipôles moléculaires alignés. Quatre ligands distincts (3,5-

bifluoropyridine, 3-fluoropyridine, 2-fluoropyridine et 4-aminopyridine) possédant des amplitudes et des directions différentes des moments dipolaires moléculaires (principalement induits par de puissants groupes fonctionnels électrolytiques / dons sur le cycle pyridine) ont été choisis pour se coordonner sur des hétérostructures MoS_2 / phtalocyanine de zinc (ZnPc) et MoS_2 / phtalocyanine de cobalt. Les analyses FET montrent un décalage V_{th} positif par des ligands avec un dipôle positif, tandis que lorsque les ligands possèdent un dipôle négatif, V_{th} a un décalage négatif. La modulation de la densité des porteurs de charge monte à 10^{12} / cm^2 dépassant les dopants moléculaires traditionnels. Un effet si important peut être attribué uniquement à la présence à la fois de la plate-forme MPc et de grands dipôles dans le ligand, se limitant à l'alignement des dipôles moléculaires dans la direction z. De plus, nous avons observé une modulation systématique des propriétés optiques (spectres PL et Raman) du MoS_2 induite par le ligand axial, révélant une tendance identique de dopage.

Le 5ème projet a étendu la vision du 4ème projet, au lieu de simples ligands pyridiniques, nous avons ajouté des fonctionnalités photochromiques (précisément 4- (4 - ((4- (trifluorométhyl) phényl) diazényl) phényl) pyridine) sur le cycle pyridine, pour réaliser un dopage dipolaire collectif dynamique à la surface de MoS_2 et WSe_2 (noté comme MX_2). Le complexe synthétisé, possédant des configurations dépliée et pliée, se comporte comme un interrupteur moléculaire sur une surface. Le groupe fonctionnel électro-attractif fort à l'extrémité du ligand pourrait induire un grand moment dipolaire perpendiculaire au plan basal de MX_2, modulant ainsi le niveau de Fermi de MX_2 par dopage dipôlaire. La direction et l'amplitude du moment dipolaire sont dynamiques, elles sont régies par le mouvement de la liaison C-N=N-C. Par conséquent, une modulation dynamique du niveau de Fermi est obtenue en commutant l'interrupteur moléculaire entre les états déplié et replié. Le phénomène est révélé dans les FET de MoS_2 et WSe_2 où un décalage réversible de la densité des porteurs de charge jusqu'à $4{,}38 \times 10^{12}$ / cm^2 est observé en irradiant l'interrupteur moléculaire avec de la lumière UV et visible. Le contrôle de l'interrupteur moléculaire pourrait également être exploré sur d'autres prototypes de dispositifs exprimant des fonctions sophistiquées pour des applications complexes, par exemple, la jonction PN et les circuits logiques. La première démonstration de dispositifs sur le contrôle de l'interrupteur moléculaire réside dans la jonction Schottky latérale de WSe_2 où la direction de rectification pourrait être modulée par la tension de grille arrière et l'irradiation lumineuse grâce au décalage de niveau dynamique de Fermi. Non seulement des dispositifs uniques pourraient être contrôlés par des interrupteurs moléculaires, mais des dispositifs multiples pourraient également être manipulés, formant ainsi des circuits électroniques intégrés. À cet égard, le WSe_2 de type-p et le MoS_2 de type-n sont fabriqués en série pour former un circuit inverseur binaire. Les interrupteurs

moléculaires, qui pourraient contrôler simultanément le dopage du PMOS et du NMOS, agissent comme une « grille flottante moléculaire ». Par conséquent, un dispositif logique à mémoire est réalisé avec une sortie logique programmable par la lumière. La fenêtre de mémoire créée par la grille flottante moléculaire atteint 20V sur diélectrique SiO_2, défiant la technique traditionnelle de grille flottante diélectrique-métal-diélectrique qui nécessite un processus de fabrication compliqué et une puissance électrique élevée. Les valeurs logiques en mémoire «0» et «1» pourraient être programmées et effacées par la lumière UV et Vis, permettant une manipulation rapide et pratique une fois incorporées dans des circuits électroniques.

Dans cette thèse, une étude systématique de l'interaction entre les matériaux 2D et les molécules organiques a été réalisée avec une large sélection de molécules et de matériaux 2D. Ces travaux de recherche montrent une compréhension approfondie des notions physiques et chimiques à la fois pour les matériaux 2D en physique des semi-conducteurs et pour les molécules en (photo)chimie organique. Les travaux couvrent également les innovations dans l'exploitation des matériaux 2D fonctionnalisés avec des molécules dans les FET à haute performance, des diodes P-N, des photodétecteurs et des circuits logiques à mémoire. Cette thèse a démontré que l'utilisation de molécules organiques pour ajuster les propriétés des matériaux 2D est une approche puissante étant donné la grande variété de molécules organiques à interagir activement avec les semi-conducteurs à épaisseur atomique. En particulier, la modulation efficace des propriétés électroniques enrichit la polyvalence des semi-conducteurs 2D, offrant de grandes opportunités à la science chimique combinée avec l'électronique, jouant des rôles de dopants moléculaires, d'agents de réparation et de commutateurs. Les résultats présentés dans la thèse ont révélé qu'en sélectionnant ou en concevant délibérément les structures moléculaires, d'excellentes propriétés des matériaux 2D de base peuvent être obtenues. Ces approches se sont avérées pratiques, économiques et respectueuses de l'environnement, offrant des opportunités pour les futures technologies de la prochaine génération.

Abstract of Thesis

Two-dimensional (2D) materials have attracted great attention during the last decade, benefitting from their rich variety of chemical and crystal structures defining unique physical and chemical properties overall outperforming traditional nanomaterials.[1,2] More specifically, the electronic and optical properties could either be tuned by varying the atomic combinations and structural motif, or by varying the number of layers in the same type of material.[3,4] The reduction of thickness to sub-nanometer range in the channel of field-effect transistors (FET) with 2D materials overcomes the short-channel effect of traditional silicon-based industry, and improves the efficiency of gate control, providing alternative solutions for semiconductor fabrication in the post Moore's law era.[5] The ultra-flat surface makes it facile for 2D materials to stack up with each other, forming Van der Waals heterostructures which could serve as active materials of elementary unit in electronic devices such as FETs and p-n junctions.[6,7]

Apart from the intrinsic high-performances of 2D materials as semiconductors, their large surface-to-volume ratio and flat surfaces enables them to interact actively with the local environment, including neighbouring organic molecules.[8,9] These molecules, either physisorbed or chemisorbed on the surface of 2D semiconductors, are able to markedly influence the properties of the latter component.[10-12] In this regard, this thesis covers the study of interactions between organic molecules and 2D semiconducting materials from both fundamental physico-chemical point of view and application aspects in electronic devices. The topics of this thesis comprise a wide selection of molecules and 2D materials, including:

i. Tuning the optical properties of monolayer transition metal dichalcogenides (TMDs) with small aromatic molecules.

ii. Doping few-layer black phosphorus (BP) with common organic solvent molecules and demonstrated the influence as field-effect transistors.

iii. Tuning the structural and electronic properties of few-layer indium selenide (InSe) with self-assembled surfactant molecules and the application towards ultra-high performance photodetectors.

iv. Constructing supramolecular periodic potentials on the surface of MoS_2 by axially

coordinated ligands on metal phthalocyanine.

v. Realizing dynamic control of 2D electronic devices by on-surface molecular switches containing photoswitchable ligands.

The 1st project focuses on studying the effect of small aromatic molecules on single layer transition metal dichalcogenides (TMDs), in particular molybdenum disulfide (MoS_2) and tungsten diselenide (WSe_2). We have chosen 5 molecules with single benzene ring by varying the position and electron-donating/-withdrawing properties of the substituent group (Figure 1). By spin-coating each molecule onto monolayer mechanical exfoliated MoS_2 and WSe_2, charge transfer is observed between aromatic molecules and 2D materials in low-temperature photoluminescence (PL) spectra with different magnitude and directions. DFT calculations have revealed that electron-rich molecules (benzene, m-xylene and p-xylene) induces to n-doping on 2D materials whereas electron-deficient molecules (1,3-TFMB and 1,4-TFMB) are p-dopants. This could be reflected experimentally by calculating the charge carrier density change through mass action law, which is obtained from the intensities of neutral exciton peak and charged exciton peak. Therefore, the molecular density that are physisorbed onto monolayer MoS_2 is estimated to be around $10^{13}/cm^2$. The overall results demonstrated that the functional groups on aromatic molecules are key roles to govern the charge transfer process to/from 2D monolayer TMDs, and the effect of such doping could not be neglected during the manipulation of the materials.

The 2nd project discusses the effect of common organic solvents on few-layer black phosphorus (BP). As a narrow-bandgap (~0.3 eV for few-layer) anisotropic semiconductor, few-layer black phosphorus shows high-mobility ambipolar characteristics in chromium/gold (Cr/Au) contacted field-effect transistors (FET). We have selected 9 common solvent molecules, namely acetone, benzene, chloroform, ethanol, hexane isopropanol (IPA), m-xylene, p-xylene and toluene. By spin-coating the solvent molecules in nitrogen-filled glovebox, the transfer curves of FETs show distinct shifts towards different molecules. The threshold voltage (V_{th}) of FETs, being a critical factor for evaluating the charge carrier density change by doping (Δn), is seen to be negatively shifted with benzene and toluene, and positively shifted with hexane, chloroform, acetone, IPA and ethanol, averagely speaking. The Δn achieved $10^{12}/cm^2$, being a similar magnitude in contrast with traditional strong molecular dopants. The error of the doping evolutes also largely with the dielectric constant, ε_r ,where solvent molecules with large ε_r shows large error bars from repeated set of measurements. To investigate the origin of such degeneration, DFT calculation was conducted and figured out two major mechanisms of the doping: 1) Charge transfer between

molecules and BP; 2) Molecular dipole induced doping. The work function shift of BP/molecule systems revealed large dependence on charge transfer for each molecule, while for high ε_r solvents, the molecular dipoles provide large screening effect up to +0.157 eV for ethanol. Considering the molecules to be randomly distributed on surface, large molecular dipoles would distribute higher disorder in doping than small ones. This could therefore explain the observation of error bar variation within different solvent molecules. The doping also induces redshift and blueshift of the out-of-plane Raman mode (A_{1g}) on BP, originated also from the electron density change in the material.

The 3rd project reveals a first demonstration of molecular doping on InSe. Our work first aimed at dielectric engineering of InSe FET using trap-free polymer BCB, increasing the field-effect mobility from 0.01 cm^2/Vs to over 688 cm^2/Vs. A further doping by ionic surfactant molecule, didodecyldimethylammonium bromide (DDAB), an obvious n-doping and a further enhancement of the field-effect mobility has been observed. The four-probe field-effect mobility enhances up to 2875 cm^2/Vs at room temperature, mainly attributed to the increase of electron concentration in the channel and the occupation of selenium vacancies by bromine ion. The molecular functionalization is found to be beneficial not only to standard FET devices, but as InSe is one of the best 2D material for photoresponsive applications, the molecular functionalizations are also beneficial for photoresponsive properties of InSe. In this work, molecular doping of InSe has been applied in three distinct prototypes of photodetectors: InSe phototransistors, lateral asymmetric InSe p-n junction and vertical BP/InSe Van der Waals (VdW) p- n junctions. In the first device prototype, photoresponses of InSe on SiO_2, InSe on BCB and InSe/DDAB on BCB are compared. By applying light pulses from 300 nm to 690 nm, a selective response of ultraviolet (UV) range of wavelength is observed. A shortening of response time from > 300 ms to 16 ms is present after functionalizing the InSe with DDAB on BCB while the photocurrent is boosted in the order of 10^7. This is attributed to the reduction of scattering of photogenerated carriers both from the modification of dielectric layer below InSe, and from the defect-healing and screening effect of the self-assembled molecule on top. This effect brings an ultrahigh responsivity reaching 10^6 A/W at 365 nm with light power at 50mW/cm^2. The linearity factor α which is calculated through $I_{ph} \propto P^{\alpha}$ also shows increase from 0.448 for InSe to 0.658 for InSe/DDAB, indicating reduction of charge traps. The second device prototype involves the fabrication of lateral P-N junction of InSe using asymmetric electrode, to be specific, Palladium (Pd, work function ~5.6 eV) and Chromium (Cr, work function ~4.4 eV)).The Schottky diode shows rectification at zero gate voltage in the pristine case. By covering half of the channel with h-BN and dope the Cr-contacted side with DDAB, a higher built-in potential is formed with an evident increase of rectification ratio from 198 to

716.The photoresponsive time appears in the sub-millisecond scale after the molecular functionalization. Furthermore, a high responsivity (R) and external quantum efficiency (EQE) is observed in the doped PN junction exceeding 10^3 A/W and 3×10^5 % with high detectivity (D*) reaching 4×10^{11} Jones. The last device prototype is realized by stacking InSe on top of BP, where the two materials forms type-Ⅱ band alignment. Similar molecular functionalization strategy has been employed thus obtaining a reduced photoresponse rise/decay time to 0.96/2.97 ms, being 20-fold smaller than unfunctionalized ones. Analogous to the lateral P-N junction, the R and EQE has seen an exponential increase to 103 A/W and 3.5×10^5% respectively, greatly exceeding the currently reported values in literature. It is worth to note that in all forms of photodetector devices, the operating voltage is V_g=0 V and V_d=1 V, being much lower than most of the high-performance devices reported in literature. The low-power-consumption and high-responsive characteristics of the devices makes molecular functionalization an economical and practical approach to achieve the next-generation smart optoelectronics.

The 4th project involves the formation of organic-inorganic heterostructure using metal-phthalocyanine and monolayer MoS_2. It is well known that metal phthalocyanines forms self-assembled monolayers on 2D materials. Benefitting from the periodic structure on MoS_2 surface, axial coordination using pyridinic ligands was applied to create aligned molecular dipoles. Four distinct ligands (3,5-bifluoropyridine, 3-fluoropyridine, 2-fluoropyridine and 4-aminopyridine) possessing different magnitude and directions of molecular dipole moments (mainly induced by strong electron-withdrawing/donating functional groups on pyridine ring) were chose to coordinate on MoS_2/zinc phthalocyanine (ZnPc) and MoS_2/cobalt phthalocyanine heterostructure. FET analyses show positive V_{th} shift by ligands with positive dipole, while when ligands possess negative dipole, V_{th} is seen to have negative shift. The modulation in charge carrier density mounts to $10^{12}/cm^2$ exceeding the traditional molecular dopants. Such huge effect can be solely attributed to the presence of both MPc platform and large dipoles in the ligand, confining to the alignment of molecular dipoles in the z-direction. Furthermore, we have observed systematic modulation of optical properties (PL and Raman spectra) of MoS_2 induced by the axial ligand, revealing identical trend of doping.

The 5th project extended the vision of the 4th project, where instead of simple pyridine ligands, we added photochromic functionalities (namely 4-(4-((4-(trifluoromethyl)phenyl)diazenyl)phenyl)pyridine) on the pyridine ring, to realize dynamic collective dipole doping on the surface of MoS_2 and WSe_2 (denoted as MX_2). The as synthesized complex behaves as molecular switches on surface containing *unfolded* and *folded* configurations.

The strong electron-withdrawing group at the end of the ligand could induce large dipole moment perpendicular to the basal plane of MX_2, therefore modulating the Fermi level of MX_2 by dipole-induced doping. The direction and magnitude of the dipole moment is dynamic, which is ruled by the motion of C-N=N-C bond. Hence, a dynamic modulation of the Fermi level is achieved by switching the molecular switch between *unfolded* and *folded* states. The phenomenon is revealed in FETs of MoS_2 and WSe_2 where a reversible shift of charge carrier density up to $4.38\times10^{12}/cm^2$ is present by irradiating the molecular switch with UV and vis light. The molecular switch control could also be explored on other device prototypes expressing sophisticated functions, for example, PN junction and logic circuits. The first demonstration of devices on molecular switch control resides in the lateral WSe_2 Schottky junction where the rectification direction could be modulated by back-gate voltage and light irradiation thanks to the dynamic Fermi level shift. Not only single devices could be controlled by molecular switches, but multiple devices could also be manipulated, yielding integrated electronic circuits. In this regard, p-type WSe_2 and n-type MoS_2 are fabricated in-series to form a binary inverter circuit. The molecular switches, which could control the doping of both PMOS and NMOS simultaneously, acts as a "molecular floating gate". Therefore, a logic-in-memory device is realized with light-programmable logic output. The memory window created by molecular floating gate reaches 20V on SiO_2 dielectric, which challenges the traditional dielectric-metal-dielectric floating gate technique which requires complicated fabrication process and high electrical power input. The logic-in-memory "0" and "1" could be programmed and erased by UV and Vis light, enabling fast and convenient manipulation when incorporated into electronic circuits. In this thesis, a systematic study of the interaction between 2D materials and organic molecules have been achieved comprehending a wide selection of molecules and 2D materials. The research shows deep understanding of the physical and chemical notions both for the 2D materials in semiconductor physics and for the molecules in organic (photo)chemistry. The work also covers innovations in harnessing the molecular functionalized 2D materials in high-performance field-effect transistors, P-N diodes, photodetectors and logic-in-memory circuits. This thesis demonstrated that the use of organic molecules to tune the properties of 2D materials is a powerful approach given the large variety of organic molecules to be actively interact with the atomically-thin semiconductors. Especially, the effective modulation of electronic properties enriches versatility of the 2D semiconductors, bringing large opportunities to the combine chemical science with electronics, performing roles as molecular dopants, repairing agents and switches. The results presented in the thesis revealed that by deliberately selecting or designing the molecular structures, excellent properties of the base 2D materials can be achieved. These approaches are proved to be convenient, economic and environmental friendly, providing opportunities for the future next-generation technologies.

References

1 Geim, A. K. & Novoselov, K. S. The Rise of Graphene. *Nat. Mater.* **6**, 183-191, doi:Doi 10.1038/Nmat1849 (2007).

2 Novoselov, K. S. *et al.* Electric Field Effect in Atomically Thin Carbon Films. *Science* **306**, 666-669, doi:10.1126/science.1102896 (2004).

3 Mak, K. F. & Shan, J. Photonics and optoelectronics of 2D semiconductor transition metal dichalcogenides. *Nat. Photonics* **10**, 216, doi:10.1038/nphoton.2015.282 (2016).

4 Li, L. *et al.* Black phosphorus field-effect transistors. *Nat. Nanotechnol.* **9**, 372 (2014).

5 Waldrop, M. M. More than Moore. *Nature* **530**, 144-147 (2016).

6 Wang, Y. *et al.* Van der Waals contacts between three-dimensional metals and two-dimensional semiconductors. *Nature* **568**, 70-74 (2019).

7 Geim, A. K. & Grigorieva, I. V. Van der waals heterostructures. *Nature* **499**, 419, doi:10.1038/nature12385 (2013).

8 Amsterdam, S. H. *et al.* Electronic Coupling in Metallophthalocyanine–Transition Metal Dichalcogenide Mixed-Dimensional Heterojunctions. *ACS Nano* **13**, 4183-4190 (2019).

9 Ryder, C. R., Wood, J. D., Wells, S. A. & Hersam, M. C. Chemically tailoring semiconducting two-dimensional transition metal dichalcogenides and black phosphorus. *ACS Nano* **10**, 3900-3917 (2016).

10 Lin, Y. *et al.* Dielectric screening of excitons and trions in single-layer MoS_2. *Nano Lett.* **14**, 5569-5576 (2014).

11 Yu, L. *et al.* High-Performance WSe2 Complementary Metal Oxide Semiconductor Technology and Integrated Circuits. *Nano Lett.* **15**, 4928-4934, doi:10.1021/acs.nanolett.5b00668 (2015).

12 Kang, D.-H. *et al.* Controllable nondegenerate p-type doping of tungsten diselenide by octadecyltrichlorosilane. *ACS Nano* **9**, 1099-1107, doi:10.1021/nn5074435 (2015).

Symbols and Abbreviations

Symbols

Symbols	English	Français
°C	Celcius degree	Degré Celcius
C_{di}	Capacitance of dielectric layer	Capacitance de couche diélectrique
D_n	Charge carrier density change	Changement de densité des porteurs de charge
e	Elementary charge	Charge élémentaire
E_{A-}	Trion binding energy	Energie de liaison de trion
ε_{di}	Dielectric constant of the dielectric layer	Constante diélectrique de couche diélectrique
E_F	Fermi energy	Energie de Fermi
ε_r	Relative Dielectric constant	Constante diélectrique relative
Φ_{bi}	Built-in potential	Potentiel intégré
I_{ds}	Drain-source current	Courant de drain-source
I_{sc}	Short-circuit current	Courant de court-circuit
J	Diode current	Courant de diode
J_0	Reverse bias saturation current	Courant de saturation de polarisation inverse
k	Boltzmann constant	Constante de Boltzmann
K	Kelvin degree	Degré Kelvin
L_{ch}	Channel length	Longeur du canal
μ	Field-effect mobility	Mobilité à effet de champ
m_n^*	Effective mass of electron	Masse effective d'électron
n_0	Electron density	Densité des électrons
N_C	Effective density of states of conduction band	Densité d'état effective de bande de conduction

n_{D^+}	Positive donor density	Densité de doneur positif
N_V	Effective density of states of valence band	Densité d'état effective de bande de valence
p_0	Hole density	Densité des trous
Q(x)	Induced charge by the gate along the x-axis of the channel	Charge induite par la grille le long de l'axe- x du canal
T	Temperature	Température
V(x)	Drift velocity	Vitesse de dérive
V_d	Drain voltage	Tension de drain
V_{ds}	Drain-source voltage	Tension de drain-source
V_g	Gate voltage	Tension de grille
V_{oc}	Open-circuit voltage	Tension en circuit ouvert
V_{th}	Threshold voltage	Tension de seuil
ω_A	Energy of exciton	Energie d'exciton
ω_{A^-}	Energy of trion	Energie de trion
W_{ch}	Channel width	Largeur du canal
K.E.	Kinetic energy	Energie cinétique
Φ_{XPS}	Work function of XPS instrument	Fonction de travail de l'instrument XPS
B.E.	Binding energy	Énergie de liaison
eV	Electronvolt	Electronvolt
z(t)	Tip position at time t	Position de la pointe au moment t
Dn	Cantilever-sample distance	Distance d'échantillon-cantilever
A	Oscillation amplitude	Amplitude d'oscillation
f_d	Driving frequency of the cantilever	Fréquence d'entraînement du cantilever
Φ	Phase difference between the excitation and oscillation in the cantilever	Différence de phase entre l'excitation et l'oscillation dans le cantilever
X	Neutral A exciton	Exciton A neutre
X^-	Negative trion	Trion négatif
X+	Positive trion	Trion positif
D	Defect-induced emmision	Emission induit par défauts
γ^-	Negative trion weight of mos_2	Poid de trion négatif de mos_2

I_{X^-}	Area of negative trion peak	Aire du pic de trion négatif
I_X	Area of neutral exciton peak	Aire du pic d'exciton neutre
$\Delta\gamma^-$	Trion weight change	Changement de poids de trion
μ_A	Chemical hardness of species A	Dureté chimique de l'espèce A
$\varepsilon_{electron(hole)}$	Energy of the molecular HOMO (LUMO) level for the solvent	Energie du niveau moléculaire HOMO (LUMO) pour le solvant
$\varepsilon_{electron(hole)}$	Energy of the top of the valence (conduction) band for the 2D solid	Energie du haut de la bande de valence (conduction) pour le solide 2D
N_X	Population of exciton	Polulation d'exciton
N_{X^-}	Population of negative trion	Polation de trion négatif
n_{el}	Electron density	Densité d'électron
m_X	Effective mass of exciton	Masse effective d'exciton
m_{X^-}	Effective mass of negative trion	Masse effective de trion négatif
n_{mol}	Number of molecules adsorbed per unit area	Nombre de molécules adsorbées par unité de surface
Å	Ångström	Ångström
V	Volt	Volt
nm	Nanometer	Nanomètre
$V_{th,p}$	Threshold voltage of hole transport	Threshold voltage of hole transport
E_g	Bandgap energy	Énergie de bandgap
I_{on}	On-state current of field effect transistor	Courant à l'état passant du transistor à effet de champ
I_{off}	Off-state current of field effect transistor	Courant à l'état bloqué du transistor à effet de champ
σ	Conductivity	Conductivité
SS	Subthreshold swing	Balançoire sous le seuil
D_{it}	Interface trap density	Densité des traps d'interface
G	Photoconductive gain	Gain photoconducteur
$\tau_{transit}$	Timescale of free carrier drifting in the photodetector channel	Echelle de temps de la dérive de la porteuse libre dans le canal du photodétecteur
τ_{life}	Decay time of photocurrent	Temps de décroissance du photocourant
φ_{exp}	Experimental work function	Fonction de travail expérimental
φ_{th}	Theotetical work function	Fonction de travail théorique

Abbreviations

Abbrevitions	English	Français
1,3-TFMB	1,3-Bis(trifluoromethy)lbenzene	1,3-Bis(trifluoromethy)lbenzène
1,4-TFMB	1,4-Bis(trifluoromethyl)benzene	1,4-Bis(trifluoromethyl)benzène
^{1}H-NMR	^{1}H-nuclear magnetic resonance	^{1}H-Résonance magnétique nucléaire
2D	Two-dimensional	Bidimensionnels
2-FP	2-fluoropyridine	2-fluoropyridine
3,5-FP	3,5-difluoropyridine	3,5-bifluoropyridine
3-FP	3-fluoropyridine	3-fluoropyridine
4-AP	4-aminopyridine	4-aminopyridine
AFM	Atomic force microscopy	Microscopie à force atomique
Au	Gold	Or
AZO	Azobenzene	Azobenzène
BCB	Benzocyclobutene	Benzocyclobutène
BNC	Bayonet neill–concelman	Bayonet neill–concelman
BP	Black phosphorus	Phosphor noir
BV	Benzyl viologen	Benzyl viologen
CBM	Conduction band minimum	Minimum de bande de conduction
CCD	Chrarge coupled device	Dispositif à couplage de charge
CoPc	Phthalocyanine de cobalt	Cobalt phthalocyanine
Cr	Chromium	Chrome
CVD	Chemical vapor deposition	Déposition chimique en phase vapeur
CVT	Chemical vapor transport	Transport de vapeur chimique
D^*	Specific detectivity	Détectivité spécifique
DAE	Diarylethene	Diarylethène
DDAB	Didodécyldimethylammonium bromide	Bromure de didodécyldiméthylammonium
DFT	Density functional theory	Théorie de densité foncitonnnelle
DoS	Density of States	Densité d'état
EBL	Ebeam lithography	Lithographie à fisceau d'électron

E_c	Conduction band	Bande de conduction
EQE	Efficacité quantique externe	External quantum efficiency
E_v	Valence band	Bande de valance
F4TCNQ	2,3,5,6-Tetrafluoro-7,7,8,8-tetracyanoquinodimethane	2,3,5,6-Tetrafluoro-7,7,8,8-tetracyanoquinodimethane
FePc	Iron phthalocyanine	Phthalocyanine de fer
FET	Field-effect transistor	Transistor à effect de champs
fPy	Funnational pyridine	Pyridine fonctinnelle
G	Graphene	Graphène
H_2O	Water	Eau
h-BN	Hexagonal boron nitride	nitrure de bore hexagonal
HOPG	Highly oriented pyrolytic graphite	Graphite pyrolytique hautement orienté
InSe	Indium selenide	Séléniure d'indium
IPA	Isopropanol	Isopropanol
ITO	Indium-tin-oxide	Oxyde d'étain et d'indium
KPFM	Kelvin probe force microscopy	Microscopie à force de sonde Kelvin
MIBK	Methylisobutylcetone	Méthylisobutylcétone
MIR	Mid-infrared	Infrarouge moyen
MoS_2	Molybdenum disulfide	Bisulfure de molybdène
MOSFET	Metal-oxide-semiconductor field-effect transistors	Transistor à effet de champ à structure métal-oxyde-semiconducteur
MPc	Metal phthalocyanine	Phthalocyanine de métaux
N_2	Nitrogen	Azote
NADH	Nicotinamide adenine dinucleotide	Nicotinamide adenine dinucleotide
NH_3	Ammoniac	Ammoniac
NMOS	N- Metal oxyde silicium	N-Metal oxide silicon
NO	Nitrogen monoxyde	Monoxide d'azote
NO_2	Nitrogen dioxide	Dioxyde d'azote
OTS	Octadecyltrichlorosilane	Octadecyltrichlorosilane
Pd	Palladium	Palladium
PDMS	Polydimethylsiloxane	Polydiméthylsiloxane

PESA	Photoelectron spectroscopy in ambient conditions	Spectroscopie photoélectronique en conditions ambiantes
PEYA	Photoelectron Yield counter operating in Ambient conditions	Compteur de rendement photoelectron fonctionnant dans des conditions ambiantes
PID	Proportional–integral–derivative	Proportionnelle – intégrale – dérivée
PL	Photoluminescence	Photoluminescence
PMMA	Poly(methyl methacrylate)	Polyméthacrylate de méthyle
PMOS	P- Metal oxyde silicium	P-Metal oxide silicon
R	Responsivity	Sensibilité
SMU	Sourcce-meter unit	Unité source-mètre
SP	Spiropyran	Spiropyran
STM	Scanning tunneling microscopy	Microscopie à l'effect tunnel
TCE	Tetrachroloethane	Tetrachloroéthène
TCNE	Tetracyanoethylene	Tetracyanoethylène
TFAP	44- (4 - ((4- (trifluorométhyl) phényl) diazényl) phényl) pyridine	4-(4-((4-(trifluoromethyl)phenyl)diazenyl)phenyl)pyridine
TMAH	Tetramethylammonium hydroxide	Tétraméthylammonium hydroxide
TMD	Transition metal dichalcogenide	Dichalcogénures de métaux de transition
TTF	Tetrathiafuvaluene	Tetrathiafuvaluène
UHV	Ultra-high vacuum	Vide ultra-poussé
UV	Ultraviolet	Ultraviolet
VASP	Vienna ab-initio simulation package	Vienna ab-initio simulation package
VBM	Valence band maximum	Maximum de bande de valence
VdW	Van der Waals	Van der Waals
WSe_2	Tungsten diselenide	Diséléniure de tungstène
XPS	X-ray photoelectron spectroscopy	Spectroscopie photoélectronique par rayons X
ZnPc	Phthalocyanine de zinc	Zinc phthalocyanine

List of Figures and Tables

Contents

Chapter 1 Introduction

In recent years, the rapid growth of semiconductor industry has revolutionized the human life in an unprecedented level. The basic elements in the on-chip computing, metal-oxide-semiconductor field-effect transistors (MOSFET), are key components in building logic in complementary metal-oxide-semiconductor (CMOS) technologies. Major breakthroughs have been achieved in the last century, where the advances in lithography technologies successfully multiplies the number of MOSFETs on chip to ensure the fabrication of CMOS circuits for logic computing, memory manipulation, etc. However, nowadays, in the post-Moore's law era, the developments in *silicon-based technologies* could not fulfill the growing demand of human society development that fierce competition in chip industries between countries dramatically emerges in recent years, intensifying the instability of international political and economic environment.[5,13]

Therefore, it is *urgent to break the bottleneck* and *seek for alternative solutions* to achieve a leap forward in the semiconductor industry. Especially, novel semiconducting materials are highly sought after to access new physical/electronic properties. An ideal candidate of semiconducting materials is in the family of two-dimensional (2D) materials, which attracted tremendous attention since the isolation of graphene in 2004 by K. Noveselev and A. Geim (*University of Manchester, UK; Laureates of Nobel Prize of Physics, 2010*). Such atomically thin materials benefit from their rich variety of chemical and crystal structures defining unique physical and chemical properties overall outperforming traditional nanomaterials.[1] Moreover, numerous are the different 2D semiconducting with electronic and optical properties that could either be tuned by varying the atomic combinations and structural motif, or by varying the number of layers in the same type of material. The reduction of thickness to the sub-nanometer range in the channel of field-effect transistors (FET) with 2D materials overcomes the short-channel effect of traditional silicon-based industry, and improves the efficiency of gate control, providing alternative solutions for semiconductor fabrication. Furthermore, the ultra-flat surface makes it facile 2D materials to stack up with each other, forming Van der Waals heterostructures which could serve as active materials of elementary unit in electronic devices such as photodetectors and CMOS logic gates.[7]

Although a considerable number of works on 2D material have demonstrated their potential to function as high-performance semiconductors, the enhancement of fundamental properties is limited by technical obstacles. [14] As fast yet powerful approach, molecular functionalization has become a prevailing method to tune the physical and chemical properties of 2D materials.[15,16] The diversity of existed forms of molecules defines substantial possibilities of combinations of molecule-2D material yielding functional hybrid systems. Given different chemical structure, optical and electronic properties of molecules and assemblies, threreof, they are able to influence the properties 2D materials in distinct ways. In this regard, this thesis focuses on the study of molecular functionalization of 2D materials, by deliberately selecting a wide range of molecule-2D material combination and studying the resulting physical, chemical, optical and electrical properties. The thesis is structured in the following 10 chapters:

Chapter 1 introduce a general scope of the research and the structure of the thesis.

Chapter 2 describes basic physical and chemical properties of the two-dimensional semiconducting materials that are studied in this thesis by reviewing their crystal structure, electronic properties, optical properties and offers state-of-art of the molecular functnionalization of these 2D semoconductors.

Chapter 3 introduces the basic properties of the molecules that are utilized to functionalize 2D materials in this thesis, including common solvent molecules, metal phthalocyanines, pyridines, photoswitchable azobenenes, and ionic surfactants.

Chapter 4 explains the fundamentals of the experimental techniques that are exploited in this thesis, covering both cutting-edge fabrication and characterization methods.

Chapter 5 shows how aromatic solvent molecules could influence the optical properties of monolayer transition metal dichalcogenides (TMDs), i.e., molybdenum disulfide (MoS_2) and tungsten diselenide (WSe_2).

Chapter 6 demonstrates the tuning of electrical and optical properties of few-layer black phosphorus (BP) by common solvent molecules, especially when via the fabrication of field-effect transistors (FET).

Chapter 7 explores how ionic surfactant molecule could boost the performances of few-layer indium selenide (InSe), eventually forming high-performance FETs, phototransistors, Schottky diode and PN junctions.

Chapter 8 reports a novel strategy for doping 2D materials benefitting from the molecular dipole of axial-coordinated ligands on metal phthalocyanines.

Chapter 9 demonstrates photo-modulated reversible molecular doping enabled by free-standing azobenzene ligands. The reversible doping is able to dynamically switch the threshold voltage of MoS_2, WSe_2, also the controlling the PN junction flow direction of Schottky junction. Finally, a light-modulated logic-in-memory device is achieved by exploiting the full potential of the photoswitchable molecular unit on 2D materials.

Chapter 10 shows the conclusions of the research presented in the thesis and discusses the short-term and long-term perspectives of the this work.

Chapter 2 Two-dimensional Semiconducting Materials

2.1 The family of 2D materials

Two-dimensional (2D) materials are layered materials possessing an atomic thickness.[1] They have attracted enormous attention in the last decade for their unique physical and chemical properties. To date, with more and more ultrathin layered materials being explored, the family of 2D materials have expanded notably enabling to explore novel physical phenomena. According to different chemical compositions and crystal structures, they could be classified as metallic, semiconducting, insulating in terms of electronic properties, with bandgap ranging from several meV to 6 eV (see **Figure 2.1**). Moreover, in any given 2D material the bandgap magnitude depends on its thickness. These features rise significant interests in optoelectronics. The strong Van der Waals (vdW) interaction among adjacent 2D sheets enables the formation of stacks, known as vdW, overlapping the same or different 2D materials. Those made with different materials are called vdW heterostructures and represent a viable approach to achieve functional diversification and property modulation opening novel route for exploration in sciences.[17-19]

In this thesis, to gain a broad sight on how molecules could affect the optical and electronic properties of 2D materials and their related heterostructures, we have involved three classes of layered materials with distinct crystal structures which are: a) transition metal dichalcogenides (TMDs); b) black phosphorus (BP); c) indium selenide (InSe). In this chapter, a brief introduction of the physical and chemical properties of each class of the materials will be presented, followed by the vdW heterostructures based on these materials and discussion on their optoelectronic properties. Lastly, we give a general principles and the state-of-art of molecular functionalization of 2D materials.

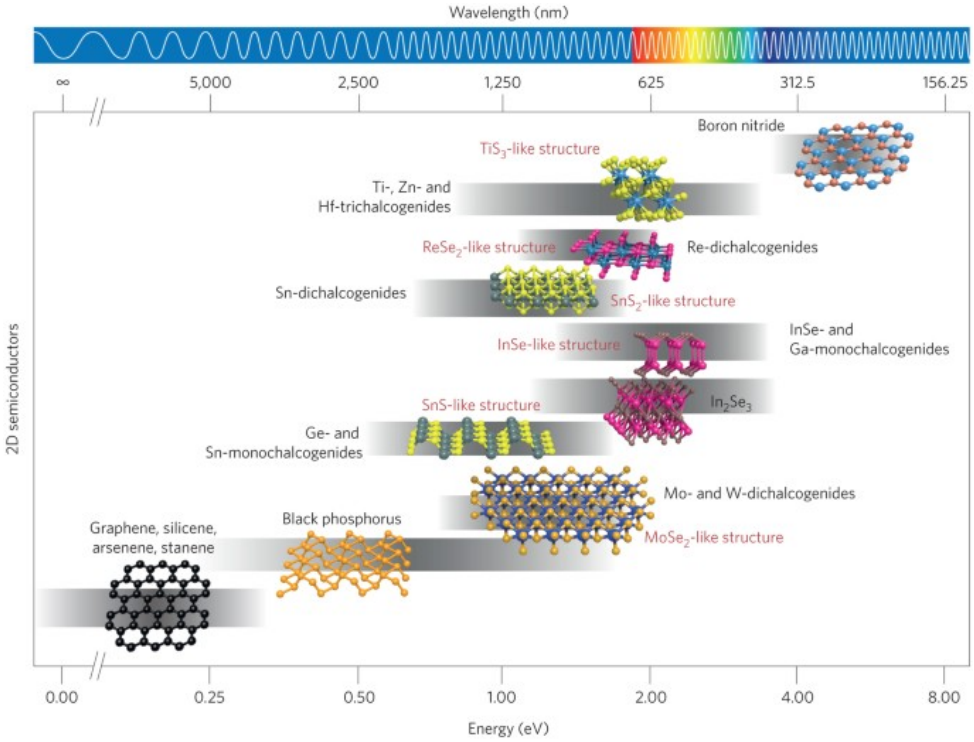

Figure 2.1: Bandgap values and corresponding wavelengths of representative materials in the 2D materials family. Figure reproduced from Ref [20].

2.2 Transition metal dichalcogenides (TMDs)

Transition metal dichalcogenides (TMDs) are the most studied class of 2D semiconducting materials. These materials benefit from layer-dependent characteristics of electronic structure, to be specific, indirect-to-direct bandgap transition from bulk to monolayer, allowing a large range of applications from (opto)electronics to valleytronics. This class of compound has many possibilities of combinations, in particular, transition metal being Ti, Zr, Hf, V, Nb, Ta, Mo, W, Tc, Re, (highlighted in blue, red, green and purple in **Figure 2.2a**) and chalcogen being S, Se and Te (marked in orange in **Figure 2.2a**).

However, not every material composed by the above-mentioned elements show excellent electronic and optical properties. Some materials are also chemically unstable to manipulate. Considering these side-effects, Group XI transition metal chalcogenides are more commonly studied, which are MoS_2, $MoSe_2$, $MoTe_2$, WS_2, WSe_2, WTe2. These TMDs share similar crystal

structure, as shown in **Figure 2.2 b-d**. They exhibit two major phases, i.e. 2H (trigonal prismatic, D_{3H} symmetry, **Figure 2.2b**) and 1T (trigonal antiprismatic, O_H symmetry, **Figure 2.2c**). As shown in **Figure 2b** and **c**, the difference between crystal structures resides in the positions of upper and bottom layer of chalcogen atoms bonded with transition metals where 2H phase displays "AbC" and 1T phase AbA" stacking sequence, respectively. The lattice group difference among phases defines distinct electronic properties for TMDs, this will be discussed in detail in **Section 2.2.1.** The single layers are stacked via vdW forces, with interlayer distance of ~6.5 Å for MoS_2 (**Figure 2.2d**). While the vdW force is strong, by top-down exfoliation approach, one can isolate monolayer with low yield. The prevailing exfoliation method for producing high-quality monolayers is mechanical exfoliation using scotch tape (see **Section 4.2.2**). Other exfoliation methods, such as gold-assisted exfoliation, provide the possibility to produce centimeter-sized large monolayers.[21,22]

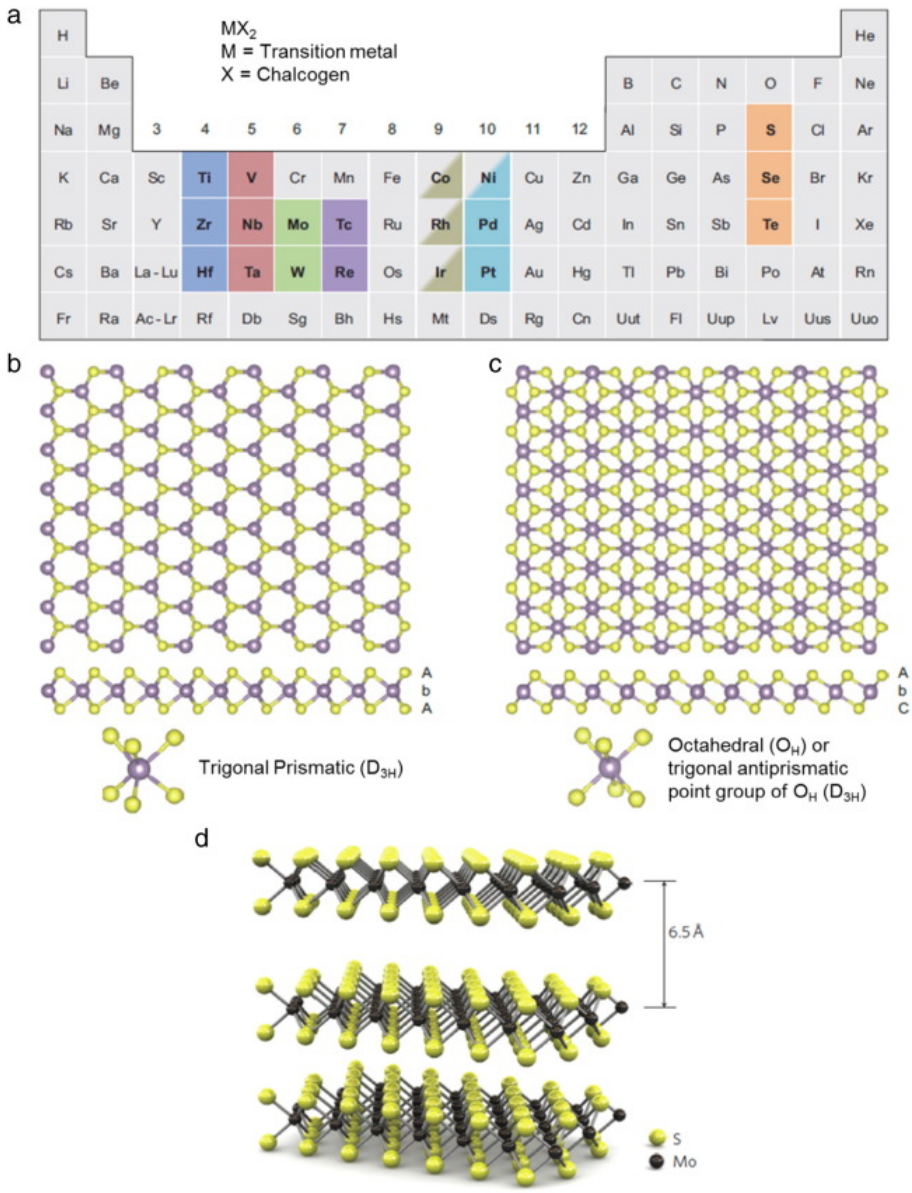

Figure 2.2: Crystal structure of TMDs. (a) Elements (highlighted) in the periodic table are those able to form layered structures of TMDs in the periodic table. (b) Top view and section view of single-layer TMD with trigonal prismatic coordination structure (2H phase). (c) Top view and section view of single-layer TMD with octahedral coordination structure (1T phase). Atom color code: purple, metal; yellow, chalcogen. (d) Structure of a 3-layer MoS_2 presenting the interlayer distance of 6.5 Å. Figure reproduced from Ref [23].

2.2.1 Electronic properties of TMDs

The electronic properties of 2D TMDs are key to understand its nature. As mentioned in the last section, different phases of the material result in distinct electronic properties. Taking MoS_2 as example, 2H phase is semiconducting, with a bandgap of ~1.8 eV in monolayer samples, while in 1T phase, the material becomes metallic (**Figure 2.2a**). 2H phase is thermodynamically more stable and its semiconducting properties are more appealing for electronics. Hence I decided to focus particularly on TMDs in their 2H phase.

By varying the number of layers stacked in the same material, the band structure changes dramatically. As is depicted in **Figure 2.2b**, in bulk MoS_2, the valence band maximum (VBM) lies at the Γ point, while the conduction band minimum (CBM) is located at K point, giving an indirect bandgap of 0.88 eV. By decreasing the layer number down to 2 layers, enlargement of bandgap is observed yet remains the Γ to K transition. Further, upon thinning the material to monolayer, the bandgap becomes direct at K point and the energy increases to 1.71 eV.[24] The lack of inversion symmetry in monolayer MoS_2 results in spin splitting at the electronic band.[24] Similar properties are observed with other 2D TMDs. However, by varying the chemical compositions, the energies of CBM and VBM compared to vacuum level are also affected. The increase of atomic number of chalcogen element (from S, Se to Te) induces an increased CBM and VBM (except for WTe_2). Similarly, by increasing the atomic number of transition metal from M to W, the CBM and VBM increase. This is because the CBM mainly originates from the repulsion between the dz^2 orbital of Mo and p_x and p_y orbitals from S. The VBM is mainly consisted of the $d_{x^2-y^2}$ and d_{xy} orbitals of Mo and the p_x and p_y orbitals of S. Hence, the d orbitals of W being higher than S, resulting in CBM and VBM of WX_2 higher than MX_2 (**Figure 2.2d**).[25]

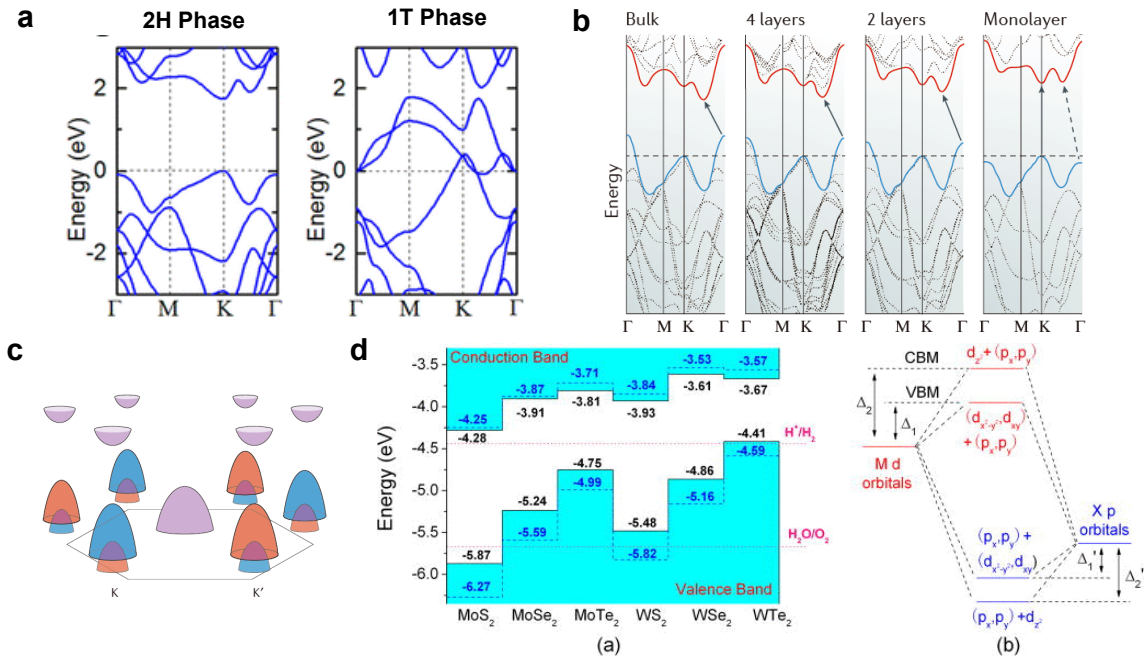

Figure 2.3: Electronic properties of 2D TMDs. (a) Electronic band structure of MoS_2 in 2H and 1T phase. Adapted from Ref [26] (b) Evolution of the band structure of 2H-MoS_2 calculated for samples of decreasing thickness. Adapted from Ref [24] (c) Schematic representation of the band structure of monolayer 2H-MoS_2, showing the spin splitting of the bands at the K and K′ points on the corners of the Brillouin zone. Orange and blue colours indicate up and down spin polarization. Adapted from Ref [24] (d) Left: Calculated band alignment for MX_2 monolayers in comparison with indicate the water reduction (H^+/H_2) and oxidation (H_2O/O_2) potentials (dotted lines). The vacuum level is taken as zero reference. Right: Schematic of the origin of CBM and VBM in MX_2. Adapted from Ref [25]

2.2.2 Optical properties of TMDs

The optical properties of TMDs have been intensively studied during the last years, due to their extraordinary versatility of excitonic landscape. Excitons are Coulomb interacted electron-hole pairs typically formed when the material absorbs photon energy. 2D TMDs feature huge Coulomb interactions due to quantum confinement, resulting in the formation of many-body quasi-particles while are rare to be observed in other types of materials. These unconventional quasi-particles include biexitons, trions, dark excitons, interlayer excitons, etc.[27,28] Large binding energies were also found in TMDs, in the range of ~0.5 eV, being extensively larger than traditional materials such as GaAs (**Figure 2.4a** and **b**).[29] The direct bandgap in the monolayers enables the recombination of electron and hole without excess phonon momentum, resulting in high quantum yield in the monolayer, which is reflected in the photoluminescence (PL) spectroscopy (**Figure 2.4c**). These combined characteristics together with the large covered spectrum range

make 2D TMDs an extremely promising candidate for light-matter interaction devices such as photovoltaics, light emitting devices, photodetectors and so on.

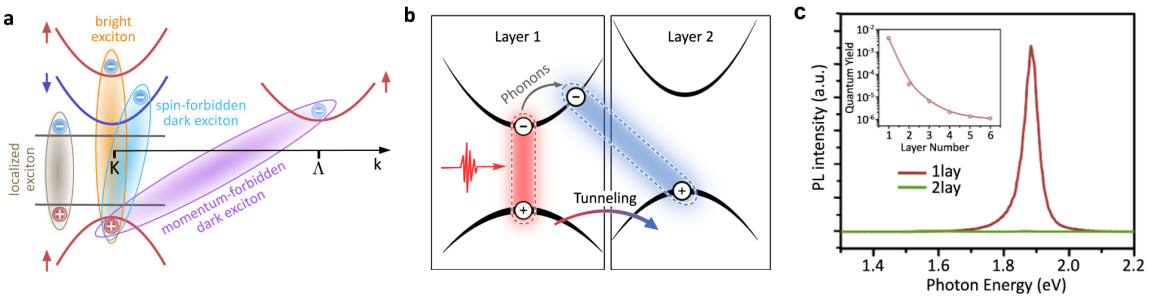

Figure 2.4: Excitons in TMDs. (a) Types of excitons in monolayer TMDs. (b) Formation of interlayer excitons. (c) Layer-dependent photoluminescence quantum yield in TMDs. Figure adapted from Ref. [27]

The excitonic properties of 2D TMDs could be tuned by external factors. In 2012, J. Shan reported the gate-modulated photoluminescence in MoS_2 FET (**Figure 2.5a**), revealing the presence of tightly bound state of two electrons and a hole, denoted as trion which appears at lower energy than neutral exciton. The energies of exciton and trion are defined by

$$\omega_A - \omega_{A-} = E_{A-} + E_F$$

Here ω_A and ω_{A-} are energies of exciton and trion, respectively. The ω_{A-} is thus the minimum energy required to remove one electron from the trion to form exciton. E_{A-} is the trion binding energy and E_F is the Fermi energy. The trion binding energy E_{A-} is extracted to be 18 meV.[30] This finding suggests that charge carrier density in monolayer MoS_2 strongly affects the PL of MoS_2, which is essential for putting them in applications. Later on, W. Yao and X. Xu reported the presence of both positively charged (X^+) and negatively charged (X^-) excitons in monolayer WSe_2, together with valley polarized excitons and trions.[31] Now at 4K temperature, even 5-partical charged biexciton can be observed.[28]

The optical properties of 2D TMDs can be modulated not only via the electrical gate, but also by means of chemical doping. This suggests that the variation of charge carrier density in 2D TMDs would largely modulate PL. In 2013, S. Mouri demonstrated the chemical doping of monolayer MoS_2 by 2,3,5,6-Tetrafluoro-7,7,8,8- tetracyanoquinodimethane (F4-TCNQ) and Nicotinamide adenine dinucleotide (NADH). The molecules, being either p-dopant or n-dopant, could effectively shift the Fermi level of MoS_2, resulting in variation of the preferred formation of exciton or trion in the material. The ratio of trion/exciton defines the total PL intensity, considering a much larger decay rate in trion than exciton.[32] Other chemical approaches, which are mostly mediated by suppressing the nonradiative recombination induced by lattice defects of TMDs to raise the

quantum yield of the PL, have also been demonstrated with the superacid treatment [33] and oxygen plasma treatment [34].

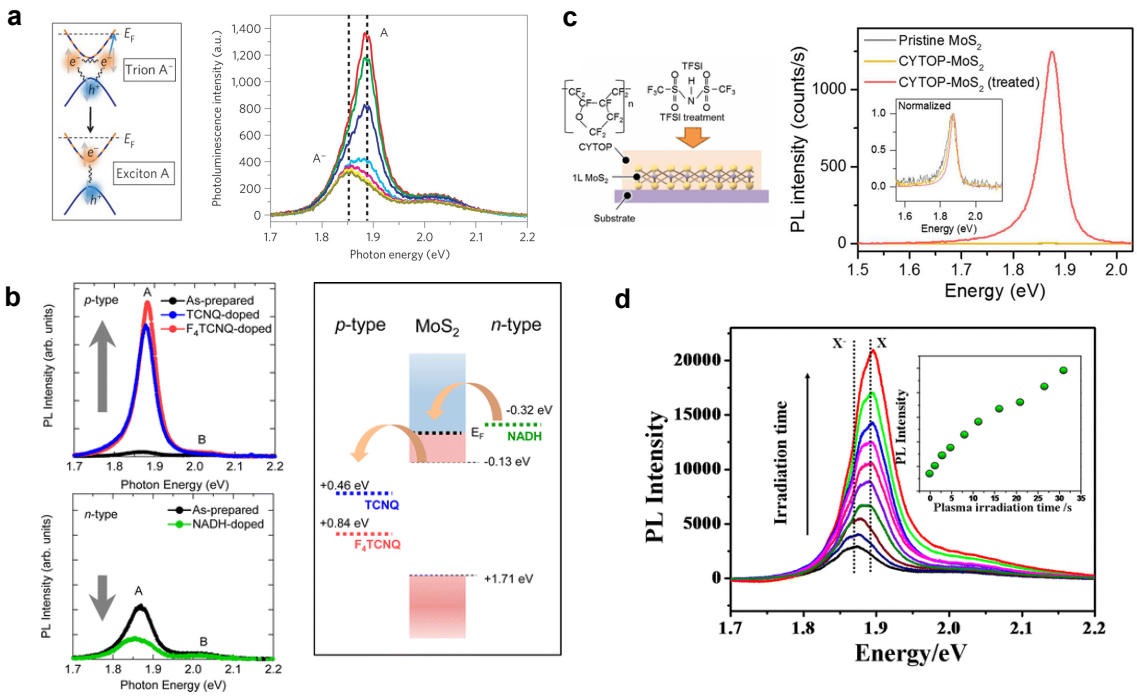

Figure 2.5: Manipulating photoluminescence intensities of 2D TMDs. (a) Back-gate-dependent photoluminescence of monolayer MoS_2. Adapted from Ref.[35] (b) Chemical doping enabled photoluminescence tuning. Adapted from Ref.[32] (c) Photoluminescence enhancement via superacid treatment. Adapted from Ref.[36] (d) Photoluminescence enhancement by oxygen plasma treatment. Adapted from Ref. [34] Other light-matter coupling affecting the optical properties have also been deeply studied, such as by designing periodic plasmonic metal patterns on top or bottom of 2D materials, the resonance matching between the nanostructures and 2D TMD will result in giant PL enhancement. [37]

2.3 Black phosphorus (BP)

BP has risen great interest since 2014, after the first demonstration of few-layer BP field-effect transistors.[4] The latter have exhibited high field-effect mobilities, which outperforms TMDs without the need of specific treatment. Such high performances paved the way towards their use as photodetectors, energy conversion, as well as bio-degradable materials. [38-41] BP shows higher chemical reactivity than TMDs, providing more possibilities for its covalent functionalization. Furthermore, as it contains phosphorus which is a non-metallic non-toxic element, BP is biocompatible thus suitable for biomedical approaches.

Unlike layered TMDs whose composing elements are transition metals and chalcogens, black phosphorus (BP) is a simple substance among the numerous allotropes of the phosphorus family with other allotropes being red phosphorus, white phosphorus, purple phosphorus, etc. Out of the three phases of black phosphorus, orthorhombic, simple cubic, and rhombohedral, only the orthorhombic phase (D_{2h}^{18} point group) is semiconducting, as shown in **Figure 2.6**. The crystal structure of BP is anisotropic in the XY plane, denoting as armchair and zigzag (**Figure 2.6b**). The interlayer distance, as shown in **Figure2.6a**, is a bit smaller than TMDs, being 5.3 Å. [42]

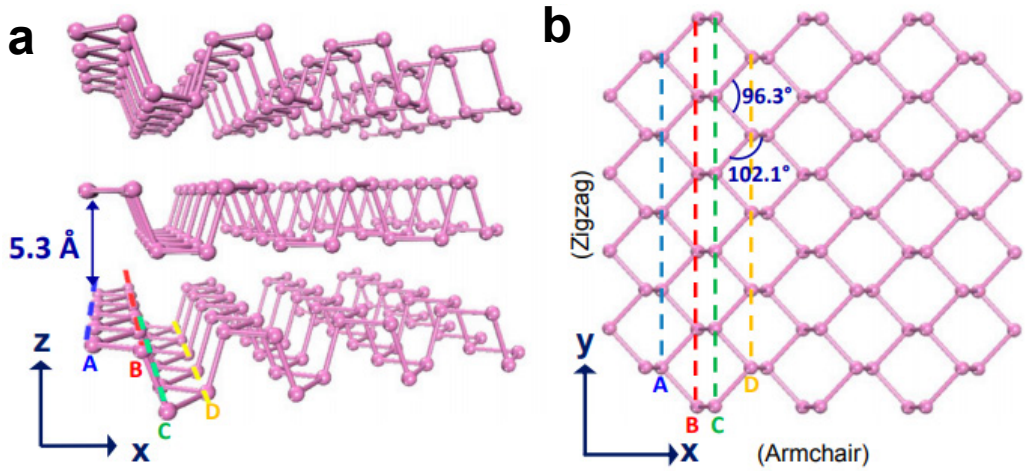

Figure 2.6: Crystal structure of BP. (a) Side view of the BP crystal lattice with interlayer distance of 0.53 nm. (b) Top view of the lattice of monolayer BP. The bond angles are 96.3° and 102.1°, showing the anisotropic structure. Adapted from Ref.[42]

2.3.1 Electronic properties of BP

Similarly to TMDs, the band structure of BP is also layer-dependent. The DFT calculated electronic band structure is shown in **Figure 2.7** where an increase of bandgap is observed with the evolution of thinning the layers. The bandgap of single layer BP is found to be ~1.8 eV, while in few-layers, it drops rapidly to ~0.3 eV. The narrow bandgap determines distinct features of BP, including transport both in electrons and holes, resulting in ambipolar field-effect transistors (FETs) with high electron and hole mobilities, excellent photoresponse at mid-infrared (MIR) region and extreme sensitivity for chemicals, etc.

BP have been widely demonstrated as electroactive materials in FETs. **Figure 2.8** shows the first demonstration of few-layer BP FET on Si/SiO_2 substrate. The FET, as shown in Figure **2.8b**, exhibits p-type dominant ambipolar transfer with high I_{on}/I_{off} ratio up to 10^6. The hole mobility increases up to ~1000 cm^2/Vs at room temperature, being much higher than TMDs which is always at the range of 10^1 to 10^2 cm^2/Vs, and also higher than the average mobility of silicon around 500 cm^2/Vs.[4] Unipolar FETs could also be achieved by contact engineering and thickness modulation, as shown in **Figure 2.8b-c**. High mobility unipolar n-type transport could be achieved with low work function Aluminum contact with flake thickness around 3 nm, enabling effective charge injection from the metal for to the conduction band, resulting in electron mobility up to ~630 cm^2/Vs at 80K (**Figure 2b**).[43] Alternatively, Van der Waals contacts fromed by hexagonal boron nitride (h-BN) under Cobalt (Co) contact, serving together as a top electrode, could also obtain high-performance unipolar electron transport. The lattice matching of Co and h-BN could greatly lower the work function of Co forming a Schottky-barrier free contact, therefore facilitates electron injection to BP channel. The electron mobility mounts up to ~4190 cm^2/Vs at 40K. (**Figure 2.8c**)[44]

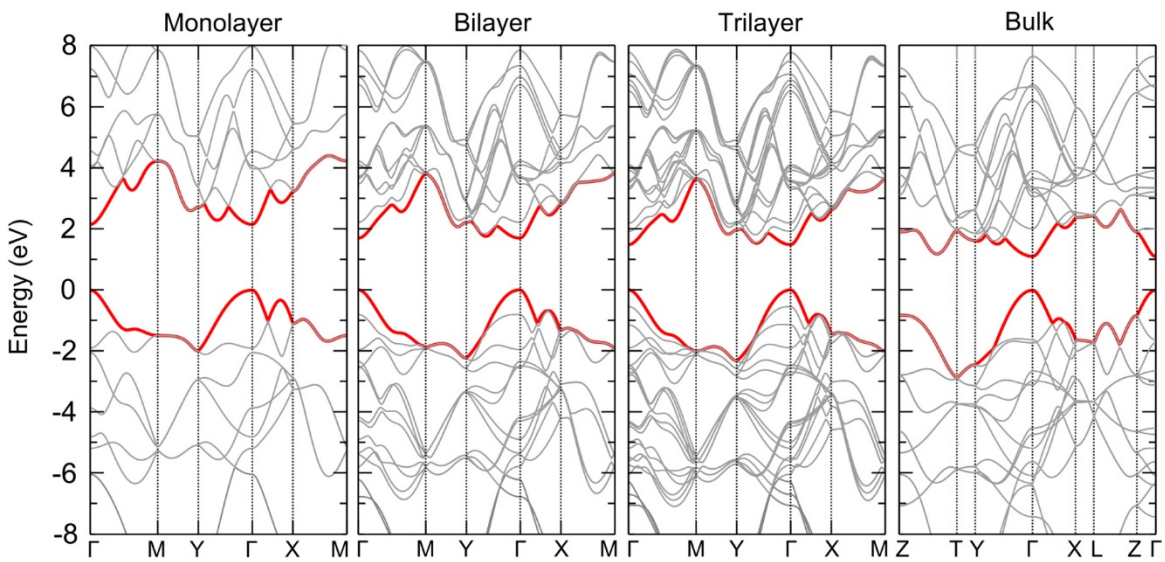

Figure 2.7: Band structure BP of different layer numbers. Adapted from Ref. [45]

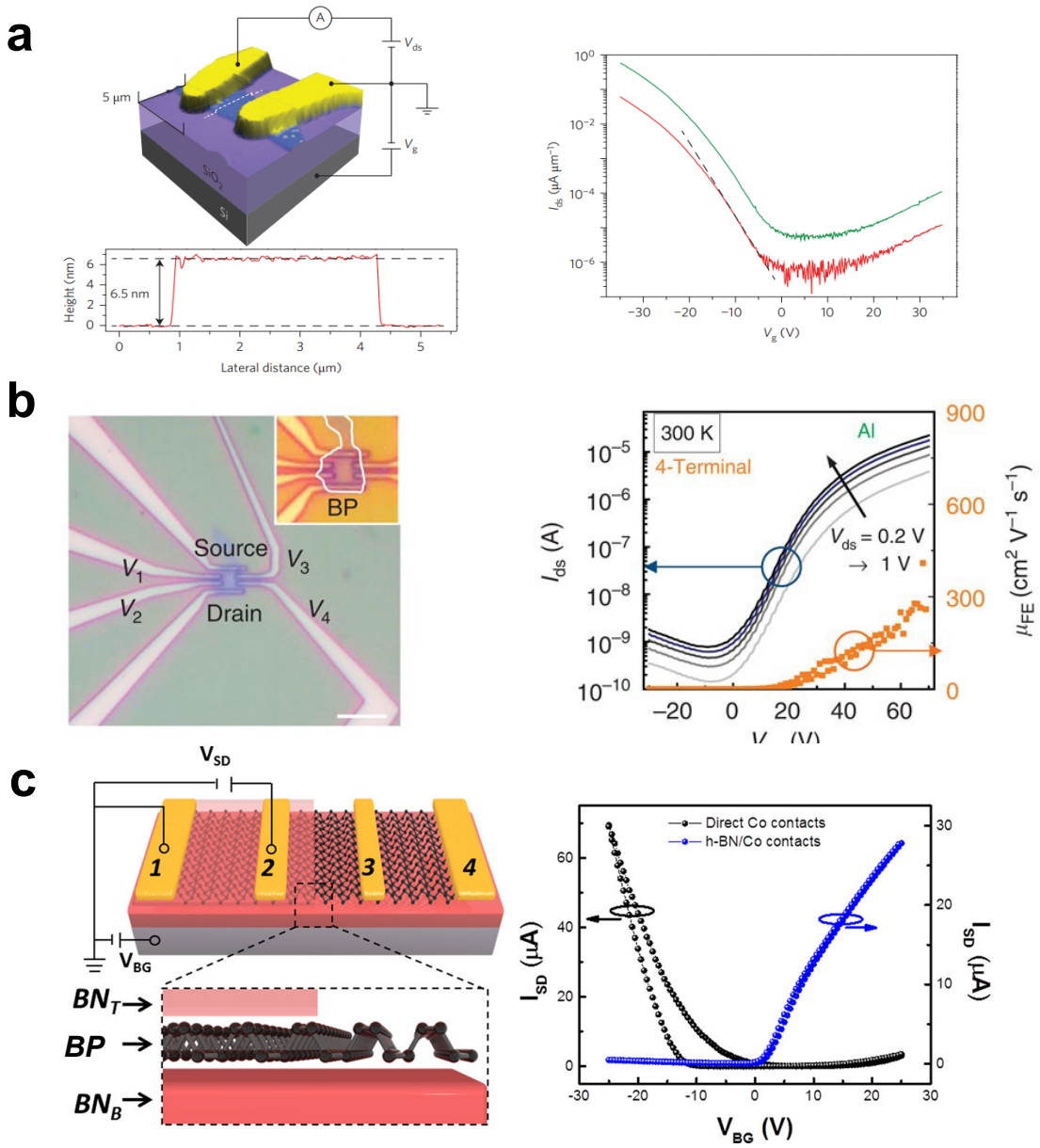

Figure 2.8: Few-layer black phosphorus field-effect transistors. (a) Ambipolar black phosphorus FET. Left: Device structure and AFM height profile of the flake in the semiconducting channel. Right: Transfer curve (Ids-Vg) of few-layer BP with drain–source voltages of 10 mV (red curve) and 100 mV (green curve). Adapted from [4] (b) N-type unipolar black phosphorus FET. Left: Device structure. Right: Transfer curve (Ids-Vg) of few-layer BP and related mobility values. Adapted from Ref.[43](c) Van der Waals contact BP FET. Left: Device structure of the Van der Waals contact. Right: Transfer curve (Ids-Vg) of few-layer BP showing both N-type and P-type unipolar FET could be achieved. Adapted from Ref.[44].

2.3.2 Optical properties of BP

The anisotropy in the crystal structure gave rise to the anisotropic optical response in black phosphorus. The photoluminescence intensity is largely dependent on the polarization of incident light and the detection angle. As demonstrated in **Figure 2.9b** (the corresponding crystal structure and the optical image of the sample is shown in **Figure 2.9a**), F. Xia et al were able to measure the PL with X (armchair) and Y (zigzag) direction of polarization.[46] The excitonic states are more dominated in the X direction than the Y direction, resulting in larger PL intensity. As PL emission are originated from these anisotropic excitons, detection from the Y axis results in very low PL yield. Similar anisotropic behavior could be found in Raman spectra, where the A_g^2 peak signifies the motion in the armchair direction. As a result, the intensity of the A_g^2 mode is highly dependent on the polarization angle, which could be found in **Figure 2.9c**. [46]

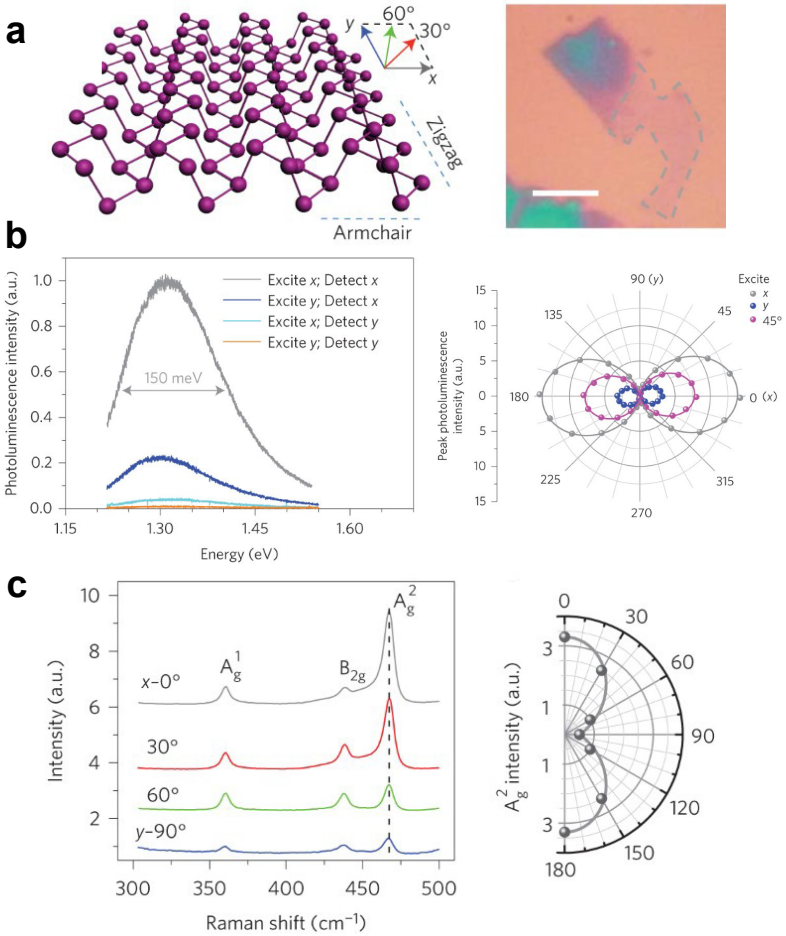

Figure 2.9: Optical properties of monolayer black phosphorus. (a) Crystal structure and optical microscope image of monolayer black phosphorus. (b) Photoluminescence spectra of monolayer black phosphorus with different excited and detected angle. (c) Raman spectra of monolayer black phosphorus with linearly polarized laser excitation. Adapted from Ref.[46]

2.3.3 Optoelectronic properties of BP

BP emerges as an important material for photodetection due to its small bandgap, which allows it to be applied for the detection of mid-infrared (MIR) light. The high carrier mobility and the large ON channel current give rise to large absolute photocurrent value and correspondingly large photoresponsivity. **Figure 2.10** reports the effective photodetection of 3.39 μm of IR light with high responsivity up to ~82 A/W at 1 nW, in vast contrast to other 2D materials such as graphene and TMDs.[47] The BP photodetectors are also highly polarization-dependent, where the photocurrent also shows anisotropy in armchair and zigzag direction, with the former being 5 times larger than the latter. [48,49]

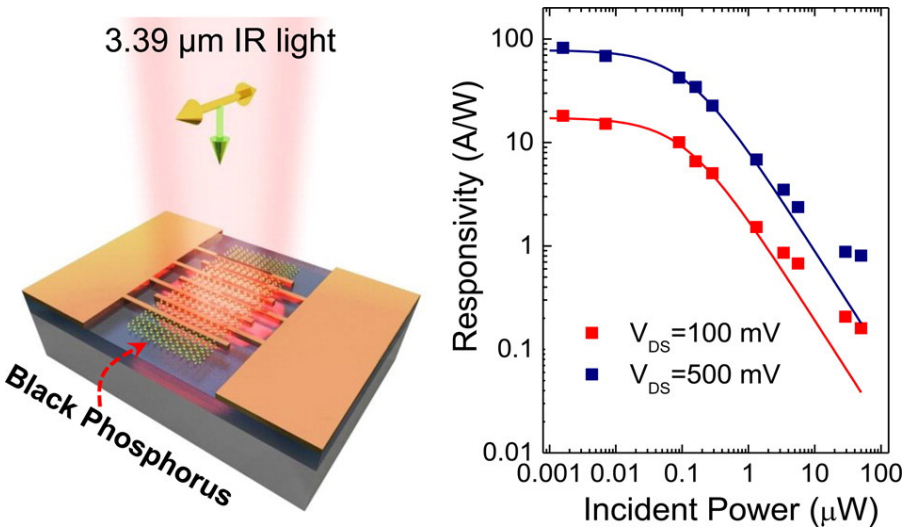

Figure 2.10: Black phosphorus mid-infrared (MIR) photodetector. Left: Demonstration of device structure. Right: Photoresponsivity of BP photodetector under different light power. Adapted from Ref.[48]

2.3.4 Chemical properties of BP

Black phosphorus is a highly reactive material which could react easily with oxygen and water. Without the participation of water, BP is oxidized to PO_x with oxidation state greater than +3 and smaller than +5. Intermediate structures are also possible, such as P_4O_9, P_4O_8, and P_4O_7. [50] While with the presence of water, PO_x could further turn to phosphoric acid by:

$$P_4O_{10} + 6H_2O \rightarrow 2H_3PO_4$$

Compositional analysis revealed that the presence of a small amount of 5% O_2 and 2.3% H_2O in Ar, the oxide layer could form with a thickness of 3 nm in 150 min.[50] Considering the percentage of oxygen and water in air to be 21% and 2~3% respectively, the air-stability of BP raises the concern for it to be manipulated correctly jeopardizing technological applications. Especially, the degradation of BP not only affects its electrical and optical properties, but since the final product of the degradation, i.e., phosphoric acid, is in liquid phase at room temperature, the flake convers to droplets, as can be seen in **Figure 2.11a** and **b**.[45] [51]

It is therefore essential to find ways to protect BP against degradation. Though many works have demonstrated effective encapsulation by staking h-BN on top of BP against air exposure, these approaches could not be applied to large-area fabrication, nor be extended to the liquid-exfoliated materials. [44,52,53]. As phosphorus provide large opportunities for chemical reactions, the possibility for chemical approach to enhance the stability of BP becomes very promising. For example, **Figure 2.11c** and **f** reports a recent work exploiting the protective chemistry using densely-packed Al^{3+} to decrease the reducibility of BP followed by forming Al-S bond with 1,2-benzendithiol in order to successfully protect BP flakes against air degradation for two months.[54] Similarly, coordination chemistry could also be extended to the chemical encapsulation of BP by growing Ti complexes on BP.[55] Oxidation of BP is on the one hand detrimental to the material, yet on the other hand, could be harnessed in forming stable oxidation layers. For example, in **Figure 2.11d** and **e**, the thin layer of PO_x could serve as platform for growing aluminum oxide layer and self-assembled silanes. [55,56]

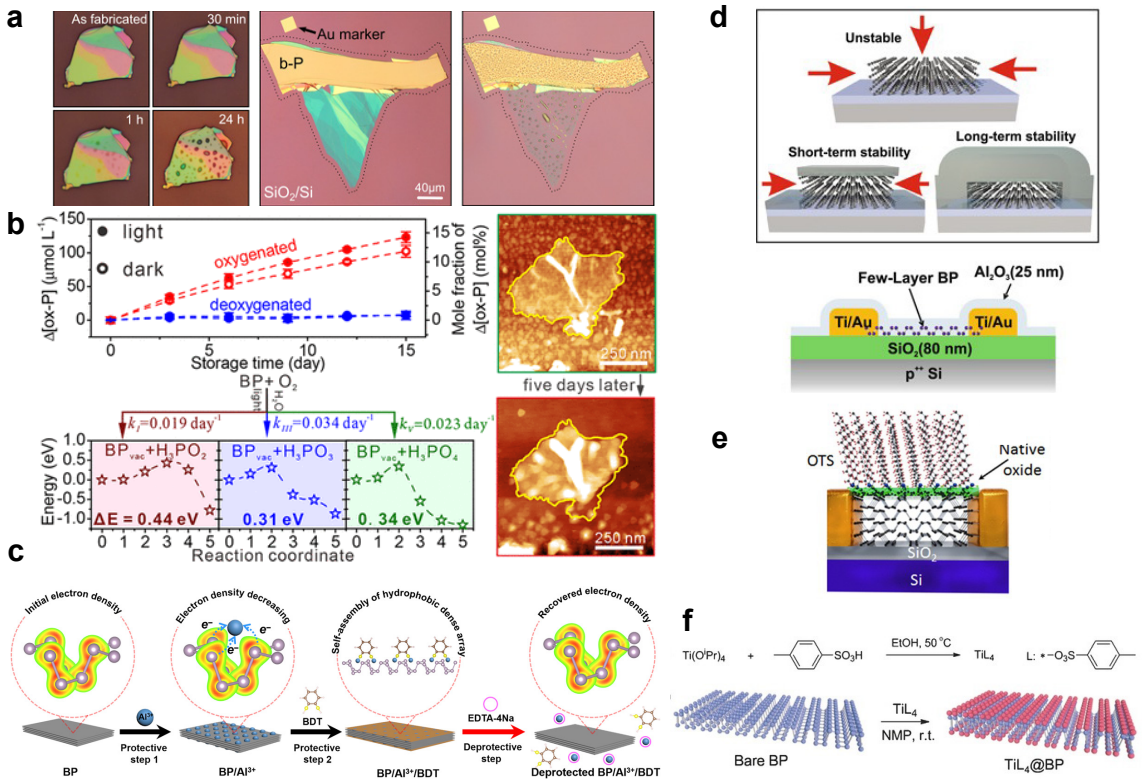

Figure 2.11: Stabilization of black phosphorus. (a) Surface degradation of few-layer BP. Adapted from Ref. [45] (b) Degradation chemistry of BP. Adapted from Ref. [51] (c) Surface functionalization of BP by protective chemistry. Adapted from Ref. [54] (d) Aluminum oxide encapsulation of BP for long-term stability. Adapted from Ref. [56] (e) Passivation of surface of few-layer BP by a monolayer of self-assembled silanes. Adapted from Ref. [57] (f) Surface coordinative functionalization of black phosphorus. Adapted from Ref. [55]

2.4 Indium selenide (InSe)

In addition to transition metal dichalcogenides (TMD, MX_2) and black phosphorus, an emerging class of 2D materials, transition metal monochalcogenides (TMM, MX) has attracted large attention in recent years. This class of materials include indium sulfide (InS), indium selenide (InSe), gallium sulfide (GaS) and gallium selenide (GaSe). Among them, InSe have shown superior properties as compared to TMDs both in the bulk form and in few-layers, such as higher charge carrier mobility, better optoelectronic response and extraordinary plasticity. The crystal structure of InSe is shown in **Figure 2.12a**. There are 3 phases of InSe, denoting ε, β, and γ. The phase ε belongs to the D_{3h}^{1} non-centrosymmetric point group and the hexagonal β phase is belonged to the D_{6h}^{4} centrosymmetric point group. The γ phase is rhombohedral and belongs to the C_{3V}^{5} non-centrosymmetric space group. The interlayer stacking is ABCABC with each layer shifted along the horizontal plane. [58] The interlayer distance is around 0.8 nm. Electronic band structure of InSe is distinct from TMDs in the direct-to-indirect band transition, where the indirect bandgap occurs in monolayer where the conduction band minimum (CBM) lies in the Γ-point in the Brillouin zone, and the valence band maximum (VBM) is at the K-point. While in bilayer, few-layer and bulk material, both VBM and VBM is at Γ-point (**Figure 2.12b**).[59] Similar to TMDs, the bandgap energy increased with respect to the decrease of layer number, of which monolayer being 2.9 eV, bilayer with sharp decrease being 2.0 eV. The bulk material (> 5 L) is found to be near 1.2 eV. Noteworthy, the indirect bandgap also largely decrease the quantum yield of photoluminescence in monolayer InSe (**Figure 2.12c**).[60] Another peculiar property of InSe, which is recently discovered in the year of 2020, lie in the extraordinary mechanical properties in the bulk material (**Figure 2.12d**). It shows ultra-low in-plane modulus due to the weak interlayer In-Se bond and the rigid In-In bond, enable to ultra-flexible deformation and high plasticity similar to metallic materials.[61]

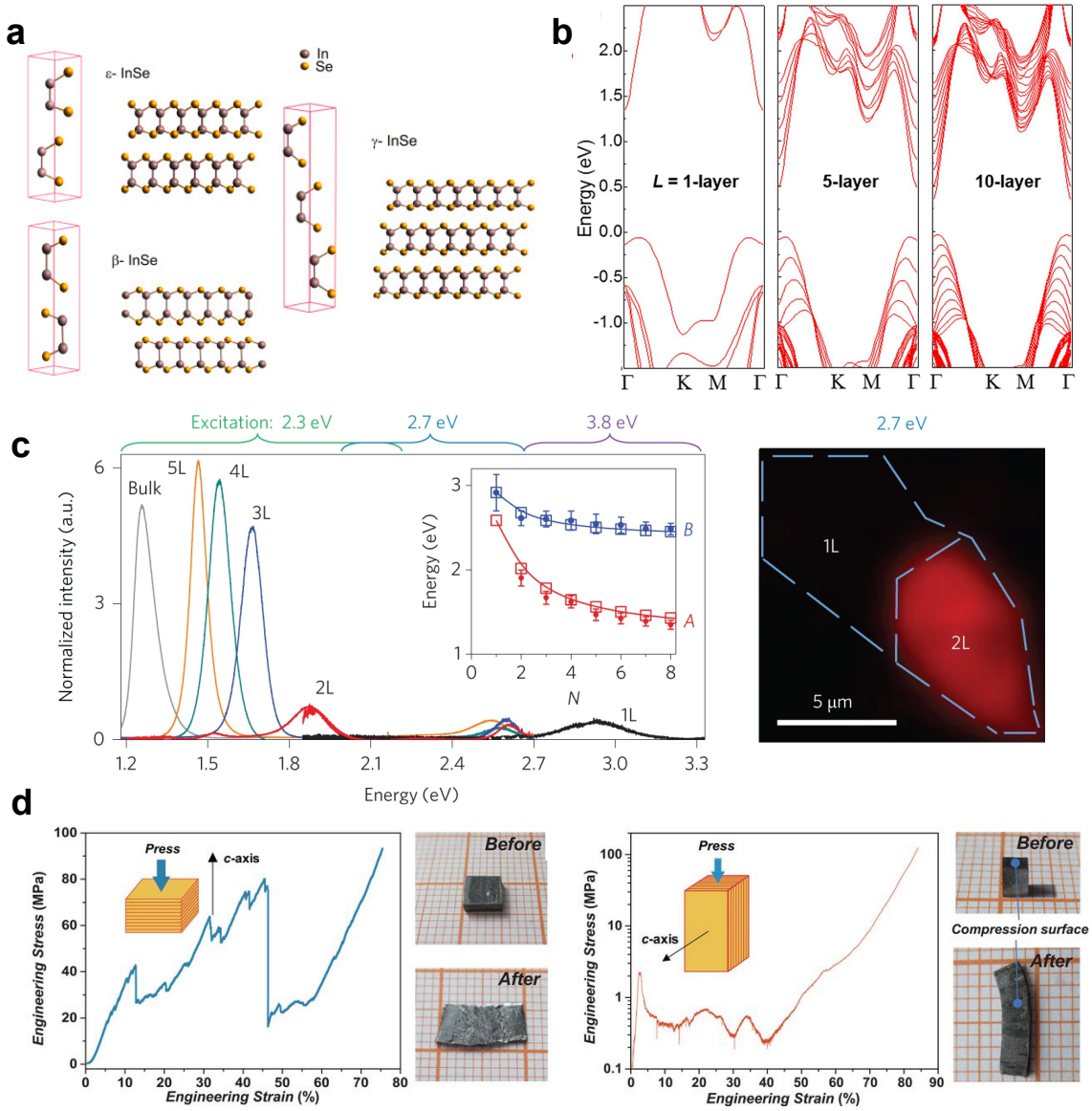

Figure 2.12: Fundamental properties of InSe. (a) Crystal structure of indium selenide (InSe) with three crystal phases. Adapted from Ref.[58] (b) Electronic band structure of 1-layer, 5-layer and 10-layer InSe. Adapted from Ref. [59] (c) Left: Photoluminescence spectra of InSe in different layer numbers. Right: Optical microscope image of the photoluminescence in monolayer and bilayer InSe. Adapted from Ref.[60] (d) Mechanical properties of bulk InSe crystal. Adapted from Ref. [61]

2.4.1 Electronic properties of InSe

In the last few years, many researches have successfully demonstrated ultra-high electron mobility in few-layer to multi-layer InSe field-effect transistors. Early in 2015, researchers already demonstrated Hall mobility of InSe over 2000K at low temperature on poly(methyl methacrylate) (PMMA) (**Figure 2.13a**). It is shown that the dielectric material is key in the mobility engineering

of InSe to reveal its intrinsic mobilities. This part is also discussed in detail in the Section 7.3.1 in Chapter 7. High electron mobility could also be achieved through surface encapsulation, by screening the charge impurities on the surface of the material which would perturb the carrier scattering in the lattice. For InSe FET, traditional approaches of surface functionalization, such as surface oxide and PMMA encapsulation have been used. These methods, as is shown in **Figure 2.13c-d**, proved to raise the electron mobility up to 10^3 cm^2/Vs. Other expensive surface encapsulation, such as using a indium layer offering both electron transfer to InSe and protection to exposure to air, has also been adopted recently, resulting in ultra-high mobility up to 10^4 cm^2/Vs at 80K.[62] Here it is notorious that InSe is also unstable in air, reacting with oxygen forming InO_x. Though InO_x is not detrimental to the electronic properties of InSe as PO_x for black phosphorus (BP), the thin layer of surface oxide often results in charge trapping and mobility decreasing, therefore raise the concern for application of high-performance and highly stable electronics. [63]

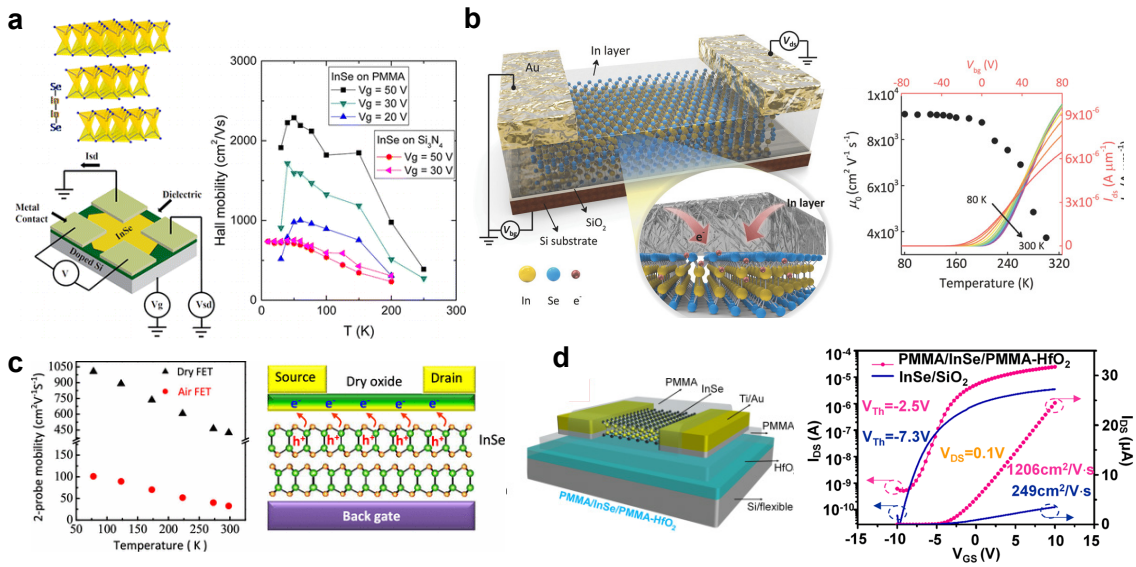

Figure 2.13: High mobility InSe field-effect transistors. (a) Dielectric-dependent mobility of InSe. Adapted from Ref.[64] (b) High electron mobility by indium encapsulation. Adapted from Ref.[65] (c) Surface oxide mediated high mobility of InSe. Adapted from Ref.[62] (d) Polymer-encapsulated high-mobility InSe FET. Adapted from Ref.[66]

2.4.2 Optoelectronic properties of InSe

Despite the ultra-high electron mobility resides in InSe FET, the material attracts more attention as photodetectors for its high photoconductivity in few-layers. In a phototransistor, the

photoconductivity is determined by the photocurrent that was generated by the separation of electron-hole pairs induced by the electrical field of the applied drain-source bias (V_{ds}). The type photocarrier (electrons or holes) generation is determined by the transit time ($\tau_{transit}$) of electrons and holes where

$$\tau_{transit} = \frac{L^2}{\mu V_{ds}}$$

where L is the channel length, μ is the mobility of the electrons or holes. It is obvious to see that the larger the charge carrier mobility, the shorter the transit time, and the more photocarriers of this type flow across the channel during the light illumination, resulting in larger photocurrent. (**Figure 2.14a**) [67] For InSe, with the ultra-high mobility of electrons in the transistor, a reasonable high photocurrent is usually observed.

Photogating effect is also commonly observed when the charge carriers are trapped in the localized states (surface states, defect, etc.) of the semiconducting material. A vertical electrical field is therefore induced by the potential difference within the positive and negative photoinduced charges, therefore shift the Fermi level and shift the transfer curve of the phototransistor. (**Figure 2.14b**) [67] Sometimes, the photogating effect is observed in InSe phototransistor because of the rich oxidative defect states in InSe.

The common parameters to evaluate photoresponse of a photodetector are responsivity (R), external quantum efficiency (EQE), photoresponse time, noise equivalent power (NEP) and detectivity (D*). The detailed calculation is demonstrated **in the** Section 7.3.1 **in** Chapter 7. R is considered to be the most key parameter that determines the ultimate performances in a photodetector in applications. Early in 2014 and 2015, the pioneering works have shown ultra-high photoresponsivity in pristine InSe, reaching 10^5 A/W (**Figure 3.23c**, [68]) and 10^7 A/W (**Figure 3.23d**, [69]) at large V_{ds} and gated condition. This value is in vast contrast with MoS_2 which normally rises to R of 10^3 A/W and attains a comparative value of WSe_2.[70,71]

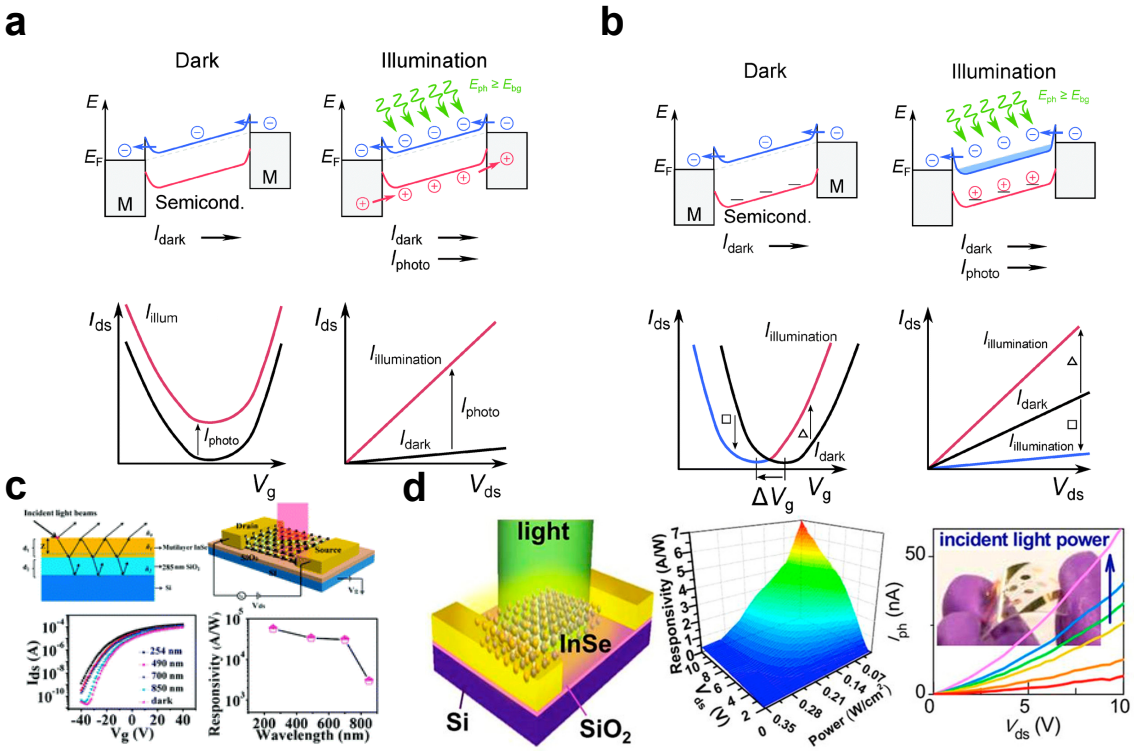

Figure 2.14: Indium selenide photodetectors. (a) Illustration of mechanism of photoconductive effect. Adapted from Ref. [67] (b) Illustration of mechanism of photogating effect. Adapted from Ref. [67] (c) InSe photodetectors on Si/SiO_2 substrate. Adapted from [68] (d) InSe photodetectors on Si/SiO_2 substrate and on flexible substrate. Adapted from Ref.[69].

Given that the pristine InSe has already shown a very high potential in photodetection, one can expect that better photoresponsive performances could be achieved by further functionalization to exploit the extreme potential of the material. Therefore, many researchers stated to seek for enhanced light-matter interaction in InSe phototransistors. This includes surface p-doping using $AlCl_3$ to achieve lower dark photocurrent to enhance the I_{light}/I_{dark} ratio (**Figure 2.15a**) [72]; Using the polarization of ferroelectric polymer to increase responsivity and reduce response time (**Figure 2.15b**) [73]; Increase the photoresponse by surface plasmonic effect of transition metal carbides. (**Figure 2.15c**) [74] These surface functionalization techniques indicated that InSe is highly suitable for producing high-performance photodetectors.

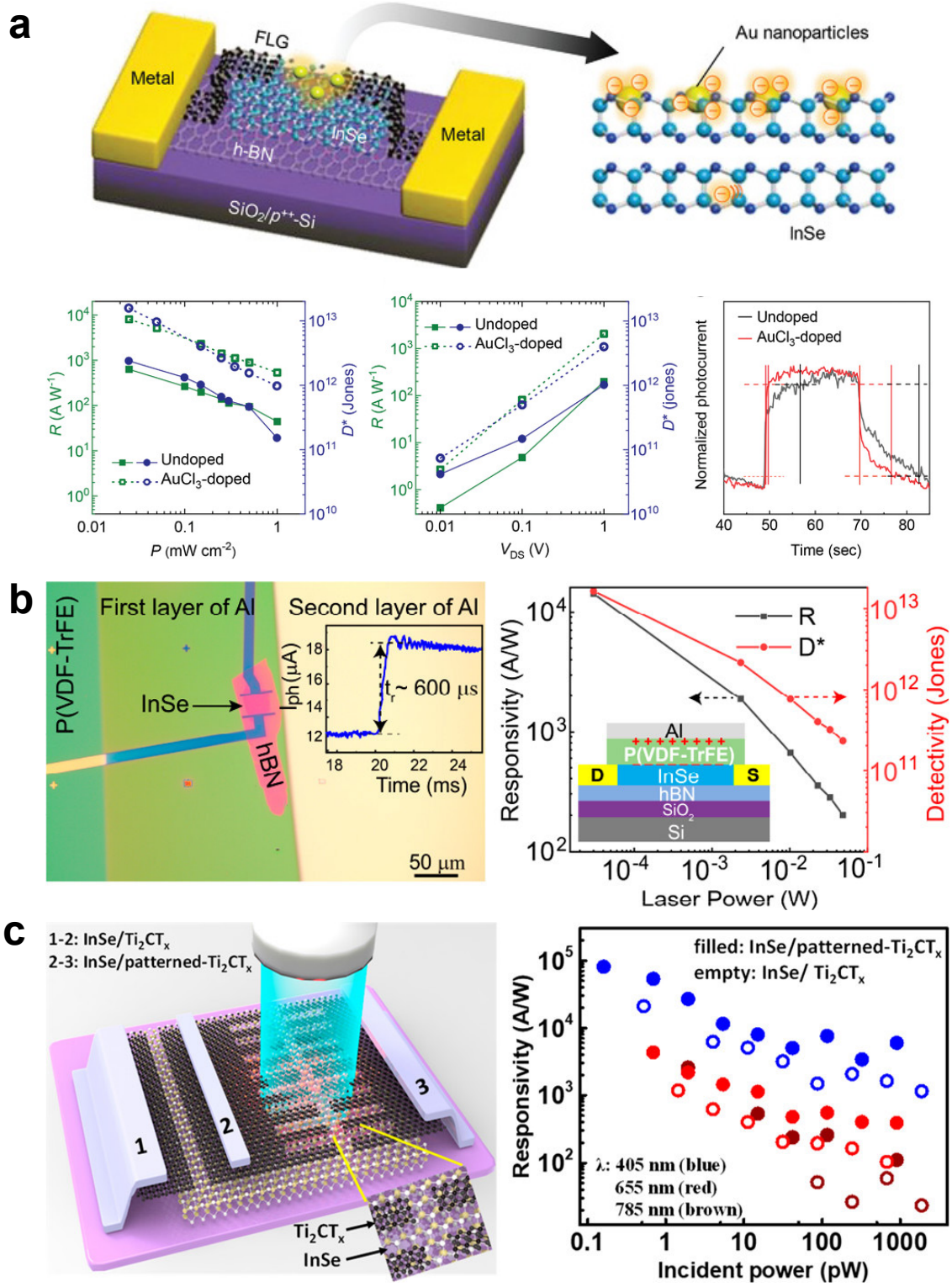

Figure 2.15: Photodetection enhancement of InSe. (a) $AlCl_3$ surface doped InSe photodetector. Adapted from Ref.[72] (b) Ferroelectric-gated InSe photodetector. Adapted from Ref.[73] (c) Transition metal carbide enhanced InSe photodetector. Adapted from Ref. [74]

2.5 Van der Waals (vdW) heterostructures

2.5.1 2D-2D vdW heterostructure

The emergence and development of van der Waals (vdW) heterostructures of 2D materials greatly expanded the scopes for fundamental studies on the physics of these systems. The stacking of different 2D materials kept together by the strong interlayer vdW force provides access to new physical functions. Nowadays, vdW electrode of graphene and dielectric/encapsulation layer of hexagonal boron nitride (h-BN) have become a common approach for exploring the physical phenomenon and improving the performances of electronic devices. On the other hand, by stacking 2D semiconducting materials with different energy band alignment, p-n junctions, tunnelling junctions and avalanche junctions could be obtained to form high-performance diodes for rectification, photodetector, etc. [67,75-77] The simple fabrication route by mechanical superposition of materials allows a wide selection of materials and combination considering the large 2D materials family. (**Figure 2.16a**) Bottom-up growth of heterostructures is also a major route through high-quality vdW heterostructure fabrication. (**Figure 2.16a**) Recently, based on ground-breaking findings in the superconductivity of bilayer graphene, stacking 2D materials at different lattice angles becomes a hot issue. The lattice mismatch of twisted 2D heterostructure enables induces Moiré patterns and ultimately being responsible for new optical and electronic properties of 2D materials. (**Figure 2.16b**) [78]

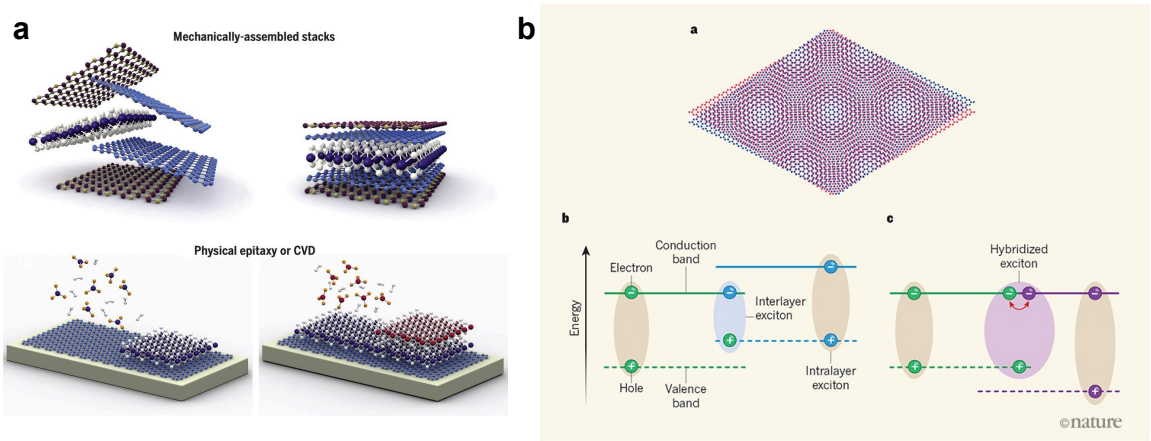

Figure 2.16: Stacking of van der Waals (vdW) heterostructures. (a) Mechanical assembling of 2D heterostructures and direct epitaxy and CVD growth of heterostructures. Adapted from Ref.[79] (b) Moiré heterostructures and its optical properties. Adapted from Ref.[78]

2.5.2 2D-organic vdW heterostructure

Not only vdW heterostructures could be produced by the combination of same/different 2D materials, materials from other families could also form stable vdW interaction with 2D materials, offering access to a modest variety of extraordinary functions. Organic materials have become attractive candidates for their excellent optoelectronic properties. Organic semiconductors, such as pentacene and rubrene possess high hole mobility that are comparable to some 2D semiconductors such as WSe_2, are able to form type II band alignment with typical n-type semiconductors such as MoS_2. **Figure 2.17a** and **b** depicts the vertical heterostructure of MoS_2 and pentacene. The mix-dimensional vdW heterostructure could perform as P-N diodes demonstrating excellent broadband photoresponse. (**Figure 2.17a**) Additionally, the heterostructure undergoes distinct charge transfer which lead to excitons with charge transfer signature in the heterostructure. (**Figure 2.17b**) Not only semiconductors play an important role in the formation of 2D vdW heterostructures, but self-assembled molecules which could closely pack on the 2D surface serves as active layers in the heterostructures as well. A responsive head group like a photochromic molecule could generate tunable periodic potential on the 2D surface, therefore affecting the electronic properties in the heterostructure. (**Figure 2.17c**) [80-82]

The cases demonstrated above is just a tip of iceberg. Thanks to the diversity of organic molecules and functions thereof that could easily be designed, a huge variety of novel organic-2D vdW heterostructures suggesting striking performances can be developed.

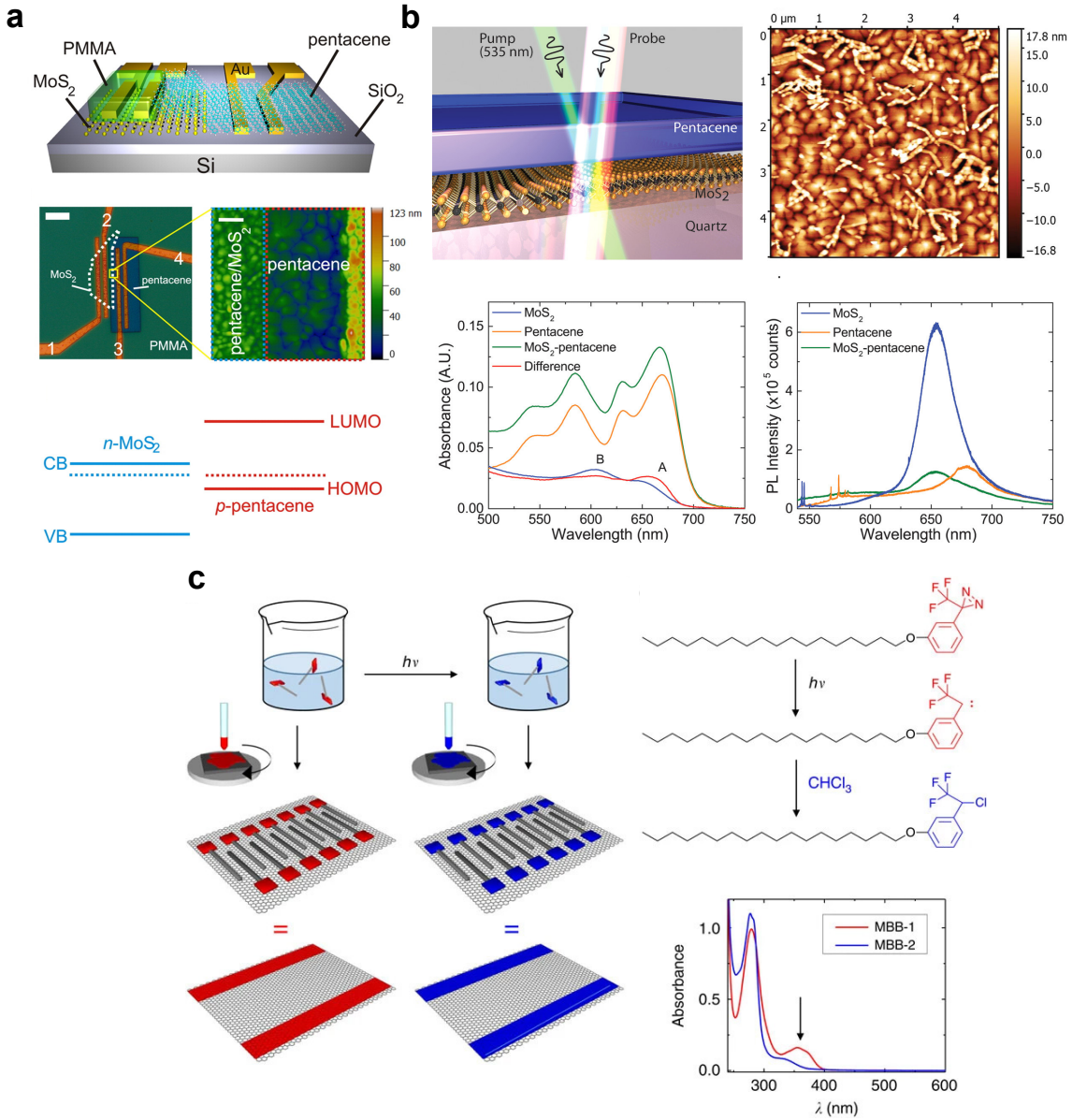

Figure 2.17: 2D-organic van der Waals (vdW) heterostructures. (a) P-N heterostructures formed by MoS_2 and pentacene. Adapted from Ref.[83] (b) Charge transfer excitons in MoS_2-pentacene heterostructure. Adapted from Ref.[84](c) Periodic potential in heterostructure of graphene and self-assembled molecular layer. Adapted from Ref.[80]

2.6 Conclusion and outlook

In this chapter, a brief introduction of the physical and chemical properties of 2D materials, including transition metal dichalcogenides (TMDs), black phosphorus (BP), indium selenide (InSe)

has been involved, together with a presentation of van der Waals (vdW) heterostructures produced with 2D materials and the organic molecules.

Despite thus overview is not complete in every aspect of the material that have been applied in this thesis, it offers the fundamental understanding and background of the main component utilized in this thesis work thus could be useful for the comprehension of the research results that are presented in the next chapters.

Chapter 3 Molecular Dopants

3.1 Introduction

In this chapter, a general introduction of the molecular dopants that are included in the following chapter is presented. This includes organic molecules like small solvent molecules, metal phthalocyanines, pyridines and ionic surfactant molecules.

3.2 Small solvent molecules

Solvents are defined as liquids capable to dissolve a solute yielding a solution. [85] In organic chemistry, they are widely used as dispersant for molecules to promote reactions. Moreover, polymers that bear long chains, are always found to be dispersible in solvents for specific applications. There is a broadest variety of solvent organic molecules including short alkanes, alcohols, ketones, and simple substituted aromatic rings. They are employed in chemical, biochemical, industrial and pharmaceutical applications. In the study of 2D materials, organic solvents are applied not only for washing the surface of the layered material. A good matching of surface tension between the 2D material and the solvent molecule enables the solvent to be intercalated into the layers of 2D material, enlarging the vdW gap between the layers thereby yielding the exfoliation of 2D nanosheets from bulk materials.[86]

Solvent molecules should not be considered as inert liquids. In **Chapter 5** and **Chapter 6** of this thesis, we will show that organic solvent molecules are able to influence the electronic and optical properties of the 2D monolayer and few-layer semiconductors. This is the case of popular molecules like acetone, benzene, chloroform, ethanol, hexane, isopropanol (IPA), m-xylene, p-xylene, toluene, 1,3-bis(trifluoromethyl)benzene (1,3-TFMB) and 1,4-bis(trifluoromethyl)benzene (1,4-TFMB). The chemical structures of these molecules are presented in **Figure 3.1**. Their basic physical and chemical properties (melting point, boiling point, dipole, surface energy, etc.) are listed in **Table 5.1** in **Chapter 5** and **Table 6.1** in **Chapter 6**.

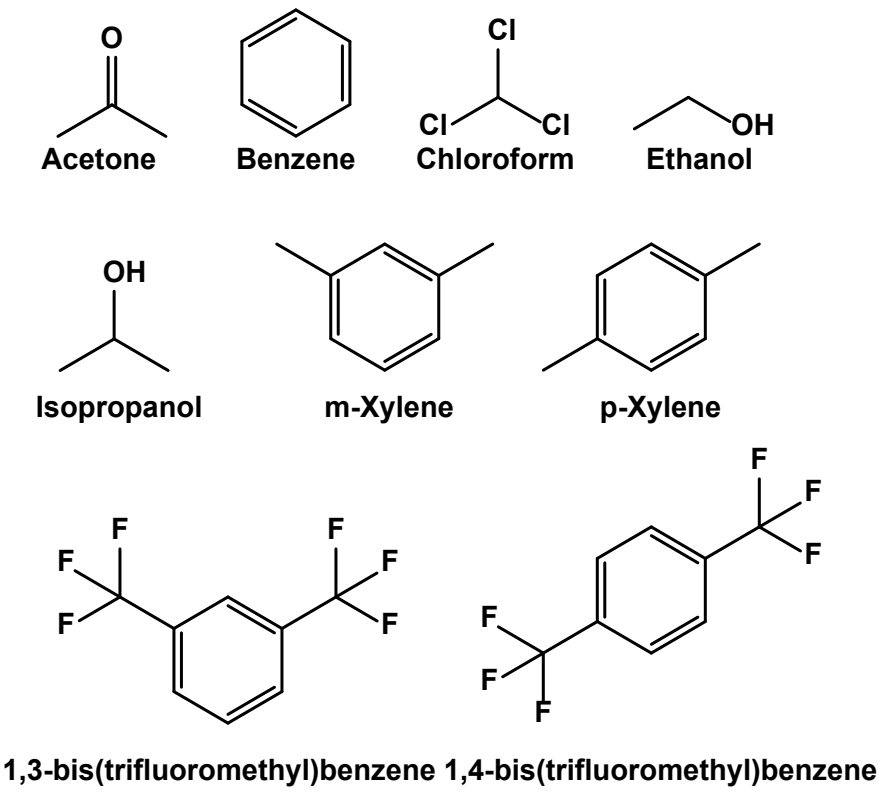

Figure 3.1: Chemical structure of small solvent molecules studied in Chapter 5 and Chapter 6 of this thesis.

3.3 Metal phthalocyanines

Metal phthalocyanines (MPcs) (**Figure 3.2**)are a class of The 18-π-electron macromolecules that bare a phthalocyanine ring and a metal center, first synthesized by Linstead and co-workers during the 1930s.[87-89] The series of molecules were first synthesized as organic colorants, as they are usually in bluish or greenish color in the unsubstituted form due to the wide bandgap. The color may differ in a small range according to different metal cores and functional groups on the phthalocyanine ring. Later, more electrochemical, optical, biological and optoelectronic properties have been explored with the family of MPcs, for applications in photocatalysis, organic electronics, phototherapy, etc. The coordination of the transition metal with Pc ligands results in stable chemical compound, by the contribution of the preorganization of the macrocyclic ring.[90] Thus, the host macrocyclic Pc ring remains the planar conformation even after the binding of metal core.

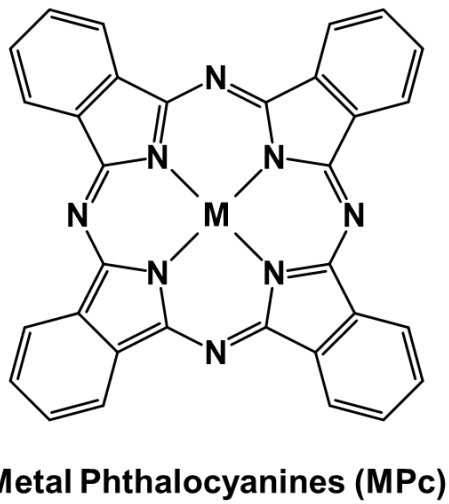

Figure 3.2: Chemical structure of metal phthalocyanines (MPc)

3.3.1 Coordination of transition metals

The complexation between the metal core and the ligands determines the conformation of the metal(M)-ligand(L) bond and the number of ligand coordinated are confined by the atomic orbitals of the center metal atom. Transition metals, in organometallic chemistry, are defined as the elements which have partly filled *d* or *f* shells. Representative elements, such as Co has the electron filling of $3d^74s^2$. The filling result in paramagnetism in some elements.

The coordination of metal and ligands occurs by means of both σ and π bonding, as is depicted in **Figure 3.3**. In phthalocyanines, the coordination of metal is mainly through the σ bond given that pyridinic nitrogen are good σ donors. The octahedral configuration gives 6 coordination sites where 4 have been occupied by the phthalocyanine ring. The complex results to be very stable when the metal core could fill the void.

The coordination largely influences the properties of both the central metal and the ligand. In the crystal field theory, the metal core is considered as cation and the ligands are ions that are electrostatically attracted to the metal core. The repulsive interaction resulting from energy splitting of the orbitals which rises energy levels. **Figure 3.4**. The energy difference of the split orbitals depends also on the nature of ligand.

In addition, many phthalocyanine derivatives have been developed via substitution on the side ring to increase solubility and functionality. The ligand coordination could also happen in the axial position, depending on the orbital configurations of the metal core, raising the coordination

number to up to 6.

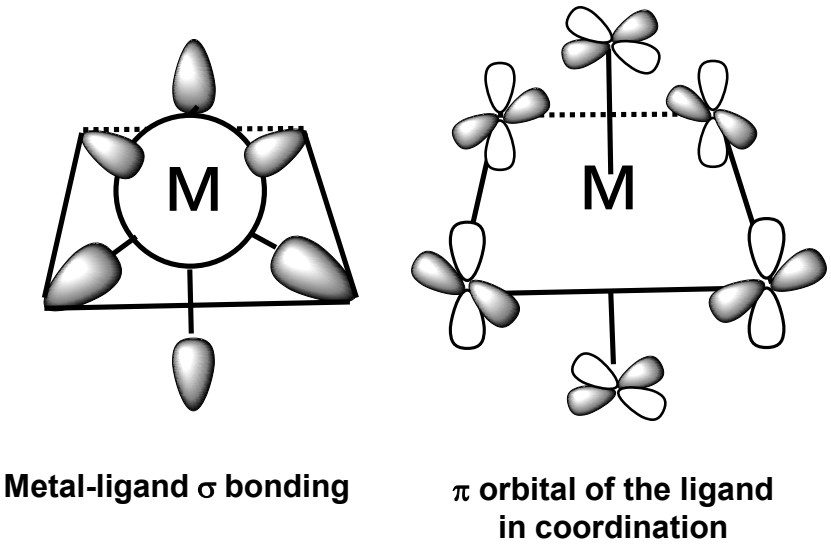

Figure 3.3: Orbital structure of σ and π bonding of transition metal in octahedral conformation.

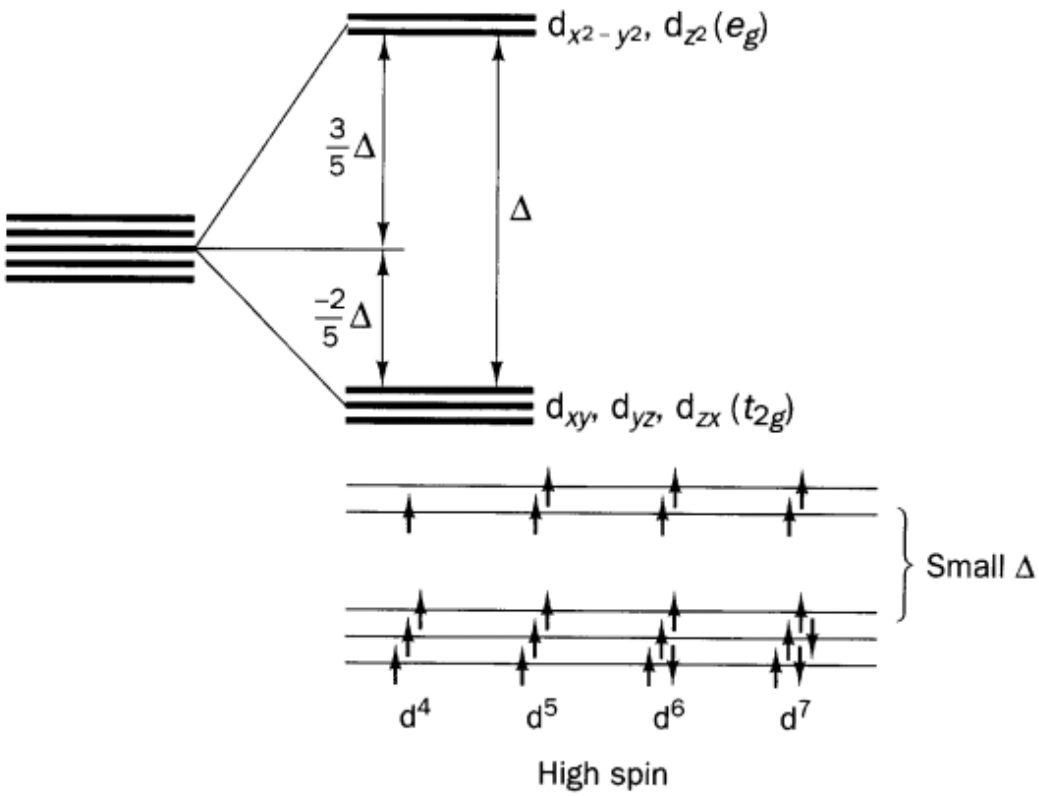

Figure 3.4: The *d* orbital splitting in an octahedral crystal field after the repulsion term common to both sets has been deleted. Adapted from Ref [91].

3.3.2 Electronic properties

MPcs usually possess bandgaps in the visible light range, being suitable for organic optoelectronics. The reduction potential ([MPc]/[MPc]$^-$) and the ionization potential([MPc]+/[MPc]) could be electrochemically measured, to approximately define the bandgap of the complex. Given the complexity of the molecular orbitals in MPc, computational methods are always adopted to calculate the origins of highest occupied molecular orbital (HOMO) and lowest unoccupied molecular orbital (LUMO). Figure 3.5 from Ref [92] demonstrates that the HOMO resides mostly at a_{1u} orbital, and LUMO at $2e_g$ orbital. The first oxidation removes electrons in the Pc ring and the reduction regards to addition of one electron on the metal orbital. Comparing HOMO and LUMO levels of different MPcs, iron phthalocyanine (FePc) and cobalt phthalocyanine (CoPc), whose spin state S is not equal to 0 in the d orbitals, manifests highest HOMO and LUMO energies. While fully filled d orbital would result in lower HOMO and LUMO levels.

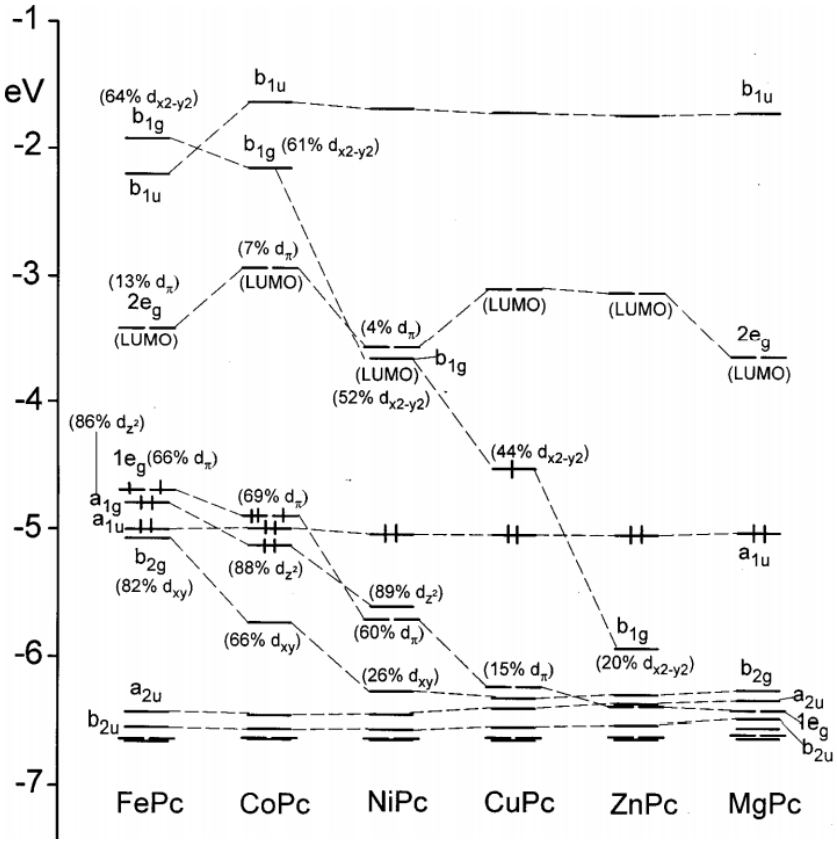

Figure 3.5: Molecular orbital levels of selective MPcs. Adapted from ref [92].

3.4 Pyridines

3.4.1 Pyridines as ligands

Pyridines are heterocyclic aromatic rings with one nitrogen atom and five carbon atoms, analogue to the benzene molecule (**Figure 3.6**). The electron lone pair on the nitrogen defines the Lewis basic properties, with the sp^2 orbital pointing directly out of the aromatic ring, ready for coordinating with the metal core. The pyridines are strong ligands causing large *d* orbital splitting in the metal. As is shown in **Figure 3.7**, σ bonding occurs by sp^2 hybridization while orbital overlap. Moreover, the π* orbitals in the aromatic ring also participates in the overlapping, acting as acceptors of metal orbitals. Therefore, the conformation of coordinated pyridines experiences a dual confinement both from the σ and the π bonding, which is defined by the geometry of the metal *d* orbital.

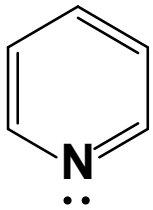

Figure 3.6: Chemical structure of pyridine.

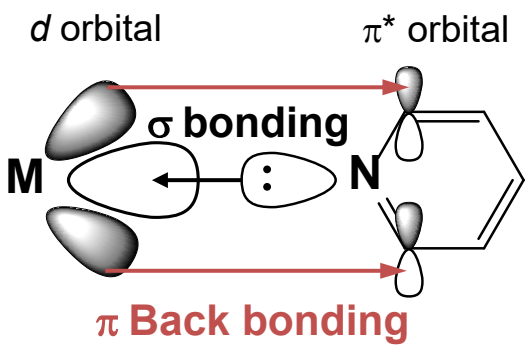

Figure 3.7: Orbital structure of pyridine-metal bonding.

Based on the stable and facile coordination between pyridine and metal, in this thesis, especially in **Chapter 8** and **Chapter 9,** we focus on constructing axial ligand using functional pyridines, aiming to assemble a directional confined system of molecular dipoles on the 2D surfaces.

3.4.2 Photochromic azopyridines

Photochromic molecules undergo conformational changes when absorbing photon energy. They usually exhibit two stable states separated by a potential barrier (ΔE), as shown in **Figure 3.7a**.

When a photon hits the isomer A, the molecule receives the energy to overcome the potential barrier yielding isomer B. The isomer B could also be reversibly changed back to A, by irradiating with another wavelength. In some cases, thermal energy can be exploited to trigger the back-isomerisation to the initial state A.

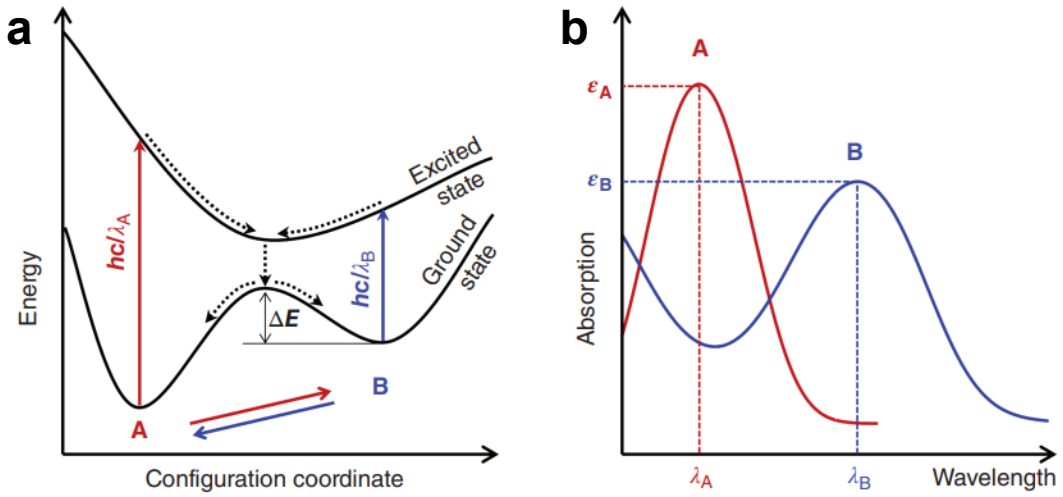

Figure 3.7: Photoisomerization between two isomers A and B induced by light. (a) The potential energy diagram and (b) the schematic absorption spectra of the isomerization. [93]

Many are the photochromic molecules known as tetracene, phenylhydrazine, phenylosazone, and naphthalenone, etc. Yet, considering the efficiency of switching and stability of the (meta)stable states, the more commonly-studied photochromic molecules are spiropyran (SP), diarylethene (DAE) and azobenzene (AZO) (see **Figure 3.8**).

Typically, the isomerization of spiropyran and azobenzene is accompanied by a large dipole moment change. In spyropyran, a net dipole moment change of ~13 Debye is observed in the isomerisation from close to open form. For unfunctionalized azobenzenes, the net dipole from trans to cis form amounts to ~3 Debye.

Photochromic molecules can be equipped with functional groups to add functionalities or to promote its interaction with other molecular systems or materials. Among them, the high chemical reactivity of azobenzene enables its functionalization, making it possible to explore new functionalities. Therefore, it has become the most widely-used photoswitching unit in supramolecular chemistry, biological chemistry, materials science, and even electronics.

UV-Vis absorption spectra of azobenzene is shown in **Figure 3.9**. The trans to cis isomerisation

can be replaced via two distinct mechanisms, each associated to a light absorption at 365 (π-π* transition) 455 nm (n-π* transition). The isomerisation is kinetically favourable, where a colour change could be visible by naked eye. The n-π* band is usually in lower intensity since it is symmetry forbidden.

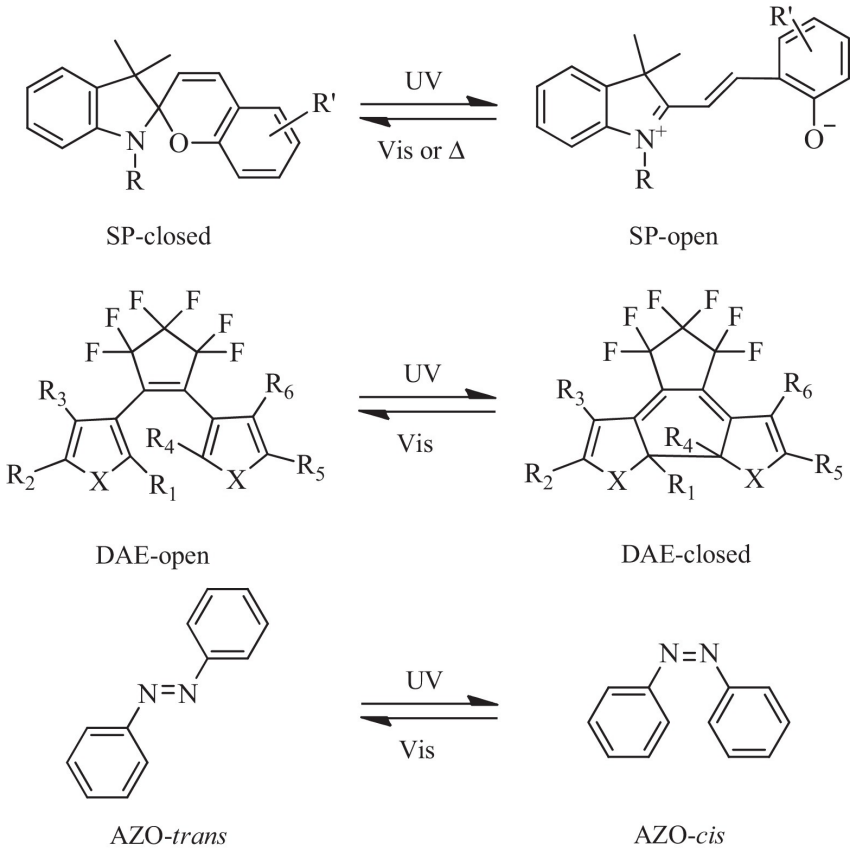

Figure 3.8: Photoisomerization of typical photochromic molecules. Figure adapted from Ref [94].

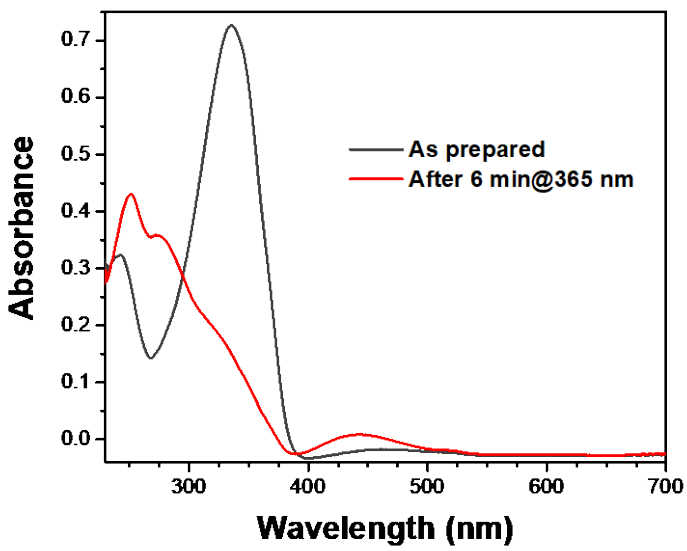

Figure 3.9: UV-Vis absorption spectra of azobenzene in trans (black curve) and cis (red curve) form.

Azobenzenes have vastly been applied for dynamically modifying the properties of materials, especially in responsive smart materials and electronics. In 2D materials, several previous works, demonstrated that azobenzene is a powerful candidate for reversible doping, enhancing the photoresponse, etc.[95-98] They are a best example for demonstrating the strong influence of molecules on 2D materials, and will be progressing to show more functionalities towards applications, as is shown in **Chapter 9** of this thesis.

3.5 Ionic surfactants

Surfactant molecules are widely used both in scientific research and in daily life. They comprise usually a long hydrophobic tail and a hydrophilic head group. They are able to self-organize in solution, and on surfaces, due to the surface tension matching. The head group can either be cationic or ionic, and stabilized by the counter ion. Molecules, such as sodium dodecyl sulfate (SDS), cetyltrimethyl ammoniumbromide (CTAB), tetradecyl trimethyl ammonium bromide (TTAB) and sodium cholate (SC) are commonly used for dispersing nanomaterials, including carbon nanotubes, gold nanoparticles and 2D materials. The charged surfaces of the nanomaterial firstly attract a diffusion layer of counter-ions forming an electric double layer. Then an effective surface charge is created resulting in Coulomb repulsion between nearby charged colloidal particles. [99] The surfactant ions are usually dissociated and participates the modification of surface potential of the nanomaterial, and making the surface more ionic, resulting in enhanced solubility in aqueous solutions.

Similarly, this effect could be observed on solid substrates. As demonstrated in Ref [100], didodecyldimethylammonium bromide (DDAB) can form self-assembled layer on ultra-flat surface of HOPG with the alkyl tail pointing to the surface. This work was key as it demonstrated that ionic surfactants can self-assemble stably on 2D flat surfaces, forming ordered structures. The latter can act as stable and powerful molecular dopants, as discussed in **Chapter 7**.

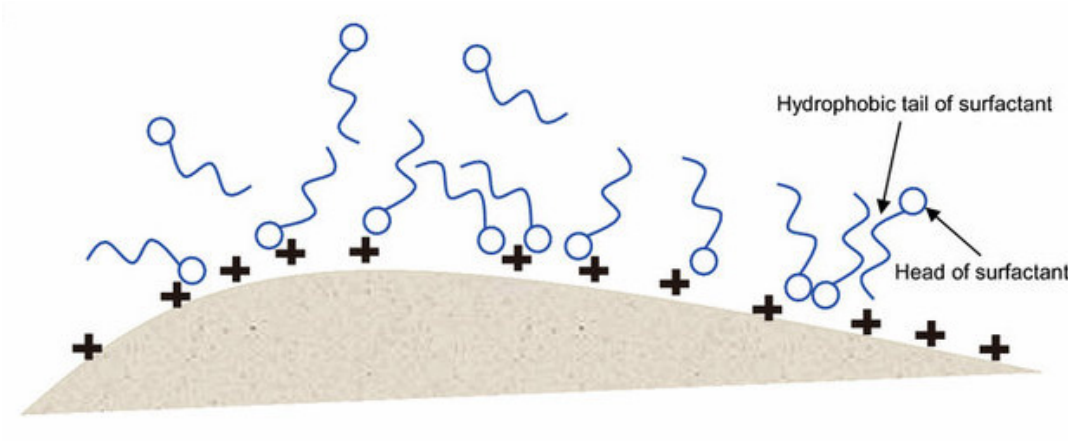

Figure 3.10: Schematic representation of ionic surfactant molecules adsorbed on charged surface. Figure adapted from Ref [101].

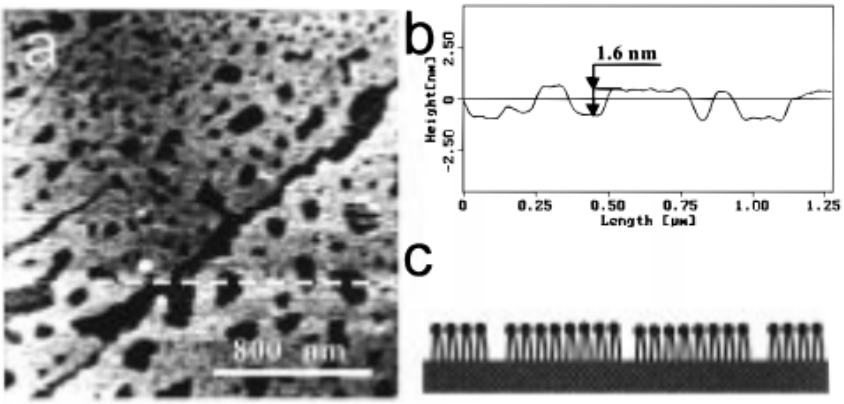

Figure 3.11: Example of didodecyldimethylammonium bromide (DDAB) self-assembled on HOPG surface. Figure adapted from Ref [100].

Chapter 4 Experimental Techniques

4.1 Introduction

The experimental techniques employed in this thesis can be subdivided into six major groups: sample preparation, molecular functionalization, device fabrication, optoelectronic characterizations, spectroscopic characterizations, and surface characterizations. The first three parts are techniques for fabricating and functionalizing 2D materials with specific targets. The last three parts are characterizations techniques which provide proofs for the fabrication and functionalization. In this chapter, we will present a general review of these techniques which will be structured to support the elucidation of experimental data in **Chapter 5** to **Chapter 10**.

4.2 Preparation of 2D materials

4.2.1 Substrate preparation

Heavily n-doped silicon covered with thermally oxidized SiO_2 dielectric layer is the prototypical substrate utilized in this thesis. The wafer is purchased from external provider (Fraunhofer IPMS, Germany) with typical oxide layers used in this project being 90 nm and 270 nm thick (relative dielectric constant ε_r=3.9). In order to facilitate the fabrication of devices based on 2D materials, a customized pattern (named "Strasbourg") developed by previous colleague in the group (Dr. Simone Bertolazzi) are adopted (see **Figure 4.1**) The pattern contains periodic cross markers and numbers deposited with 30 nm gold (Au) with 10 nm indium-tin-oxide (ITO) as adhesion layer for better locating the randomly distributed 2D flakes. Large square pads are distributed at the border of the chip for further electrode patterning and wire bonding.

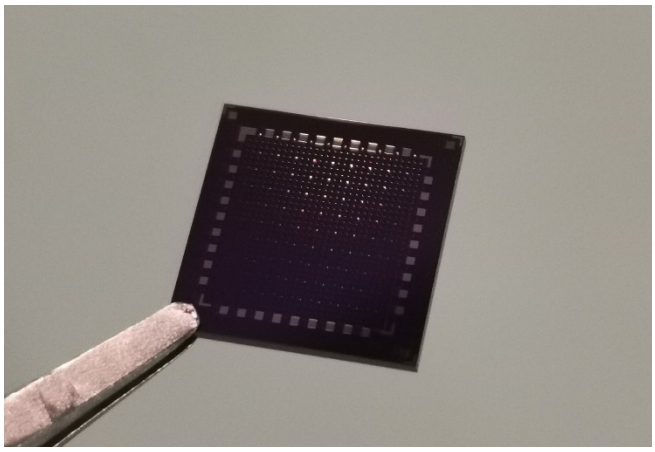

Figure 4.1: Photo of pre-patterned Si/SiO_2 (270 nm) substrate for fabricating optoelectronic devices based on 2D materials.

The standard cleaning process of substrate cleaning consists of a sonication bath of acetone and isopropanol (IPA) for 20 min to remove the protective photoresist on the SiO_2 surface. A further surface treatment by UV/Ozone is usually required, to decompose the organic contaminants on surface. The UV/Ozone treatment is widely applied in surface cleaning following a series of photochemical reactions, including following steps: *1)* Use the 185-nm UV light to decompose O_2 into triplet atomic oxygen $O(^3P)$. *2)* The triplet atomic oxygen $O(^3P)$ combines with O_2 to generate ozone (O_3). *3)* Use the 254-nm UV light to dissociate O_3 to form O_2 and singlet atomic oxygen $O(^1D)$ which is a strong oxidant, eventually react with surface organic contaminants. The products of the reactions are usually NO_x, CO_2, H_2O and O_2 which are highly volatile to be easily desorbed from the substrate surface.

4.2.2 2D materials preparation

4.2.2.1 Mechanical exfoliation

Mechanical exfoliation is a wide-spread technique for producing high-quality mono- to few- layer 2D materials.[1,102] The breaking of interlayer van der Waals (vdW) forces by tearing apart adjacent sheets of 2D materials using scotch tape or other adhesive bands provide simple yet highly effective solutions for conducting optoelectronic studies. The exfoliation process consists of three steps: **1) obtaining bulk crystals.** The high-quality bulk crystals grown by chemical vapor transport (CVT) method are purchased from HQ graphene, Netherlands. Figure 4.2 shows representative photos of the crystals used in the thesis. The crystal structures of different materials also defines the physical properties of the bulk crystal, for example, the shape and

reflective colors are distinct from one another. **2) Exfoliating the bulk crystal to thinner flakes using an adhesive media.** Bulk crystals are exfoliated by folding and unfolding the tape for several times. Commonly used adhesive tapes are scotch tape (3M), Blue tape (Nitto) and polydimethylsiloxane (PDMS) film (Gel-Pak). The adhesion force of the adhesive materials is determinative to the size and thickness of exfoliated flakes. **Figure 4.3a** shows the appearance of distributed flakes on different adhesive materials. Usually, the size of flakes is larger on blue tape due to small peeling force (< 10N/m) thus obtaining larger high-quality flakes. However, for some bulk crystals, the blue tape is not sufficient for detaching layers from the bulk materials due to the larger interlayer interaction. In this case, scotch tape is an ideal candidate for pre-exfoliation. **3) Transfer the exfoliated flakes onto a specific substrate.** The adhesive tape with exfoliated 2D materials is spread and placed onto the surface of the substrate. An additional pressing is exerted to improve the interaction between the 2D material and the substrate. Then the tape is peeled off gently with the assistance of tweezer for a more delicate control. This process serves as a further cleavage to obtain thinner materials. (**Figure 4.3b**)

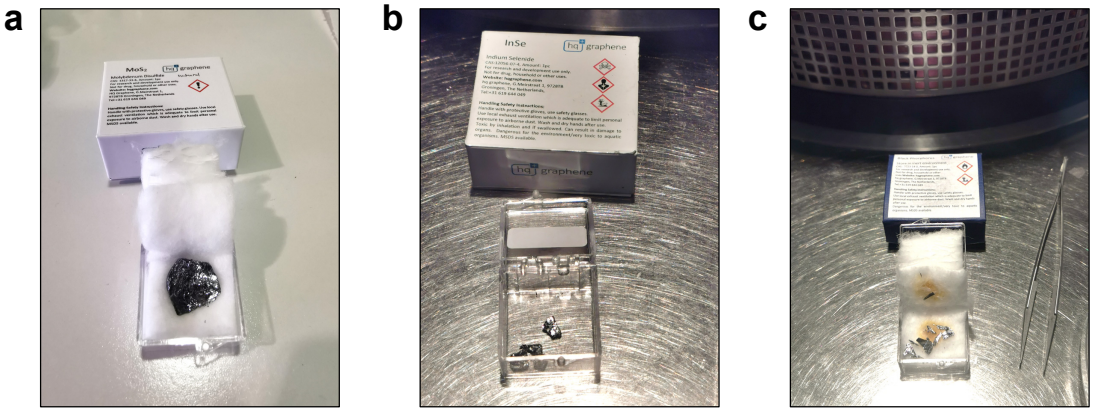

Figure 4.2: Bulk crystals of (a) MoS_2, (b) InSe and (c) black phosphorus (BP). Due to the chemical instability of InSe and BP in air, the bulk crystals are stored in a nitrogen-filled glovebox with oxygen and water level below 1 ppm.

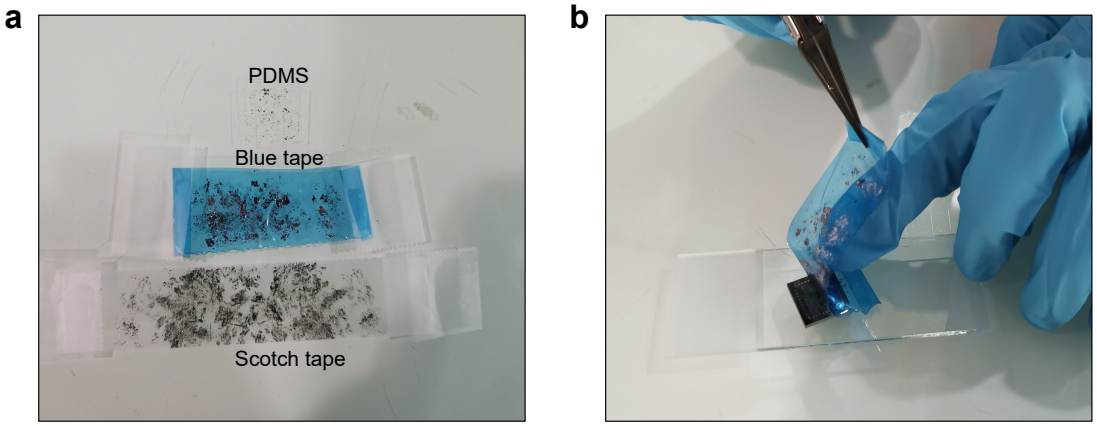

Figure 4.3: Mechanical exfoliation of 2D materials. (a) Examples of exfoliated materials (MoS_2) on different materials. (b) Transfer of exfoliated flakes onto Si/SiO_2 substrate.

The exfoliated 2D material are identified under a bright-field CCD-camera-combined optical microscope without any additional filter or polarizer. Top illumination from the lens results in distinct optical contrast for different layer numbers of material. **Figure 4.4** shows a typical optical microscope image of MoS_2, with 30% optical contrast for monolayer and 0% for bulk material. Note that for different 2D materials, the contrast might differ. Therefore, beyond optical microscope, combined techniques such as photoluminescence and Raman spectroscopy (See **Chapter 4.6**), and atomic force microscopy (See Chapter 4.7) are frequently utilized to identify layer numbers.

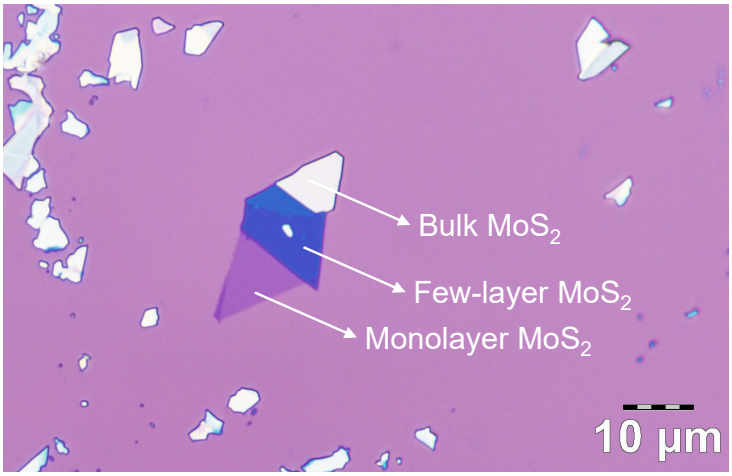

Figure 4.4: Optical microscope image of monolyer, few-layer and bulk MoS_2 on Si/SiO_2 (270nm) substrate.

In addition, for highly chemically unstable 2D materials such as BP and InSe, the exfoliation process takes place in the glovebox. Especially for BP which degrades rapidly within hours in air, the substrate with exfoliated flakes are coated with polymethyl methacrylate (PMMA) prior to

taking out of the glovebox for identifying the flakes with the microscope in air. We adopt the bilayer coating (600K/950K) of PMMA which are resist for the E-beam lithography in the next step of device fabrication.

4.2.2.2 2D vdW heterostructure production

Although recent progress has demonstrated 2D heterostructures by chemical vapor deposition (CVD) approach to produce large-area materials, the prevailing method for building up Van der Waals (vdW) heterostructures still relies on the conventional dry transfer. This approach allows us to obtain high-quality heterostructures with a controlled manner, which is critical for the use of optoelectronics, given the fact that stacking materials with ideal band alignment could serve as 2D PN junctions, and by controlling the mismatching angle of lattice of different materials, new eye-catching physical properties such as superconductivity, Moiré excitons have emerged. On the other hand, the use of mono- to few-layer graphene (G) as ultra-thin transparent electrode and hexagonal boron nitride (h-BN) as insulating dielectric or encapsulation layer is very common in the research community, which has been proved to be highly efficient. In this thesis, especially for the work presented in Chapter 7, the PDMS-assisted dry transfer, which is depicted in **Figure 4.5a** with the home-made transfer setup shown in **Figure 4.5b**. The setup contains a micromanipulator with X, Y and Z direction control, and a supportive glass slide which is adjusted to the high of the microscope stage. The transfer process contains six steps: 1) Exfoliating bottom and top materials on target substrate and PDMS respectively. This step is identical to the mechanical exfoliation described in **Section 4.2.2.1**; 2) Identifying the flakes on the target substrate and mark the location of the flake; 3) Place the backside of PDMS onto the bottom side of the supportive glass slide thus the flakes are facing towards the target substrate; 4) Lowering the microscope stage and adjust the positions of the PDMS using the wheel of micromanipulator under the microscope lens to focus and identify the top flakes until it reaches ideal alignment with the bottom flake; 5) Move up back the microscope stage until the top and bottom flakes are stacked with each other under the microscope. An external pressure or heat is beneficial for the formation of vdW heterostructure; 6) Peeling the PDMS gently by controlling the Z-direction wheel in the micromanipulator.

A resulting example of the transferred flake onto Si/SiO_2 substrate is shown in **Figure 4.5c**. The method is capable to produce 2D heterostructures in high yield, with precise control over the flake thickness and size, meanwhile being arbitrary and versatile in the type of stacking, especially when multiple layers of different materials are required.

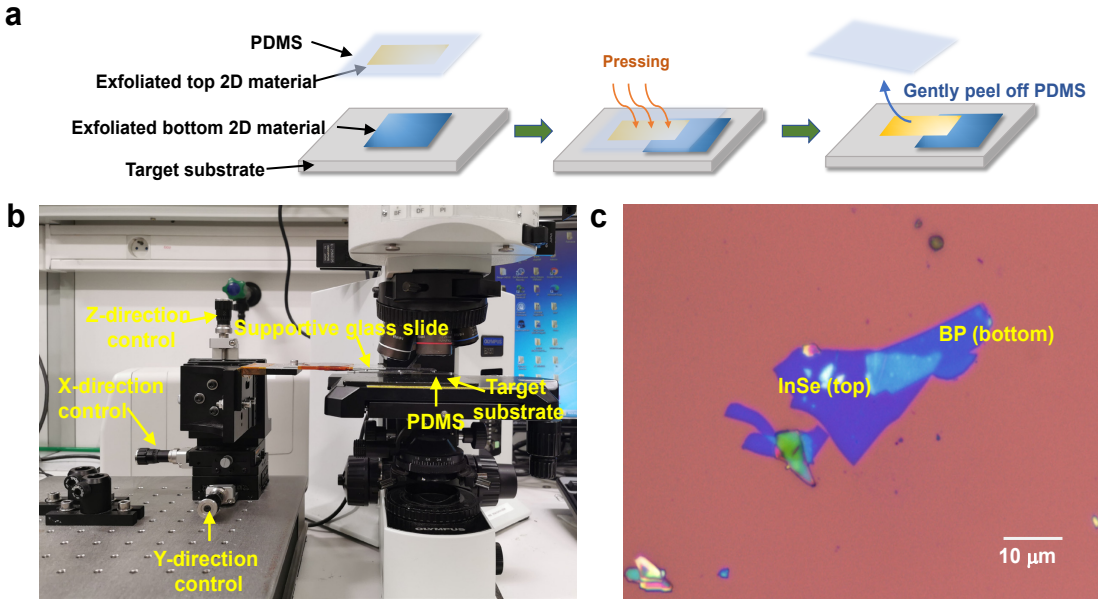

Figure 4.5: Dry transfer of 2D heterostructures. (a) Schematic demonstration of PDMS-assisted dry transfer. (b) Photo of the experimental setup for dry transfer which contains an optical microscope and a home-made transfer setup. (c) Optical microscope image of transferred heterostructures in which BP was firstly exfoliated onto the Si/SiO_2 substrate and InSe was transferred onto the substrate to partially cover the BP flake by PDMS.

4.3 Molecular functionalization process

4.3.1 Spin-coating

Spin-coating is a wide-spread technique for preparing homogeneous thin-films, depositing materials from solutions on a target substrate. Generally, a spin-coater comprises a vacuum pump to stabilize the substrate in the middle to counter the large centrifuge force from the rotation. The process flow is shown in **Figure 4.6**. The first step is to drop-cast the solutions containing the molecule. The physical behaviour of the solvent defines the quality of spin-coated film, with viscosity, surface tension and boiling point being important factors. After the droplet of solution is deposited onto the substrate, the spin-coater starts to spin at an appropriate accelerated rotation speed. The centripetal force and the surface tension of the solution drives the large part of the

solution to be expelled from the surface and an even coating is formed. The rotational speed of this step often determines the thickness of the final film. Finally, at a constant high speed of rotation, solvents are evaporated to form a dry film.

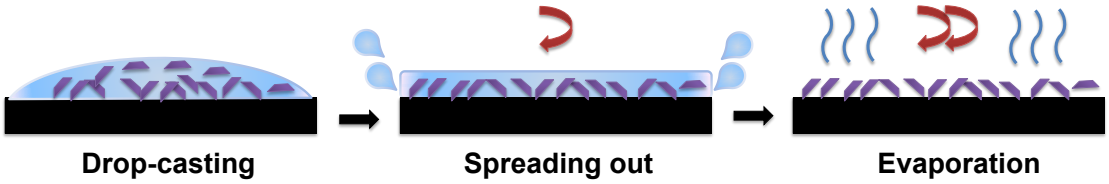

Figure 4.6: Schematic representation of the process of spin-coating.

4. 3.2 Molecular self-assembly in solution

In this thesis, the key part for constructing molecular functionalized 2D materials relies on the solution-processable molecular self-assembly on surface. This approach has been widely applied for studying the molecular properties on surfaces, especially by means of scanning tunneling microscopy (STM). Here we focus on the supramolecular interaction which enables such molecules to physisorb on flat surfaces forming periodic 2D patterns. These interactions are usually non-covalent, including hydrogen and halogen bonds, vdW forces, ion–dipole interaction, dipole–dipole interaction and π–π stacking.[103] (**Figure 4.7**) The results of the self-assembly can yield the formation of molecular superlattices. By carefully designing the molecular structure, the superlattices could generate periodic potentials and Moiré patterns which would largely influence the substrate underneath. In this regard, we take advantage of the natural properties of the supramolecular chemistry to construct such superlattice on ultra-flat 2D surfaces. The general approach is to immerse the substrate with exfoliated 2D flakes in a beaker containing the solution of the self-assembled molecule. When molecules approach the surface, the molecule-substrate interaction (vdW force in most cases) competes with the molecule-molecule interaction and molecule-solvent interaction, ultimately reaching thermodynamic equilibrium to form the first layer of self-assembly, or self-assembled monolayers. Excess molecules might pile up for form multiple layers, yet largely dependent on the attraction between molecules in a spatial regime. The multilayers of molecules are always found to be unstable compared to vdW interaction with the substrate and the excess of multilayer molecules are easily to be removed by washing with proper solvents.

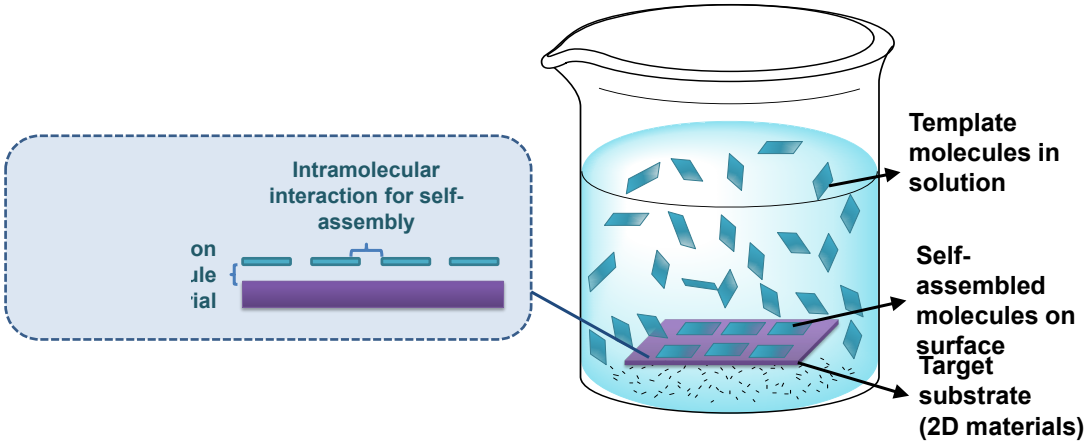

Figure 4.7: Schematic representation of molecular self-assembly in solution adopted in this thesis.

4.4 Device fabrication

4.4.1 E-beam lithography

Electron-beam lithography is a commonly-used microfabrication technique for producing high-resolution patterns by polymer resists. In a lithography process, there are two types of resists: positive tone resists and negative tone resists. In positive resists, the electron-beam exposed area are removed after the development while in negative resists, the exposed area will remain on the surface after developing. Here, we adopt poly(methyl methacrylate) (PMMA) as positive tone resist due to the small electrode area compared to the substrate area in order to achieve fast pattern writing. The core of the technique is the de-polymerization of PMMA via highly focused electron beam. As shown in **Figure 4.8**, the mechanism of EBL is to attain polymer scission under highly-focused electron beam. Due to the solubility change in methyl isobutyl ketone (MIBK)/isopropanol (IPA) developer within different polymerization degree, the region which is irradiated by the electron beam is washed away by the developer while the unirradiated region remains to be covered by the resist.

Figure 4.9 depicts the relevant steps of the lithographic the procedures for fabricating nanodevices using EBL. Here we utilize the standard double-layer PMMA resist (600K and 950K) to enhance the resolution of patterning. The advantage of double-layer resist is that, the different molecular weight of the polymers in the two layers would react with electron beam at different

scale. The lower polymerized 600K PMMA chain are easier to break up yielding shorter fragments when compared to the higher polymerized 950K PMMA under the same exposure dose. Therefore, a slightly larger area is patterned on the bottom layer after the development and an undercut is formed in the exposed region. The presence of the undercut would largely facilitate the liftoff process, which will be discussed in the **Session 4.4.3**. This also defines EBL i.e. a highly precise technique which allows us to reach sub-10 nm of resolution.

The standard procedure of EBL explored in this thesis comprises the following steps:

1. Spin-coating 200μL solutions of 600K PMMA (solid contents: 4.0%) at 4000RPM for 60s and bake at 180 °C for 3min, and the resulting film thickness is ~0.23μm.
2. Spin-coating 200μL solutions of 950K PMMA (solid contents: 4.0%) at 2000RPM for 60s and bake at 180 °C for 3min, and the resulting film thickness is ~0.43μm..
3. Writing of the designed patterns with ideal dose of electron beam (for fine and course features, the writefield is in different size, so the writing step and dose may differ according to different conditions. Dose test are also required before establishing a procedure.). The acceleration voltage for electrons is 20 kV.
4. After having written the pattern, immersion of the chip into developer (1:3 ratio of MIBK:IPA mixture) for 40s. Then immediately immerse into the stopper (IPA) for 20s. Dried up with the nitrogen gun.

Note that for EBL, the lithography takes place in a clean room.

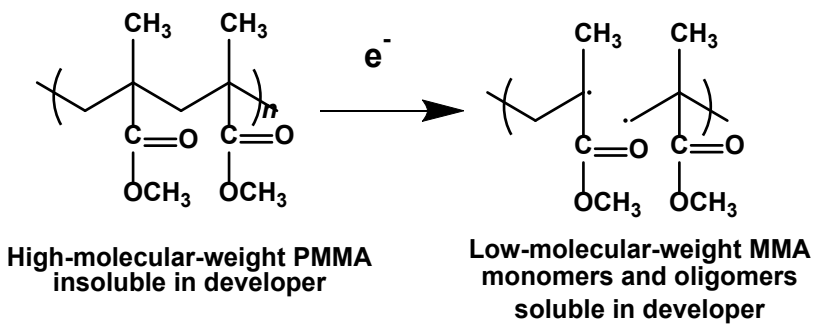

Figure 4.8: Chemical mechanism of EBL patterning using PMMA as resist.

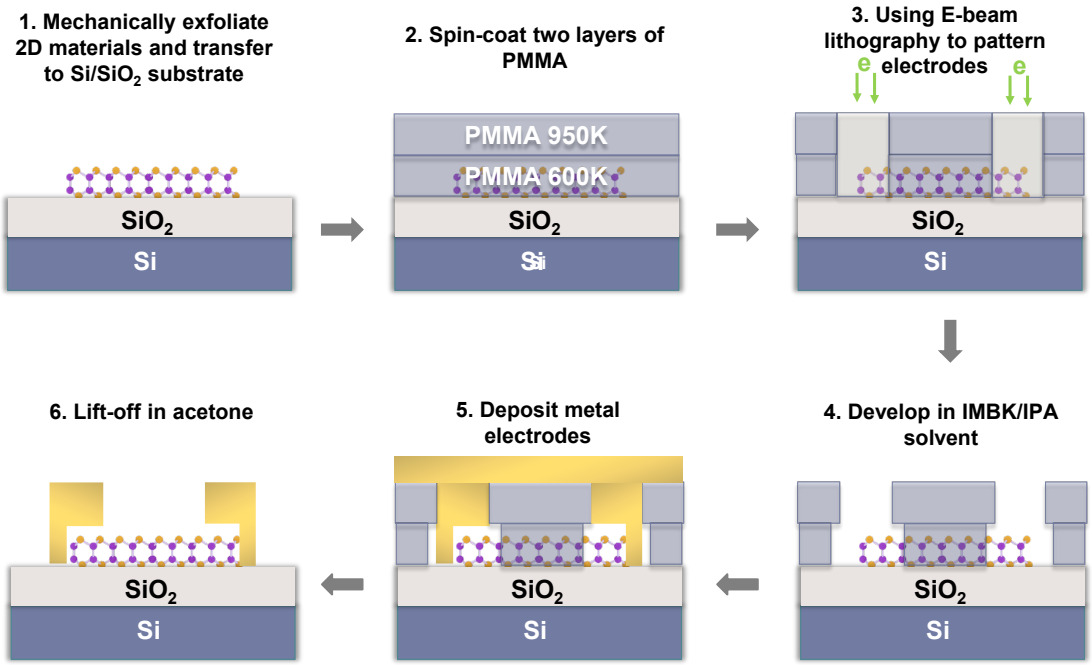

Figure 4.9: Process flow of E-beam lithography.

4.4.2 UV photolithography

The fundamentals of UV photolithography are similar to EBL, which is to control the solubility of polymers under certain chemical reaction in the patterned area. Herein, the positive resist contains two components: the novolac resins (phenol-formaldehyde copolymer) and the photosensitizer (diazoquinone) where the latter are usually incorporated into the former via bonding. A photochemical reaction takes place when UV light source is shone on the resist. The Wolff rearrangement occurs when photons are abdorbed by the diazaoquinone, producing product that is soluble in the base developer (tetramethylammonium hydroxide (TMAH)). Comparing to EBL, UV lithography can achieve lower resolution (~2μm) due to the confinement of the laser spot. Yet it is more advantageous for large area lithography and for writing fast course patterns since the manipulation and parameter tuning requires less skills in general.

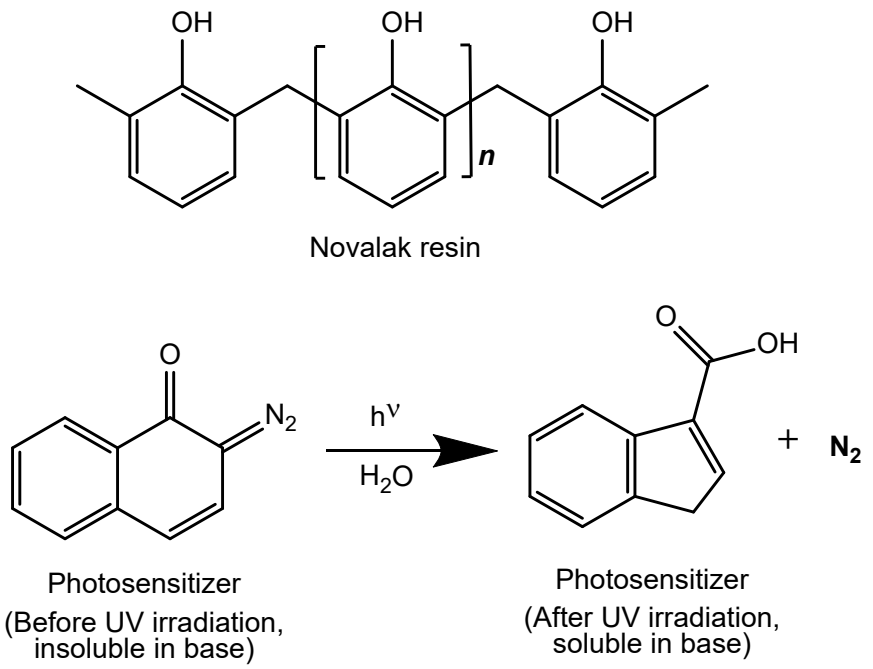

Figure 4.10: Chemical structures of the positive resist and the photochemical reaction of the photosensitizer.

The standard procedure of UV lithography by laser writer in this thesis are described as follows:

1. Spin-coat 200μL solutions of AZ1505 photoresist (solid content: 17.7%) at 3000RPM for 45s and bake at 120 °C for 1min, and the resulting film thickness is ~0.58μm.
2. Writing the designed patters with ideal exposure dose of UV light (for fine and course features, different magnification of lens coupled with UV laser is used, Dose test are also required before establishing a procedure.).
3. After having written the pattern, the chip was immersed into developer (TMAH) for 15s. Then immediately immersed into the stopper (Millipore water) for 15s. Then dried up with a nitrogen gun.

Note that for UV lithography, the fabrication takes place in a clean room.

4.4.3 Metal deposition and lift-off

Electrical contacts are key element for optoelectronic devices, which greatly determines the performances of the devices. Various conductive materials are widely used for fabricating electrodes. The most commonly used materials for electrodes are metal. They are stable and they can offer a wide selection of work functions enabling optimal charge injection for all types of

semiconducting materials. In nanofabrication, metal deposition is always followed by lithography. In this thesis, we mainly adopt thermal evaporation and E-beam evaporation which will be described in detail in the following **Section 4.4.3.1** and **4.4.3.2**.

4.4.3.1 Thermal evaporation

Thermal evaporation is a common method for thin film deposition which is not limited to metallic materials. Organic molecules, inorganic salts and novel organometallic materials could all be thermally evaporated to form thickness-controlled high-quality thin film. The evaporation is based on Joule effect, where heat could be generated when current passes through a resistor. Common thermal evaporating system is illustrated in **Figure 4.11**. Key components, as can be easily identified in the Figure, are resistive crucible which contains certain amount of source metal, vacuum system to isolate the deposition system from the ambient environment, the target substrate for evaporation, and a microbalance placed at the same level of the substrate to monitor film thickness.

A good vacuum is crucial for a high-performance film deposition to reduce the collision of vaporized metal atoms with other chemical species. In this thesis, all metal depositions are achieved below 10^{-6} mbar which usually requires a turbo pump to run overnight. After that, a large current is applied across the crucible. The temperature increase in the local position will heat the metal in the crucible until it reaches vaporizing temperature. Most metal that we used in this thesis undergoes solid-liquid-vapor phase transition where a meltdown of the metal observed before vaporizing. While for chromium (Cr) in particular, a sublimation occurs when heating up. As a result, a higher current is always applied for chromium although the boiling point is not extremely high.

The vaporized metal atoms reach the substrate and form thin films. The deposition speed and thickness are monitored by the microbalance, which is usually made of quartz. During the evaporation, the material is also deposited on the surface of the microbalance, resulting in weight change. The oscillation frequency of quartz precisely captures the weight change. And by calculating certain parameters including the mass of the metal, one could deduce the thickness change of the thin film.

The thermal deposition guarantees uniform and flat deposited surfaces. As the deposition rate is always below 1 nm/s, it is ideal for fabricating top-contact electrodes for 2D semiconducting devices. The high vacuum in the deposition chamber also helps to produce a clean 2D material-

metal interface for better charge injection.

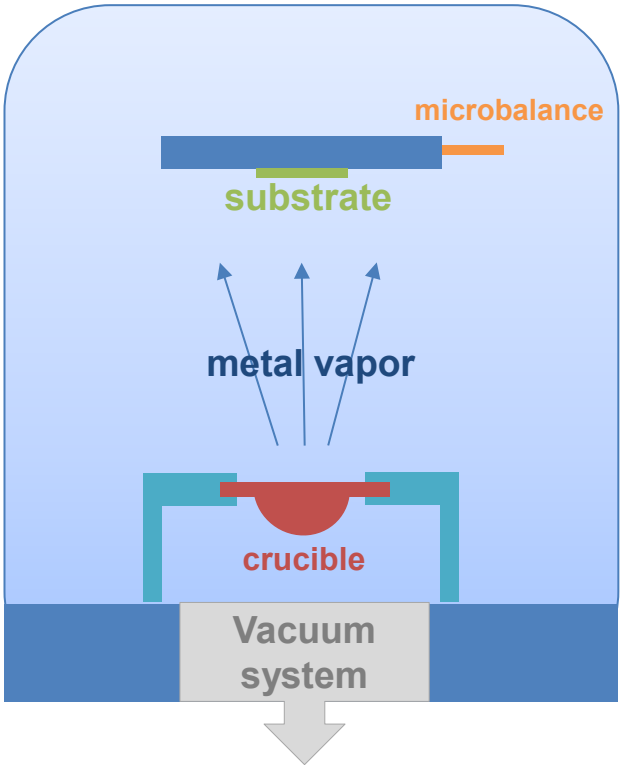

Figure 4.11: Illustration of the thermal evaporation mechanisms.

4.4.3.2 Electron beam (E-beam) deposition

An alternative technique for depositing high-quality thin metal film is E-beam deposition where the metal vapor is generated by hitting the metal source with electron beam. **Figure 4.12** demonstrates the mechanism of E-beam evaporation. Similar to thermal evaporation, high vacuum is necessary for evaporation. The main difference resides in the heating of materials where in this technique, a high-energy electron beam generated by the filament is targeted to the source crucible. The major advantage for E-beam evaporation is the localized heating of material without reaching the vaporization temperature of the metal, thus suitable for evaporation high-melting-point materials. The reduced heating area compared to thermal evaporation also prevents the overheating of the substrate, which is sometimes detrimental to the resist polymer causing deformation of the pattern and failure for lift-off.

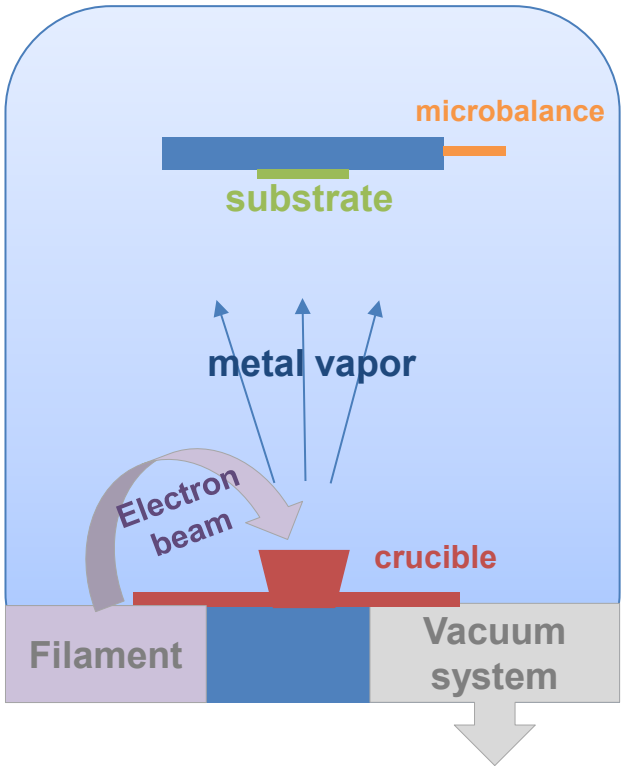

Figure 4.12: Illustration of the Ebeam evaporation mechanisms.

4.4.3.3 Lift-off

Both for E-beam lithography and UV photolithography, warm acetone (50 °C) is used as the solvent for lift-off. This process is to dissolve the resist and the metal layer on top of the resist, leaving the metal electrode only in the patterned region (See Figure 4.9). The final result of each step of nanofabrication could be found in Figure 4.13.

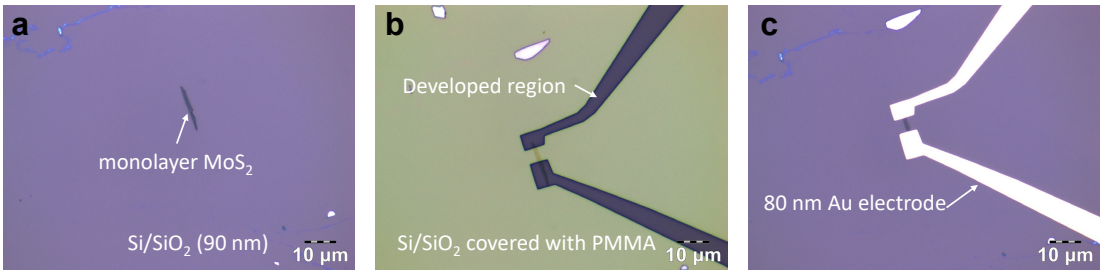

Figure 4.13: Optical microscope image of each step of the monolayer MoS_2 field-effect transistor: (a) Before lithography; (b) After development; (c) After lift-off.

4.4.3 Post-annealing treatment

Contaminants from the device fabrication usually affect the physical and chemical properties of 2D materials. Resist and solvent residues are strong dopants to 2D materials that modifies the electronic properties of 2D materials, impeding the future manipulation as optoelectronic devices and sometimes covers the intrinsic properties of materials which are undesirable for fundamental studies. Therefore, a post-annealing is necessary to remove the contaminants and reveal the genuine material behaviours.

In this thesis, post-annealing after nanofabrication is applied to all devices. The vacuum annealing system reaching 10^{-7} mbar equipped in the evaporator are utilized with the heating temperature above 150°C.

4.5 Optoelectronic characterization techniques

4.5.1 Electrical measurement

In this thesis, electrical measurements are realized with a probe station equipped with an optical microscope with CCD camera in a nitrogen (N_2)-filled glovebox as is demonstrated in Figure 4.14. The metallic chuck is responsible for global back-gating and is isolated from the probes for connecting the electrodes of the devices. The positions of the probes are controlled by the micromanipulators.

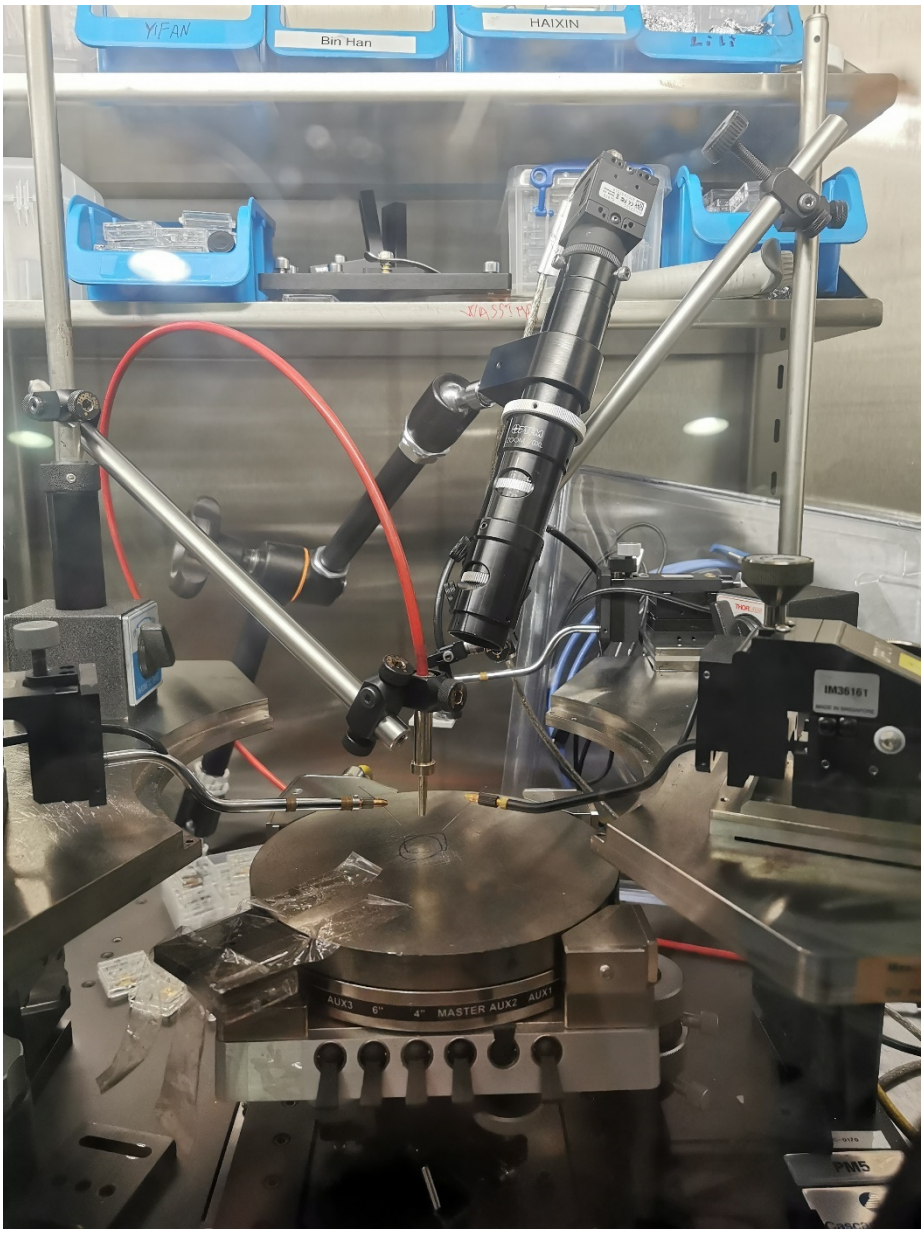

Figure 4.14: Photo of a probe station in the glovebox with an optical fiber.

4.5.1.1 Field-effect transistor measurement

Metal-oxide-semiconductor field-effect transistors (MOSFET) are the key building blocks in modern electronics. They are commonly responsible for the logic gate which enables fast and precise computing. Typical device configuration of monolayer MoS_2 field effect transistor (FET) is depicted in **Figure 4.15**. The devices are composed of 3 terminals, namely gate (G), drain (D) and source (S). Monolayer MoS_2 behaves as n-type FET with SiO_2 as gate dielectric and gold (Au) as drain-source electrode. The large Fermi-level pinning effect results in pure electron injection from

the contact to the semiconducting channel, resulting in unipolar n-type transport. Upon a drain-source bias (V_{ds}), the current I_{ds} flows from the drain electrode (D) to the source electrode (S) through the semiconducting channel. The gate electrode controls the conductance of the channel, therefore modulating the magnitude of I_{ds}. Generally, for a semiconducting material, as shown in **Figure 4.16**, at V_g=0, as monolayer MoS_2 is intrinsically an n-type semiconductor, the Fermi level (E_F) is near the conduction band E_c (**Figure 4.16a**). By adding a negative gate bias, the surface charge is negative causing the conduction band (E_c) and valence band (E_v) to bend up at the interface, Therefore, the conduction band is far from the Fermi level near the interface, causing dramatic reduction of majority charge carrier (electron) density. Oppositely, upon a positive gate bias, the conduction band and the valence band bend down at the interface, therefore causing negative charge accumulation at the interface. Considering the atomic thickness of 2D materials, the spatially resolved charge distribution does not change too much in the semiconducting body at z-axis. Thus, the charge carrier density modulation at the interface by gate voltage could be considered as the modulation for the whole 2D material. Therefore, a greater gate control of 2D material is always observed compared to traditional semiconducting materials. The global gate control causes the ON and OFF state of the FET, realizing the binary data computing.

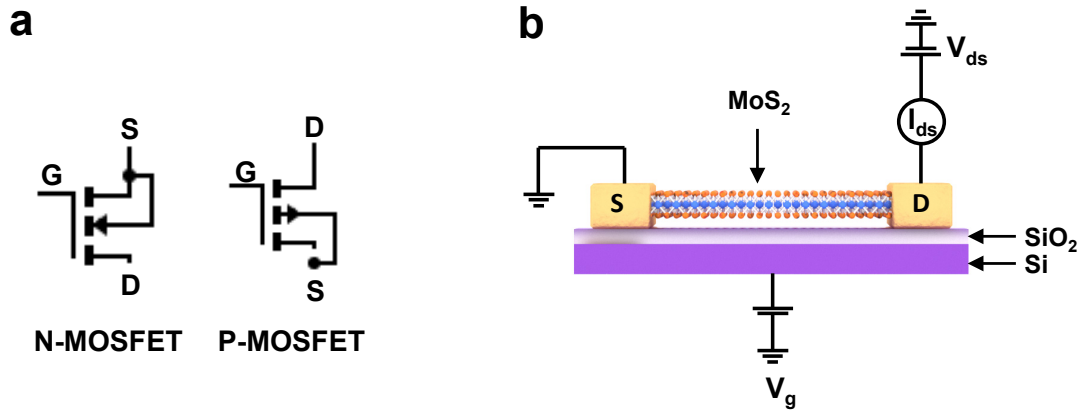

Figure 4.15: Electronic configuration of 2D field effect transistors. (a) Electronic symbol of N-MOSFET and P-MOSFET. (b) Device architecture of a monolayer MoS_2 FET.

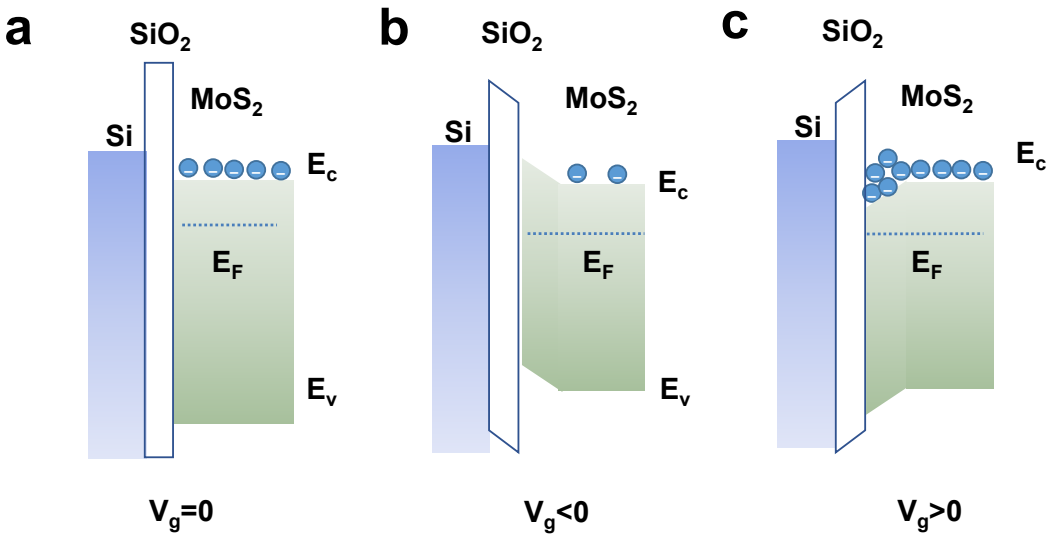

Figure 4.16: Band diagram of the MoS_2 FET with the control of (a) zero, (b) negative and (c) positive gate voltages. Here the gate electrode is Si and the oxide is SiO_2 (dielectric constant- 3.9).

The occupation of electrons (holes) at certain quantum state of energy E follows the Boltzmann distribution where

$$f(E) = Aexp(-\frac{E}{k_0T})$$

where k_0 is the Boltzmann constant, T is the temperature and $A = exp\frac{E_F}{k_0T}$.

Define N_C to be the effective density of states (DoS) of the conduction band,

$$N_C = 2(\frac{m_n^* k_0 T}{2\pi\hbar^2})^{3/2}$$

So, the electron density n_0 follows

$$n_0 = N_C \exp(-\frac{E_C - E_F}{k_0T})$$

Similarly, the hole density p_0 could be solved to be

$$p_0 = N_V \exp(\frac{E_V - E_F}{k_0T})$$

where N_V is the effective density of states (DoS) of the valence band.

Therefore, by integrating the distribution between E and $E + dE$, one can obtain the electron density n_0 at the conduction band to be

$$n_0 = 2(\frac{m_n^* k_0 T}{2\pi\hbar^2})^{3/2} \exp(-\frac{E_C - E_F}{k_0T})$$

where m_n^* is the effective mass of electron, $\hbar$ is the reduced Planck constant.

In an intrinsic semiconductor, $n_0 = p_0$. While when doping occurs, the possibility of electrons which occupy the charged impurity states can not fit the Fermi distribution. Here,

$$n_0 = n_D^+ + p_0$$

where n_D^+ is the ionized donor density.

$$n_D^+ = \frac{N_D}{1 + g_D \exp\left(-\frac{E_D - E_F}{k_0 T}\right)}$$

Here N_D is the donor density and E_D is the donor energy, g_D is the degeneracy factor of the donor level which equals 2.

The equation is highly dependent on temperature and here we consider only at strong ionized region at high temperature, $n_0 \gg N_D, p_0 \gg N_D$. The intrinsic charge carriers are much more numerous than the ionized impurities, and the conduction from the impurities could be neglected.

The discussions above are important since in most of the work presented in the next chapters focus on the doping of 2D semiconductors with molecules. The doping is usually evaluated by the charge carrier density change, where taking n-type semiconductor for example,

$$\Delta n_0 = n_{0,after} - n_{0,before} = N_C exp \frac{E_{F,after} - E_{C,after}}{E_{F,before} - E_{C,before}}$$

The subscripts "before" and "after" correspond to the carrier density before and after doping.

However, as E_C could not usually be measured directly by common experimental approaches, we use FET model to extrapolate the charge carrier density change for most of our work.

$$\Delta n_0 = \frac{C_{di}\, \Delta V_{th}}{e} = \frac{\varepsilon_{di}\, \Delta V_{th}}{t_{di}\, e}$$

Where Δn_0 is the change in electron density, C_{di} is the capacitance of dielectric layer, e is the elementary charge, and ε_{di} is the dielectric constant of dielectric layer, ΔV_{th} is the change of threshold voltage in transfer curve and t_{di} is the thickness of dielectric layer.

The threshold voltage corresponds to the onset of gate voltage which draws the FET to strong inversion region. **Figure 4.17** shows a typical transfer curve of a monolayer MoS_2 FET. By fitting the linear region, the extrapolated point to X axis correspond to the value of $V_{th} + \frac{1}{2}V_{ds} \approx V_{th}$. With this method, it is possible to achieve numerical evaluation through the doping without sophisticated measurements.

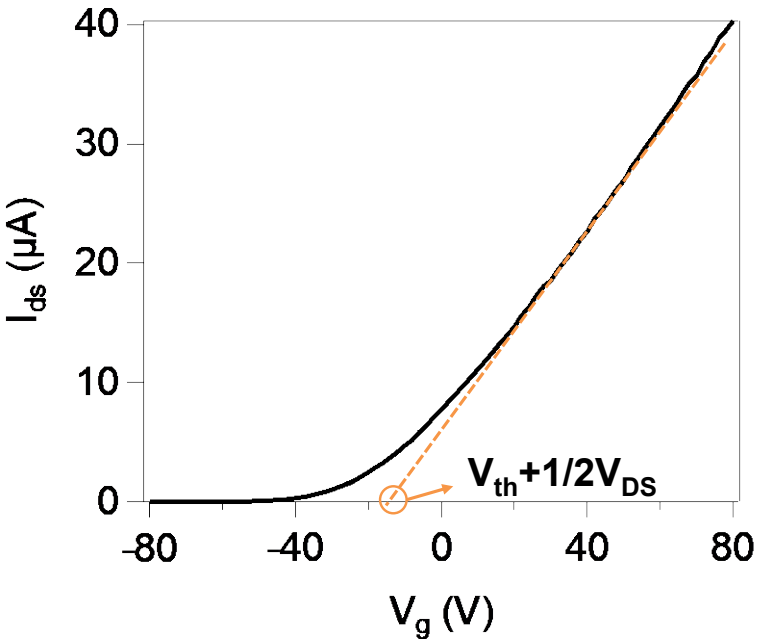

Figure 4.17: Representative transfer curve of monolayer MoS_2 showing the extrapolation of V_{th} through the linear region.

When V_g is greater than V_{th}, the indued charge Q by the gate along the x-axis of the channel is expressed as

$$Q(x) = -C_{ox}(V_g - V(x) - V_{th})$$

where $V(x)$ is governed by $V_{ds} = |V(x = L_{ch}) - V(x = 0)|$, L_{ch} represents the channel length.

Taking the $Q(x)$ into the calculation of drain − source current I_{ds}, one can obtain

$$I_{ds} = -v(x)Q(x)W_{ch}$$

W_{ch} is the channel width and $v(x)$ is the drift velocity which is related to the field − effect mobility μ, where

$$v = \mu \frac{\partial V}{\partial x}$$

Therefore, it is possible to obtain

$$I_{ds} = \mu C_{ox} \frac{W_{ch}}{L_{ch}} [(V_g - V_{th})V_{ds} - \frac{{V_{ds}}^2}{2}]$$

Thus,

$$\mu = \frac{L_{ch}}{W_{ch} C_{ox} V_{ds}} \frac{dI_{ds}}{dV_g}$$

The field-effect mobility μ is an important parameter to evaluate a semiconducting material, given that the scattering from impurities and defects in the material largely limit the carrier to

flow along the channel region. Especially for 2D materials, the predicted field-effect mobility is always several magnitudes larger than the experimental value, caused by the rich scattering centers when thinning down the material. The enhancement of carrier mobilities, mainly by limiting the scattering on the interface and the defective sites, has become an important issue, which would also be discussed in detail in Chapter 7. [104,105]

4.5.1.2 P-N junction measurement

When a p-type semiconductor is in contact with an n-type semiconductor, it forms the two-terminal device, p-n junction. The Fermi level alignment of the two materials causes band bending at depletion region and generates built-in potential Ψ_{bi} which is equal to

$$\Psi_{bi} = \frac{kT}{q}\ln\left(\frac{N_D N_A}{{n_i}^2}\right) = \frac{kT}{q}\ln\left(\frac{n_0}{p_0}\right)$$

(see **Figure 4.18**)

The ideal current-voltage characteristics follows the Schockley equation where

$$J = J_0[\exp\left(\frac{eV}{kT}\right) - 1]$$

where J is the diode current, J_0 is reverse bias saturation current.

The evaluation of a PN junction relies on certain parameters, including rectification ratio and ideality factor. The detailed evaluation is discussed in detail in Chapter 7 for specific 2D-based PN junction devices. [104]

A major feature of P-N junctions is the photovoltaic effect where photogenerated electron-hole pairs could be separated by the internal electrical field (or built-in potential across the junction). The generated current is the short-circuit current (I_{sc}) and the photocurrent flow would induce accumulation of opposite charge carriers, denoting open-circuit voltage (V_{oc}).

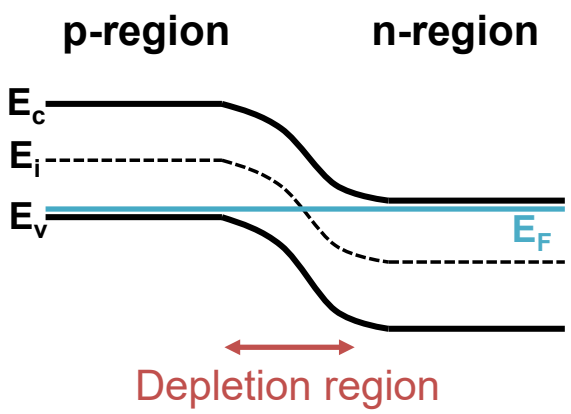

Figure 4.18: Band diagram of PN junction.

4.5.2 Photodetector measurement

The photo of photodetector measurement setup is demonstrated in **Figure 4.19** where an optical fiber is installed in the glovebox connected to a monochromator (Polychrome, Till) placed outside the glovebox. As shown in **Figure 4.19**, the monochromator light source is connected to a 150W Xenon light. The wavelength control of the monochromic light is realized by an entrance aperture which scatters the white light into broadened spectrum, and an exit slit to filter the light of narrow bandwidth of 2 nm minimum and 15 nm maximum. The light intensity control is enabled by the motorized exit slit. The light intensity is different for each wavelength and calibration is required from time to time on account of the intensity decay of the Xenon light. The most recent light intensity calibration from 300 nm to 690 nm of wavelength with 5 nm step is reported in **Annex 1**.

The photocurrent is directly measured through the device connected to a source-meter unit (SMU), (Keithley 2636). The energy of incident photo causes the dissociation of electron-hole pairs in a photodetector, resulting in increased photocarrier in the 2D semiconductor channel, which is reflected as photocurrent (**Figure 4.19**), with the assistance of an external drain-source bias.

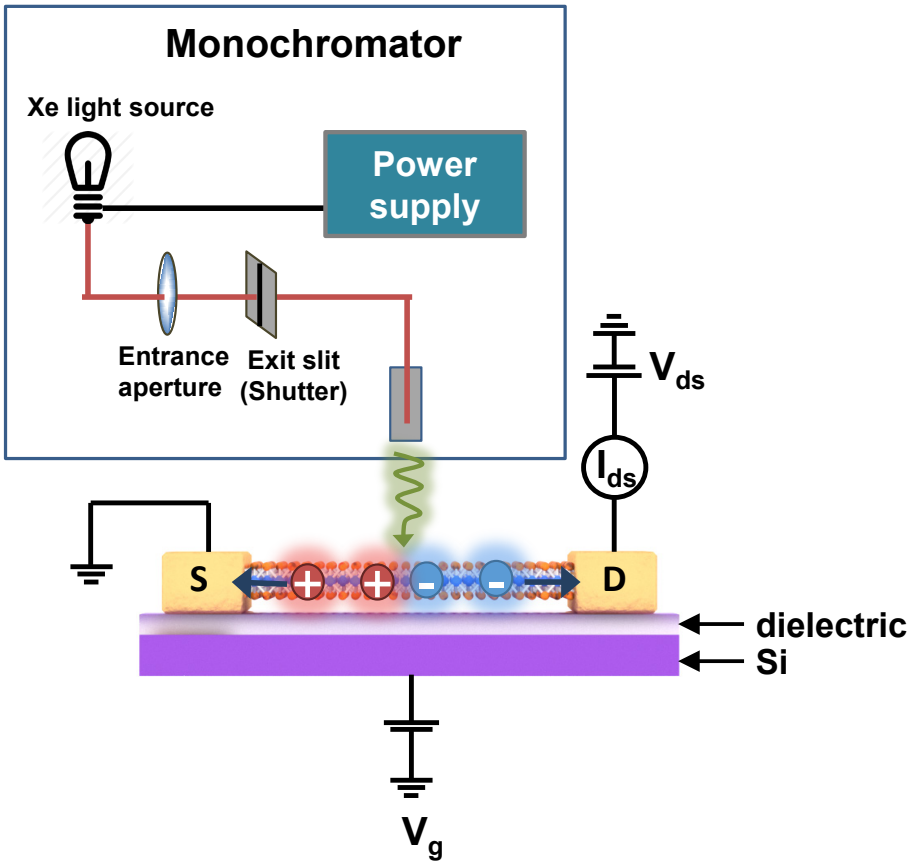

Figure 4.19: Schematic representation of the photodetector measurement.

4.5.3 Logic inverter characterization

A binary logic inverter consists of an n-FET and a p-FET connected in-series, forming a 4-terminal device. As shown in **Figure 4.20**, the logic inverter required simultaneously input two signals, V_{IN} and V_{DD}, and output one signal, V_{OUT}. One electrode of the device is needed to be grounded as potential reference. In order to attain this goal, we connect one dual-channel SMU (Keithley 2636) with one mono-channel SMU (Keithley 2635). The former provides voltage source input, and the latter serves for recording the output signal. Logic manipulation could attain in this way, as presented in **Figure 4.20** where input and output logic states are in opposite value.

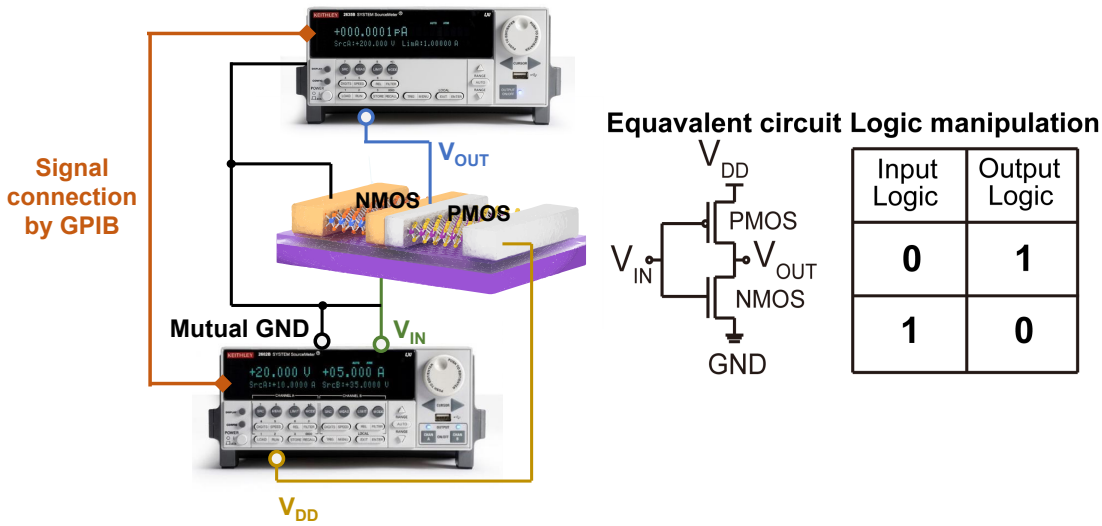

Figure 4.20: Schematic illustration of logic inverter measurement setup, the equivalent circuit and logic manipulation.

4.6 Spectroscopic characterization techniques

4.6.1 Photoluminescence (PL) and Raman spectroscopy

Photoluminescence (PL) spectra are recorded through the Renishaw InVia Raman spectrometer. The schematic representation of the key elements for the measurement could be found in **Figure 4.21**. The excitation laser is 532 nm. The system is combined with a charge coupled device (CCD) camera, allowing to get spatially resolved spectroscopic information. Different gratings are selected for different measurements. For PL, a grating of 300 l/mm is adopted while for Raman spectroscopy, the value is 2400 l/mm.

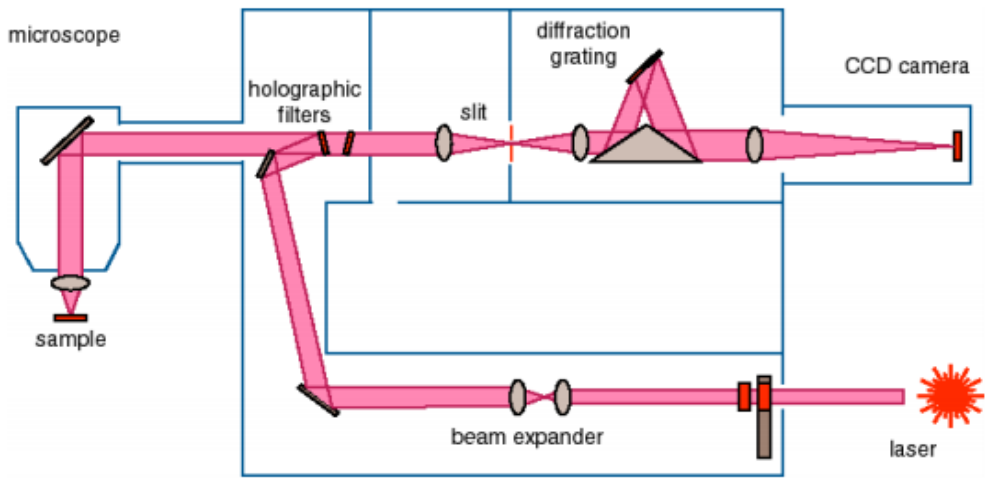

Figure 4.21: Schematic representation of Renishaw Raman spectrometer (Source: Renishaw Raman spectrometer Manual).

4.6.2 Low-temperature photoluminescence spectroscopy and gate-modulated low-temperature photoluminescence spectroscopy

Both low-temperature and gate-modulation combined PL spectroscopy are recorded with the help of a temperature control stage (Linkam THMS600 and HFS600E-PB4). The Linkam THMS600 holder adapted on Renishaw inVia spectrometer is shown in **Figure 4.22a**. The liquid nitrogen is placed in a metallic sealed container with an outlet tube which could be directly connected to the holder. Another tube is connected for liquid nitrogen outlet, which is eventually connected to the pumping system of the controller, to form a circulation around the sample in the stage. The temperature could be decreased as low as 77K with a maximum speed of 150°C /min. The sample is physically isolated with liquid nitrogen, but thermally synchronized with the outer part of the stage where the temperature is monitored by an external controller. An additional blower is placed beside the transmission window for the laser to avoid moisture which deflects the laser before arriving on the sample.

The Linkam HFS600E-PB4 is similar to Linkam THMS600 except additional electrical connections could be attained. Four micromanipulators with Tungsten probes are equipped in the sample chamber, enabling electrical contact to the sample. The manipulators are wired with BNC connectors, which are linked to external SMU for electrical measurements. For the specific electrical-gated PL measurement described in Chapter 5, two probes (one for gate electrode, the other for grounding) are utilized. As the probes might slide during the closure of the top sealing

cap and due to the bad adhesion between the gold electrode and SiO_2, silver paste is utilized for stabilizing electrical contacts.

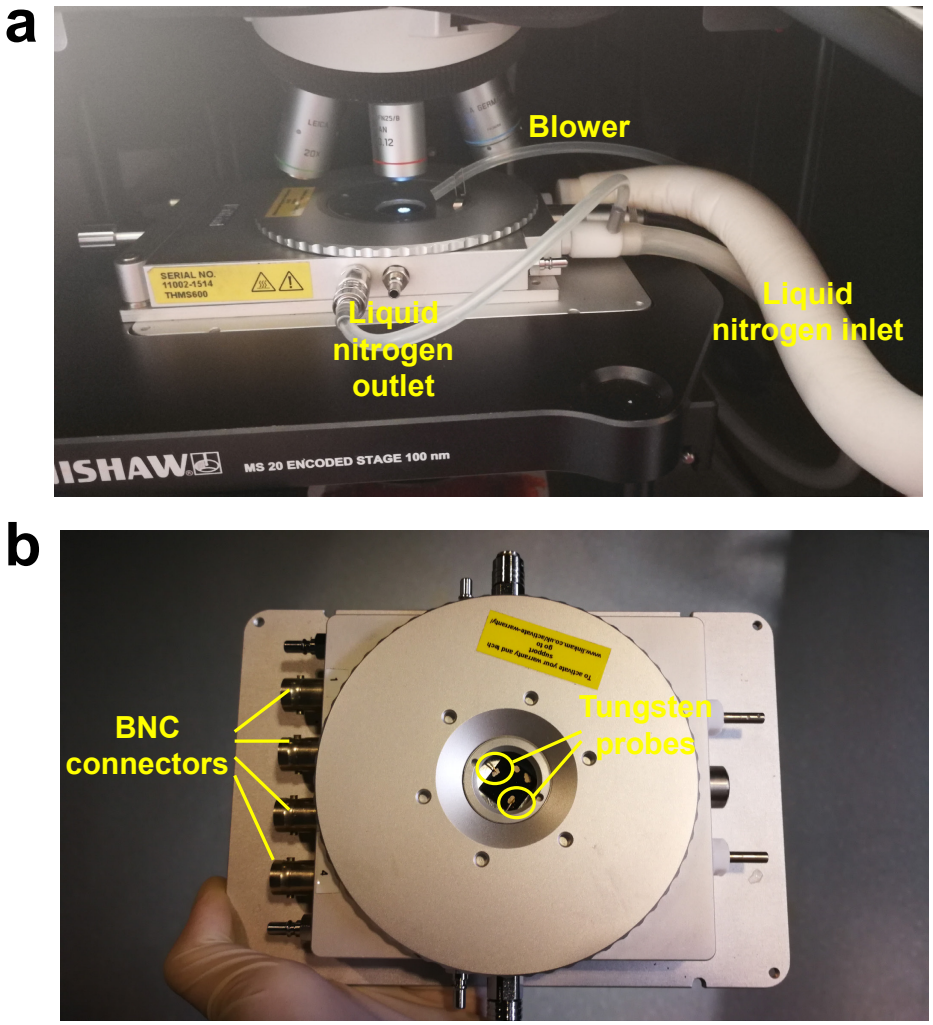

Figure 4.22: Low-temperature Photoluminescence and Raman measurement. (a) Photo of Linkam temperature controlling TMHS600 stage equipped onto Renishaw Raman spectrometer. (b) Photo of Linkam HFS600E-PB4 with probes and BNC connectors.

4.6.3 X-ray photoelectron spectroscopy (XPS)

X-ray photoelectron spectroscopy (XPS) is a powerful technique for characterizing surface properties. The principle of XPS spectroscopy is based on the famous photoelectron equation by A. Einstein where

$$K.E. = E_{ph} - \Phi_{XPS} - B.E.$$

here, $K.E.$ stands for the kinetic energy of the photoelectron measured in the detector system, Φ_{XPS} is the work function of the XPS instrument and $B.E.$ is the binding energy of the instrument. Usually, the $K.E.$ is the measured quantity in the instrument while $B.E.$ is used to construct XPS spectrum. The $B.E.$ reflects the environment where the photoelectron resides in before being excited with X-ray, which is the chemical element and related bonding. The X-ray source in our experimental setup is generated by Aluminum K-alpha anode, with photon energy of 1486.6 eV and line width of 0.85 eV.

For different elements, the accessibility of X-ray to the orbitals differs greatly. Some emission takes place at K level, and other at L level or M level, therefore differs the K.E. that is recorded (**Figure 4.23**). When the element presents various chemical states, XPS can serve as a best tool for defining the chemical environment for its sensitivity. Note that the Auger electron, which occurs via a de-excitation process, holding smaller kinetic energy than the photoelectron, are not negligible in the XPS spectra.

Ultra-high vacuum (UHV) is always required during the analysis in order to avoid collision of photoelectron with other chemical species. As shown in **Figure 4.24**, the analysis chamber is under a constant low pressure of 10^{-8} mbar. A flood gun of Argon ion is always applied when measuring insulating samples to avoid electrostatic charge which could eventually shift the binding energy.

In the analysis of 2D materials, XPS plays an important role since most of the chemical and physical processes for the flat material are on surface. Chemical functionalization, which could dramatically modify the bonding environment of certain element, could be detected with XPS resulting in new peaks. While physical functionalization, especially physorption of strong dopants, could cause peak shift of 2D materials. Taking **Figure 8.2** in **Chapter 8** as example, the strong n-doping from the physisorbed molecule drives an increase in electron density around the Mo and S elements in monolayer MoS_2, causing redshift of binding energies.

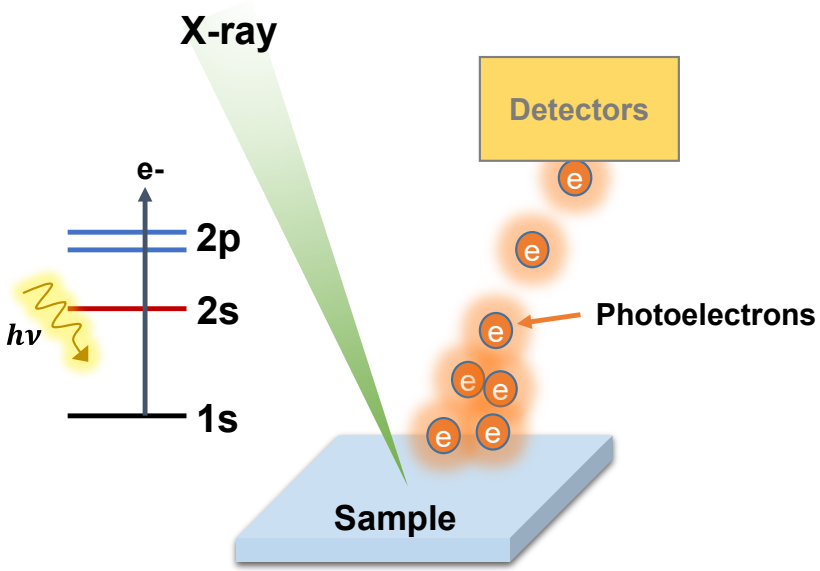

Figure 4.23: Mechanism of photoelectron generation and the schematic representation of XPS instrument.

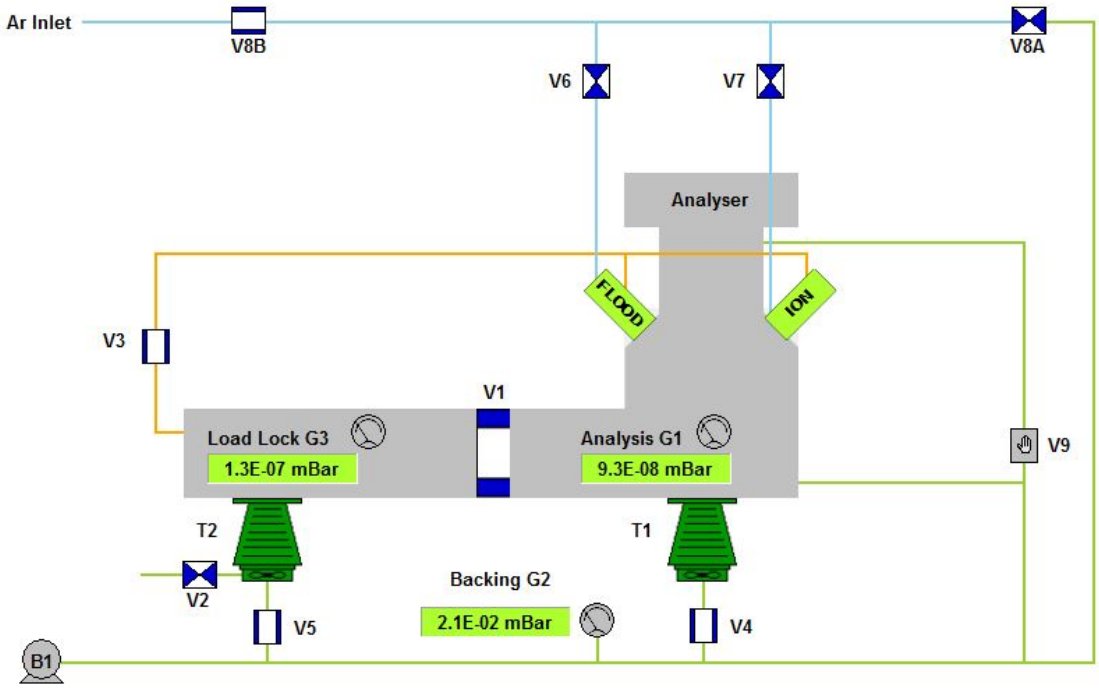

Figure 4.24: Scheme of the Thermo Fischer XPS instrument used in this thesis.

4.6.4 Photoelectron spectroscopy in ambient conditions (PESA)

Similar to XPS, the photoelectron spectroscopy in ambient conditions (PESA) resolves the material

properties benefitting from the photoelectric effect. It is an equipment for evaluating the work function of a metal or semiconducting material, using photon energy from UV light source of 3.4~6.8 eV. The core levels of the elements are therefore hard to access through the low photon energy, and the photoelectronic effect is limited by the emission from the valance band. Hence photoelectric effect occurs at the Fermi level of the material, or work function for metal.

The principle of measurement is explained in **Figure 4.25**, where the emitted photoelectron excited by UV light is attached with an oxygen molecule. The charged oxygen drifts to the anode (A) via Suppressor Grid (Gs) and Quenching Grid (Gq), followed by a discharge pulse signal generation in the preamplifier output (V_s). The energy of the photoelectron is amplified by 10^5 to 10^7 times through an acceleration of electrical field. The signals are transmitted to the controller. The number of counts detected are measured for a certain range of pre-set photon energy. When the energy is above the Fermi level, the photoelectron count is seen to be increased largely. Therefore it is possible to extract the Fermi level (or work function) in ambient condition.

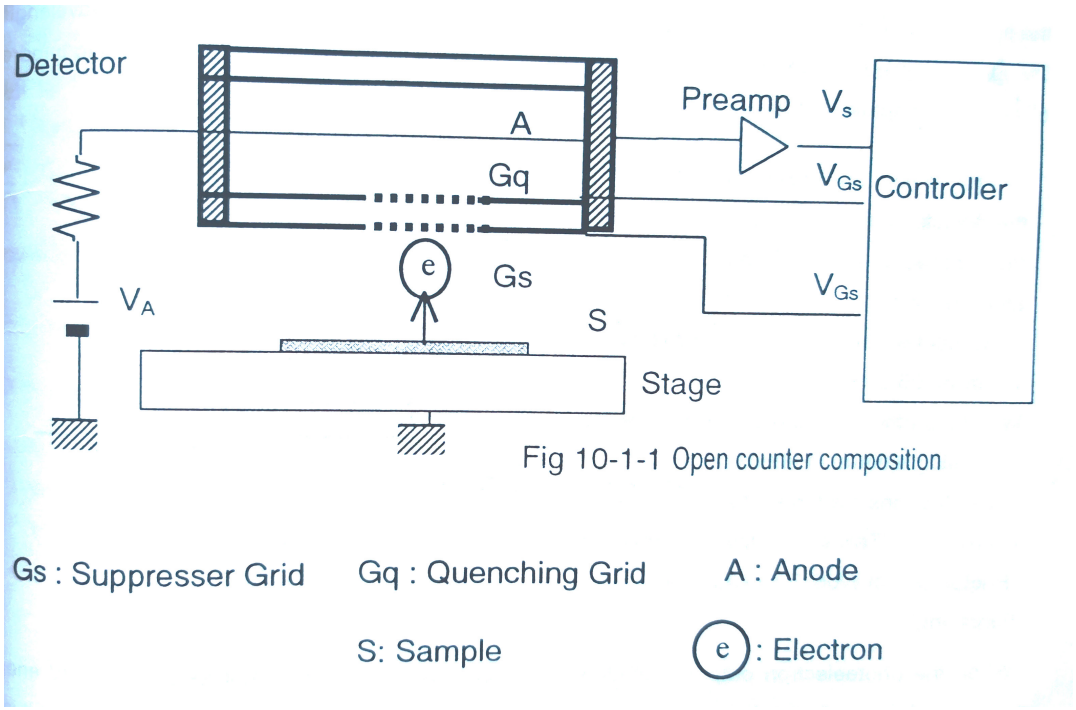

Figure 4.25: Scheme of the measurement principle of Riken AC-2 photoelectron spectrometer. (Source: RIKEN KEIKI CO.,LTD)

4.7 Surface characterization

4.7.1 Atomic force microscopy

Atomic force microscopy (AFM) measures the morphology of a surface on the nanometric scale. It is an essential technique for the research of 2D materials for monitoring the thickness, cleanliness, and the overall crystal quality of the material. More importantly, in this thesis, as molecular functionalization of 2D materials takes place on surfaces of the latter, the thickness change, morphology change according to molecular assembly on surface could be easily visualized by AFM. Prevailing measuring modes of AFM are contact mode and tapping mode. In contact mode, the tip is touching the surface and the dominating force between the tip and sample is repulsive. In tapping mode, there is a distance of ~ 50-150 Å between the sample and the tip with attractive Van der Waals force being the symbol to be recorded. The former mode generally provides good resolution but faces the damage of material by the shear force on the tip. The latter mode is less invasive, yet it reaches lower spatial resolution because of the smaller magnitude of the detected forces. Since most organic molecules form soft layers that are fragile against the contact-mode scanning, in this thesis, all measurements were done with tapping mode of AFM.

Figure 5.25 shows the setup of typical tapping-mode AFM. The functional parts consist of a cantilever with TESPA-V2 tip, a photodiode for recording the laser beam reflection governed by the deflection of cantilever oscillation according to the movement of the tip and electronic units such as amplifier to translate the signal, and a proportional–integral–derivative (PID) controller with piezodriver to modulate the dynamic positional change. By integrating the spatially resolved information, the morphology information is able to be mapped.

Information collected by AFM for molecular functionalized 2D materials are primarily the heigh profile change and phase change. They are originated from the tip-sample force which is given by

$$z(t \gg 0) = d + Acos(2\pi f_d t + \phi)$$

where $z(t)$ is the tip position at time t,d is the cantilever-sample distance, A is oscillation amplitude, f_d is the driving frequency of the cantilever and ϕ is the phase difference between the excitation and oscillation in the cantilever.[106] The phase ϕ reflects the intrinsic mechanical and viscoelastic properties of the material when interacting with the surface. This parameter is important for the functionalization of 2D materials because it allows to evaluate the homogeneity of the molecular physi-/chemi-sorption of the tens of micrometer scale of a 2D flake. Sometimes, when the molecule interacts differently with the substrate than the 2D material (e.g. molecular self-assembly orientation difference), the variation could be visualized in the phase image.

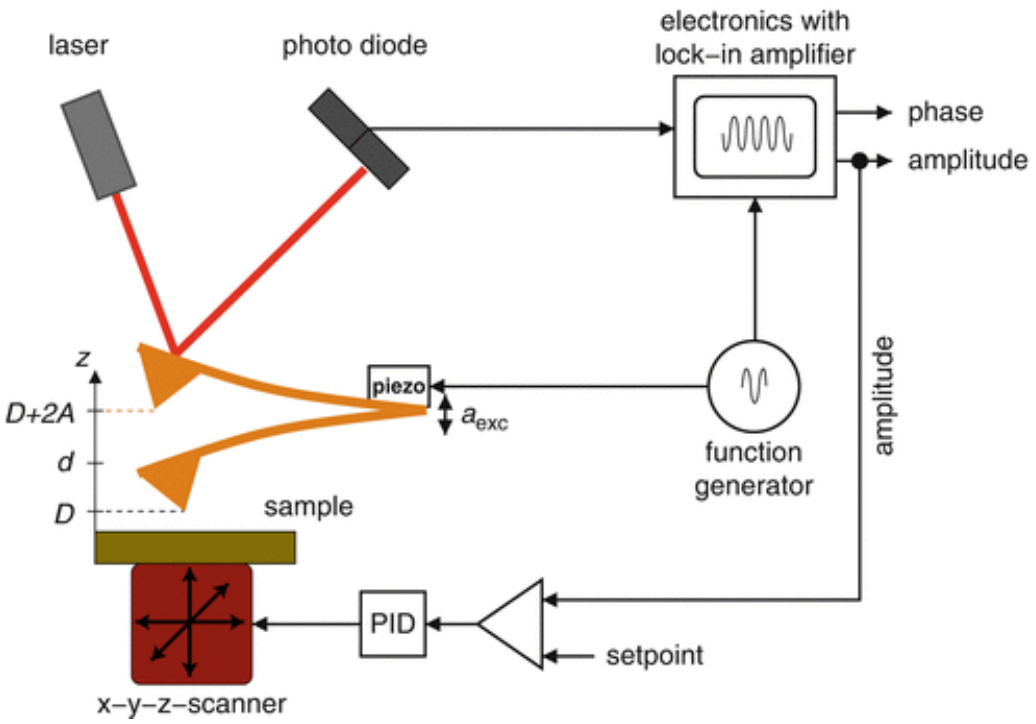

Figure 4.25: Setup of a dynamic force microscope operated in the tapping mode. Figure adapted from Ref.[106]

4.7.2 Kelvin probe force microscopy

The Kelvin probe force microscopy (KPFM) is an alternative module in AFM for measuring the work function of the sample. The principle comes from:

$$\Delta\Phi = \frac{\Phi_{tip} - \phi_{sample}}{e}$$

where $\Delta\Phi$ is the electrostatic contact potential difference between the tip and the sample, Φ_{tip} and ϕ_{sample} are the work function of the tip and sample respectively, and e is the elementary charge. In this thesis , we use PtIr coated Si tip with work function of ~5.4 eV.

As is shown in **Figure 4.26**, in addition to the tapping mode function of AFM, for KPFM, a AC voltage and an adjustable DC voltage are applied on the tip to generate potential signal. The sample is connected to the ground. The measurement of the potential takes place after defining the profile of the surface using tapping mode and a constant tip-sample distance is applied in this case. Thus, localized surface potential could be measured in a 2D plane.

For 2D materials, the molecular doping largely modifies the surface potential of the semiconducting material. While in other techniques, such as UPS and semiconductor device

analysis, the work function tuning by molecular doping is an averaged effect through the 2D plane of tens of micrometer size, with KPFM, small changes of potential down to meV range can be measured in tens of nm sized regions, significantly increase the precision of doping analysis.

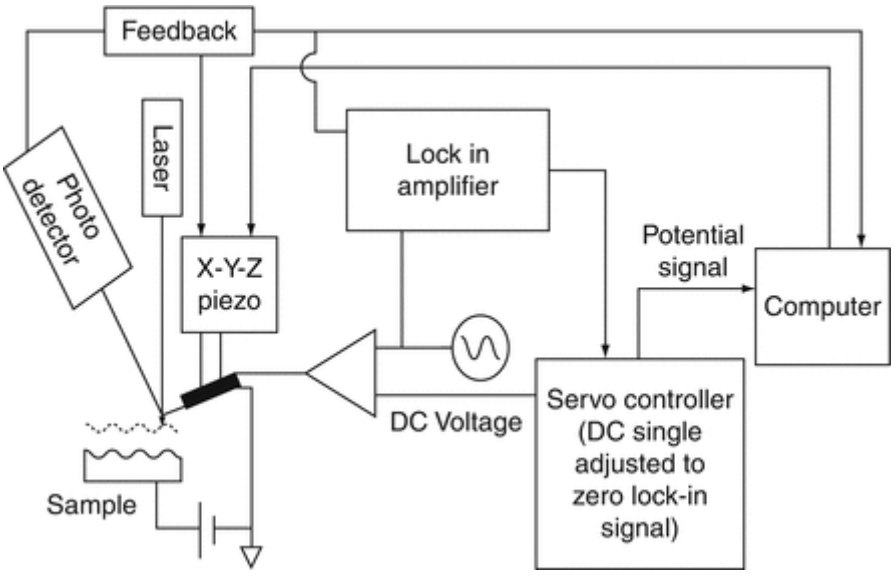

Figure 4.26: Schematic representation of the KPFM scan.

Chapter 5 Tuning the optical and Electronic Properties of Transition Metal Dichalcogenides

5.1 Introduction

During the last decade, two-dimensional (2D) materials have attracted remarkable attention owing to their unique physical and chemical properties. Among them, transition metal dichalcogenides (TMDs) are semiconducting systems that exhibit an indirect-to-direct bandgap transition from bulk to monolayer, large exciton binding energies, and inversion symmetry breaking, which are attractive for a large range of applications from (opto)electronics to valleytronics [3,107-111]. The largest surface-to-volume ratio in the crystal structure of monolayer TMDs makes them extremely sensitive to changes in the environment.[112] In this regard, the simple physisorption of atoms and molecules represents a powerful method to modulate their optical and electrical properties.[112,113]

Highly polar physisorbed molecules including F4TCNQ and NADH,[32] hydrazine,[114] benzene viologen,[115] have been utilized for the chemical doping of monolayer TMDs. Interactions between these molecules and TMDs induce charge transfer, thus modifying the Fermi level and tuning the electronic and optical properties of the material. In monolayer TMDs, strong electron-hole Coulomb interactions enable the formation of stable optically generated excitons at room temperature;[116,117] these excitons are building blocks for the generation of many-body bound states such as electron-bound exciton (negative trion) or hole-bound exciton (positive trion)[118,119]. Accordingly, electron/hole concentrations modified by physisorbed molecules effectively influence the formation of excitons and trions in TMDs.

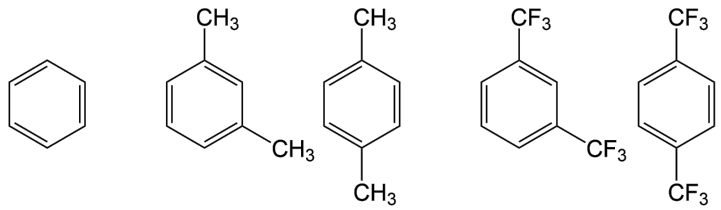

Scheme 5.1: Chemical formula of benzene, m-xylene, p-xylene, 1,3-bis(trifluoro)methylbenzene (1,3-TFMB), and 1,4-bis(trifluoromethyl)benzene (1,4-TFMB).

Although a great effort has been devoted to the non-covalent functionalization of monolayer TMDs via molecular physisorption to improve fundamental properties[120] such as photoluminescence tuning,[32,114,121,122] electron/hole doping[123,124] and device contact improvement,[125] the simple interaction of a functionalized benzene ring (being frequently a fragment of solvent molecules) and monolayer TMDs has not yet been fully unraveled.[126] Despite the fact that typical solvent molecules are seemingly considered as inert media, aromatic molecules have been proved to cause n- or p-doping with distinct functional groups through π-π interactions with graphene.[127] Unfortunately, similar studies on TMDs have not yet been reported. To gain a comprehensive understanding over the effect of physisorbed molecules on monolayer TMDs, we focused here our attention to the benzene and its derivatives depicted in **Scheme 5.1**, i.e. benzene, m-xylene, p-xylene, 1,3-bis(trifluoro)methylbenzene (1,3-TFMB) and 1,4-bis(trifluoromethyl)benzene (1,4-TFMB)) as aromatic molecules, and MoS_2 and WSe_2 as representative TMD monolayers acting as platforms for physisorption. The functionality of aromatic molecules is therefore modified through simple substitution in the *meta* and *para* position with either more apolar methyl ($-CH_3$) or more polar trifluoromethyl ($-CF_3$) groups. The melting point, boiling point and total dipole moment of each molecule are listed in in **Table 5.1**. Importantly, benzene, m-xylene and p-xylene are commonly used as solvents to dissolve complex organic molecules for functionalization of 2D materials and for device fabrication. These aromatic solvents could be unintentionally physisorbed on 2D materials resulting in changes in physical and chemical properties. Thus, understanding the effect of these molecules on monolayer TMDs is a crucial issue to be addressed not only for unveiling molecule-TMD interactions but also for device optimization. We reveal here on the occurrence of charge transfer between physisorbed molecules and monolayer TMDs, leads to change in electron/hole density and trion/exciton intensity ratio. Through low-temperature photoluminescence (PL) measurements performed at 78 K corroborated with Density Functional Theory calculations, we quantify n or p nature of doping for each molecule deposited on monolayer TMDs. Our results provide a text-book proof-of-concept on

the use of physisorbed aromatic molecules on single-layer TMDs to dope the 2D material in a controlled fashion.

Molecules	Melting point*	Boiling point*	Total dipole moment ‖μ‖ (D)
Benzene	**5.5°C**	**80°C**	**0.00**
m-xylene	**-48°C**	**139°C**	**0.42**
p-xylene	**13°C**	**138 °C**	**0.15**
1,3-TFMB	**-**	**116 °C**	**2.92**
1,4-TFMB	**-**	**116 °C**	**0.57**

Table 5.1: Physical properties of molecules.

*Data taken from the source of purchase Sigma-Aldrich (Merck).

5.2 Experimental methods

5.2.1 Sample preparation

Monolayer MoS_2 and WSe_2 flakes were mechanically exfoliated from commercially available molybdenum disulfide (Furuchi, Japan) and tungsten disulfide (HQ Graphene) crystals using the scotch tape method. The flakes were transferred onto SiO_2 (90 nm) / Si substrate, and their thickness was monitored by optical microscope combined with Raman spectroscopy and Atomic Force Microscopy (AFM). The samples were thermally annealed at 200 °C inside a vacuum chamber to desorb atmospheric adsorbates. Then, they were no longer exposed to air after the annealing and were characterized only under inert atmosphere (N_2-filled glovebox). Anhydrous solvents from Sigma Aldrich were opened in glovebox filled with N_2. To exclude the dielectric screening caused by environmental changes after depositing solvent molecules, we drop-cast each solvent molecule on monolayer TMDs, and spin-dried at 2000 RPM for 60 s to guarantee the presence of limited number molecules physisorbed on the surface of the TMD.

5.2.2 Low-temperature photoluminescence spectroscopy

Photoluminescence spectra were recorded in inert atmosphere (N_2) by using a Renishaw inVia spectrometer equipped with 532 nm laser in aid of Linkam TP95 temperature controller. Samples were mounted in the glovebox and immediately measured after annealing to avoid exposure to air. The spectra were taken a different temperature, spanning from room temperature (298 K) down to 78 K. The excitation power was kept below 1 mW to avoid local heating damage effects. The resolution amounted to ~1 meV.

5.2.3 Device fabrication and electrical characterization.

Back-gated FETs were fabricated on thermally oxidized heavily *n*-doped silicon substrates (Fraunhofer Institute IPMS, ρ_{Si} ~ 0.001 Ω·cm, t_{ox} = 90 nm) by means of E-beam lithography with polymethyl methacrylate (PMMA) resists, thermal evaporation of Au (80 nm) and lift-off in acetone. Devices were annealed in high vacuum (~10^{-7} mbar) overnight at 200 °C (Plassys ME400B). Electrical characterization was carried out at room temperature under N_2 atmosphere (glovebox) with source-measurement units from Keithley (model 2636A).

5.2.4 Computational details

Our theoretical calculations were performed using density functional theory with the projector-augmented wave (PAW) scheme, as implemented in the Vienna Ab-Initio Simulation Package (VASP).[128,129] The exchange-correlation potentials were treated by Perdew-Burke-Ernzerhof (PBE) [130] parametrization of the generalized gradient approximation (GGA) and the kinetic energy cutoff for basis set was 600 eV. Van der Waals interactions were taken into account using Grimme's semiempirical DFT-D2 corrections.[131] To model the physisorption of solvents on MoS_2 (WSe_2) monolayer, a 5×5×1 supercell was constructed and a vacuum of 25 Å thickness was used to avoid any physical interactions in the stacking direction. The first Brillouin zone integration was performed using 2×2×1 and 4×4×1 Monkhorst-Pack k-point mesh [132] for geometry optimizations and electronic structure calculations, respectively. The integral atomic positions were fully relaxed according to the Hellmann–Feyman forces until the residual forces and total energy difference remain below 1 meV/Å and 10^{-5} eV, respectively.

5.3 Results and discussions

5.3.1 Photoluminescence (PL) properties of monolayer MoS_2

The photoluminescence behavior of monolayer MoS_2 is known to be strongly temperature dependent.[30,133,134] Typical PL spectrum of monolayer MoS_2 at 78 K recorded in N_2 atmosphere is shown in **Figure 5.1a**. It exhibits four components in the range of 1.6 to 2.2 eV: a neutral A exciton (X) at ~1.88 eV and a negatively charged A trion (X^-) at ~1.90 eV, a B exciton (B) at ~2.05 eV and a defect-induced emission (D) at ~1.75 eV. The A excitons (X and X^-) are blue-shifted of 23 meV compared to room temperature due to the bandgap enlargement upon decreasing the temperature.[133] Temperature dependent studies on the photoluminescence of monolayer MoS_2 (**Figure 5.2**) reveal that localized emission caused by excitons bounded with defects (D) appears below 100 K. It is fair to indicate that such D peak is not observed in every flakes of our experiment likely because of the difference in defect density generated by mechanical exfoliation.

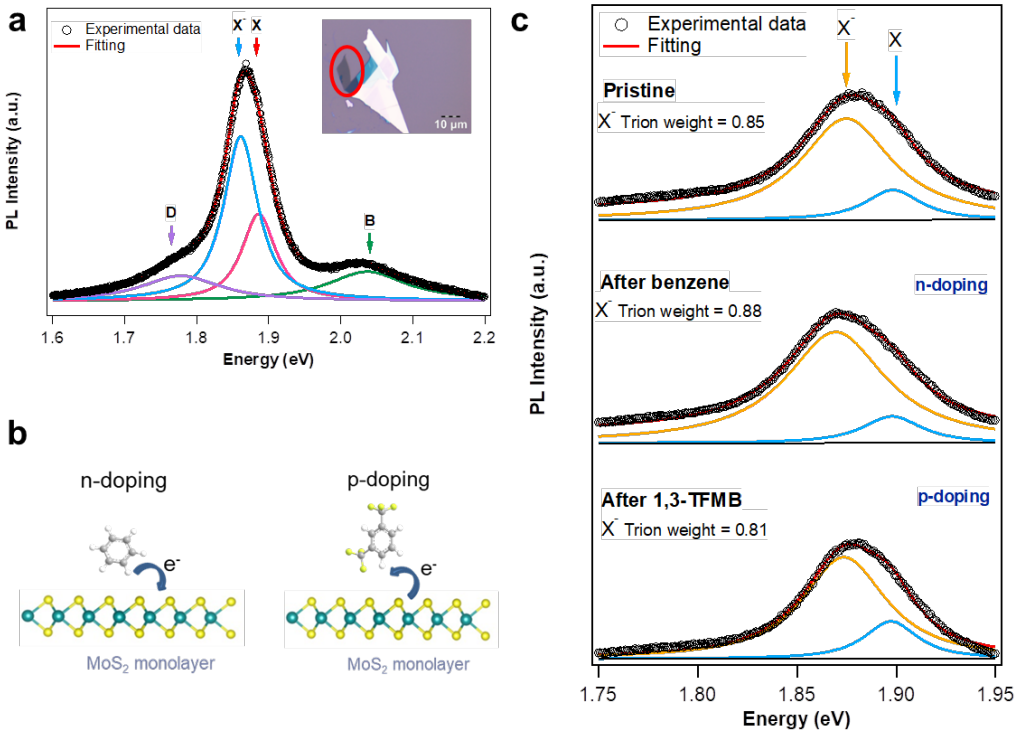

Figure 5.1: Photoluminescence spectra of monolayer MoS_2. (a) Photoluminescence spectra of monolayer MoS_2 at 78 K (inset: optical image of as exfoliated monolayer MoS_2 highlighted with a red circle. (b) Molecular representation of charge transfer between physisorbed aromatic molecules and monolayer MoS2. c) Photoluminescence spectra of monolayer MoS_2 before and after physisorption of benzene and 1,3-TFMB with calculated X- trion weight.

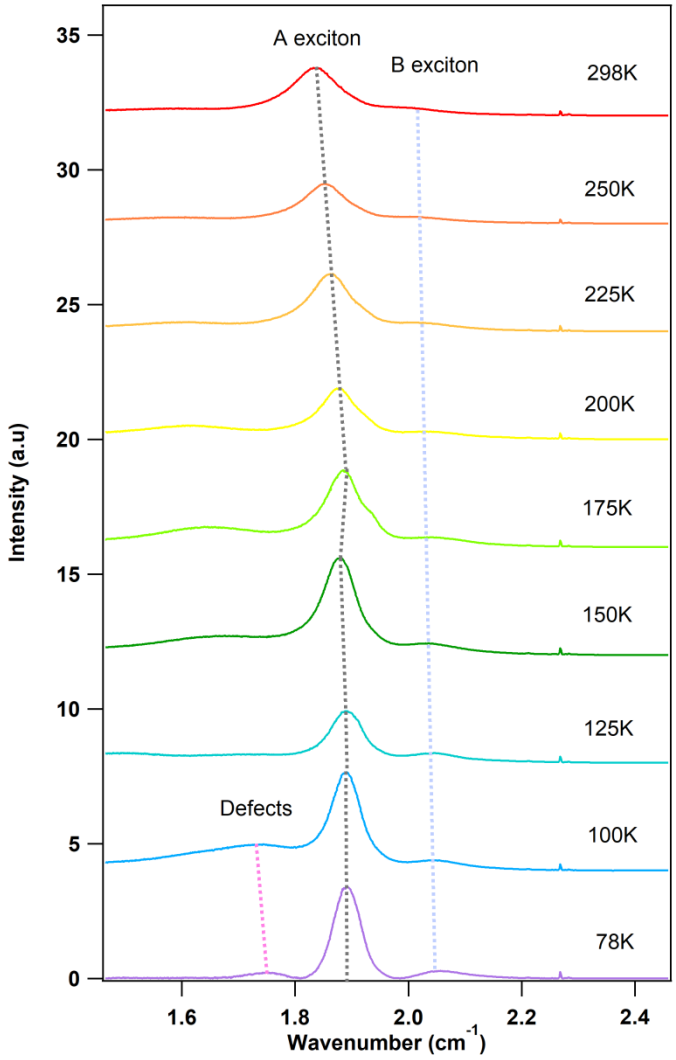

Figure 5.2: Temperature dependent photoluminescence of monolayer MoS_2.

5.3.2 Doping of monolayer MoS_2 with aromatic solvent moelcules characterized by PL spectra

The physisorption of benzene and its derivatives (i.e. benzene, m-xylene, p-xylene, 1,3-bis(trifluoro)methylbenzene (1,3-TFMB) and 1,4-bis(trifluoromethyl)benzene (1,4-TFMB)) as aromatic molecules onto monolayer MoS_2 (**Figure 5.1b**) is explored by monitoring the photoluminescence spectra. Such study provides evidence for the occurrence of chemical doping as revealed by major changes in PL emission intensity and shape.[32] Representative PL spectra of monolayer MoS_2 tuned by aromatic molecules at 78 K are portrayed in **Figure 5.1c** whereas the spectra, and related fitting, for MoS_2 with all kinds of physisorbed molecules is displayed in **Figure**

5.3.

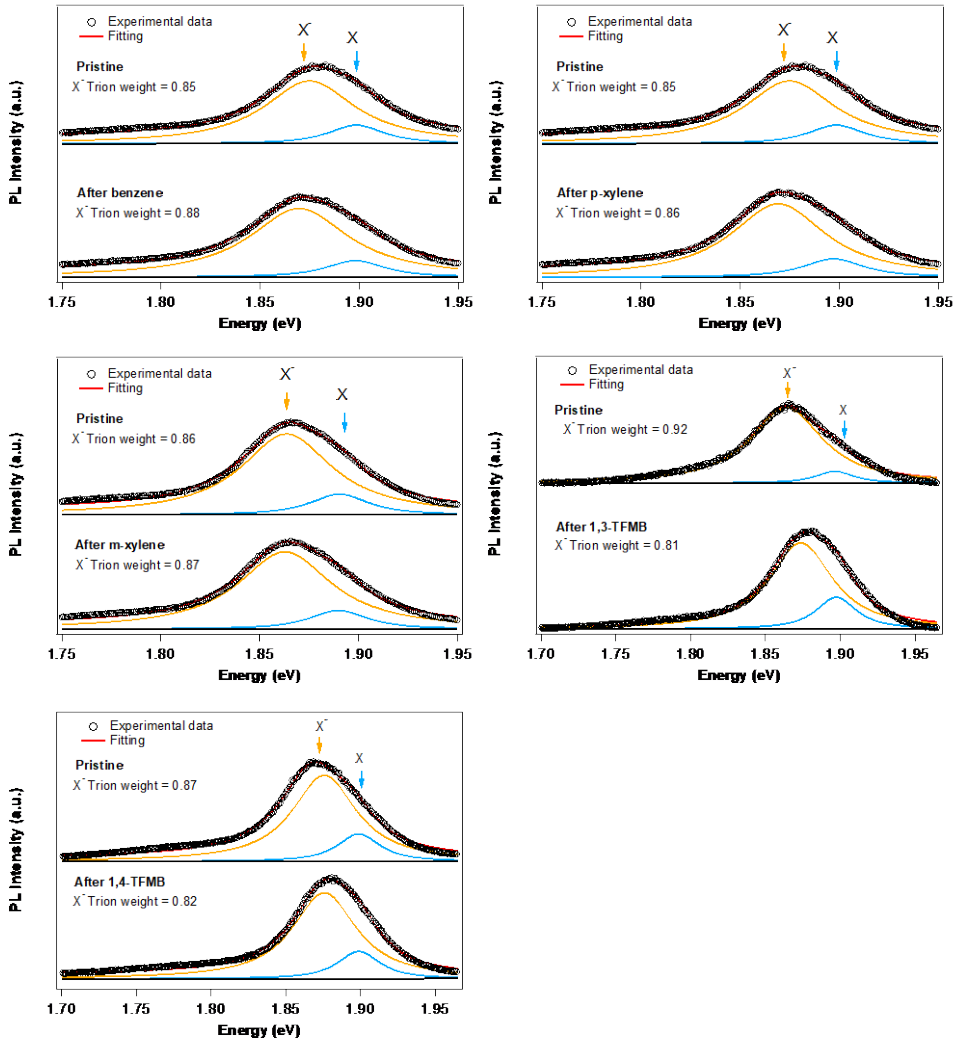

Figure 5.3. Fitted PL spectra of monolayer MoS_2 at 78K before and after physisorption of each aromatic molecules.

We focus our attention on the A peak that tracks the population of trion (X^-) and neutral exciton (X). Given that at 78 K all aromatic molecules investigated are in their solid phase, the chemical doping process might differ from those reported in previous studies carried out at room temperature. [32,114,121,122] Our data reveal that upon treatment with benzene, the spectral weight of trion increases whereas the use of 1,3-TFMB induces a decrease in the trion weight. Such effects are caused by changes in charge carrier density in monolayer MoS_2 induced by molecular doping. When monolayer MoS_2 is n-doped, the increase in electron density promotes the formation of negatively charged trion. Conversely, p-doping enables the recombination of neutral excitons into positively charged trion. The trion weight can be quantified as:

$$\gamma^- = \frac{I_{X^-}}{I_{total}} = \frac{I_{X^-}}{I_{X^-}+I_X} \tag{5.1}$$

where γ^- is the negative trion weight of monolayer MoS_2, I_{X^-} is the area of negative trion peak, I_X is the area of neutral exciton peak and I_{total} is the area of total photoluminescence intensity.Therefore,we calculate the trion weight change ($\Delta\gamma$). $\Delta\gamma^-$>0 indicates an increase in electron density upon molecular physisorption, implying a n-doping effect. Conversely $\Delta\gamma^- < 0$, denotes a decrease in electron density upon molecular physisorption, corresponding to p-doping.

To explore the origin of the trion weight change ($\Delta\gamma^-$), here we discuss different mechanisms which led to the exclusion of dipolar effects and the activation of defect-induced photoluminescence.

5.3.3 Influence of molecular dipoles and defects of monolayer MoS_2

Experimental observation of molecular dipole influence could be examined by photoluminescence behavior. We would like to discuss dipolar effects in two aspects:

5.3.3.1.1 Dipole moment variation by extrinsic vertically applied electrical field.

In the early stage of our experiments, we were curious to learn how the charge carrier density could be affected by molecular dipole under directional electrical field.

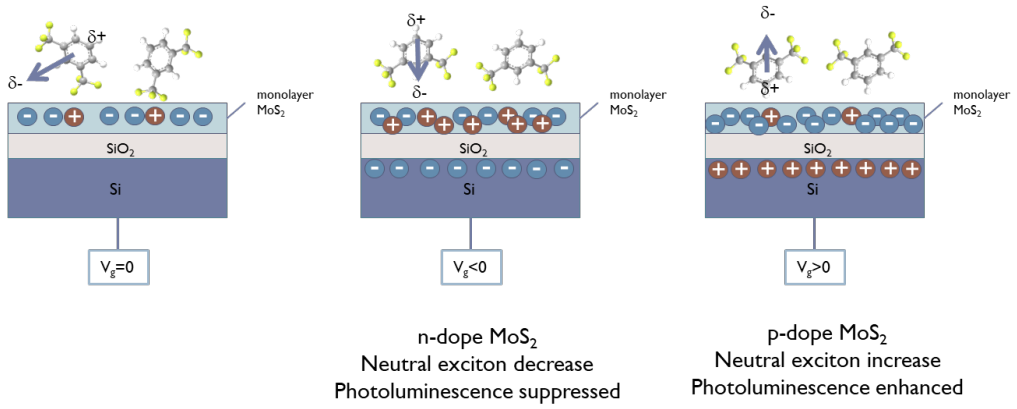

Figure 5.4: Mechanism of gate-tunable photoluminescence in the presence of molecular dipole.

As displayed in **Figure 5.4**, we have designed the experiment utilizing field-effect transistors. The electrical field was applied between the bottom-gate underneath the MoS_2 and the top electrode onto MoS_2. When electrical field is applied to the 2D-molecular system, the molecular dipoles orient along with the electrical field and tend to induce the same effect in modulating charge carrier density as gate-induced electrostatic doping. Thus, one would expect to observe a slower exciton or trion intensity change with respect to gate voltage change. We have analysed photoluminescence spectra at room temperature of monolayer MoS_2 before and after depositing benzene (D=0.00) and 1,3-bis(trifluoro-methyl)benzene (D=2.92) by sweeping a gate voltage from -30V to +30V. However, the expected results were not observed, as shown in **Figure 5.5**. Considering that the dipole moment of the molecules is rather small, the dipole-induced doping is too modest to compete with electrostatic doping determined by SiO_2 dielectric (oxide thickness: 90 nm) which could modulate ~10^{11} cm^{-1} of carrier density by varying 5 V of gate voltage. Even though the results of this experiment are not very exciting, we would like to continue the exploration of this topic using in the future molecules possessing a large net dipole moment.

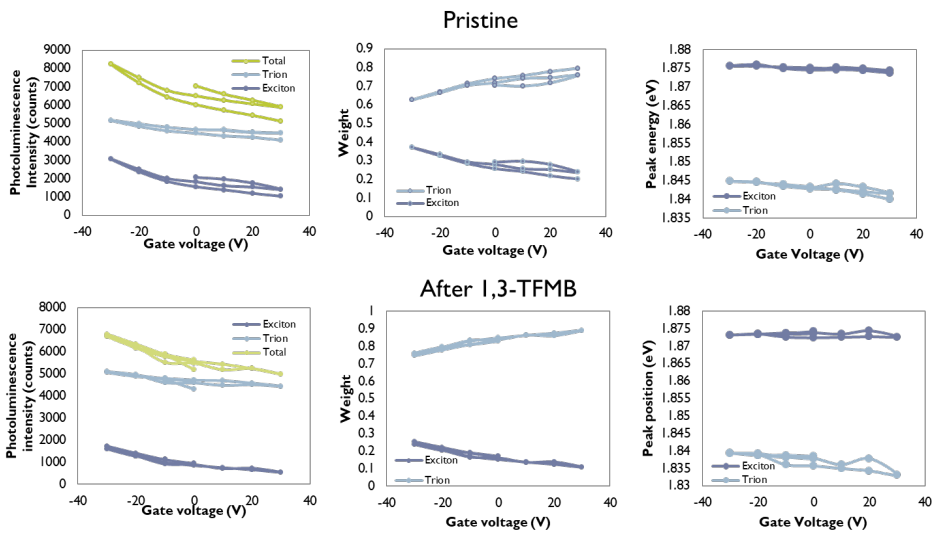

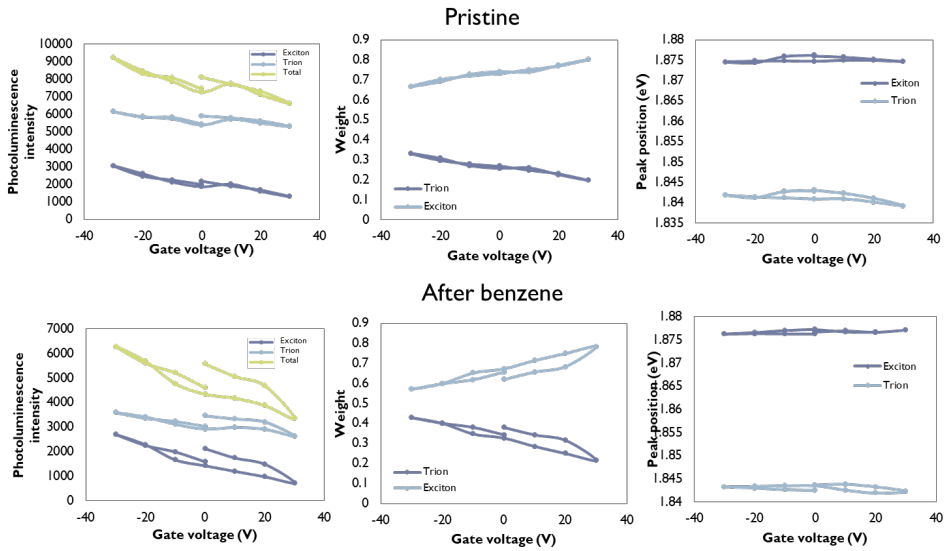

Figure 5.5: Photoluminescence intensity, trion/exciton weight and trion/exciton peak position varied by gate voltage.

5.3.3.1.2 Molecular dipole-induced doping

The molecules that we have used possess dipole moment ranging from 0 Debye for benzene to 2.92 Debye for 1,3-bis(trifluoro-methyl)benzene, the latter being still rather small compared to common organic dopants. Under 0V gate voltage, considering the limited number of molecules dispersed on the surface upon spin-coating, the built-in electrical field in the interface of molecules and 2D materials generated by molecular dipole is negligible. For example, benzene being a highly symmetric molecule, can hardly generate dipolar effect on the 2D material. The most plausible explanation on experimental results is charge transfer mechanism. Theoretical calculation presented in the next sections also supported that dipolar effects could be excluded. Therefore, in our work, dipolar effects are not taken into consideration when exploring the mechanism of charge carrier density change in 2D materials and more insight is obtained from charge transfer mechanism. Modulation could only induce an enhancement up to tens of times. However, the photoluminescence intensity measured before and after benzene treatment in our experiment is in the similar numeric scale. We have only observed the switching of trion and exciton due to charge transfer between the molecule and monolayer MoS_2. Therefore, in the context of our experiment, n-doping molecule do not assist in the defect-activated photoluminescence enhancement.

5.3.3.2 Influence of defects of MoS_2

Defect-induced photoluminescence plays an important role in tuning the optical and electrical properties of 2D TMDs. In our experiments, we have not performed any surface treatment such as UV-ozone, oxygen plasma, high temperature annealing, ion bombardment to generate defects in our experiment. The only possibility for defect-induced effect could be due to intrinsic defects.

To test if as-studied molecules could induce activation of defects upon physisorption, we have measured photoluminescence spectra at room temperature under nitrogen using CVD grown monolayer MoS_2 (6 carbon, China). CVD MoS_2 is known for possessing higher defect density than mechanical exfoliated materials. We plotted PL mapping of X^- trion peak in **Figure 5.6**. We fitted the spectra with Lorentzian and 10% Gaussian of tolerance, as is displayed **in Figure 5.7**. The mappings before and after depositing benzene have the same scale bar. It is evident that in untreated CVD flake map image, the X^- peak intensity is larger in the triangle plane than on the edges. Flake edges are often considered as defect rich regions for the breaking of crystalline structures. The sites with abundant defect density show decreased trions weight, i.e. they exhibit p-doping. After physisorptin of benzene, we have observed an enhancement of trion weight both in center and in the edge, as shown in **Figure 5.7**, which corresponds to our findings in the previous sections. Previous works have shown that excitons trapped at defect sites suppress the thermally activated nonradiative recombination, thus enhancing the PL intensity up to 90 times, whereas trion/exciton in the exciton weight in the material is dominated by simple charge transfer.

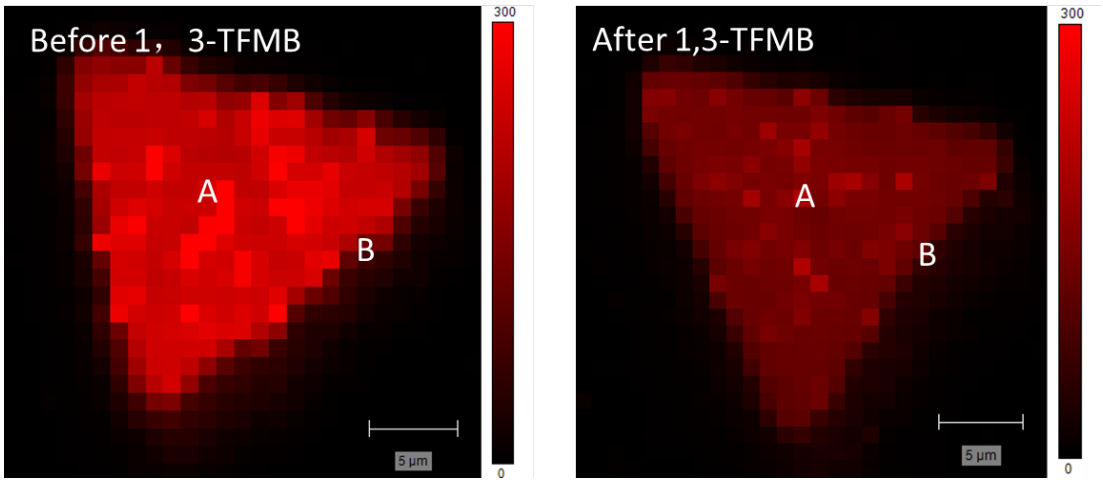

Figure 5.8: Photoluminescence mapping of X^- trion intensity CVD grown monolayer MoS_2 before and after 1,3-TFMB.

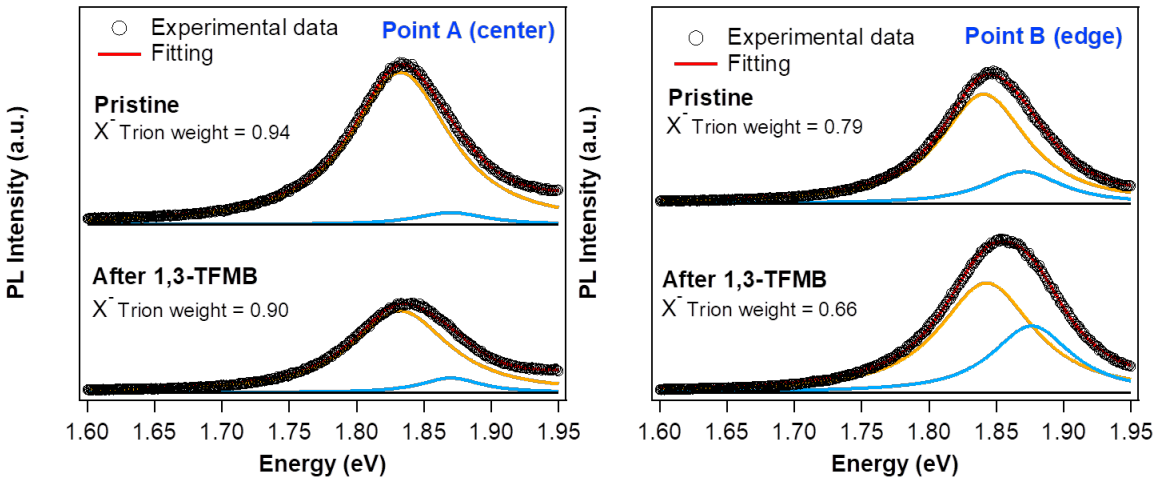

Figure 5.9: Photoluminescence spectra of CVD monolayer MoS_2 at center site and edge site before and after depositing 1,3-TFMB.

Overall, the experiments demonstrated above show that the chosen aromatic molecules display modest interaction with defect sites and limited influence on the quantum yield of radiative recombination of excitons. For the mechanical exfoliated flakes used in our project, the defect density is usually smaller when intentional treatments are not used, hence reducing any defect-induced phenomenon. In essence, our observed modulation of the properties of the 2D materials can safely be ascribed to charge transfer induced

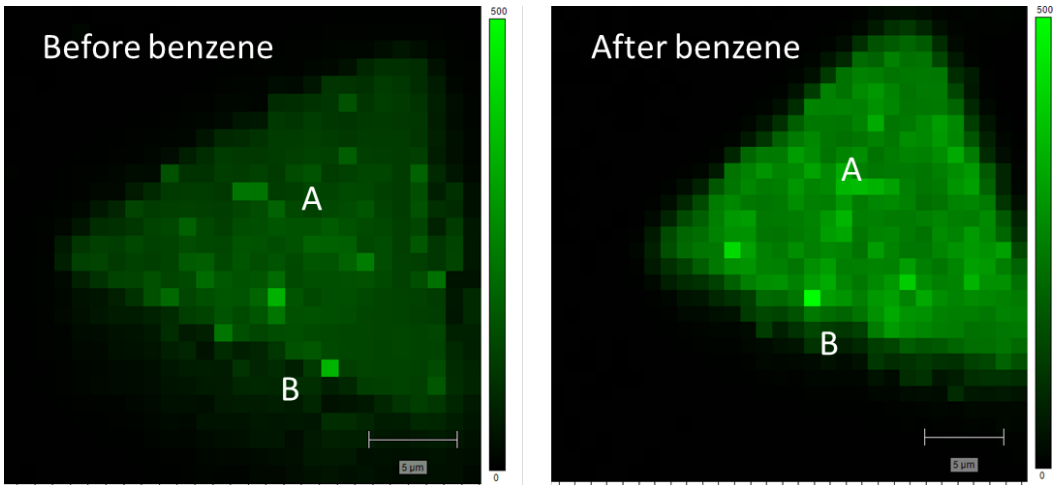

Figure 5.6: Photoluminescence mapping of X^- trion intensity CVD grown monolayer MoS_2 before and after benzene.

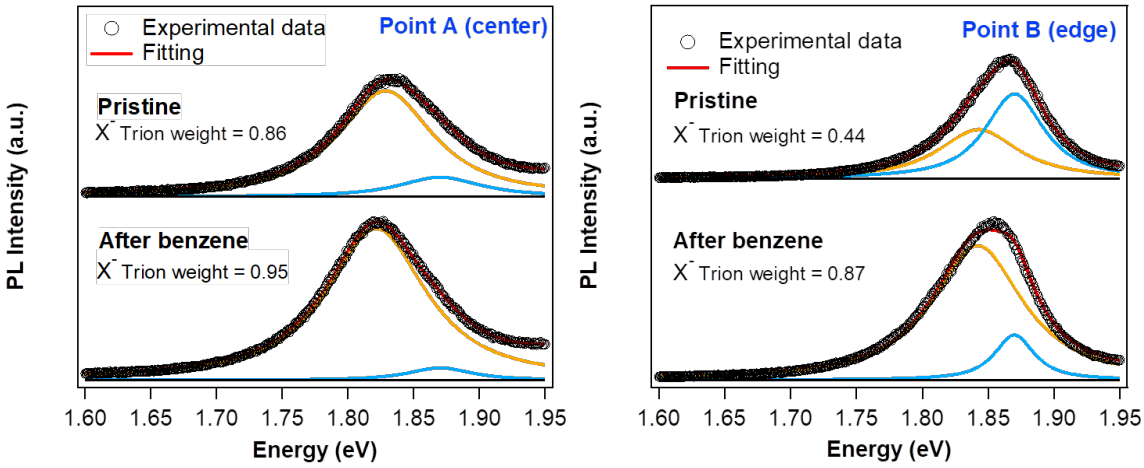

Figure 5.7: Photoluminescence spectra of CVD monolayer MoS_2 at center site and edge site before and after depositing benzene.

We have also tested if p-doping molecule could induce defect activated photoluminescence. The PL mapping of CVD monolayer MoS_2 before and after 1,3-bis(trifluoromethyl)benzene (1,3-TFMB) treatment is displayed in **Figure 5.8**. We have observed the same edge effect in the spectra recorded before and after the treatment, as discussed before. In contrast to benzene, the flake with 1,3-TFMB shows a decrease of trion intensity. The fitted spectra are portrayed in **Figure 5.9**. Besides the trion weight drop, we have not observed strong PL enhancement after physisorption of the molecule in agreement with literature describing p-dopant molecules (*e.g.* O_2, H_2O) bond to defect sites. It means that 1,3-TFMB does not facilitate the radiative recombination of excitons trapped in defect sites, but it only increases exciton/trion switching.

5.3.4 Charge transfer between monolayer MoS_2 and aromatic solvent molecule doping

This discussion made it possible to demonstrate that the observed induced doping in the TMDs is due to charge transfer between molecules and 2D materials. The trion weight change ($\Delta\gamma^-$) quantifies the ability of doping, in this specific case of MoS_2 as a result of the physisorption of the molecular monolayer, as determined by PL measurements. In the simplest approximation, when two species A and B (here the solvent molecules and the MoS_2 solid) with chemical potentials $\mu_A \neq \mu_B$ are brought into close contact, electron density N flows from the high-potential to the low-potential system until equilibration is reached: [135]

$$N = \frac{\mu_A - \mu_B}{\eta_A + \eta_B}. \qquad (5.2)$$

where μ_A and μ_B are the chemical hardnesses of A and B,respectively.To understand the difference in values of $\Delta\gamma^-$ resulting from the physisorption of different molecules, we have calculated the chemical potential and hardness values of monolayer MoS_2 and the investigated aromatic molecules.[136] In the frontier molecular orbital framework and using a finite difference approximation, these write:

$$\mu = \frac{1}{2}(\varepsilon_{hole} + \varepsilon_{electron}); \eta = \frac{1}{2}(\varepsilon_{electron} - \varepsilon_{hole}) \quad (5.3)$$

Where $\varepsilon_{hole\ (electron)}$ denotes the energy of the molecular HOMO (LUMO) level for the solvent and the energy of the top of the valence (conduction) band for the 2D solid.

As shown in **Figure 5.10**, fluorinated molecules have a smaller chemical potential due to the electron-withdrawing character of $-CF_3$ groups. The chemical potential of monolayer MoS_2 is calculated to be -5.1 eV, which is closely above that of -5.15 and -5.19 eV for 1,3-TFMB and 1,4-TFMB, respectively. Therefore, electrons tend to transfer from MoS_2 to 1,3-TFMB and 1,4-TFMB, so that electron density is decreased in monolayer MoS_2 resulting in p-doping effect. In contrast, benzene (-3.84 eV), m-xylene (-3.50 eV) and p-xylene (-3.47 eV) have higher chemical potentials than monolayer MoS_2, hence it is easier to transfer electron from the former to the latter, leading to n-doping of the 2D layer. While the chemical hardness weighted difference in chemical potential between aromatic molecules explains the type of doping of MoS_2, the quantitative agreement is limited. In other words, the sign of the calculated ΔN in Eq. (2) is consistent with the measured $\Delta\gamma^-$, but the trend with the nature of the solvent is only qualitative (see Table 2).For example, benzene has smaller chemical potential than xylenes but it gives larger trion weight change; 1,3-TFMB and 1,4-TFMB have much smaller chemical potential difference than other molecules but Δγ^- are comparable to benzene and xylenes. This is likely because of the thermodynamic stability drive to certain configurations of the self-assembled molecules on the surface of MoS_2, possibly sourcing a surface electrostatic potential, together with other effects not included in the simple model (hybridization with and electronic polarization in the solid). To better appraise these effects,we have assessed the charge transfer taking place from the solvents to the MoS_2 (WSe_2) sheet upon adsorption by applying the Bader charge analysis to the equilibrated interfaces [137]. The calculated charge transfer matches the trend of $\Delta\gamma^-$ much better than the chemical potential based model (**Figure 5.10**).

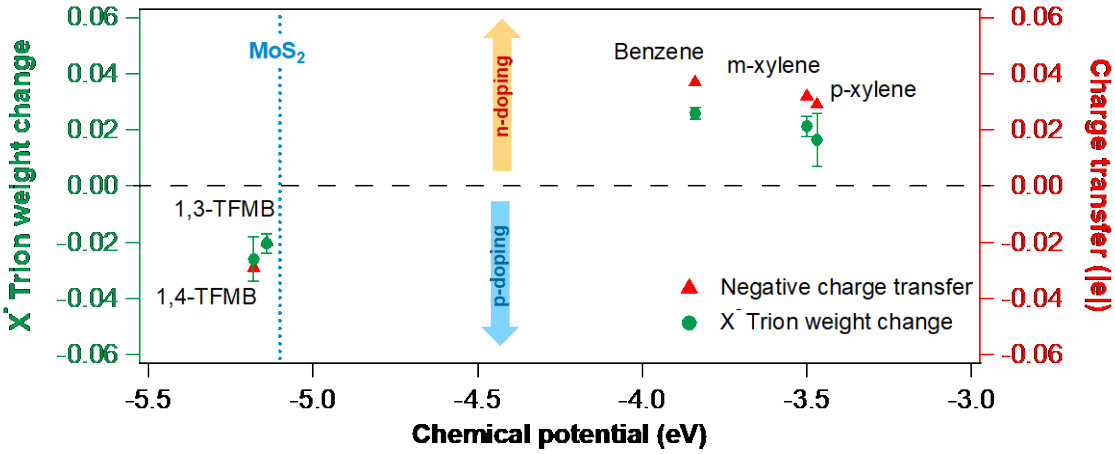

Figure 5.10: X- trion weight change and calculated Bader charge transfer (red) by physisorption of aromatic molecules from low-temperature PL measurement of MoS2 (green) as a function of chemical potential. Fluorinated molecules (1,3-TFMB and 1,4-TFMB) possessing lower chemical potential are easier to accept electrons from monolayer MoS_2; in contrast, non-fluorinated molecules (benzene, p-xylene and m-xylene) with higher chemical potential donate electrons to monolayer MoS_2.

Heterostructures	ΔN
MoS_2/Benzene	-0.596
MoS_2/m-xylene	-0.502
MoS_2/p-xylene	-0.522
MoS_2/1,3-TFBM	+0.012
MoS_2/1,4-TFBM	+0.025

Table 5.2: Charge transfer (in |e| per molecule) flow from solvent to MoS_2 calculated on the basis of Eq. 3

The correlation of $\Delta\gamma^-$ and charge transfer value can be estimated by mass action model [32]:

$$\frac{N_X n_{el}}{N_{X^-}} = \left(\frac{4m_X m_e}{\pi\hbar^2 m_{X^-}}\right) k_B T exp\left(-\frac{E_b}{k_B T}\right) \quad (4)$$

where N_X and N_{X^-} are the population of excitons (X) and trions (X^-). n_{el} is the electron

density and E_b is the binding energy of trion (~20 meV). T is the temperature (78 K). m_X , m_{X^-} and m_e are effective masses of exciton, trion and electron respectively. Considering $m_e \approx 0.35m_0$ and $m_h \approx 0.45m_0$, m_X and m_{X^-} can be calculated as $m_X = m_e + m_h = 0.8m_0$, and $m_{X^-} = 2m_e + m_h = 1.15m_0$. Hence, the trion weight can be expressed as

$$\frac{I_{X^-}}{I_{total}} = \frac{\frac{\gamma_{tr} N_{X^-}}{\gamma_{ex}\ N_X}}{1+\frac{\gamma_{tr} N_{X^-}}{\gamma_{ex}\ N_X}} \approx \frac{1.5*10^{-15} n_{el}}{1+1.5*10^{-15} n_{el}} \quad (5)$$

where γ_{tr} and γ_{ex} are radiative decay rates of trion and exciton,respectively. **Figure 5.11** demonstrates a good correspondence between the electron density change obtained from experimental data and the charge transfer predicted by DFT calculations as the electron density change of monolayer MoS_2 after the physisorption of aromatic molecules is linearly proportional to charge transfer value per molecule. By carefully excluding the doping effect from air atmosphere, our measurements shows that the modulation of charge density by solvent trace in monolayer MoS_2 is largely decreased to $10^{11}/cm^{-2}$ compared to previous studies that attain $10^{13}/cm^{-2}$.[138] Therefore, it is possible to estimate the number of physisorbed molecules on the surface of monolayer MoS_2 by considering

$$\Delta n_{el} \cdot |e| = n_{mol} \cdot \Delta\sigma^- \quad (6)$$

where Δn_{el} is the change in electron density, $|e|$ is the absolute value of elementary charge, n_{mol} is the number of molecules adsorbed per unit area (cm^2) and $\Delta\sigma^-$ is the negative charge transfer value. The estimated number of adsorbed molecules for each chemical is listed in **Table 5.3**. It is clear that xylenes have the smaller number of adsorbed molecules, whereas fluorinated molecules tend to self-assemble more densely on the surface of the MoS_2. This might be attributed to the preference of Coulomb interaction between electron-withdrawing $-CF_3$ group and the intrinsically n-doped monolayer MoS_2.

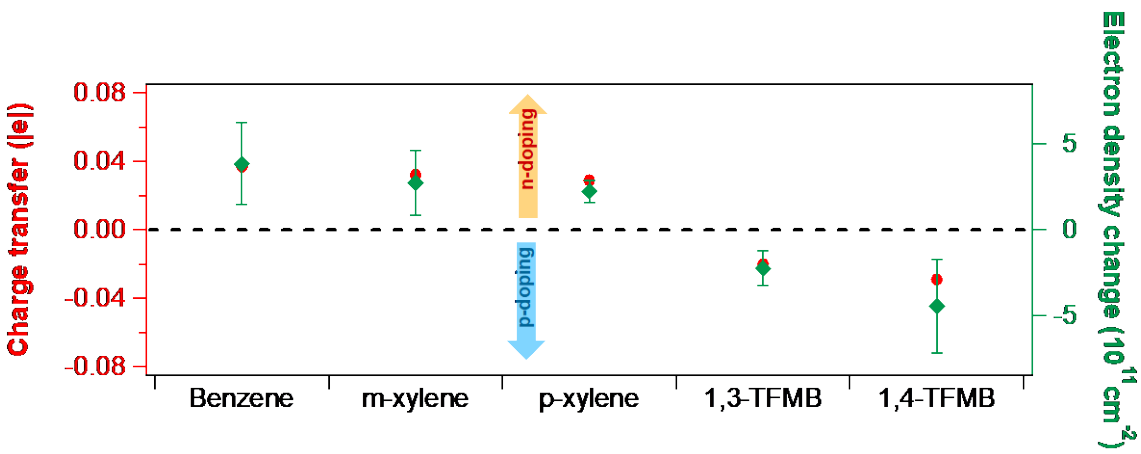

Figure 5.11: Electron density change (green) after physisorption on MoS_2 of each aromatic molecule, as calculated by mass action model and provided by a DFT/Bader charge analysis (red).

	Benzene	m-Xylene	p-Xylene	1,3-TFMB	1,4-TFMB
Number of physisorbed molecules ($10^{13}/cm^2$)	1.04	0.86	0.77	1.12	1.54

Table 5.3: Estimated number of physisorbed aromatic molecules on monolayer MoS_2 calculated from electron density change and transferred charge.

5.3.5 Influence of molecular density, distance and orientation by theoretical calculation

Meanwhile, we explore the role of molecular density, distance, orientation (molecular dipole), and MoS_2 defects on the electronic structure and optical properties of the organic-MoS_2 hybrids, both theoretically and experimentally. We focus our attention to benzene-MoS_2 and 1,3-TFMB-MoS_2 systems, as these two molecules feature the strongest n- and p-doping effects, respectively.

5.3.5.1 Influence of the density of molecules on MoS_2 surface

Here, we increased the density of benzene (and 1,3-TFMB) molecules by decreasing the size of the unit cell. The most stable configurations obtained after full relaxation are shown below (**Figure 5.12**):

The Bader charge analysis shows that increasing the density of molecules on MoS_2 monolayer leads to a decrease in the charge transfer per molecule, an effect associated with electronic depolarization. Yet, the work function increases with molecular density, tracking the higher amount of charge transfer per surface area.

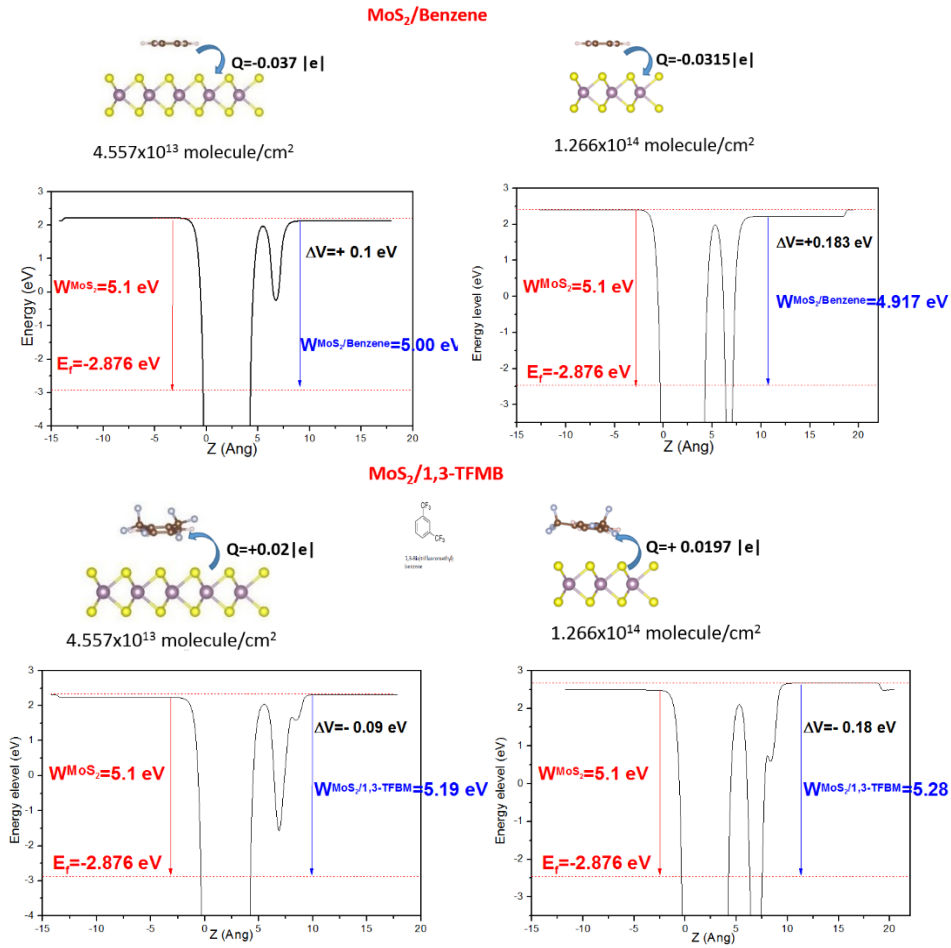

Figure 5.12: Bader charge transfer between donor (Benzene) and acceptor (1,3-TFMB) molecules at two different coverage densities. The average potential profiles show the variation of the work function.

5.3.5.2 Influence of inter-layer distance

The calculations were conducted on a 5x5x1 supercell box size (density of XXX), applying a vertical strain to change the interlayer distance between molecules and MoS_2 by -0.5Å and +0.5Å. (**Figure 5.13**)

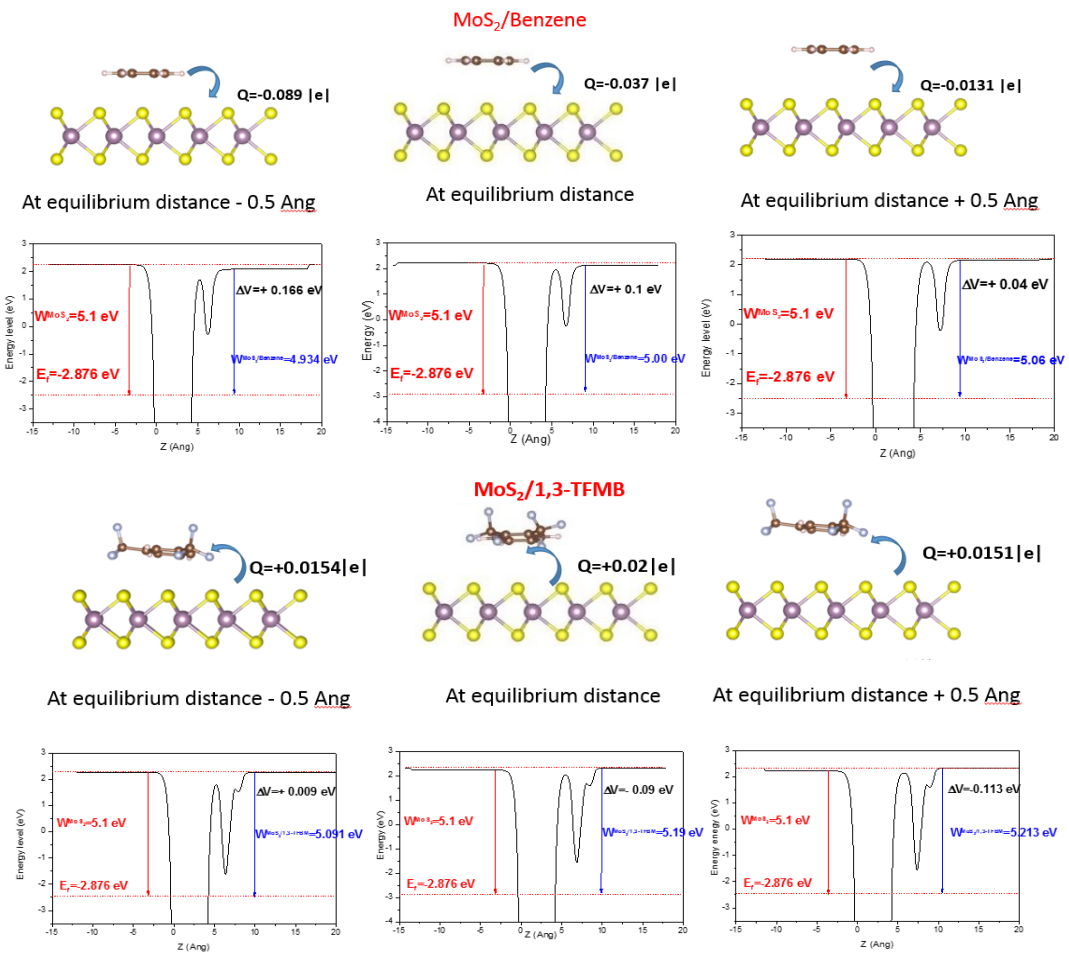

Figure 5.13: Variation of Bader charge transfer and work function as a function of interlayer distance. We decreased artificially the interlayer distance by 0.5 A° in the first case (left figures), and we increased it by +0.5 A° in the second case (right figures). The figures in the middle corresponding to equilibrium distance obtained after structural relaxations.

The results obtained for benzene are in line with expectations, namely the amount of charge transfer between molecules and MoS_2 increases when the interlayer distance is reduced. The deviation observed at small contact distances for 1,3 TFMB is due to a slight reorientation of the molecules, investigated further in the next section.

5.3.5.3 Influence of molecular orientation

The molecules are inclined here to some degree, while maintaining the distance between the centre of the molecules and the MoS_2 surface close to the equilibrium value (**Figure 5.14**).

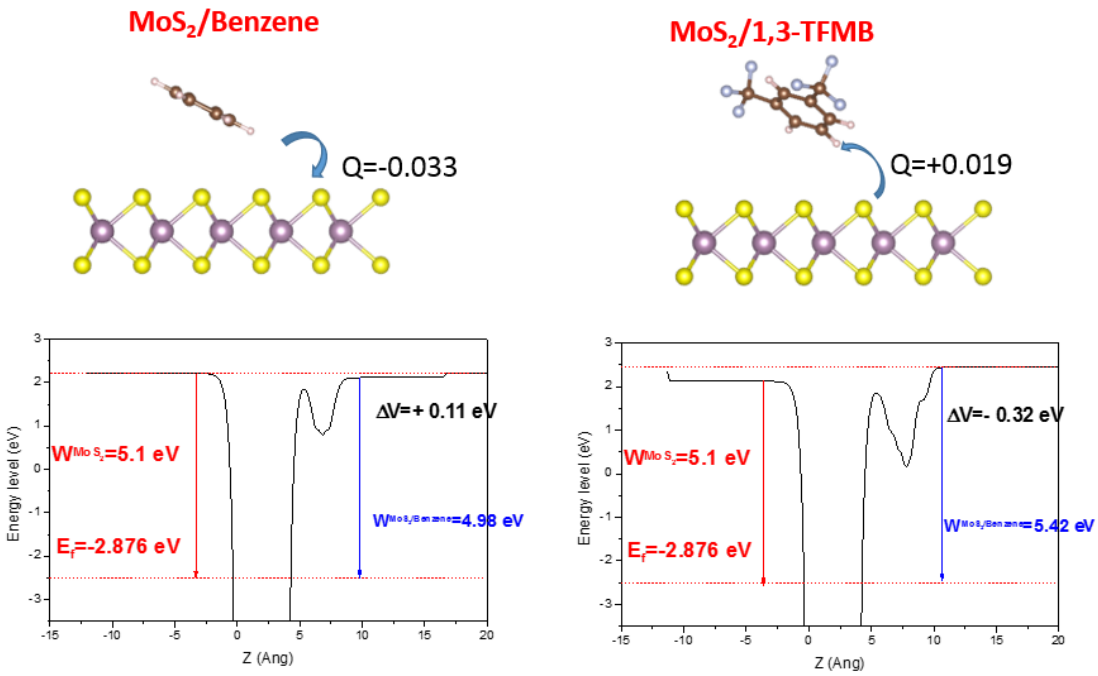

Figure 5.14: Variation of Bader charge transfer and work function after inclination of the angle between the basal planes of molecules and MoS_2.

5.3.6 Estimating the physisorbed molecular densities on MoS_2

By comparison to the flat configuration considered above, introducing a tilting angle between the molecules and MoS_2 has a negligible effect on the charge transfer and the resulting work function in the case of benzene. The same applies for the charge transfer in the 1,3-TFMB case, yet a very large change in work function is predicted in that case. This obviously results from the electrostatic vacuum level shift induced by the out-of-plane component of the molecular dipole, which for the specific orientation displayed above adds up to the direct charge transfer contribution. In amorphous layers, however, we expect these orientational effects to roughly cancel out for the weakly polar molecules studied here.

5.3.7 Pholuminescence (PL) properties of monolayer WSe_2

In contrast to monolayer MoS_2, the photoluminescence behavior of monolayer WSe_2 exhibits multiple possibilities for trion recombination. At low temperature, the coexistence of neutral excitons and positively charged excitons or negatively charged excitons and biexcitons is observed

by changing temperature (4 K, 10 K, 30 K, 60 K) and device structure.[31,139,140] To investigate the influence of aromatic molecules deposited on monolayer WSe_2, we first study here its excitonic characteristics at 78 K on SiO_2 substrate. The temperature dependence of monolayer WSe_2 is similar to MoS_2 whereby, upon decreasing the temperature, the exciton peak is blue-shifted. Defect-induced emissions appear below 200 K as multiple peaks in the range of 1.60 eV to 1.65 eV in which the intensity is dependent on the quality of the flakes. Moreover, at room temperature, a single excitonic peak at 1.66 eV is observed. Below 100 K, this peak is split into two independent components at ~1.72 eV and ~1.70 eV (**Figure 5.15**).

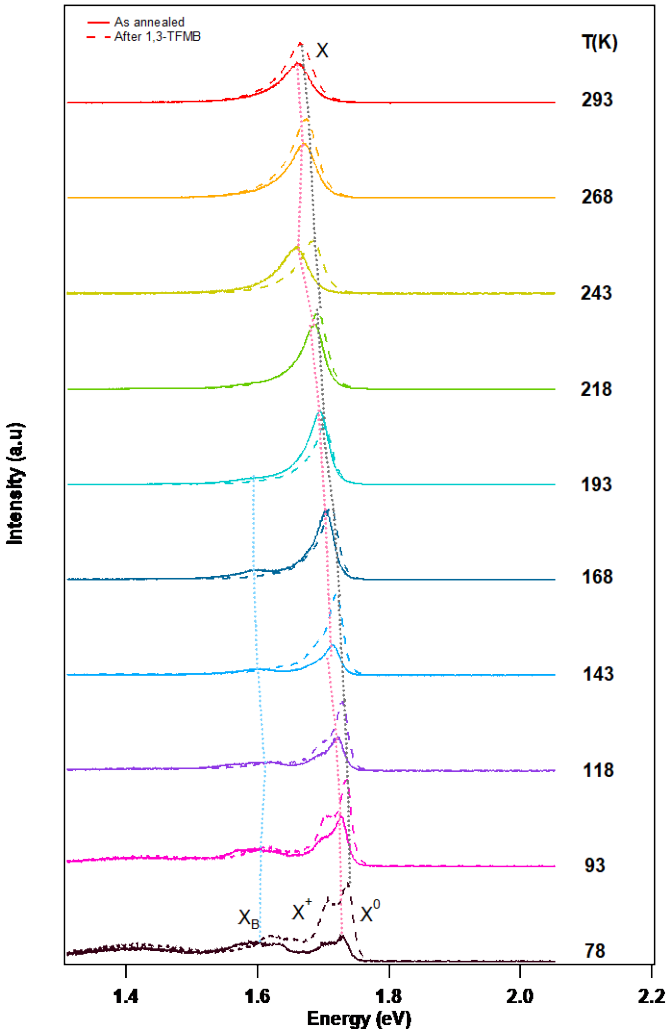

Figure 5.15: Temperature dependent photoluminescence of monolayer WSe_2 before and after depositing 1,3-TFMB.

To assign the origin of these two excitonic components, field-effect devices were fabricated by E-beam lithography to induce electrical tunable doping. **Figure 5.16a** and **b** portray the schematic and optical image of the device, respectively. As displayed in the scheme in **Figure 5.16d**, by

adding a gate voltage on FET device, it is possible to modulate charge carrier density in WSe_2 monolayers, and therefore to tune the proportion of excitons and trions. Upon applying negative gate voltage, electrons in monolayer WSe_2 are attracted to the ground via the gold electrode, the electron density in the material is therefore largely decreased and neutral excitons tend to capture excess holes to form positive trion. On the contrary, when applying a positive gate voltage, more electrons are attracted to the channel, therefore negative trion recombination is facilitated. **Figure 5.16c** shows the PL spectra of monolayer WSe_2 at 78 K under -5 V, 0 V and +5 V gate voltage, respectively. At 0 V, apart from the peak at~1.65 eV, two other peaks, namely trion at ~1.70 eV and exciton at ~1.72 eV are observed. At -5 V, the intensity of the trion peak increases. Considering the increase in hole density by increasing negative gate voltage, we assign this peak as positive trion (two holes and one electron combined). This also implies that our material is intrinsically p-doped even after annealing, which is inconsistent with former works where either protection layer of h-BN was added or the experiment was performed at lower temperature[31]. At +5 V, when more electrons are injected into monolayer WSe_2, the negative trion (two electrons and one hole combined) emission at ~1.69 eV dominates. We extract the binding energy of positive trion and negative trion at 78 K to be 17~22 meV and 31~40 meV respectively by calculating the difference of trion emission energy and neutral exciton energy. We have also observed quantum-confined Stark effect by applying higher gate voltage and a substrate-induced hysteresis in PL mapping under small gating steps, yet this is beyond the scope of this work.

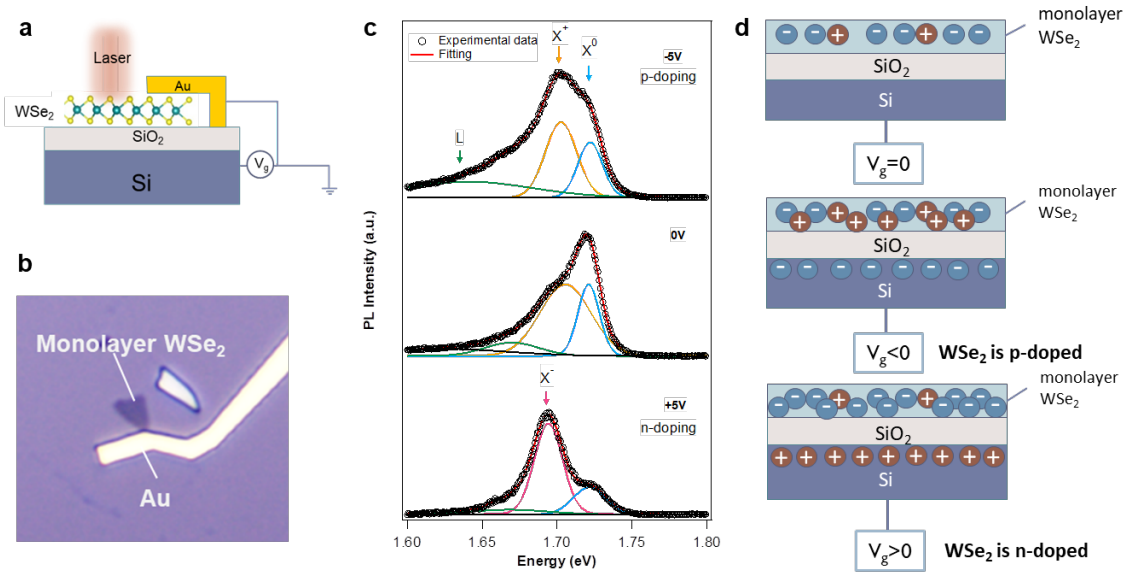

Figure 5.16: Gate-induced photoluminescence of monolayer WSe_2. (a) Schematic representation of the device for gate-induced photoluminescence in monolayer WSe_2, and (b) its corresponding optical image. (c) PL spectra of monolayer WSe_2 at 78 K under -5, 0, +5V, demonstrating the recombination of

neutral exciton (X^0) and positive trion (X^+) at 0V and -5V, and the existence of neutral exciton (X^0) and negative trion (X^-) at +5V. (d) Modulation of charge carrier by gating. The change in carrier density results in electrostatic doping on monolayer WSe_2 and affects the recombination of positive or negative trions.

5.3.8 Doping of monolayer WSe_2 with aromatic solvent molecules characterized by PL spectra

After studying the peak position of each type of exciton emission in our experimental conditions, we focus our attention on the effect of chemical doping on monolayer WSe_2. With no gate voltage applied to the flake, we only discuss the neutral exciton and positive trion. We quantify the positive trion as

$$\gamma^+ = \frac{I_{X^+}}{I_{total}} = \frac{I_{X^+}}{I_X + I_{X^+}} \tag{5.7}$$

where γ^+ is the positive trion weight of monolayer WSe_2, I_{X^+} is the area of positive trion peak, and I_X is the area of neutral exciton peak and I_{total} is the area of total photoluminescence intensity.Therefore,we calculate the trion weight change ($\Delta\gamma^+$) to evaluate the charge transfer doping of molecules on monolayer WSe_2.

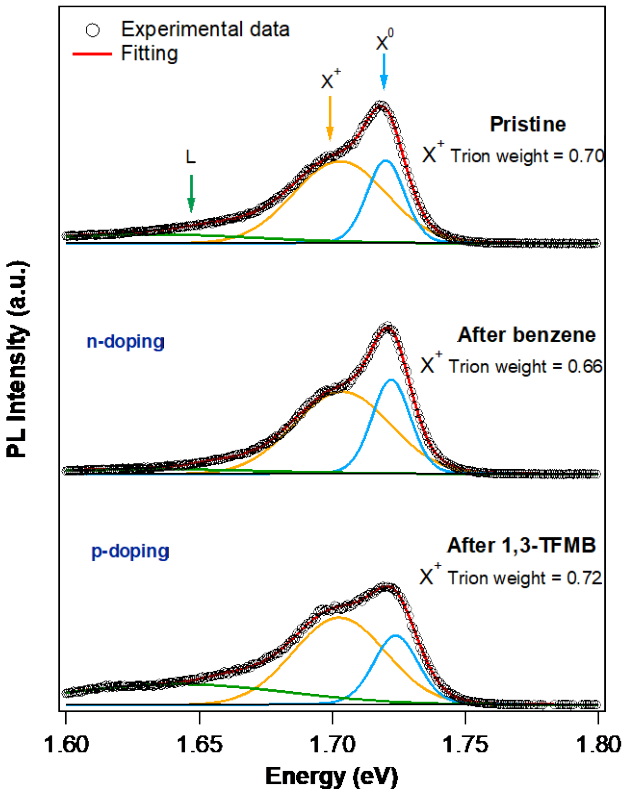

Figure 5.17: Photoluminescence spectra of monolayer WSe_2 before and after physisorption of benzene, and 1,3-TFMB with calculated X^+ trion weight.

Figure 5.17 shows typical fitted PL spectra before and after doping with aromatic molecules at 78 K. The spectral weight change of trion induced by benzene indicates n-doping and that 1,3-TFMB is a p-dopant. For other aromatic molecules, we find similar type of doping as monolayer MoS_2 as is seen in detailed PL spectra in **Figure 5.18**.

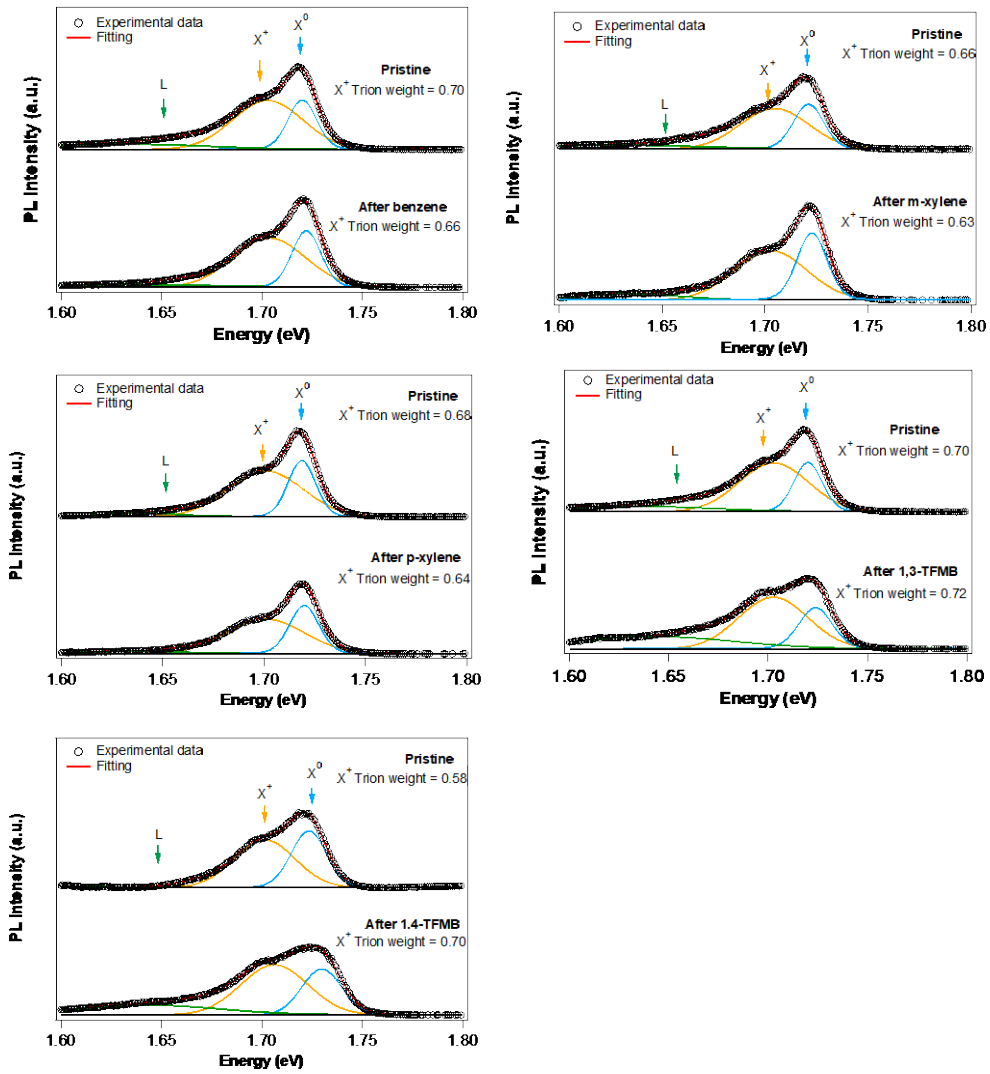

Figure 5.18: Fitted PL spectra of monolayer WSe_2 at 78 K before and after physisorption of each aromatic molecule.

To elucidate the consistency of doping, we have calculated the chemical potential of monolayer WSe_2 to be -4.33 eV, which is nearly 1 eV above the fluorinated molecules but still 1 eV lower than the other molecules, suggesting that the charge transfer direction between the molecules and monolayer WSe_2 should be the same as in MoS_2. Both calculated charge transfers and trion weight changes reveal that benzene has the largest n-doping ability and that 1,4-TFMB p-dopes the monolayer WSe_2 the most. Both xylenes have trivial influence on carrier density change in monolayer WSe_2. (**Figure 5.19**)

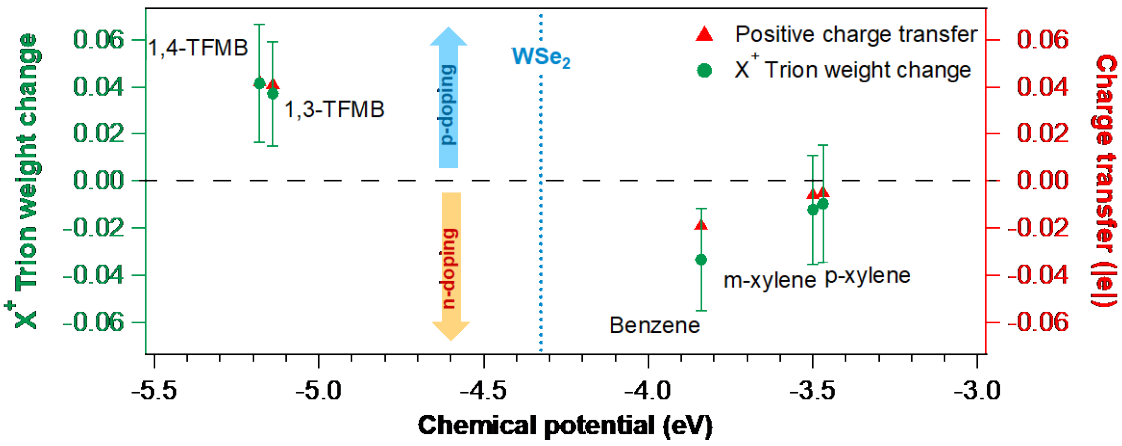

Figure 5.19: X^+ trion weight change and calculated DFT/Bader charge transfer (red) by physisorption of aromatic molecules from low-temperature PL measurements of monolayer WSe_2 (green) as a function of chemical potential. Fluorinated molecules (1,3-TFMB and 1,4-TFMB) possessing lower chemical potential are more prone to accept electrons from monolayer WSe_2; in contrast, non-fluorinated molecules (benzene, p-xylene and m-xylene) with higher chemical potential donate electrons to monolayer WSe_2.

5.4 Conclusions

In summary, our spectroscopic investigation provides unambiguous evidence of the full potential of the physisorption of small aromatic molecules on MoS_2 and WSe_2 to tune their opto-electronic properties via charge transfer. The PL study performed at 78 K demonstrated for the first time that tunable chemical doping can be achieved on both 2D materials through a subtle choice of simple aromatic molecules and their dosing on the surface. In particular, while fluorinated aromatics determined a p-doping, an n-doping was observed for the other methyl-substituted molecules. The calculated charge transfer of fluorinated solvent molecules on MoS_2 could be comparable to traditional organic p-dopants tetracyanoquinodimethane (TCNQ) and tetracyanoethylene (TCNE), while typical n-dopants tetrathiafuvaluene (TTF) and benzyl viologen (BV) could donate electrons beyond the ability of aromatic solvents.[121] Charge carrier modulation by optical response is found to be two orders of magnitude lower in charge carrier density than previous studies at room temperature in air[32,138] by freezing the system at low temperature in inert atmosphere. The combined experimental analyses and DFT calculations utilized in this study represents a novel

technique for estimating the density of physisorbed molecules in 2D surfaces. Furthermore, we have investigated for the first time the gate-tunable photoluminescence and defined binding energy of both positive and negative trions of monolayer WSe_2 at 78K through field-effect transistor.

Our results clearly indicate that care should be taken when choosing the solvent for the cleaning of the 2D materials or as "dispersant" for their chemical functionalization with larger (macro)molecules, since it can introduce strong electronic effects like doping. On the other hand, solvent molecules are clearly multifunctional systems since they both act as dispersant for the 2D materials and can enable the tuning of their opto-electronic properties.

Overall, our findings are instrumental both for fundamental and more applicative studies as many relevant solvents consist of small aromatic molecules, which therefore cannot be considered as inert media in the processing, but rather as a powerful tool for tuning the TMD properties and device optimization.

Chapter 6 Studying the solvent effect on few-layer black phosphorus

6.1 Introduction

Two-dimensional (2D) materials have revolutionized the field of materials- and nano-science owing to their exceptional physical and chemical properties. Few-layer thick black phosphorus (BP), which is experiencing a fast growth as a novel class of 2D materials, has demonstrated excellent properties as semiconducting material in CMOS.[4,141] The high electron and hole mobility, in-plane anisotropy and size-tunable direct bandgap from bulk (0.3 eV) to monolayer (2.1 eV) make it suitable for fabricating optoelectronic devices in a broad spectral range.[41,46,142] Compared to multilayer transition metal dichalcogenides (TMDs), black phosphorus displays larger surface-to-volume ratio and higher molecular adsorption energy, which renders it extremely sensitive to changes in the environment.[143-145] In this regard, the simple physisorption of atoms and molecules is a powerful method to modulate optical and electrical properties of BP.[16,112]

Physisorbed molecules including TCNQ, F_4-TCNQ, TCNE, TTF, PTCDA, antimonene and supramolecular networks showed to be able to both tune the properties of few-layer BP and passivate its surface.[146-151] These molecules interact at the non-covalent level with BP by doping it via either charge transfer or molecular-dipole-induced shift in work function. In the former case, the energy level alignment determines the doping, by favoring the transfer of an electron from the molecule to the BP (or vice versa). Conversely, dipole-mediated doping occurs when a polar molecule is physisorbed on BP. In this case, the dipoles generate an electric field which functions as a local gate, by shifting the work function of BP and thus inducing doping. More specifically, the extent of the doping also depends on the mutual orientation of the dipolar group with respect to the normal to the surface. In some cases, the two effects coexist and are difficult to be separated.

While it is rather obvious that large aromatic organic systems such as those mentioned above could determine the chemical doping of BP, it is not well-established whether small molecules physisorbed on BP could also lead to major changes in optical and electronic properties of the 2D material. [147,148,152,153] Small molecules have been reported to induce charge transfer on BP, thus modifying their Fermi level and overall tuning the electronic and optical properties of the material. The high sensitivity of BP to H_2O, NO, NO_2 and NH_3 makes such a 2D material a valuable active component for high-performance humidity and gas sensors. [147,150,152,153] However, the effect on BP of solvent molecules, which are often considered to be common small chemical agents in both the process of material production (especially liquid phase exfoliation), device fabrication and functionalization, have been seldom considered in previous works.

Solvent molecules have been demonstrated to induce a multitude of effects on TMDs including modifying the charge carrier density, influencing the exciton and trion formation, and bringing solvatochromic effect.[10,138,154,155] However, a similar level of understanding on the simple interaction of a solvent residue and BP has not yet been achieved. Numerous studies have demonstrated that solvents are indispensable during the exfoliation and functionalization of BP, yet under the assumption of considering solvents to be inert in the tuning of electrical and optical properties of black phosphorus. [147,148,152,156,157] It is therefore imperative to unveil the effect of physisorption of different solvents on the properties of black phosphorus.

In this work, we have carried out a systematic experimental and computational investigation on the effect of physisorption of common organic solvents on BP. We targeted 9 common solvents, namely acetone, benzene, chloroform, ethanol, hexane isopropanol (IPA), m-xylene, p-xylene and toluene. We have demonstrated that solvent molecules significantly modify the charge carrier density in BP field-effect transistors (FETs) and influence Raman signals by doping, which arises from a combination of charge transfer and molecular-dipole-induced shift in work function. Our results provide a text-book proof-of-concept on the use of physisorbed solvent molecules on 2D materials to controllably dope BP.

6.2 Experimental methods

6.2.1 Sample preparation.

Few-layer black phosphorus were mechanically exfoliated from bulk crystal (HQ Graphene) by using the scotch tape method and transferred onto thermally oxidized heavily *n*-doped silicon substrates (Fraunhofer Institute IPMS, $\rho_{Si} \sim 0.001\ \Omega\cdot$cm, t_{ox} = 90 nm) in a nitrogen filled glovebox. Their thickness was monitored by optical microscope combined with Raman spectroscopy and Atomic Force Microscopy (AFM). The samples were thermally annealed at 200 °C inside a vacuum chamber to desorb atmospheric adsorbates. Then, they were no longer exposed to air after the annealing and were characterized only under inert atmosphere (N_2-filled glovebox). Anhydrous solvents were opened inside the glovebox. To exclude the dielectric screening caused by environmental changes after depositing solvent molecules, we drop-cast each solvent molecule on few-layer BP, and spin-dried at 2000 RPM for 60 s to guarantee the presence of limited number molecules physisorbed on the surface of the BP. The desorption of solvent molecules was performed by thermal annealing at 200°C under N_2 atmosphere.

6.2.2 Device fabrication and electrical characterization

As-exfoliated few-layer BP were coated with 2 layers of PMMA (Allresist, 600K/ 950K) immediately after exfoliation to avoid air exposure. Top-contact (5 nm Cr/ 40 nm Au) field-effect transistors were fabricated by standard E-beam lithography and lift-off in warm acetone in glovebox. All devices were annealed under vacuum at 200°C overnight to remove absorbents. The characterization of device performance was realized by Keithley 2636A under N_2 atmosphere.

6.2.3 Raman spectroscopy

Raman and Photoluminescence spectra were recorded in inert atmosphere (N_2) by Renishaw inVia spectrometer equipped with 532 nm laser in a nitrogen-filled sealed holder (Linkam). Samples were mounted in the glovebox and immediately measured after annealing or after molecule deposition to avoid exposure to contaminant chemicals. The excitation power was kept below 1 mW to avoid local heating damage effects. The wavenumber (energy) resolution was ~1 meV.

6.2.4 AFM measurement

AFM imaging was carried out by means of a Bruker Dimension Icon set-up operating in air, in tapping mode, by using tip model TESPA-V2 (tip stiffness: k=42 N/m).

6.2.5 XPS measurements

XPS analyses were performed with a Thermo Scientific K-Alpha X-ray photoelectron spectrometer operating with a basic chamber pressure of ~10^{-9} mbar and an Al anode as the X-ray source (x-ray radiation of 1486 eV). Spot sizes of 400 μm and pass energies of 200.00 eV for wide energy scans and 10.00-20.00 eV for scans were used.

6.2.6 Computational details

Density functional theory (DFT) calculations were carried out within the projector-augmented wave (PAW) scheme, as implemented in the Vienna Ab-Initio Simulation Package (VASP).[18] The generalized gradient approximation of Perdew-Burke-Ernzerhof (GGA-PBE) was used to describe the exchange-correlation potential.[158] Grimme's semi-empirical DFT-D2 corrections were included to take into account the van der Waals interactions between BP surface and molecules. The kinetic energy cutoff for basis set was chosen at 600 eV. [159] A 5×5×1 supercell model was built and a vacuum of 30 Å thickness along the perpendicular direction was used to avoid any physical interactions between periodic images. Monkhorst-Pack k-point mesh of 2×2×1 and 4×4×1 were chosen to sample the Brillouin zone for geometry optimizations and self-consistent calculations, respectively.[160] The geometric structure was considered to be converged when the residual force on each atom was less than 1×10^{-3} eV/Å.

6.3 Results and discussions

Solvent molecules are known to determine dielectric screening and doping when physisorbed on the surface of 2D semiconducting materials.[10,161] To explore the effects of solvents on BP, field-effect

transistors (FETs) were fabricated by E-beam lithography by using mechanically exfoliated BP flakes as prototypical electroactive material. In order to avoid undesirable degradation, all manipulations were done under nitrogen atmosphere, inside a glove box. All the solvents used in this work are anhydrous. The relevant properties and source of the commercial solvents are listed in **Table 6.1.**

Solvent	Chemical Formula	Chemical Structure	Boiling point (°C)	Enthalpy of evaporation (kJ/mol)	Surface tension (dynes/cm)	Dielectric constant	Source
Acetone	C_3H_6O	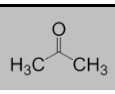	56.3	29.9	22.86	20.7	Merck
Benzene	C_6H_6		80.1	33.8	28.18	2.27	Merck
Chlorofrom	$CHCl_3$		61.2	36.2	27.5	4.81	Merck
Ethanol	C_2H_6O		78.3	42.4	22.18	24.5	VWR
Hexane	C_6H_{14}	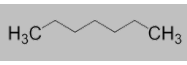	69	32.1	18.4	1.89	Merck
IPA	C_3H_8O	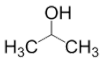	82.4	45.3	21.7	17.9	Merck
m-xylene	C_8H_{10}	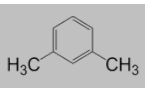	139.1	42.57	28.9	2.37	Merck
p-xylene	C_8H_{10}	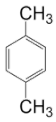	138.4	42.57	28.36	2.27	Merck
Toluene	C_7H_8		110.6	38	28.4	2.38	Merck

Table 6.1: Properties of solvents used in this work

Figure 6.1 shows typical transfer curve (I_{ds} *vs* V_g) of a few-layer black phosphorus FET before and after physisorption of solvent molecules. The thicknesses of BP flakes were defined by AFM measurements with the representative device shown in **Figure 6.2** comprising a 2.5 nm thick BP flake (**Figure 6.2**). All the devices were measured at drain-source voltage V_{ds}=1 V and gate voltage V_g ranging from -30 V to 30 V. The as-annealed BP transistors show p-type dominant ambipolar transport characteristics. After depositing solvent molecules, the transfer curves were found to be markedly different depending on the employed molecule. As revealed in **Figure 6.1 a** and **b,** in a typical BP FET in our experiment, the threshold voltage in hole transport ($V_{th,p}$) shows a negative shift of 1.8 V after the physisorption of m-xylene. Comparatively, acetone induces a positive shift of 7.7 V, see **Figure 6.1**.

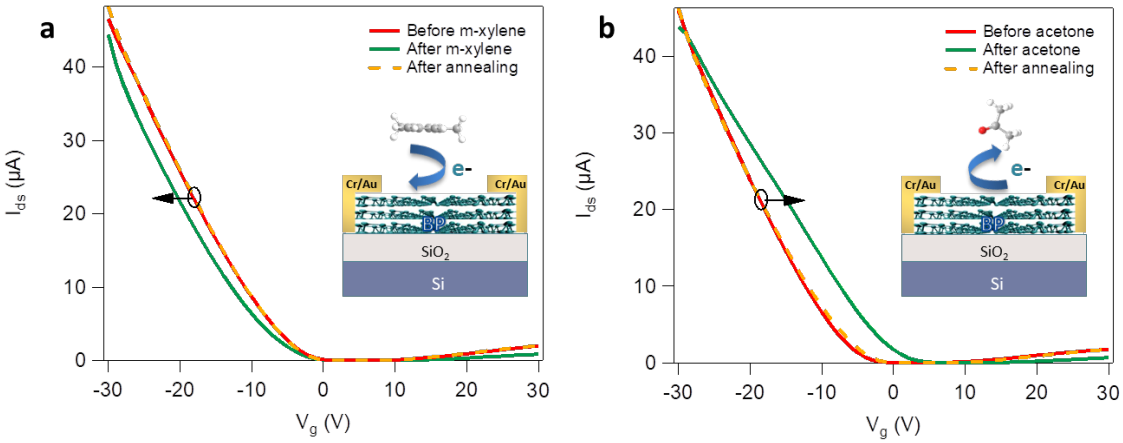

Figure 6.1: Typical transfer curve of few-layer black phosphorus field-effect transistor before and after physisorption of (a) m-xylene, and (b) acetone.

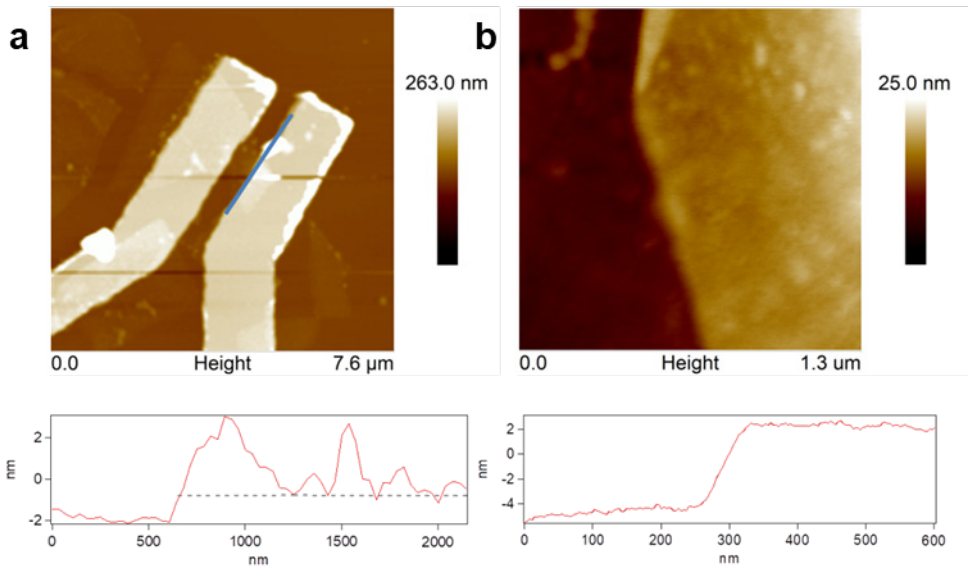

Figure 6.2: Topographical AFM image of a BP FET device with flake thickness of (a) ~2.5 nm, and (b) ~6.5 nm. The hills in the height profile are caused by rapid degradation occurred when measuring in air.

The physisorption process was demonstrated to be reversible by performing a thermal annealing treatment in N_2 atmosphere, as shown in the orange dashed curves in the graphs and in the XPS analysis in **Figure 6.3**.

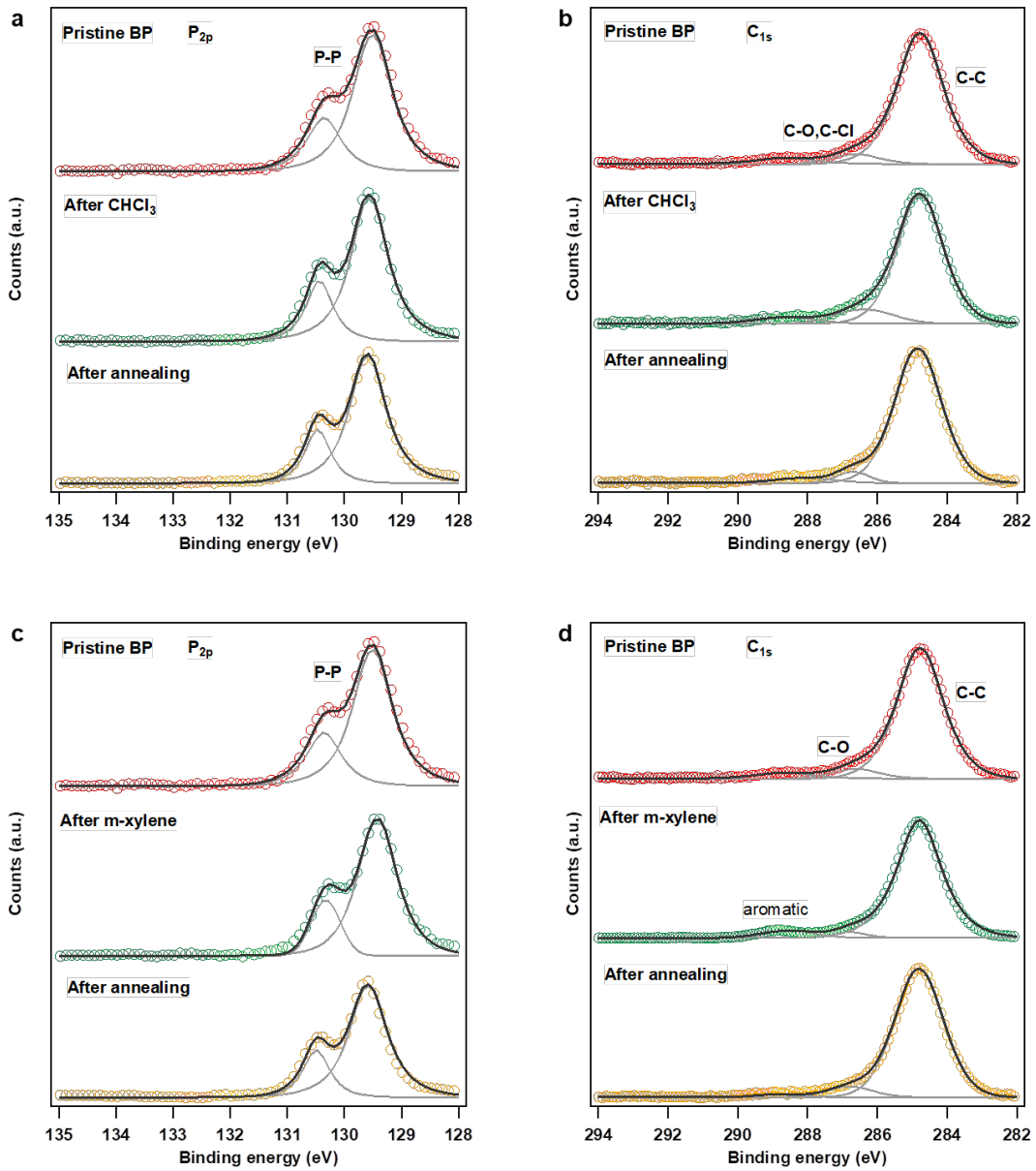

Figure 6.3: XPS analysis of P_{2p} and C_{1s} peaks of exfoliated BP flakes on Si/SiO_2 (90 nm) substrate before and after (a) and (b) chloroform and (c) and (d) m-xylene (bottom). The phosphorus peak (P_{2p}) showed no oxidation peak with as exfoliated samples, after depositing molecules, and after annealing in N_2, indicating that no oxidation occurs during our process. In carbon (C_{1s}), the physisorption of $CHCl_3$ brings augmentation of sp^3 carbon peak at 286.4 eV, which is then decreased to original level after annealing. The physisorption of m-xylene lead to the rise of π–π^* peak, and the diminishment of this peak is observed after annealing.

We have analyzed 9 different solvents on 10 devices (BP thickness < 5 nm) and we have analyzed their threshold voltage change upon physisorption of solvent molecules. Detailed transfer curves

and average threshold voltage change values of all nine solvents on BP are plotted in **Figure 6.4** and listed in **Table 6.2**.

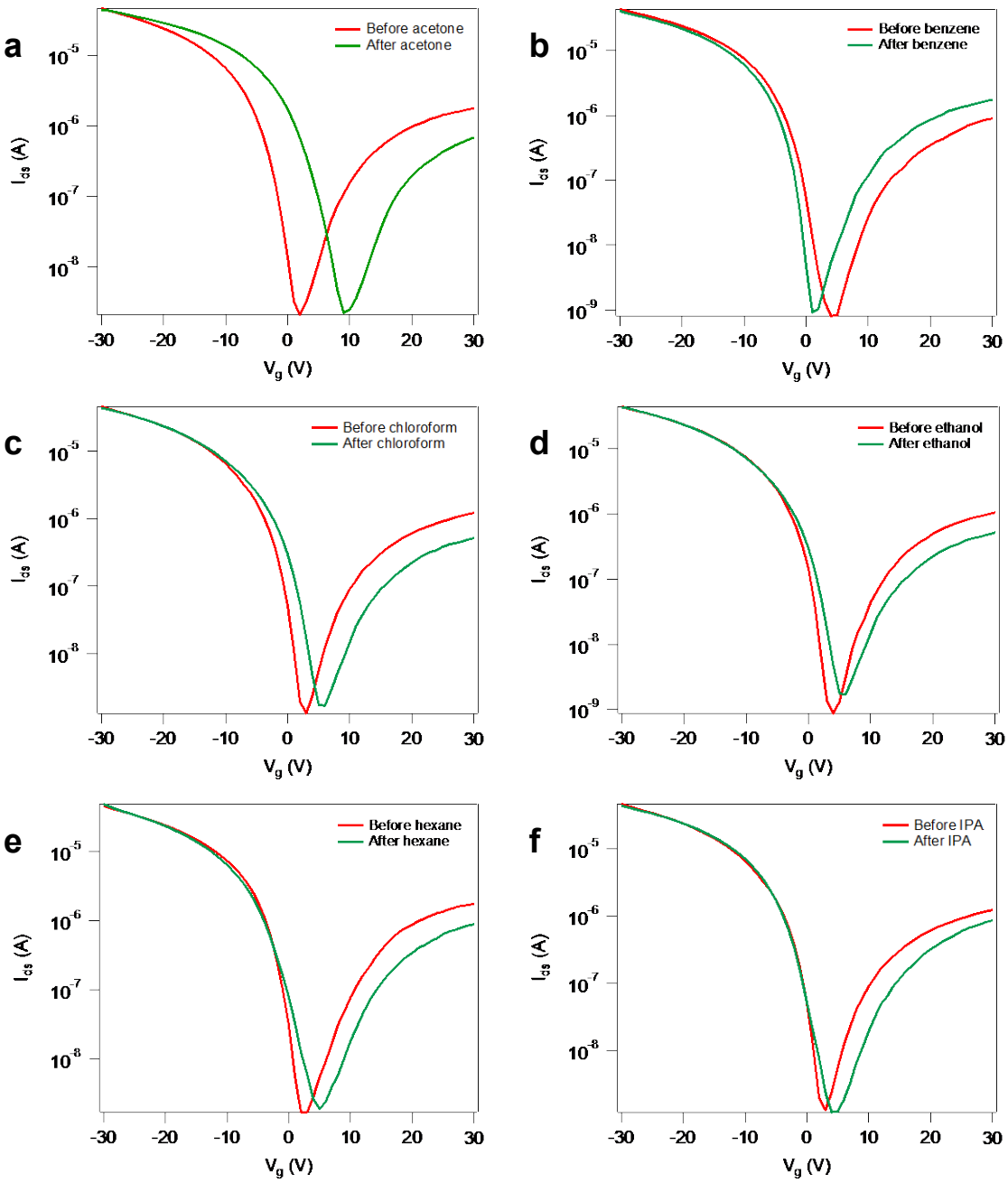

Figure 6.4 (see also next page): Transfer curve (logI_{ds} vs V_g) of few-layer BP before and after physisorption of (a) acetone, (b) benzene, (c) chloroform, (d) ethanol, (e) hexane, (f) IPA, (g) m-xylene, (h) p-xylene, and (h) toluene.

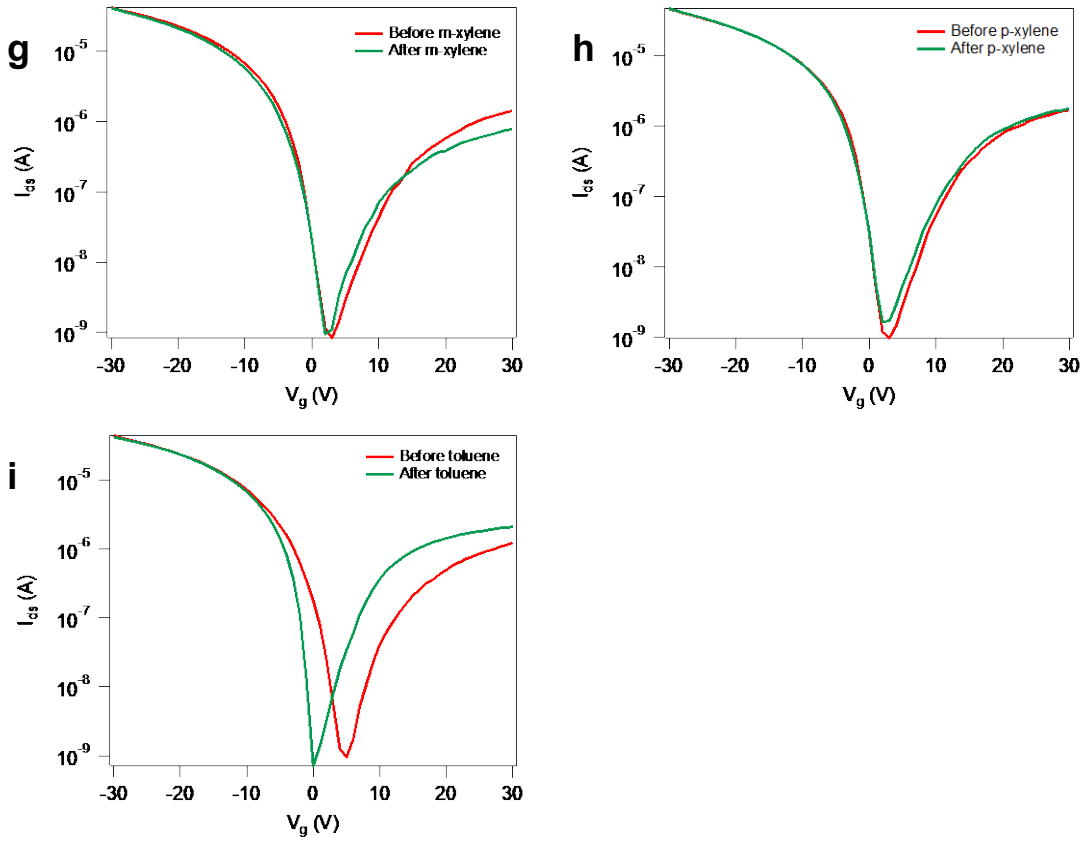

Figure 6.4 (continued): Transfer curve ($\log I_{ds}$ vs V_g) of few-layer BP before and after physisorption of (a) acetone, (b) benzene, (c) chloroform, (d) ethanol, (e) hexane, (f) IPA, (g) m-xylene, (h) p-xylene, and (h) toluene.

Solvent	Dielectric constant	Charge carrier density change ($10^{12}/cm^2$)	Average threshold voltage change (V)
Hexane	1.89	2.88 ± 1.96	1.20
Benzene	2.27	-2.89±1.60	-1.21
p-xylene	2.27	0.240±1.02	0.10
m-xylene	2.37	-0.98±1.18	-0.41
Toluene	2.38	-2.72±1.85	-1.13
Chlorofrom	4.81	1.42±1.11	0.59
IPA	17.9	1.32±2.38	0.55
Acetone	20.7	3.52±2.31	1.47
Ethanol	24.5	1.78±3.81	0.74

Table 6.2: Carrier density and threshold voltage change of each solvent on BP measured from FETs.

Among the solvents investigated, toluene and benzene give negative shift of $V_{th,p}$ to thin-layer BP, p-xylene and m-xylene do not too affect much the transfer characteristics, while hexane, chloroform, acetone, IPA and ethanol yield a positive shift of the $V_{th,p}$. To better quantify the solvent effect in FETs, we have calculated the charge carrier density change Δn resulting from physisorption of solvent molecules:

$$\Delta n = \frac{C_{ox}\,\Delta V_{th}}{e} = \frac{\varepsilon_{ox}\,\Delta V_{th}}{t_{ox}\,e} = 2.40 \times 10^{12} \Delta V_{th}\ cm^{-2} \qquad (6.1)$$

where Δn is the change in hole (positive charge) density, C_{ox} is the capacitance per unit area of 90 nm SiO_2, e is the elementary charge, and ε_{ox} is the dielectric constant of SiO_2, ΔV_{th} is the change of threshold voltage in p-type transport and t_{ox} is the thickness of SiO_2.

The linear relationship between shift in $V_{th,p}$ and hole density change after physisorption of molecules reveals that, as most semiconducting materials, few-layer BP is rather sensitive to the solvent residues able to modulate the charge carrier density up to 10^{12} /cm^2 (values for all the solvent molecules are listed in **Table 6.2**). Such a value is significant and comparable to traditional dopants that also attain charge modulation in the range 10^{12} /cm^2.[157] The reversible nature of the effect and the differential V_{th} shift recorded with small error render thin-layer BP a promising material for solvent vapor sensing with high accuracy.

To explore the origin of charge carrier density modulation in BP by physisorbed solvents, we have taken into account two major factors: 1) charge transfer between solvent molecules and BP, 2) molecular dipole induced doping. First, to evaluate the charge transfer ability of the solvents, DFT calculations have been carried out with solvent-BP systems and the charge transfer has been estimated by using a Bader charge analysis, as shown in **Figure 6.5**. We have found that, at equilibrium configuration, physisorbed benzene, p-xylene, m-xylene, and toluene donate electrons to BP whereas hexane, chloroform, ethanol, acetone and IPA are prone to act as electron acceptors. Charge transfer from solvents to BP (or vice versa) could thus result in a modification in charge carrier density in semiconducting BP. Therefore, we compared DFT calculation results to the charge carrier density change in thin layer BP FETs in **Figure 6.7**. Overall, the experimental results qualitatively match nicely the results of the Bader charge transfer analysis, indicating that direct electron transfer plays a dominant role. More specifically, in hexane, benzene, p-xylene, m-xylene, toluene and chloroform, the carrier density changes comply perfectly with a charge transfer mechanism with a small error bar. However, there is significantly more scattering of the results for IPA, acetone and ethanol, which cannot be fully rationalized based on charge transfer only.

Considering that IPA, acetone and ethanol possess a much larger dielectric constant (ε_r all $>$ 15) than hexane, benzene, p − xylene, m − xylene, toluene and chloroform (ε_r all $<$ 5), we conclude that the local electrostatic potential created by molecular dipoles at the BP surface is non negligible in these cases. Therefore, we next proceed with the theoretical evaluation of the molecular dipole effects.

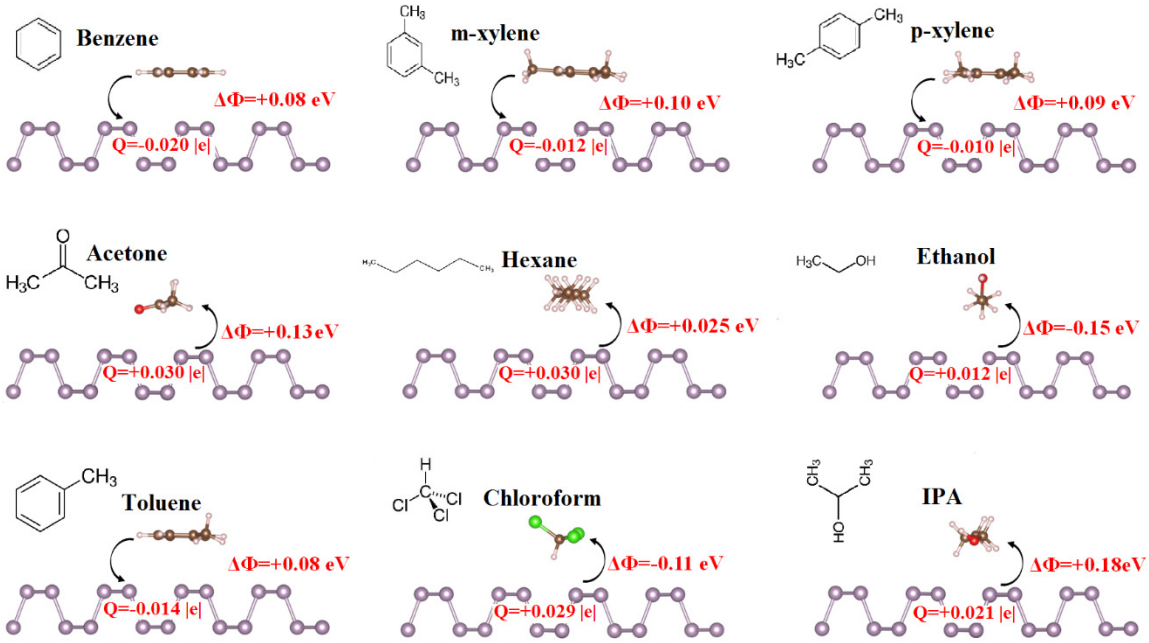

Figure 6.5: Equilibrium geometry of the various solvent molecules deposited on BP together with the Bader charge transfer (Q) between donor (acceptor) molecules and BP and the workfunction shift (ΔΦ) due to the presence of the molecular dipole (The latter is obtained by plotting the plane averaged electrostatic potential across the solvent molecule along the stacking direction, as illustrated **Figure 6.6**).

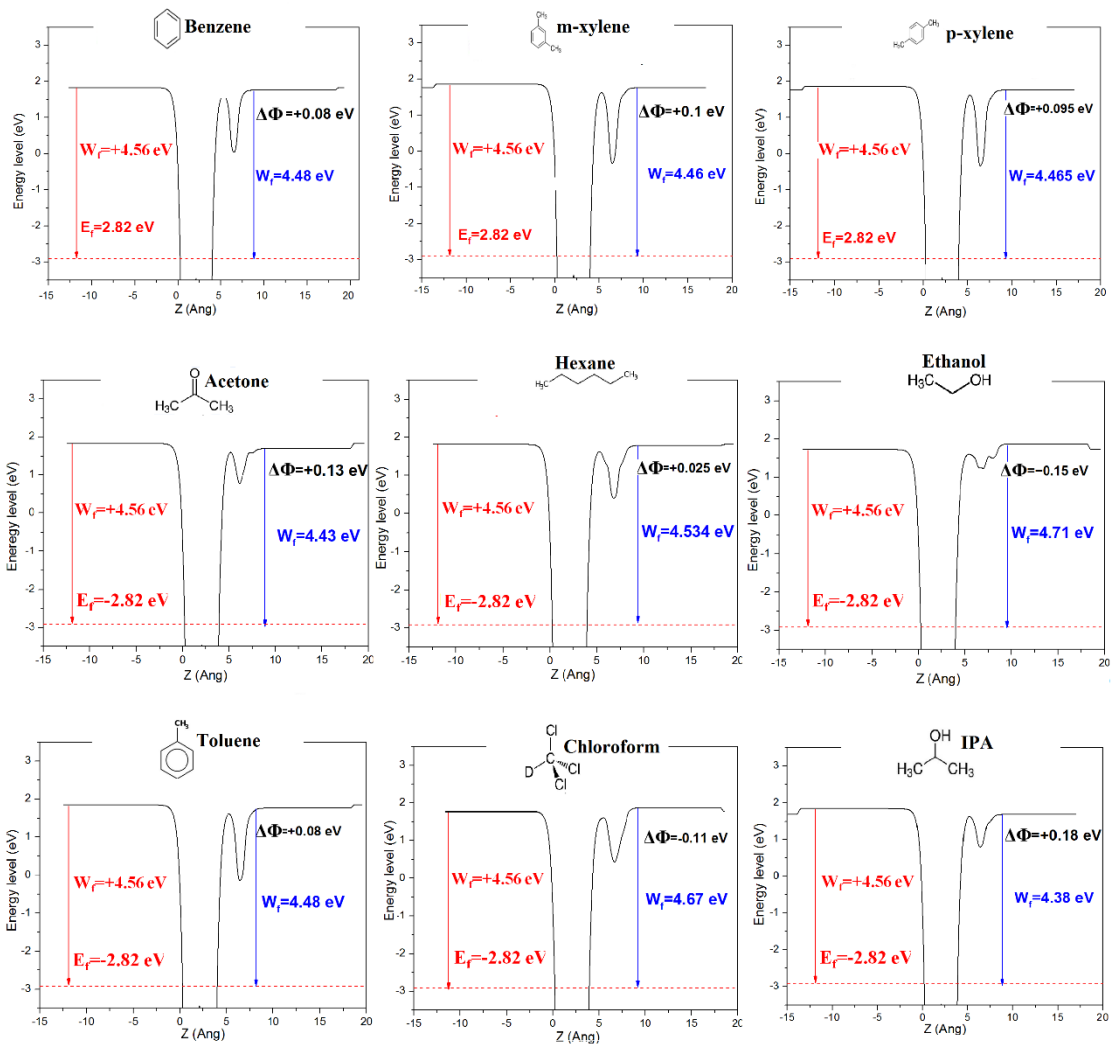

Figure 6.6: Plane averaged electrostatic potentials V (z) of molecules adsorbed on phosphorene. Δϕ (eV) is the shift in vacuum level associated to the molecule defined as the difference between the electrostatic potential on the phosphorene side and on the molecular side.

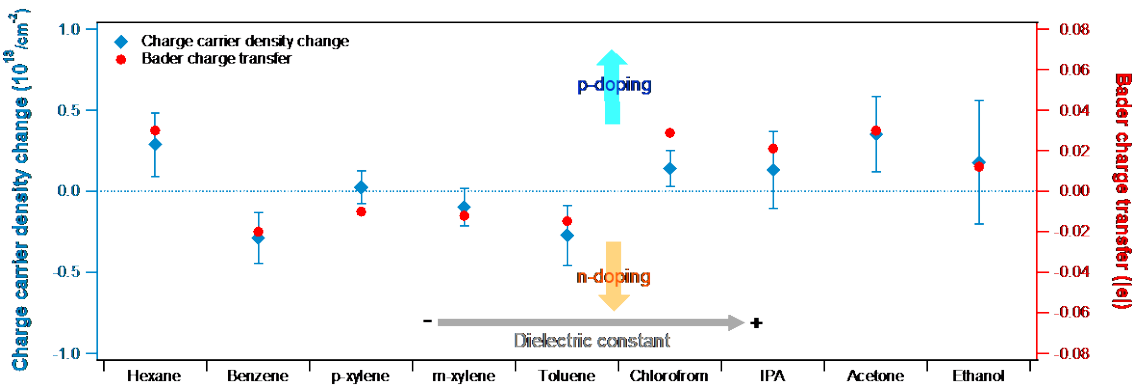

Figure 6.7: Charge carrier density change of BP FET after physisorption of solvent molecules and calculated Bader charge transfer in solvent-phosphorene systems.

To cast light onto the effect of molecular dipoles, we first calculated the dipole moment of each molecule investigated at adsorption equilibrium on BP. The results are reported in **Table 6.3**. They reveal that solvent molecules with large dielectric constant maintain their comparatively larger dipole moment even in the physisorbed geometry onto BP (though still much lower than common organic dopants such as octadecyltrichlorosilane (OTS)). It is difficult to assess quantitatively how solvent molecule dipoles influence the charge carrier density of two-dimensional BP, owing to the difficulty in measuring the molecular areal density (the solvents are volatile at room temperature). To gain a deeper insight into the competition between charge transfer and dipole moment in solvent molecule/BP systems, we have calculated the molecular dipole contribution and charge transfer contribution on the work function shift of black phosphorus, as indicated in **Table 3**. The work function of two-dimensional materials notoriously varies with charge transfer from/to the physisorbed molecules and the normal component of the dipole moment of the adsorbed molecules.[162] From **Table 3**, we observe, as expected, that the variation in work function of BP is determined primarily by molecular dipoles in acetone, chloroform, ethanol and IPA, while charge transfer represents the dominant contribution in the case of m-xylene, p-xylene, benzene, hexane and toluene adsorptions. Among the 9 solvents considered in our work, the molecular contribution to the modification of work function by acetone, ethanol and IPA is around 10 to 100 times larger than other solvent molecules, i.e. prior to charge transfer mechanism; the permanent dipole in these three molecules gives larger impact to the doping of BP. When a considerable number of solvent molecules with non-negligible dipoles are physisorbed onto the surface of BP, a local electric field emerges from the dipole, acting as a local gate to BP. The work function of BP is thus modulated by the molecular gating effect, thus inducing doping.[15] Since the physisorption of these solvent molecules do not necessarily form self-assembled monolayers on BP surface, the dipole orientation on the devices with

channel length of a few micrometers is likely disordered. This explains the larger error bars in the experimental results displayed in **Figure 6.6** for molecules with a larger dipole moment.

The electronic interaction of BP with the physisorbed molecules depends on the number of molecules physisorbed in a given surface area. However, it is extremely complicated to experimentally quantify the precise number of physisorbed molecule on BP because of the rapid evaporation process of solvents at room temperature. For solvent molecules with a small dipole moment (hexane, benzene, toluene, m-xylene, p-xylene and chloroform), since the charge transfer mechanism is dominant, and in view of the good matching between experimental and theoretical results of charge transfer vs charge carrier density, an estimation of the number of molecules taking part to charge transfer processes can be obtained with the following equation:

$$\Delta n_{hole} \cdot |e| = n_{mol} \cdot \Delta\sigma^{+} \qquad (2)$$

where Δn_{hole} is the change in hole carrier density, $|e|$ is the absolute value of elementary charge, n_{mol} is the number of molecules adsorbed per unit area (cm^2) and $\Delta\sigma^{+}$ is the positive charge transfer value. The results are listed in **Table 6.4**. The estimated number of physisorbed molecules is in the range 10^{13} to 10^{14}, which is comparable to the doping of common organic molecules.

For solvent molecules with larger dipole moments, we estimate qualitatively the number of molecules physisorbed in a given surface area from literature reported values of surface tension and enthalpy of evaporation of solvent (**Table 6.1**). An indirect way to gain insight into the affinity of the solvent molecules for the BP consists in the ability of the given solvent to disperse the 2D material, e.g. in the case of liquid phase exfoliation. Previous work revealed that BP is poorly dispersed in solvents with lower surface tension such as acetone, IPA and ethanol, which implies an unfavorable adhesion of these solvent molecules onto the surface of BP.[163] In other words, the number of molecules physisorbed in a given surface area of BP for these three solvents is smaller when compared to aromatic solvents. It is also worth noting that among polar solvents, BP displayed a better dispersion in IPA than in ethanol because of reinforced hydrogen bond interactions and larger surface tension in IPA, whereas it is barely dispersed in acetone.[38]

Systems	Molecular dipole (D)	Work function (eV)	Molecule contribution	Charge Transfer contribution
BP		4.560	-	-
BP/acetone	3.040	4.430	-0.103	-0.028
BP/Chloroform	1.010	4.670	+0.130	-0.020
BP/Ethanol	1.542	4.710	+0.157	-0.007
BP/toluene	0.432	4.480	+0.022	-0.102
BP/Hexane	0.030	4.534	+0.006	-0.032
BP/IPA	1.748	4.380	-0.127	-0.053
BP/Benzene	0	4.480	+0.003	-0.083
BP/m-xylene	0.420	4.480	-0.015	-0.065
BP/p-xylene	0.15	4.465	-0.015	-0.080

Table 6.3 Calculated work function of BP modulated by physisorption of solvent molecules.

Solvent	**Hexane**	**Benzene**	**p-xylene**
Number of physisorbed molecules ($10^{13}/cm^2$)	9.6	14.8	2.4
Solvent	**Chlorofrom**	**m-xylene**	**Toluene**
Number of physisorbed molecules ($10^{13}/cm^2$)	4.9	8.1	18.6

Table 6.4: Estimated number of physisorbed solvent molecules with dipole moment <1D on few-layer BP calculated from hole density changes and charge transfer values.

Alongside the versatile modulation of charge carrier density in few-layer BP, the presence of physisorbed solvent molecules also enables to tune other key parameters in BP FETs. In first instance, the field-effect carrier mobility μ, which could be estimated as:

$$\mu = \frac{L}{WC_{ox}V_{ds}}\frac{dI_{ds}}{dV_g}$$

where L and W are the channel length and width, respectively. $\frac{dI_{ds}}{dV_g}$ of solvent,which is denoted as μ_{after}/μ_{before} in **Figure 6.8a**. We have found a decrease in both hole and electron mobility with all μ_{after}/μ_{before} smaller than 1. The overall degradation of charge carrier mobility might be attributed to the introduction of charge impurity by solvent molecules that enhanced scattering effect. Thus,the motion of charge carriers are hindered. [157] Hole mobility is less affected, with μ_{after}/μ_{before} amounting to 0.81 in acetone and 0.98 in benzene. The electron mobility decreased sharply, with μ_{after}/μ_{before} spanning from 0.48 for m-xylene to 0.66 for benzene. This contrast originates from different carrier transport mechanisms in holes and electrons in BP. The hole transport was found to be dominated by phonon scattering and was barely influenced by charge-

charge scattering so that the modulation of charge carrier concentration weakly affects the mobility. Conversely, electron mobility was mostly limited by charge-charge scattering, implying that charge impurity introduced from surface functionalization would largely affect the motion of charge carriers. Hence, the physisorption of solvent molecules largely reinforces the scattering effect which prevents the transport of electrons and decreased the electron mobility in a larger extent than hole mobility.[157,164]

I_{on}/I_{off} ratio is another key indicator for evaluating BP devices, which could be deduced by:

$$\frac{I_{on}}{I_{off}} = \frac{I_{ds,max}}{I_{ds,min}}$$

where $I_{ds,max}$ and $I_{ds,min}$ represent maximum and minimum value of drain-source current on transfer curve. **Figure 6.8b** and **c** displays the I_{on}/I_{off} ratio before and after the deposition of solvent molecules. It reveals that in pristine BP FETs, the I_{on}/I_{off} ratio ranges between 10^5 to 10^6 for hole conduction and 10^4 to 10^5 for electron conduction for all tested devices. The physisorption of solvent molecules did not affect the I_{on}/I_{off} ratio while stable off current values were monitored, indicating that the bandgap E_g could not be modified by the limited number of molecules ($\sim 10^{13}/cm^2$) physisorbed onto BP by internal built-in potential.[165] Furthermore, solvent molecules are also observed to yield an enlargement of the hysteresis in the transfer curves due to additional dipolar doping induced by vertical electrical field when the gate voltage is applied. Detailed results are shown in **Figure 6.9**.

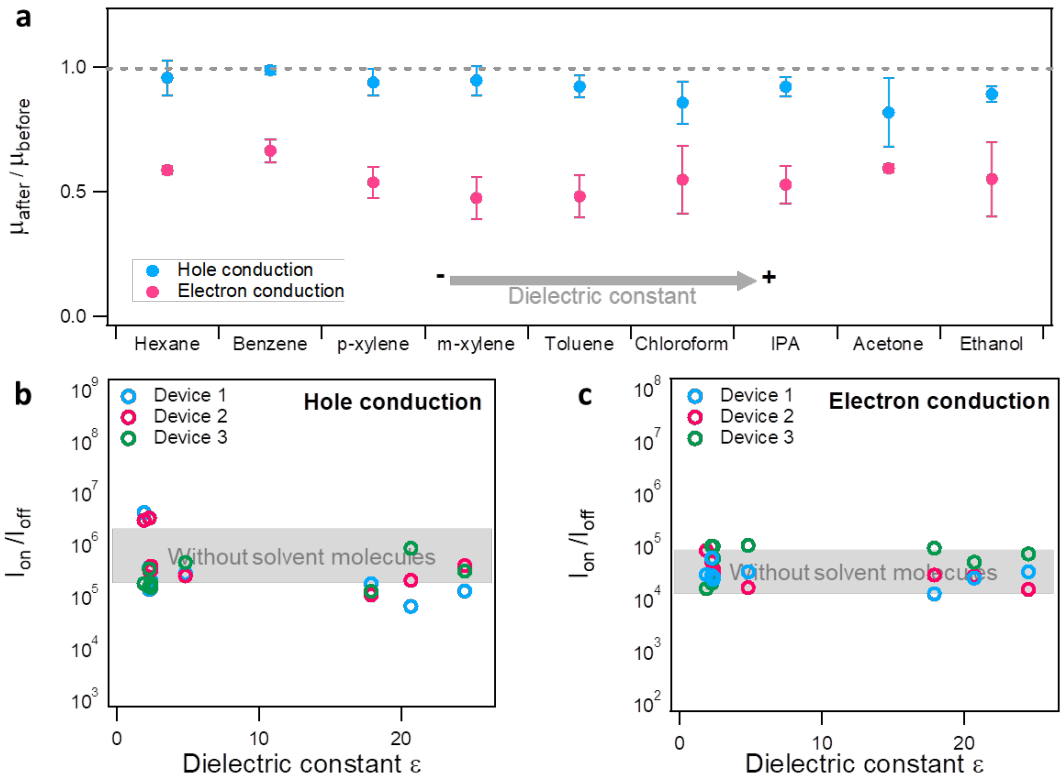

Figure 6.8: Other electrical characterization of BP FET with physisorbed solvent molecules. (a) Analysis of hole and electron mobility of BP FET before and after physisorption of molecules, and I_{on}/I_{off} ratio of (b) hole conduction branch and (c) electron conduction branch of three BP FETs before and after depositing solvent molecules in the order of increasing dielectric constant. The coloured bands marked with "Without solvent molecules" indicate the typical I_{on}/I_{off} ratio range determined before physisorption of molecules.

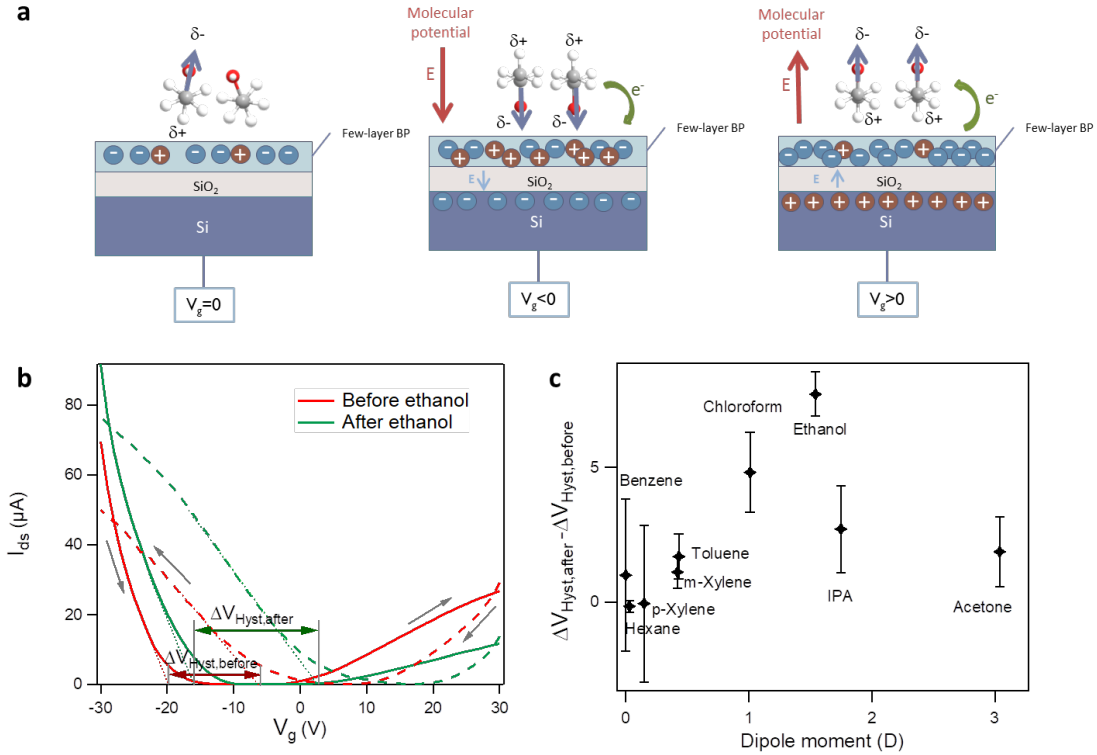

Figure 6.9: Hysteresis change in transfer curve of BP FET by solvent molecules. (a) Scheme of dipolar effect on hysteresis. (b) Example of hysteresis enlargement after the physisorption of ethanol. (c) Hysteresis change value versus dipole moment of solvents. In particular, the electrical filed is applied between the bottom gate under BP and top electrode onto BP. When electrical field is applied to the 2D-molecular system, the molecular dipoles orient along with the electrical field and tend to induce the same effect in modulating charge carrier density as gate-induced electrostatic doping. Thus, one would be expected to observe a slower carrier density change with respect to gate voltage change.

To further characterize solvent effects on BP FETs, we explored the change in optical properties of BP upon solvent physisorption. Unlike TMDs whose photoluminescence (PL) spectra could reflect the level of doping by solvent molecules via the quantification of the exciton and trion intensity, photoluminescence of black phosphorus has barely been studied due to their small band-gap in few-layer materials and high exciton anisotropy.[46,161,166] The complex behavior of excitons and trions made it difficult to quantify the charge density modulation by physisorbed molecules, as shown in **Figure 6.10**.

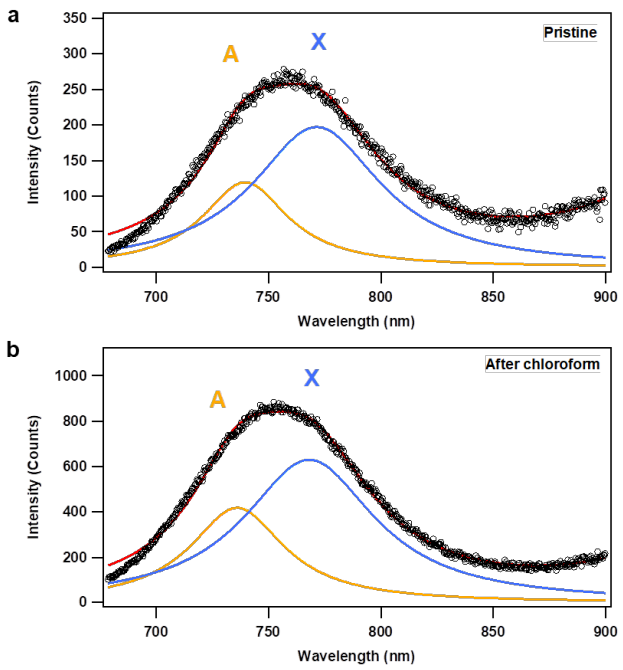

Figure 6.10: Photoluminescence spectra of few-layer black phosphorus in N_2 at room temperature before and after deposition of chloroform.

Therefore, we focus mainly on the Raman spectra of few-layer BP which are regarded as fingerprint to properties of BP.[4] For the sake of consistency with electrical measurements on BP FETs, all Raman spectra were directly recorded from devices. Pristine and solvent treated BP devices were transferred in a N_2 filled spectroscopy holder immediately after each electrical measurement, ensuring the same conditions as for electrical characterizations. The spectra were compared before and after the spin-coating of solvents and were normalized to the silicon peak at 520.3 cm^{-1}. Three Raman modes were detected, as shown in **Figure 6.11a** and **b**. Among the three modes, in-plane vibration modes B_{2g} and A^2_g are found to be more inert to surface adsorption than out-of-plane mode A^1_g in thin BP flakes. A red-shift of the A^1_g mode was observed in toluene (Δ =—1.787 cm^{-1}), benzene (Δ =—2.372 cm^{-1}), m-xylene (Δ =—0.694 cm^{-1}), as a result of an increase in electron concentration who tends to soften the vibrations.The A1g mode of ethanol (Δ =+0.484 cm^{-1}), hexane (Δ =+1.851 cm^{-1}), chloroform (Δ =+1.138 cm^{-1}), IPA (Δ= +1.687 cm^{-1}) undergoes a blue shift, corresponding to the hardening of BP vibrations by hole doping.[167] The Raman trend in the switch of doping is in accordance to the charge transfer measurements in BP FETs, as shown in **Figure 6.11c**, except for volatile solvents such as acetone and p-xylene due to its low coverage on BP under laser excitation. As for B_{2g} and A^2_g modes, peak shift has values less than 1 cm^{-1} for most of the solvents yet still keeps

the same trend as A^1_g mode, revealing that electron/hole concentration also yields variations the in-plane vibration modes.

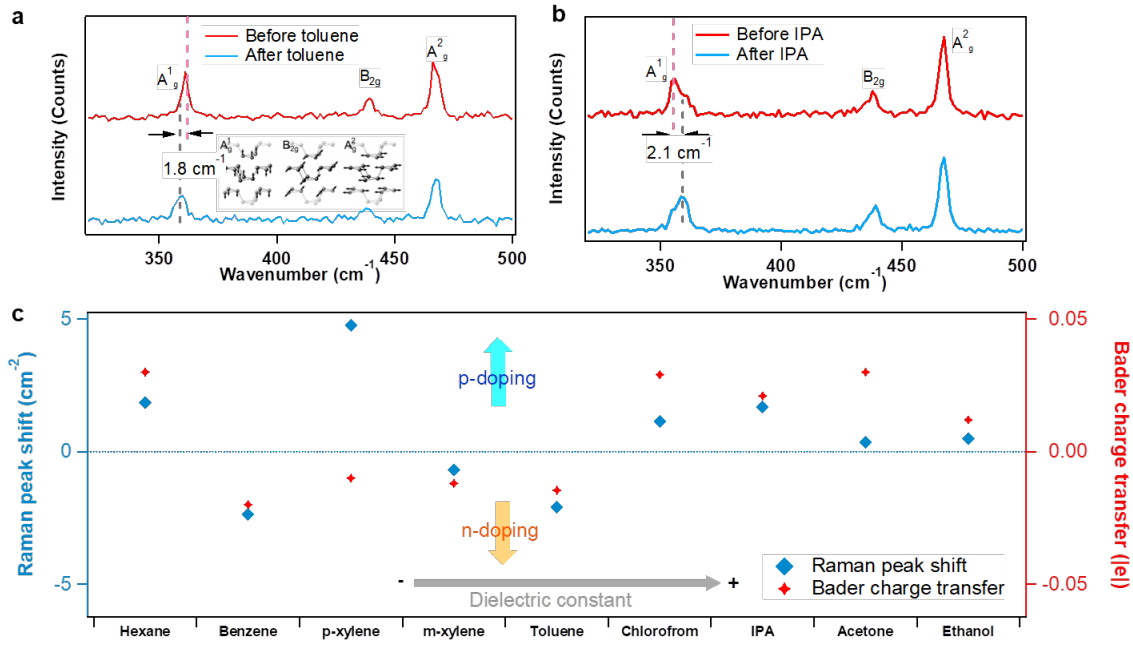

Figure 6.11: Raman spectroscopy of few-layer BP upon physisorption of solvent molecules. (a) and (b) representative Raman spectra of n-doping (toluene) and p-doping (p-xylene) solvent molecules. The dashed lines highlight the obvious shift in A^1_g mode. (c) Comparison of the A^1_g mode shift of few-layer BP (in blue) before and after physisorption of solvent molecules compared to corresponding charge transfer changes (in red).

6.4 Conclusions

In summary, our electrical and spectroscopic study provided unambiguous evidence of the power of the physisorption of solvent molecules on few-layer black phosphorus to tune their opto-electronic properties via charge transfer and/or dipolar interactions. In particular, our electrical measurement on field-effect transistors demonstrated for the first time that tunable chemical doping can be achieved on black phosphorus using the modest doping brought into play by the physisorption of common solvent molecules. Our results revealed that solvent molecules could not only modulate the charge carrier density up to $10^{12}/cm^2$, but also affect carrier mobility and Raman shift to a large extent. Our findings are of importance both for fundamental and more applicative investigations since numerous solvents are made of small aromatic molecules, which

should therefore not be considered as inert media in the processing, but rather as a potent remote control for tuning the properties of 2D materials and consequent device optimization.

Chapter 7 Molecular-functionalized few-layer indium selenide for ultra-high performance photodetectors

7.1 Introduction

Photodetectors capable of sensing light from ultraviolet (UV) to infrared (IR) have become key devices in a broad range of technologies comprising optical sensing, image recognition, motion detection, remote control, biomedical imaging, etc.[168-171] Two-dimensional (2D) materials have been extensively studied during the last decade as promising photodetecting materials owing to their fast response, high responsivity, photodetectivity and broad wavelength detection. The wide selection of materials with tunable bandgap obtained by altering the layer numbers and the simple formation of van der Waals (vdW) heterostructures enabled to reach high responsivity (10^6~10^7 AW^{-1}), high detectivity (D^*) (10^{10}~10^{13} Jones) and ultrafast photoresponse (on the ms timescale). [65,68,74,142,168,172-175] However, the operation of these high-performance devices requires high bias voltage yielding large power consumption. Such an issue represents a strong handicap for various technological applications such as photosensor in extreme environment, bio-medical imaging, portable devices, etc. 2D InSe has recently attracted a great attention because of its ultrasensitive photodetection characteristics outperforming common 2D semiconducting materials such as MoS_2 and WSe_2. [65,68-71,172,176] Such high performances was achieved by means of complex and specific techniques such as ion implantation and nanopatterning, which unfortunately drastically increase the fabrication costs.[60,65,74] A powerful route for tuning physical and chemical properties of 2D materials, which has been thoroughly applied to graphene, TMDs and BP, consists in molecular functionalization via covalent and non-covalent strategies, resulting in doping, defect healing, increase in bio-compatibility, etc. [15,16] Surprisingly, such approach has not yet been attempted with InSe for obtaining high-performance devices. Moreover, despite the high electron mobility of InSe, little effort has been devoted in combining InSe with other 2D materials to generate highly responsive p-n

photodetectors. This urges us to find viable strategies for the construction of high-performance photodetectors based on InSe and InSe-based p-n junctions.

In this chapter, we show how the functionalization with a common surfactant molecule represents a powerful strategy to boost the (opto)electronic performances of 10-15 nm thick InSe flakes exfoliated from commercial crystals yielding to major property enhancements in InSe based phototransistor, lateral Schottky junction and BP-InSe vdW p-n heterostructures. For the first time we have also fabricated high-responsivity, fast response, low power input 2D phototransistors through a lithography-compatible route in which the performances are enhanced via the functionalization with organic molecules.

7.2 Experimental methods

7.2.1 Sample preparation

BCB dielectric was prepared by diluting Cyclotene 3022-46 (Dow Chemistry) is to 20%vol with mesitylene. The solution is spin-coated onto thermally oxidized heavily *n*-doped silicon substrates (Fraunhofer Institute IPMS, $\rho_{Si} \sim 0.001\ \Omega\cdot$cm, t_{ox} = 270 nm) at 4000RPM and post-anneal at 290 °C resulting film thickness of 100 nm. For InSe phototransistors and asymmetric Schottky junctions, few-layer InSe (10-15 nm thick) were mechanically exfoliated from commercially available InSe crystals (HQ Graphene, Netherlands) using the scotch tape method and transferred on SiO_2 or BCB in a N_2-filled glovebox. Their thickness was monitored by optical microscope combined with Raman spectroscopy and Atomic Force Microscopy (AFM). For BP-InSe heterostructures, few-layer BP flakes (5-10 nm thick) were first mechanically exfoliated onto BCB substrate in glovebox. Few-layer InSe (10-20 nm thick) were immediately transferred onto BP by PDMS to form van der Waals heterostructure. The samples were thermally annealed at 100 °C inside a vacuum chamber to desorb atmospheric adsorbates and to reinforce the van der Waals contact. For molecular functionalization, didodecyldimethylammonium bromide (DDAB) solution (Tokyo Chemical Industry Co., Ltd (TCI)) with 10^{-6}, 10^{-5}, 10^{-4}, 10^{-3}, 10^{-2}, 10^{-1}, and 1g/L of concentration were spin-coated at 2000 RPM onto InSe. A post thermal annealing at 120 °C is applied on hotplate in N_2-filled glovebox.

7.2.2 Device fabrication

InSe devices were patterned by photolithography (AZ1505 photoresist and MIF726 developer, Micro Chemicals) using laser writer LW405B from Microtech. For InSe photoFET and BP/InSe P-N photodetector, were thermally evaporated with Plassys MEB 300 following a lift-off process in warm acetone to obtain the final source and drain electrodes. For asymmetric Schottky junctions, one electrode was first patterned with laser writer and 60 nm Pd was deposited with Egun evaporator Plassys ME300, after lift-off in warm acetone, a second electrode was patterned followed by thermal deposition of 5 nm chromium and 40 nm of gold by Plassys MEB300B equipped in the glovebox. The devices were rinsed with acetone and 2-propanol to remove resist residues. All devices were annealed under vacuum at 100°C to remove absorbents.

7.2.3 Electrical characterizations

The characterization of device performance was realized by Keithley 2636A under N_2 atmosphere. For optoelectronic characterizations, a Polychrome V system (Thermo Fisher) was used as monochromatic light source. The output power has been calibrated by a PM100A Power Meter (Thorlabs).

7.2.4 Raman spectroscopy

Raman and Photoluminescence spectra were carried out in inert atmosphere (N_2) by Renishaw inVia spectrometer equipped with 532 nm laser in a nitrogen-filled sealed holder (Linkam). Samples were mounted in the glovebox and immediately measured after annealing or after molecule deposition to avoid exposure to contaminant chemicals. The excitation power was kept below 1 mW to avoid local heating damage effects. The wavenumber (energy) resolution was ~1 meV.

7.2.5 AFM measurement

AFM imaging was performed by means of a Bruker Dimension Icon set-up operating in air, in tapping mode, by using tip model TESPA-V2 (tip stiffness: k=42 N/m).

7.2.6 KPFM measurement

A Bruker Icon AFM was employed for KPFM experiments. Topography and surface potential (or contact potential difference) images were simultaneously collected with Pt/Ir coated silicon probes (Bruker SCM-PIT-V2, resonant frequency $\approx$ 75 kHz, k $\approx$ 3 N•m^{-1}) at ambient conditions in the amplitude modulation mode. Macroscopic Kelvin Probe (KP) measurements were performed by using a 2-mm-diameter gold tip amplifier (Ambient Kelvin Probe Package from KP Technology Ltd) at ambient conditions. The calibration of the probe was performed against a freshly cleaved HOPG surface (4.475 eV). [177]

7.2.7 XPS measurements

XPS analyses were carried out with a Thermo Scientific K-Alpha X-ray photoelectron spectrometer with a basic chamber pressure of ~10^{-9} mbar and an Al anode as the X-ray source (x-ray radiation of 1486 eV). Spot sizes of 400 µm and pass energies of 200.00 eV for wide energy scans and 10.00-20.00 eV for scans were used.

7.2.8 Computational details

All DFT calculations were performed using the VASP code[55] and the projector-augmented wave (PAW) basis set. Exchange and correlation effects are treated at the Perdew–Burke–Ernzerhof (PBE) level with the dispersion forces treated by Grimme correction (PBE+D2), with a kinetic energy cut-off of 500 eV and using a Monkhorst-Pack sampling of 3×3×1 for the Brillouin zone (BZ) integration on the unit cell replicated 4x4x1 times with the vacuum spacing set to be 40 Å to avoid the interaction with periodic images.[158,159,178,179] Dipole moment correction was employed along the 'c' axis (Z direction & perpendicular to the InSe surface). Geometries of pristine and defective (-3% Se vacancies) InSe surfaces, as well as the DDAB adsorbed heterostructures, were fully optimized at the PBE/GGA level of theory prior to the calculation of work function. DDAB molecules were considered with two butyl (C_4) linkers (dibutyl-dimethyl-ammonium, bromide) instead of two decyl (C_{10}) linkers connecting the central nitrogen atom, so as to limit the computational cost. The work function (φ) of all the systems was calculated as difference of Fermi energy (E_f, taken as the middle of the band gap) and the electrostatic potential at vacuum level (E_p) at the hybrid (HSE06) level of theory.

7.3 Results and discussions

7.3.1 Dielectric engineering InSe field-effect transistor

In order to cast light onto the role of the dielectric characteristics of the substrate, as-exfoliated flakes were transferred onto both Si/SiO_2 and polymer-coated Si/SiO_2 substrate. **Figure 7.1a** displays the transfer (V_g-I_{ds}) curve of InSe on SiO_2. It reveals modest transport performances with electron mobilities around 0.01 cm^2/Vs, being considerably lower than other 2D semiconductors. Such low performances can be ascribed to the abundance of charge traps at the $InSe/SiO_2$ interface which is detrimental to photodetection, also limiting the use of as-prepared InSe as a platform for molecular functionalization, because the leakage current would have a similar magnitude of the drain-source current, yielding device instability. [180,181] Therefore, it is imperative to improve the local environment where InSe is embedded, and in particular its dielectric characteristics. Towards this end, divinyltetramethyl disiloxanebis(benzocyclobutene) (BCB) was chosen as trap-free dielectric polymer for its easy processability, high thermal and chemical resistance, being an optimal choice for microfabrication of 2D materials.[98] The precursor-free solution-processable and lithography-friendly characteristics made BCB much more advantageous compared to other trap-free dielectrics such as poly(methyl methacrylate) (PMMA, highly soluble in common solvents), polyimide (PI, usually precursor-involved) and hexagonal boron nitride (h-BN, very costly for both CVD-grown and exfoliated materials). The hysteresis of transfer curves have been largely decreased by 30V compared to pure SiO_2 supported devices (**Figure 7.2a**). The top-contact device architecture is depicted in **Figure 7.1b**. The resulting capacitance of the in-series capacitor drops from 12.7 nF/cm^2 for SiO_2 to 6.05 nF/cm^2 for BCB. The 2D conductivity (σ) is determined as $\sigma = \frac{I_{ds}}{V_{ds}}\frac{L}{W}$ where I_{ds} is the drain-source current and V_{ds} is the drain-source bias voltage of the field effect transistor, while L and W are length and width of the 2D channel, respectively. As shown in **Figure 7.1a**, 2D conductivity (σ) of InSe drastically increases in devices from $(1.99\pm0.966)\times10^{-4}$ μS on SiO_2 to 25.30 ±11.19 μS on BCB, with turn-on voltage fixed around 0V, thereby indicating the unchanged degree of doping on different dielectrics. Similarly, the field-effect mobility (μ) which could be evaluated as was determined by the following equation:

$$\mu = \frac{L}{WC_{ox}V_{ds}}\frac{dI_{ds}}{dV_g}$$

where L and W are the channel length and width, respectively. $\frac{dI_{ds}}{dV_g}$ is the maximum slope

extracted from the linear region of the transfer curves. The value of InSe undergoes a major increase from a max value of 0.0116 cm^2/Vs on SiO_2 to 688.2 cm^2/Vs on BCB. The mechanism could be explained through **Figure 7.1c** where large defect densities (e.g. point defect P_b center) are formed during the thermal oxidation of silicon, in addition to the polarized surface optical (SO) phonon modes in Si-O bond oscillatory motions, limiting the mobility of electron transport by introducing localized states and participating in Coulomb scattering.[182-185] Furthermore, the interface trap density D_{it} could be estimated through:

$$SS = (\frac{d(log_{10}I_{ds})}{dV_g}) \approx ln10\frac{kT}{e}(1+\frac{eD_{it}}{C_{ox}})$$

where SS is the subthreshold swing, k is the Boltzmann constant, T is the temperature. The obtained D_{it} for SiO_2 and BCB is 2.7×10^{13} $cm^{-2}eV^{-1}$ and 4.0×10^{12} $cm^{-2}eV^{-1}$, respectively. By using BCB as a gate dielectric, the interface trap density D_{it} between InSe and the dielectric has decreased by one order of magnitude, leading to a more effective screening of Coulomb scattering, thus increasing the charge carrier mobility and channel conductance.

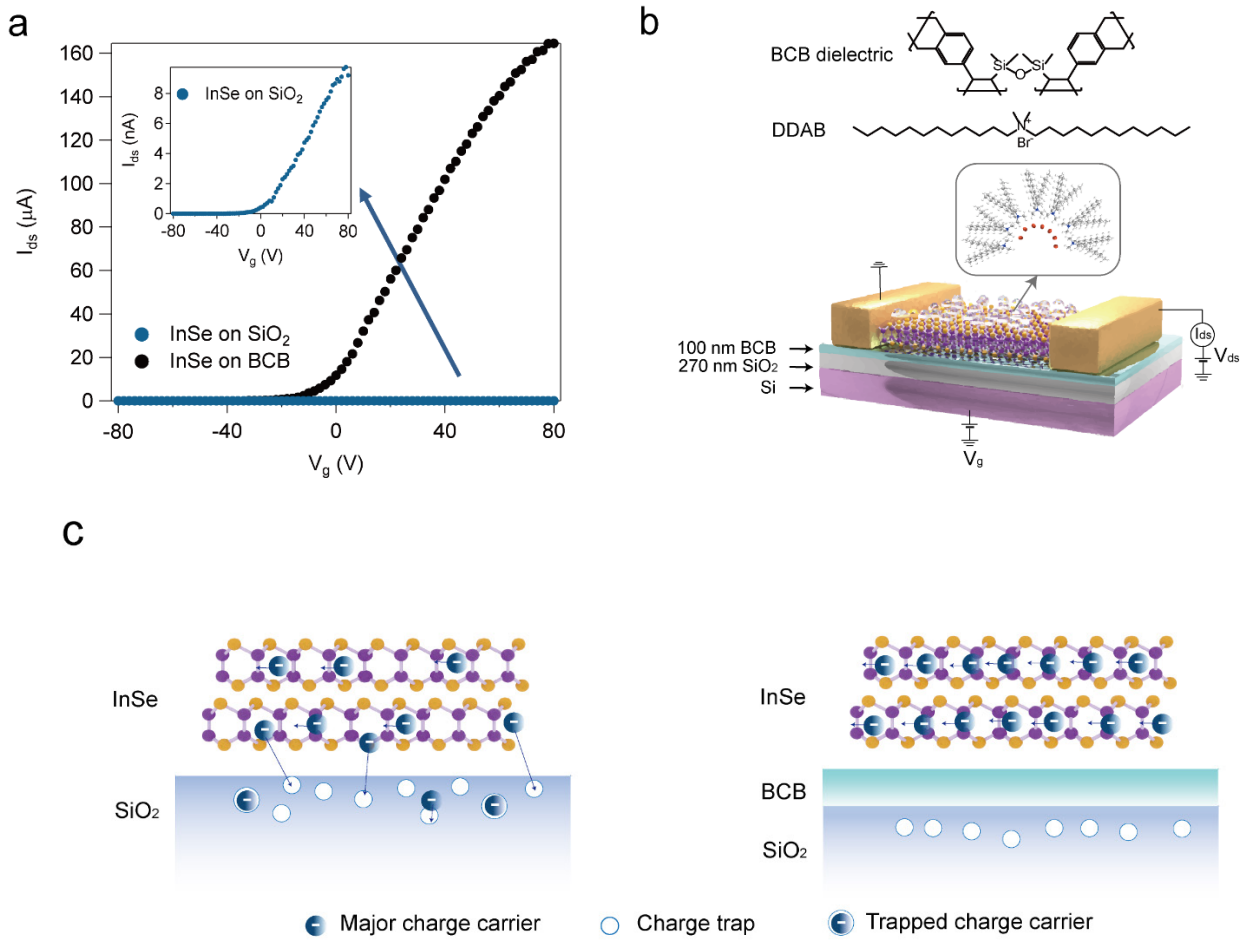

Figure 7.1: Dielectric engineering of few-layer InSe. (a) Comparison of transfer (V_g-I_{ds}) curve of InSe FET onto SiO_2 and BCB. The inset shows the zoom of transfer curve on SiO_2. (b) Illustration of device structure and the chemical structure of BCB polymer and DDAB molecule used in this work. (c) Scheme of the mechanism of charge transport enhancement of InSe on SiO_2 and BCB.

7.3.2 Ionic molecular doping of InSe field effect transistor

Although the use of BCB dielectric largely improves the channel conductivity of InSe, the device is in OFF state at V_g=0 V. This raises a major concern in operating the photodetector with low power and the photocurrent value would be limited by the unfavourable charge injection from the metal contact. This problem can be overcome by lowering the Schottky barrier via doping. For 2D materials, molecular doping has become a most viable approach to tune the Fermi level of

semiconducting materials thanks to the large surface-to-volume ratio for physi(chemi)sorption.[127,186-188] Instead of employing the most common doping strategies of 2D materials based on aromatic molecules, we have focussed our attention to a well-established surfactant molecule, didodecyldimethylammonium bromide (DDAB), containing ionic moiety that can effectively interact with the surface of InSe. Transfer curves of InSe FET were measured after spin-coating the solution in TCE from 10^{-6} g/L to 1 g/L concentrations. **Figure 7.3** shows that the threshold voltage (V_{th}) shifts negatively with increasing concentrations. The output curve changes displayed in **Figure 7.2b-c**).

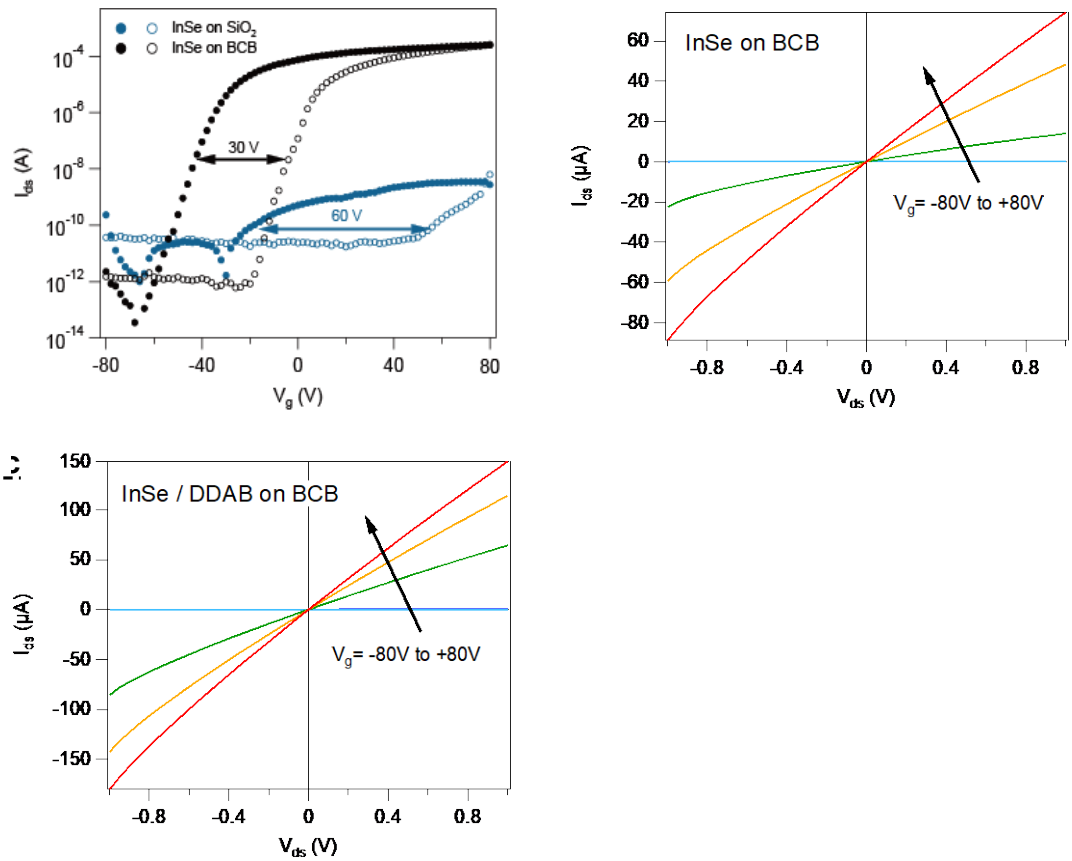

Figure 7.2: Current-voltage characteristics of InSe FETs. (a) Comparison of the hysteresis of InSe FET on SiO_2 and BCB. A decrease of 30V is observed after the dielectric engineering. The presence of 30V of hysteresis is attributed to the surface oxide of InSe in the chemical form of InO_x unintentionally introduced during the nanofabrication which acts as charge traps.[62,63,189,190] Gate –dependent output curves of InSe (b) before and (c) after doping with DDAB.

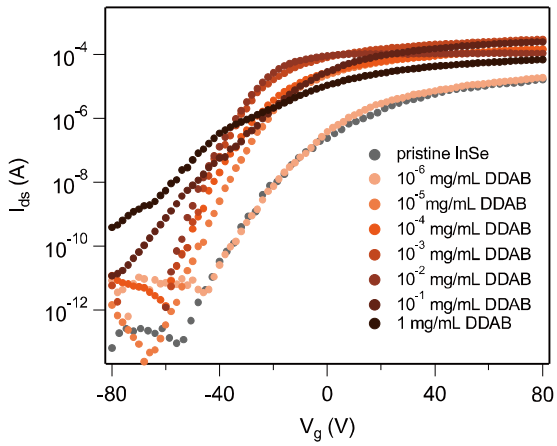

Figure 7.3: Transfer (V_g-I_{ds}) curve of InSe FET functionalized with DDAB with different concentration.

The maximum ΔV_{th} obtained within 25 devices with the highest concentration amounts to 42.58 V, corresponding to 1.7× 10^{12}/cm^2 of charge carrier density change, which was calculated through

$$\Delta n = \frac{C_{ox}\,\Delta V_{th}}{e} = \frac{\varepsilon_{ox}\,\Delta V_{th}}{t_{ox}\,e}$$

where Δn is the change in electron (negative charge) density, C_{ox} is the capacitance per unit area of 270 nm SiO_2, e is the elementary charge, and ε_{ox} is the dielectric constant, ΔV_{th} is the change of threshold voltage and t_{ox} is the thickness of dielectric. The V_{th} before molecular doping amounts to 8.29±17.74 V for SiO_2 and to 15.69±2.83 V for BCB. We exclude possible doping from the solvent after thermal annealing, which is ruled out in by means of the control experiment reported in **Figure 7.4** where the FET transfer curves indicates that, compared to the pristine device, the spin-coating of a 100 μL droplet of TCE determines a slightly n-doping of the InSe, with a large decrease in mobility. After a thermal annealing at 120 °C, the original state with barely no doping of the InSe is re-adopted.

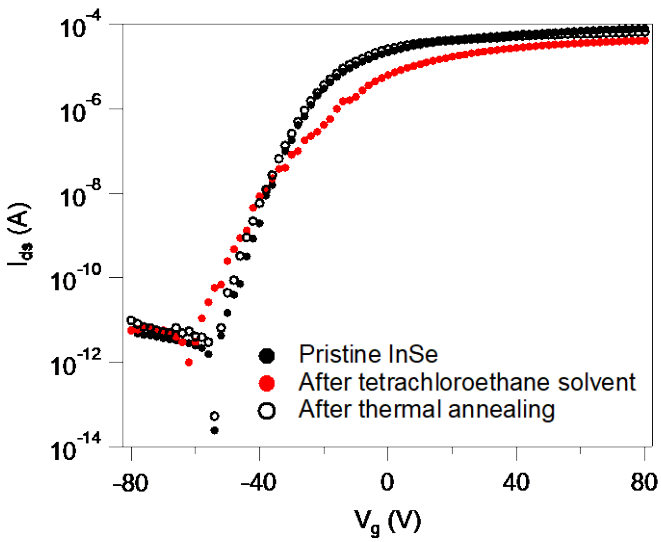

Figure 7.4: Control experiment with the solvent.

For 2D materials, molecular doping has become a most viable approach to tune the Fermi level of semiconducting materials thanks to the large surface-to-volume ratio, high chemical reactivity and sensitivity. The choice of molecules from the huge library of molecules to functionalize with specific 2D material is crucial. [161,191]Fermi level shift in 2D materials could be monitored by Kelvin probe force microscopy: **Figure 7.5a** shows the surface potential image of a 5.5 nm thick InSe flake before and after its functionalization with DDAB. [187,191] The profile in **Figure 7.5b** reveals that the molecular functionalization determines an increase in surface potential of 200 meV. The resulting work function φ obtained in InSe flake region calibrated with respect to $\varphi_{Pt/Ir}$ shows a decrease from 4.9 to 4.7 eV, indicating the Fermi level lifting towards the conduction band of InSe (**Figure 7.6**). Furthermore, **Figure 7.5a** provides evidence for a uniform magnitude in surface potential across the flake, denoting a homogeneous modulation of electronic properties of InSe upon DDAB functionalization.

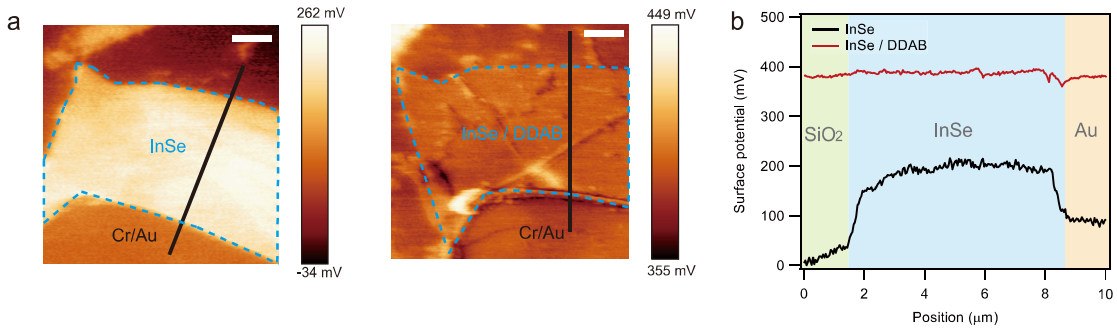

Figure 7.5: (a) Surface potential measured by Kelvin probe force microscopy (KPFM) of few-layer InSe of before and after functionalization with DDAB (scale bar: 3 μm) and (b) the corresponding line potential profile of marked in black line in (a).

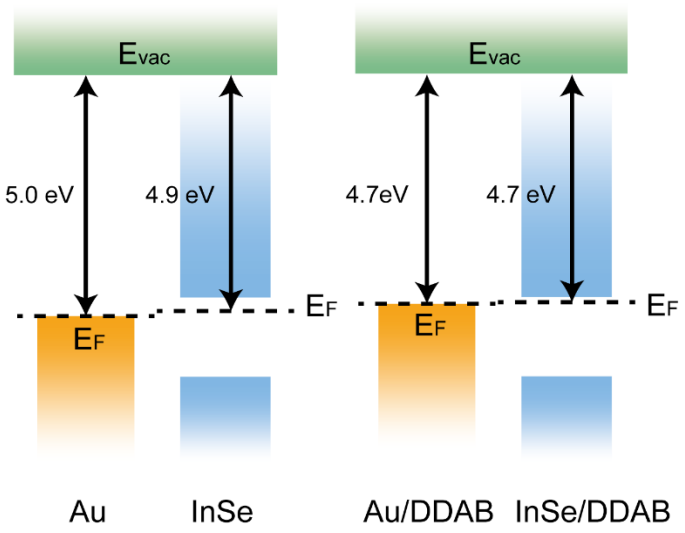

Figure 7.6: Illustration of Fermi level shift of InSe before and after functionalization with DDAB. Chromium (Cr) /gold (Au) electrode is fabricated as top electrode partially covering the flake for grounding where the chromium is the real contact metal material underneath and gold is a protective layer on top for chromium against oxidation. When spin-coating DDAB on the whole device, the surface of Cr/Au electrode is inevitability covered with the molecule. Given the high wok function of gold, DDAB could also induce doping effect on the electrode surface. Therefore, a decrease of work function after the molecular functionalization could be observed both on InSe and Cr/Au.

To fully interpret the origin of such strong doping induced by simple ionic surfactant such as DDAB, Density Functional Theory (DFT) calculations were performed to model the hybrid InSe/DDAB system. Since defects (e.g. Se vacancies) could be generated both during the synthesis of InSe crystal and the delamination by mechanical exfoliation, we considered InSe single layers in either the pristine form (dubbed 'InSe' in the following) or including 3% Se vacancies (InSe-3%SeV) (**Figure 7.7**).

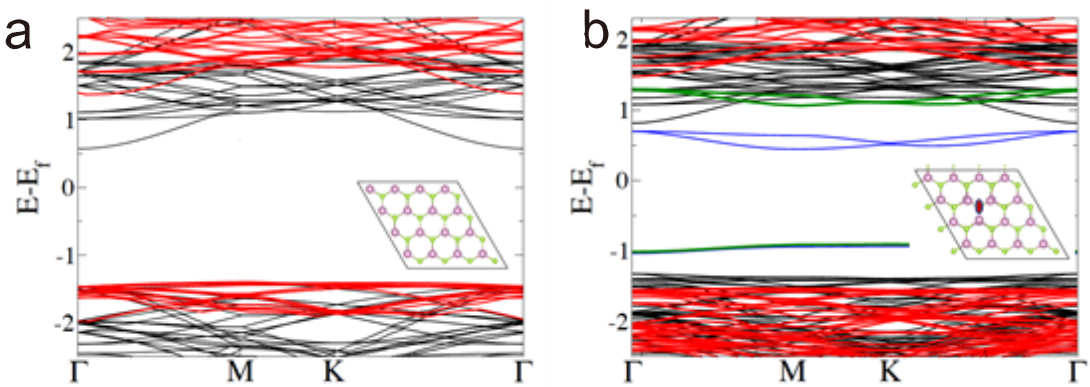

Figure 7.7: Electronic structure of InSe. Electronic band structure of (a) pristine and (b) defective (-3% Se vacancy) InSe monolayers, computed at the GGA/PBE (black) and HSE06 (red) levels. Mid-gap defect (one filled and two empty) states due to Se vacancy (**Figure7b**) are indicated in green (blue) for calculation at HSE06 (PBE/GGA) level. In (a) and (b), only few HSE06 bands (color: red) are shown close to valence band maximum (VBM) and conduction band minimum (CBM), for clarity. Fermi level (E_f) is set to the middle of electronic band gap obtained at HSE06 level of theory.

We explored two molecular conformations for adsorption, with conformation 1 (denoted as InSe (-3%SeV)/DDAB-1) and conformation 2 (denoted as InSe (-3%SeV)/DDAB-2) corresponding to the Br ion being far and close to the InSe surface, respectively (**Figure 7.8-7.12**).

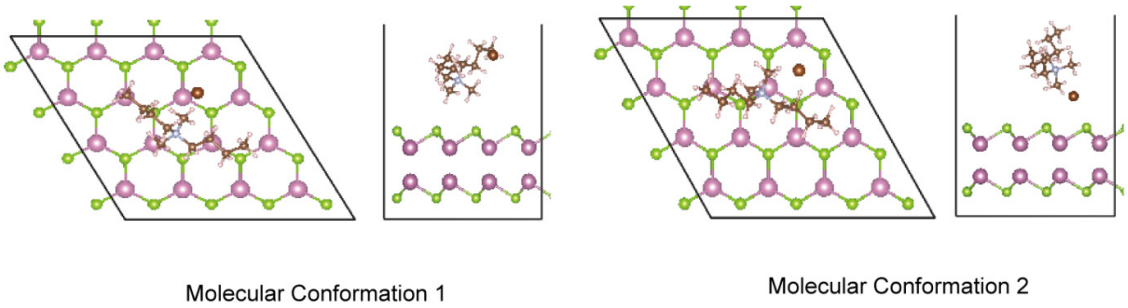

Figure 7.8: Schematic representation of DDAB physisorbed onto InSe in conformation 1 and conformation 2.

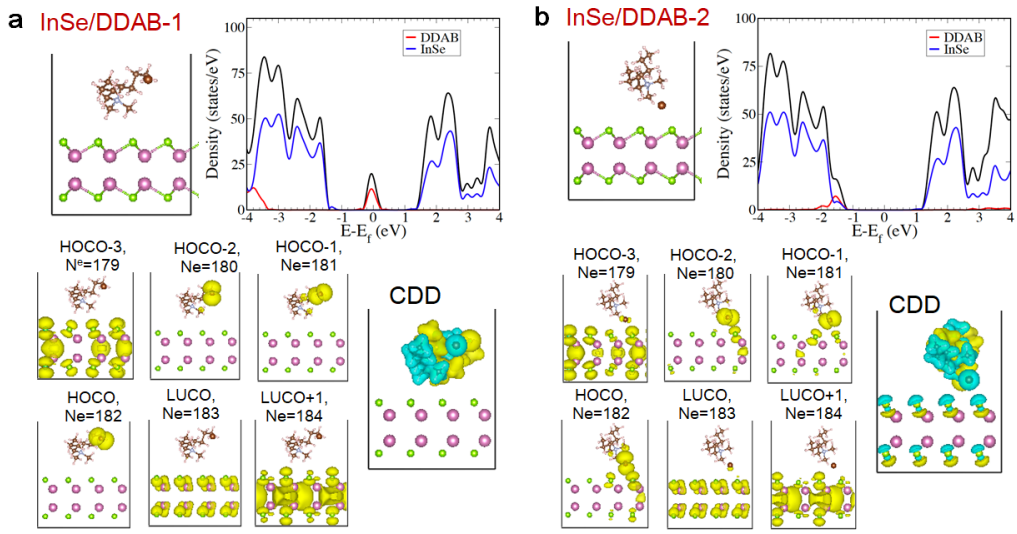

Figure 7.9: Atomic positions and electronic structure of InSe/DDAB heterostructures for DDAB adsorbed on pristine InSe surface. Atomic positions (optimized geometry) and electronic structure of InSe/DDAB heterostructures for DDAB adsorbed on pristine InSe surface when (a) Br atom is farther away from the basal plane of InSe: Conformation-1 and (b) Br atom is closer to the basal plane of InSe:

Conformation-2, along with their respective charge density difference (CDD) and partial Density of States (pDOS) plots, computed at the HSE06 level of theory. Electronic states pertaining to DDAB (in red as shown in pDOS), primarily localized on Br atom (left image: crystalline orbitals N_e=180 to N_e=182), appear within the InSe band gap for Conformation-1, whereas, in Conformation-2, these states interact with the InSe surface with a strong hybridization. More specifically, in Conformation-2, the DDAB (localized) electronic states interact with the electronic states pertaining of InSe surface in the vicinity of VBM (right image: crystalline orbitals N_e=180 to N_e=182). Fermi level (E_f) is set to the middle of electronic band gap obtained at HSE06 level of theory. HOCO and LUCO correspond to highest occupied crystalline orbital and lowest un-occupied crystalline orbitals, respectively.

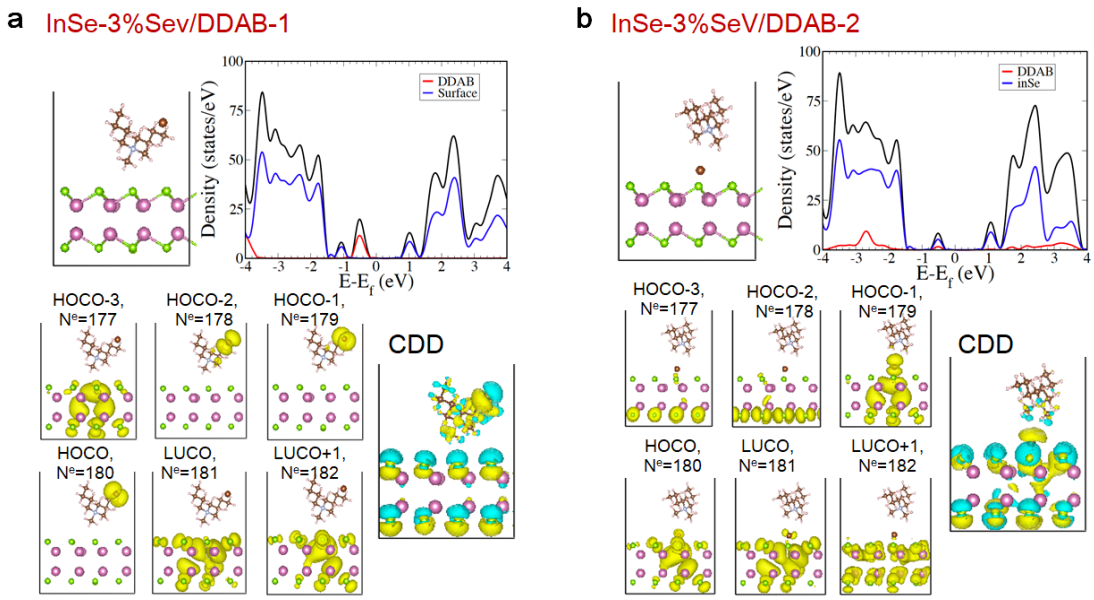

Figure 7.10: Atomic positions and electronic structure of InSe-3%SeV/DDAB heterostructures for DDAB adsorbed on defective InSe (-3% Se vacancy) surface. Atomic positions (optimized geometry) and electronic structure of InSe-3%SeV/DDAB heterostructures for DDAB adsorbed on defective InSe (-3% Se vacancy) surface when (a) Br atom is farther away from the basal plane of defective InSe: Conformation-1 and (b) Br atom is closer to the basal plane of defective InSe: Conformation-2, along with their respective charge density difference (CDD) and partial Density of States (pDOS) plots, computed at the HSE06 level of theory. Electronic states pertaining to DDAB (in red as shown in pDOS), primarily localized on Br atom (left image: crystalline orbitals N_e=178 to N_e=180), appear within the InSe band gap for Conformation-1 and does not show any noticeable interaction with the mid-gap defect states (in blue – within the band gap, as shown in pDOS), whereas, in Conformation-2, these (localized) states interact with the InSe surface with a strong hybridization. More specifically, in

Conformation-2, these DDAB (localized) electronic states show strong and explicit interaction with the mid-gap defect states formed due to Se vacancy in defective InSe surface (right image: crystalline orbitals N_e=178 to N_e=180). Fermi level (E_f) is set to the middle of electronic band gap obtained at HSE06 level of theory. HOCO and LUCO correspond to highest occupied crystalline orbital and lowest un-occupied crystalline orbitals, respectively.

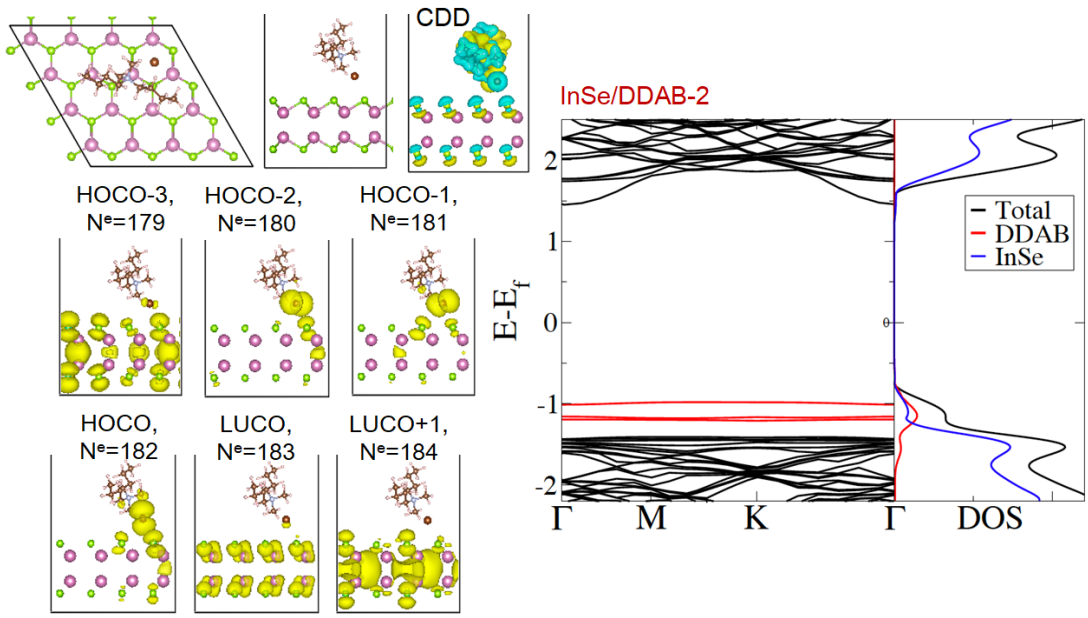

Figure 7.11: Detailed atomic positions and electronic bands of DDAB adsorbed onto pristine InSe. Atomic positions with optimized geometry, pertaining to Config2: InSe/DDAB-2 heterostructure, wherein DDAB is adsorbed atop pristine InSe monolayer with Br- atom closer to surface, along with the charge density difference (CDD) plots (top-left); Electronic band structure (right) of InSe/DDAB:2 heterostructure is presented along the pDOS plot, computed at the HSE06 level of theory. Energetic states due to DDAB molecule (dominantly localized on Br atom) are close to the VBM of pristine InSE monolayer, as indicated in red. Crystalline orbitals are shown left – middle & bottom, including the states localized on DDAB (N_e =180 to 181), demonstrates the interaction of DDAB molecule with InSe monolayer. HOCO and LUCO correspond to highest occupied crystalline orbital and lowest un-occupied crystalline orbitals, respectively. The molecular orbitals are also labeled with the corresponding band number (N_e, for a total of 364 electrons in the heterostructure), to easy the connection between electronic band structure and molecular orbitals. Fermi level (E_f) is set to the middle of electronic band gap obtained at HSE06 level of theory.

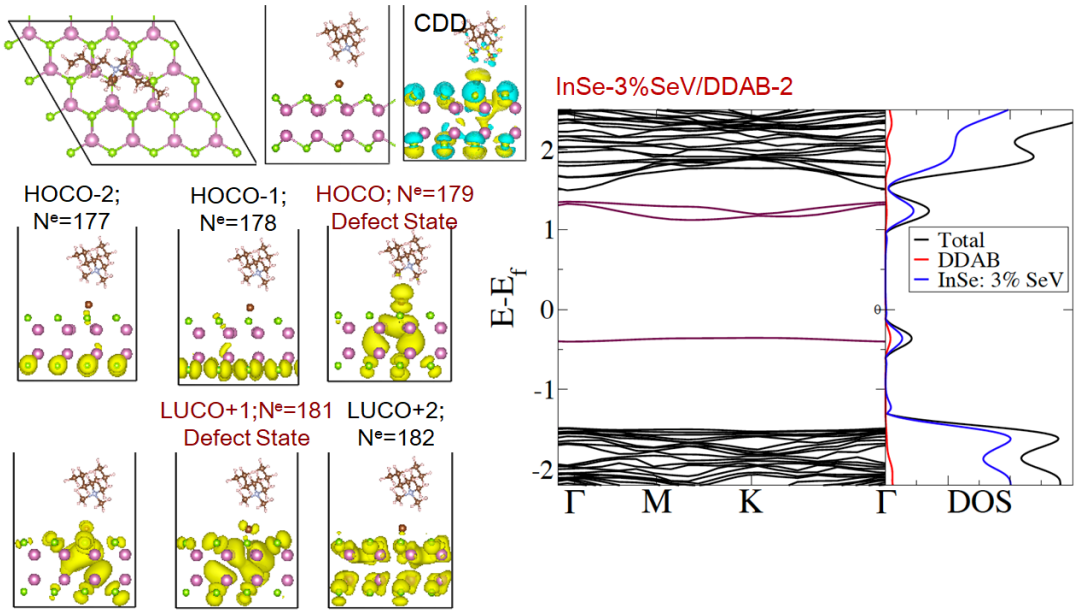

Figure 7.12: Detailed atomic positions of DDAB adsorbed on InSe-3%SeV. Atomic positions with optimized geometry, pertaining to Config2: InSe-3%SeV/DDAB-2 heterostructure, wherein DDAB is adsorbed atop defective (-3% Se vacancy) InSe monolayer with Br- atom closer to surface, along with the charge density difference (CDD) plots (top-left); Electronic band structure (right) of InSe-3%SeV/DDAB:2 heterostructure is presented along the pDOS plot, computed at the HSE06 level of theory. A strong interaction of the DDAB energetic states (dominantly localized on Br atom) with the mid-gap defect states formed due to Se vacancy is observed. The interaction is particularly strong with the localized mid-gap defect states, formed by the Se vacancies in InSe monolayer, that are close to the VBM (as represented by crystalline orbital: represented by HOCO: N_e=179) and also to those close to CBM (as represented by crystalline orbital: represented by LUMO: N_e=180 & LUMO+1: N_e=181). HOCO and LUCO correspond to highest occupied crystalline orbital and lowest un-occupied crystalline orbitals, respectively. The molecular orbitals are also labeled with the corresponding band number (N_e, for a total of 358 electrons in the heterostructure), to easy the connection between electronic band structure and molecular orbitals. Mid-gap defect states in the electronic band structures (interacting with DDAB) are represented in (dark) red. Fermi level (E_f) is set to the middle of electronic band gap obtained at HSE06 level of theory.

The resulting calculated work functions are listed in **Table 7.1**. We find that functionalization with DDAB molecules determines a work function decrease by 0.09 eV (pristine InSe) and 0.13 eV (defective InSe) in conformation 1, while the corresponding values in conformation 2 are 0.43 eV (pristine InSe) and 0.53 eV (defective InSe). The shifts in work function calculated for the two conformations are in line with the experimental values and result from the combined effect of a

partial charge transfer from the molecule to the surface (n-doping) together with a dipolar contribution (of obviously opposite signs in the two conformations considered).

System	Work function φ (eV)	Bader charge transfer (e)	Dipole moment (Debye)	Adsorption energy E_{ads} (kcal/ mol)
InSe	5.21	-na-	0.00	-na-
InSe/DDAB-1	5.12	0.10	+0.81	-14.03
InSe/DDAB-2	4.78	0.12	-1.86	-18.45
InSe-3%SeV	4.87	-na-	-0.07	-na-
InSe-3%SeV/DDAB-1	4.74	0.14	+0.63	-11.73
InSe-3%SeV/DDAB-2	4.34	0.20	-3.31	-19.55

Table 7.1: Summary of DFT calculated work function, Bader charge transfer, molecular dipole moment and adsorption energy of InSe and defective InSe functionalized with DDAB.

In contrast to successive enhancement of n-doping with the increased concentration of the spin-coated molecular solution concentration, the field-effect mobility does not exhibit significant changes up to 1g/L of molecular functionalization (**Figure 7.13**). Since the electron mobility in 2D semiconductors is largely limited by Coulomb impurity scattering, a molecular coating could serve as encapsulation to screen charge impurities. [192] High-resolution atomic force microscopy (AFM) imaging in tapping mode was performed to study the surface morphology of InSe/DDAB hybrid. It revealed that DDAB forms semi-spherical micelle based film on the surface of InSe (**Figure 7.14**), whereas the same surfactant molecules tend to form self-assembled layers on flat surfaces (e.g. HOPG).[100,193]. Upon increasing the molecular concentration, the discontinuous molecular film tends to reduce the roughness until a uniform layer is formed on the surface (**Figure 7.15)**. The full coverage was obtained when using a 1 g/L solution thereby creating an encapsulating layer which isolates the 2D material from the environment. Under such conditions, a 2.5-fold enhancement in the carrier mobility was observed when compared to unfunctionalized material, by leveraging the electron mobility from 473.5 ± 158.87 cm^2/Vs to 897.5 ± 368.9 cm^2/Vs (with a channel length/width ratio of all FETs corresponding to ca. 1). Higher concentration of DDAB (>10 g/L) have also been tried to functionalize the film. Yet the higher concentration leads to the undesired coating on the top-contacted electrode, rendering it complicated to contact the electrodes with the probes for reliable electrical measurements. This thin layer of molecules is proved not to serve as efficient encapsulation against degradation in air, given the charged nature

of the molecules that brings into play some repulsion forces between adjacent molecules hindering a close packing. Nevertheless, surface impurity scattering is not the only factor that limits efficient charge carrier transport. Taking into account the Schottky barrier at the interface between chromium and InSe, the carrier transport could be largely limited by the strong Fermi level pinning at the metal / 2D material contact.[194] Therefore, we conducted 4-terminal measurement to extract the intrinsic conductance in the InSe channel. In **Figure 7.15**, two-terminal and four-terminal measurements of both InSe and InSe/DDAB are compared. In all devices the four-terminal field-effect mobility is 1.7 to 4.5 times higher than two-terminal mobility. For DDAB functionalized InSe, electron mobility values in four-probe measurements are all above 10^3 cm^2/Vs with the highest value reaching 2785 cm^2/Vs. Upon DDAB functionalization the calculated contact resistance R_c drops from 48.98 ± 10.89 kΩ to 5.38±0.12 kΩ, thereby attaining a comparable value to low-contact-resistance graphene and Indium contact.[6,65] This indicates that the DDAB functionalization does not merely occur only the top surface of the 2D material, but the potential barrier between Cr and InSe has also been tremendously decreased because of the Fermi level shift..

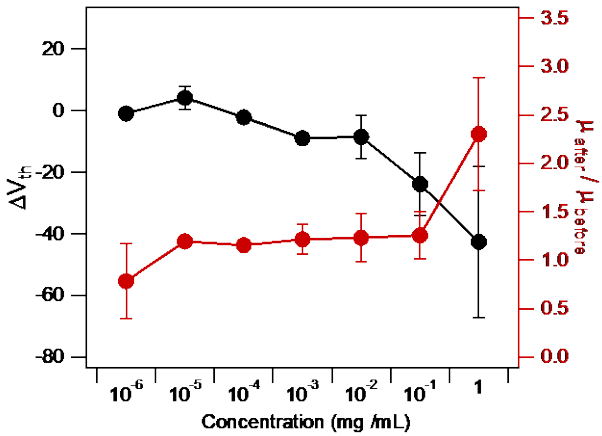

Figure 7.13: Analysis of threshold voltage (V_{th}) and field-effect mobility (μ) change of InSe FET as a result of the functionalization with different concentrations of DDAB.

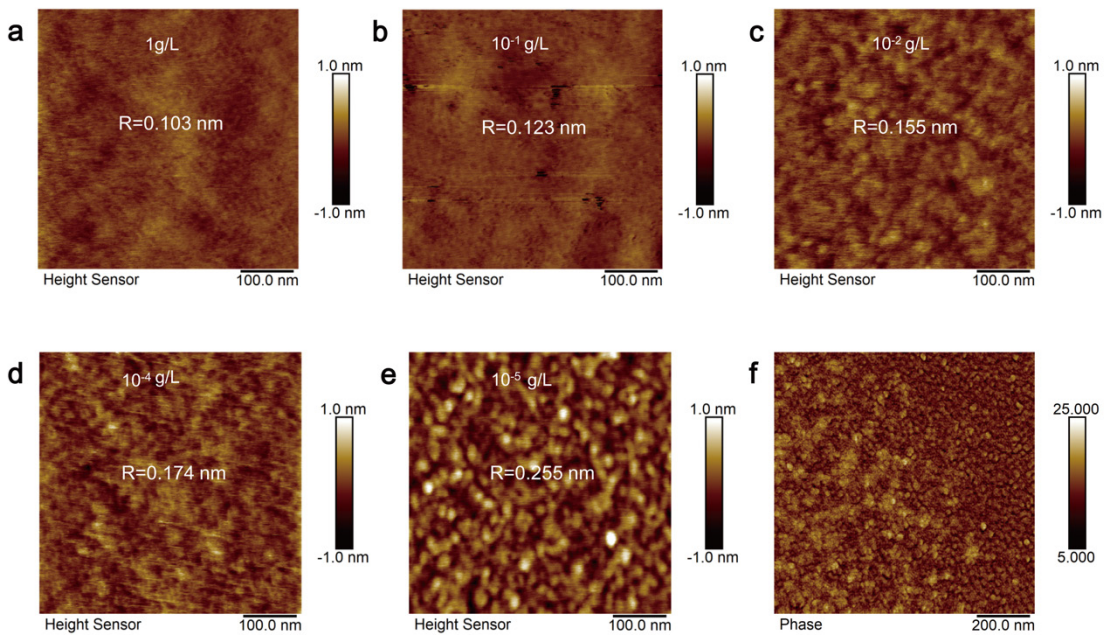

Figure 7.14: AFM images of DDAB on InSe. High resolution AFM height image of InSe functionalized by spin-coating a solution of DDAB molecule in tetrachloroethane (TCE) of the following concentrations (a) 1 g/L; (b) 10^{-1} g/L; (c) 10^{-2} g/L; (d) 10^{-4} g/L; (e) 10^{-5} g/L. (f) AFM phase image of InSe functionalized via spin-coating a 10^{-5} g/L solution of DDAB.

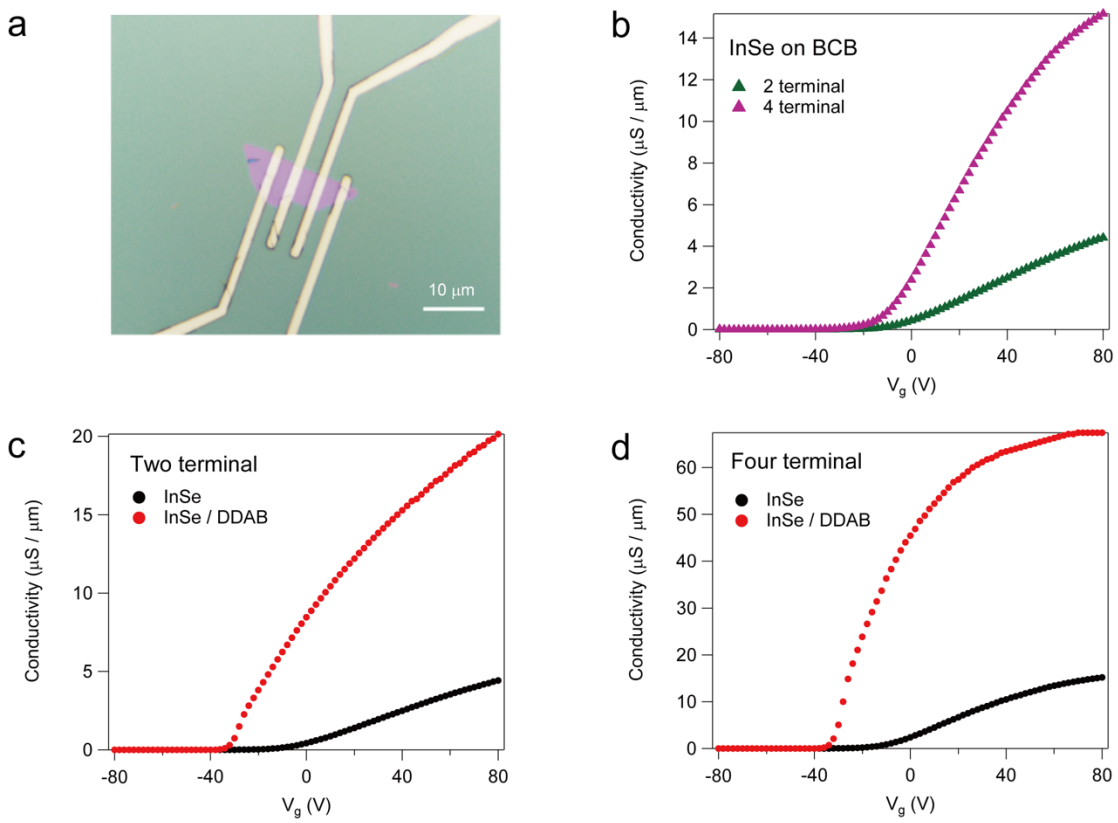

Figure 7.15. Four-terminal measurement of InSe with Cr/ Au contact. (a) Optical image of few-layer InSe device with four terminals. The gap between two adjacent terminals amount to 3.5 m. (b) Typical comparison of gate-dependent conductance of two-terminal and four-terminal measurements at V_{ds}=1V. (c)-(d) Comparison of gate-dependent conductance of InSe and InSe/DDAB obtained from (c) two-terminal and (d) four terminal measurements.

Alongside the DDAB effect on the electrical properties of InSe, we also observed major changes in the optical properties. While Raman modes of InSe (**Figure 7.16e**) have not revealed major changes upon functionalization with DDAB, indicating that the molecular functionalization does not modify the crystal structure of the 2D material, a strong modulation of photoluminescence (PL) spectra have been monitored. As is demonstrated in **Figure 7.16a**, the PL intensity on BCB has largely been magnified comparing to SiO_2. The bandwidth has also largely decreased to Lorenztian distribution, indicating smaller charge scattering from the interface between the 2D InSe and the substrate. While by functionalizing with DDAB, a quenching and a 0.8 eV redshift (**Figure 7.16b-d**) is observed. The variations in PL are in line with previous observations in other n-type 2D materials, such as MoS_2.[32] The physical meaning of the phenomenon is difficult to be addressed due to instrumental limitations, while comparing to the PL of monolayer MoS_2, which is also an n-type 2D simoconductor, PL quenching and redshift is very often to be observed when the material is strongly n-doped. (Detailed information see

Chapter 8). Therefore, the phenomenon might be originated from the strong n-doping of DDAB of InSe.

We have cross-checked the success of functionalization by measuring the XPS where no obvious shift was observed in In 3d and Se 3d peak because of the bulk materials in a macroscopic area of measurement (while the devices are based on isolated few-layer flakes), with the spot size being 400mm. However, the Br 3d peak appeared obviously after the functionalization with DDAB, indicating the stability of Br ion on InSe. (**Figure 7.16f-h**)

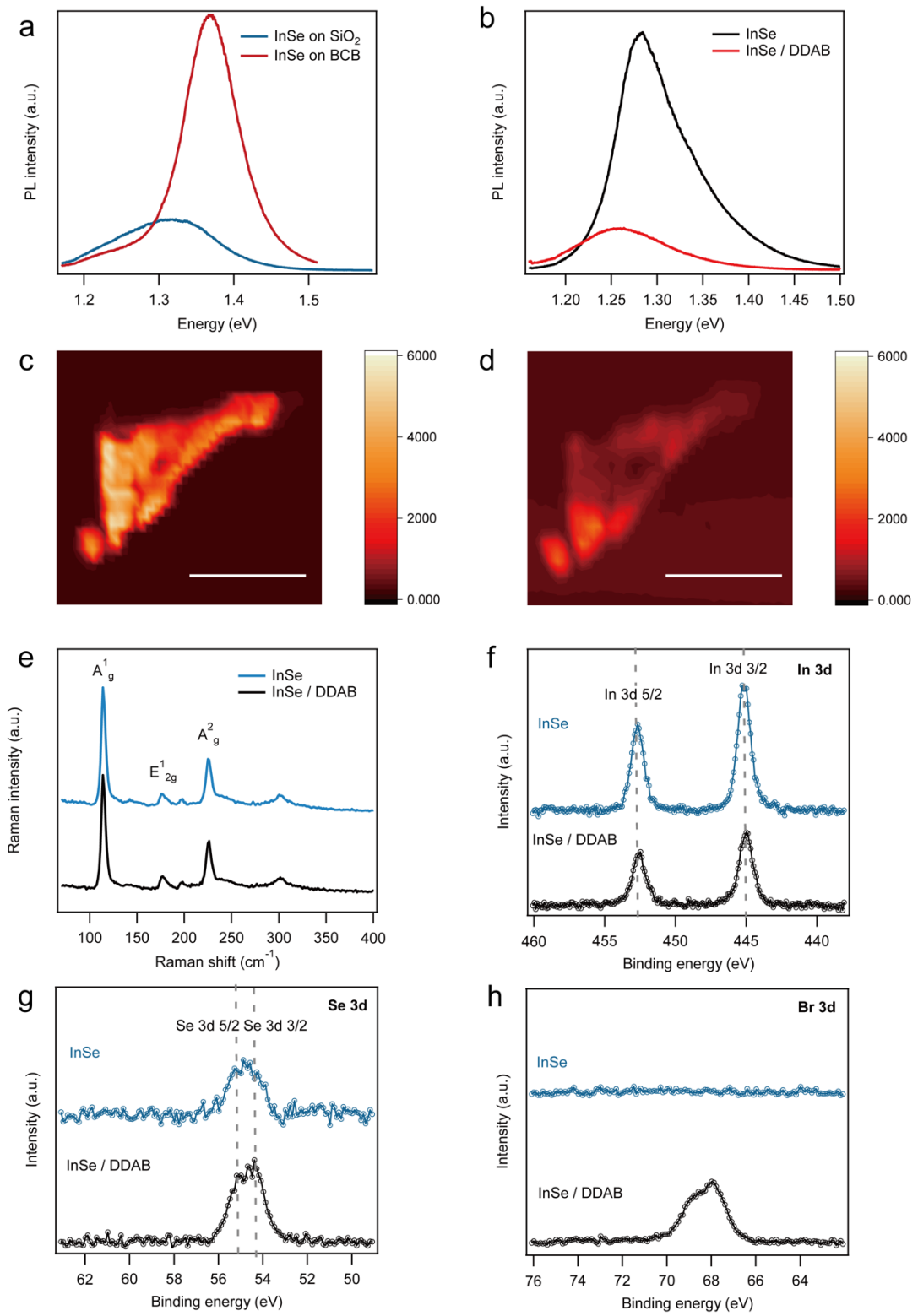

Figure 7.16: Spectroscopic characterization of functionalized InSe. (a) Photoluminescence spectra of InSe on SiO_2 and BCB substrate. (b) Photoluminescence spectra of InSe without and with DDAB functionalization. PL mapping of InSe (c) before and (d) after functionalization with DDAB. The scale bar is 10 μm. e, Raman spectra of InSe and InSe/DDAB. High resolution XPS spectra of (f) In 3d, (g) Se 3d, and (h) Br 3d of InSe and InSe/DDAB.

7.3.3 Molecular functionalized InSe field-effect phototransistor (photoFET)

Phototransistors are one among the most investigated device structures for 2D photodetectors. Their architectures are identical to bottom-gate top-contact FET, as displayed in **Figure 7.1b**. **Figure 7.17a-c** shows the gate-dependent photoresponse of InSe on SiO_2, BCB and InSe/DDAB on BCB. A prominent selective photodetection of UV light (365 nm) is observed for both InSe on SiO_2 and BCB. For phototransistor on SiO_2, even at highly gated region, the measured photocurrent is only in sub-microampere scale with I_{on}/I_{off} around 10^3. The modification of the dielectric layer with BCB leads to an efficient suppression of the undesired recombination from charge traps located at InSe/dielectric interface, thus enhancing the I_{on}/I_{off} ratio up to 10^6 (**Figure 7.17b**). The photoresponse rise /decay time has also significantly shortened from 288/447 ms on SiO_2 (**Figure 7.17d**) to 17.33/16.76 ms on BCB (**Figure 7.17e**). Nevertheless, the photoresponse is still limited by the existence of Se vacancies which could act as traps for photo-generated charge carriers. To minimize such effect, we functionalized the InSe channel with DDAB, by exploiting the propensity of the latter compound to stably adsorb on the Se vacancy sites. The healing of Se vacancies by DDAB could help to restore the crystal structure thereby suppressing the recombination of the photo-generated charges in vacancy traps. **Figure 7.17c** provides distinct evidence that such functionalization yields a higher photoresponse. Such enhancement can be ascribed not only to the contribution of Se vacancy healing, but also to the molecular doping induced shift of the V_{th} in InSe FET drawing the device to ON state at V_g=0V which would otherwise be realized by applying a large electrical gate up to 80V.[68,70,168,195]

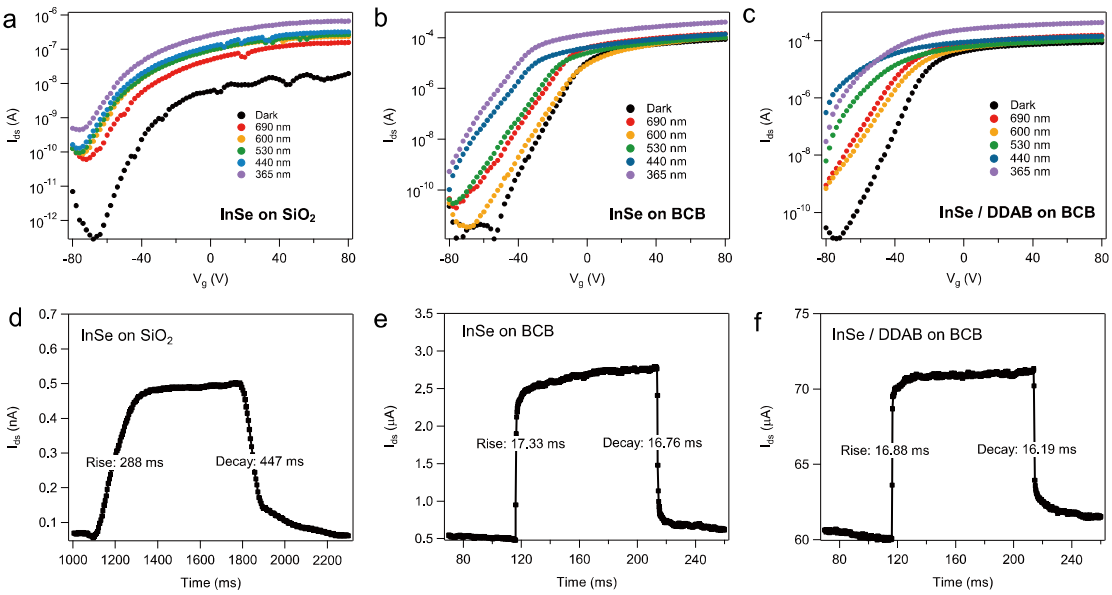

Figure 7.17: I_{ds}-V_g curve of (a) InSe on SiO_2, (b) InSe on BCB and (c) InSe/DDAB on BCB at V_g=0V and V_{ds}=1V. Time-resolved photoresponse of (d) InSe on SiO_2, (e) InSe on BCB and (f) InSe/DDAB on BCB under the illumination of 365 nm at 34.3 mW/cm^2.

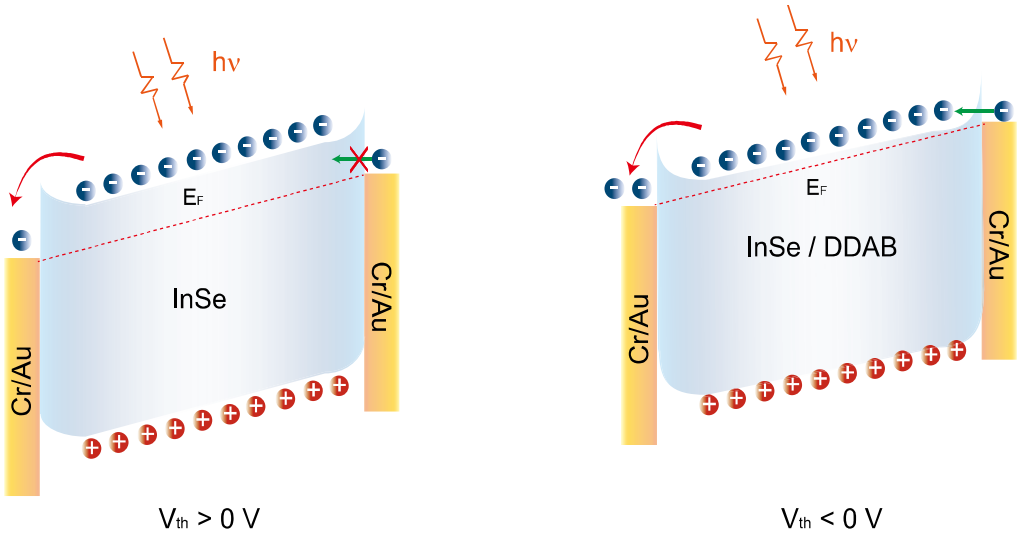

Figure 7.18: Band diagram of InSe photoFET before and after functionalization with DDAB at V_g=0V.

Therefore, with zero contribution from the gate bias, the barrier from the contact is low enough for the photocurrent to tunnel through effectively (**Figure 7.18**). Combining these two factors, we have obtained a reasonably high photocurrent of 12 μA by simply applying 1V of bias voltage in total (**Figure 7.17f**). The device performance is proved to be stable within light pulse cycles and reproducible among different devices (**Figure 7.19 and Figure 7.20**).

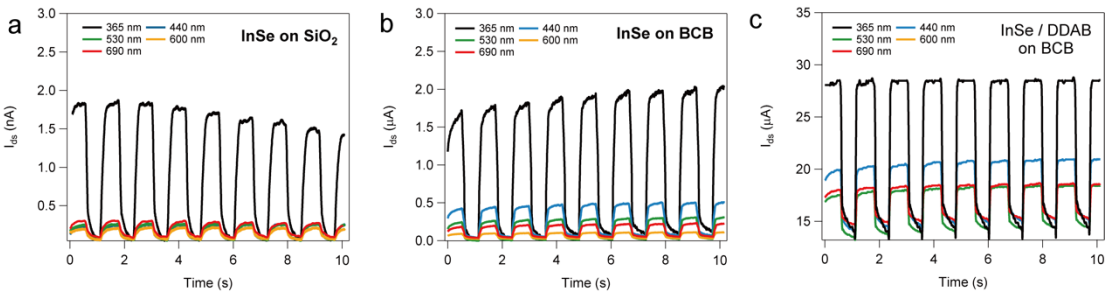

Figure 7.19: Time-resolved photoresponse cycles. Photoresponse curves of different wavelength of (a) InSe on SiO_2, (b) InSe on BCB, (c) InSe/DDAB on BCB. The incident light power is adjusted to 34.3 mW/cm^2 for each wavelength.

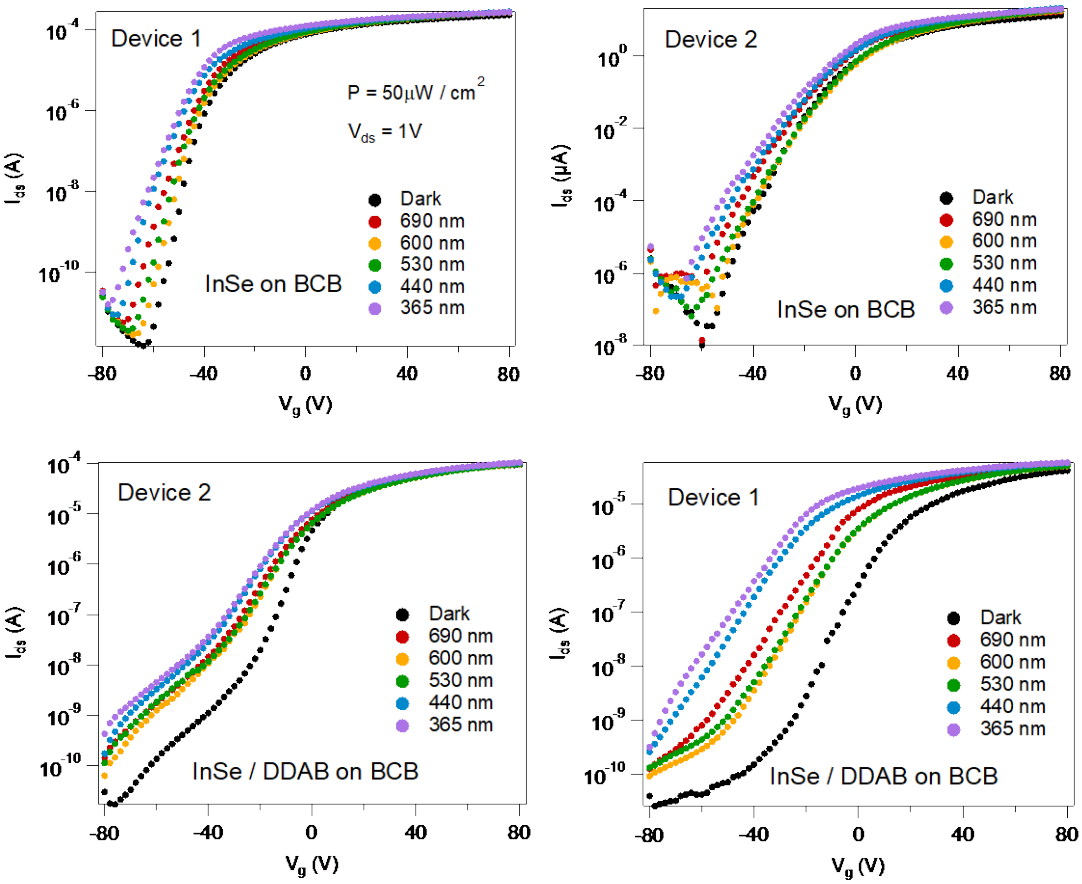

Figure 7.20: Photoresponse of two others representative InSe photoFETs before and after doping with DDAB. All devices yield statistically similar behavior upon molecular doping and photoresponse, including the devices shown in **Figure 7.17**.

Responsivity (R) of incident wavelength λ is a key parameter to evaluate photocurrent generation of photodetectors which is calculated according to the following equation:

$$R_\lambda = \frac{I_{ph}}{PS}$$

where I_{ph} is the photocurrent obtained from the difference between light current I_{light} and dark current I_{dark}, P is the incident light power density, and S is the active illuminated area.

The spectral photoresponse of incident light from 300 nm to 690 nm for InSe on SiO_2, InSe on BCB and InSe/DDAB in **Figure 7.21** reveals a single photodetective band from 300 nm to 400 nm. An exponential enhancement of 10^6 from SiO_2 to BCB as dielectric is observed. Upon functionalization with DDAB, R reaches 10^5 A/W.

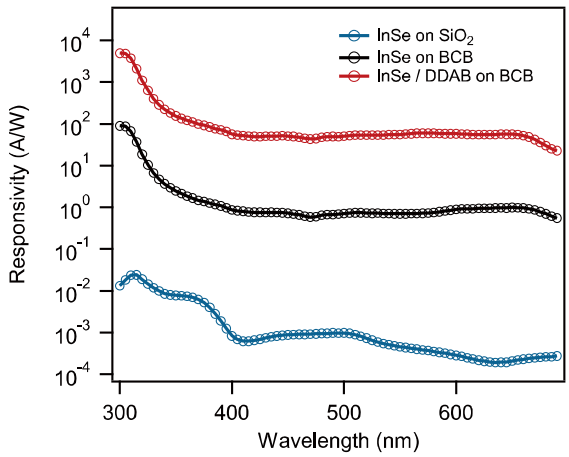

Figure 7.21: Calculated responsivity with of wavelength scan from 300 nm to 690 nm at high incident light power (34.3 mW/cm^2 for 365 nm light). The interval of wavelength is 5 nm.

Due to equipment limitation, the photocurrent values in **Figure 7.21** measured for different wavelengths correspond to difference incident power densities. The raw power densities and measured photocurrent could be found in **Figure 7.22a** to **c**. Another important parameter, external quantum efficiency (EQE) representing the efficiency of charge carrier collected per single absorbed photon., has been calculated as follows:

$$EQE = \frac{N_c}{N_I} = \frac{R_\lambda hc}{e\lambda}$$

where N_c is the collected number of charge carriers in photocurrent , N_I is the number of incident photons illuminated on the device, h is the Plank constant, c is the light speed and e is elementary charge of electron. EQE for representative wavelength is listed in **Figure 7.22d** and **e**. It showed values below 1% for InSe on SiO_2. For InSe on BCB, the EQE exceeded 8×10^5% for red light and 3×10^6 % for UV light. Along with an increase of responsivity upon the molecular functionalization, InSe/DDAB displayed an EQE as high as 1.3×10^7 % for 365 nm illumination, at light power of 50 μW/cm^2. **Figure 7.22e** shows the specific detectivity (D^*) at different wavelengths and light powers.Detectivity (D^*) could be deduced from $D^* = S^{0.5}R_\lambda/S_n$, where S_n is the noise spectral density of the current which equals to $S_n = \sqrt{S_{shot} + S_{thermal} + S_{1/f}}$. S_{shot} is the shot noise, $S_{thermal}$is the thermal noise and $S_{1/f}$ is low frequency noise. Considering the shot noise to be the major contribution to noise, D^* could be estimated as $D^* \approx \frac{R_\lambda}{\sqrt{\frac{2eI_{dark}}{S}}}$. It revealed that detectivity is selective in the UV region,with 10-fold larger values compared to other wavelengths.Moreover,the dielectric engineering also induces significant improvement in D^*,with an increase from 108 to 1011 Jones for SiO2 and BCB,respectively.The functionalization with DDAB n-dopes InSe,resulting in larger dark current.However,as the responsivity has evidenced a much larger improvement, determining a slight improvement of D^* from 10^{11} Jones

to10^{12} Jones.

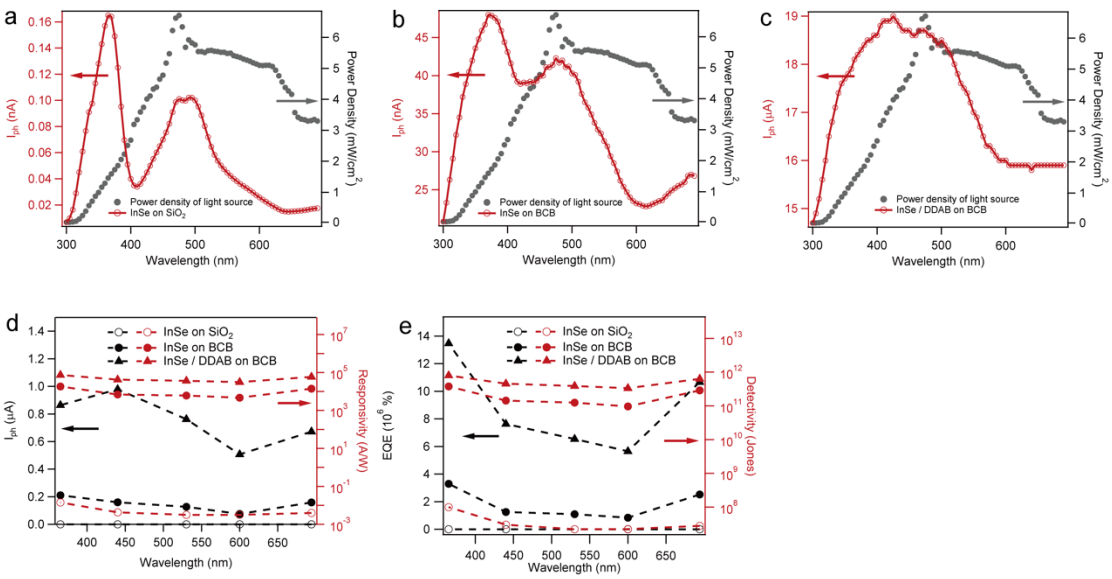

Figure 7.22: Wavelength-dependent photodetection of InSe PhotoFET. Spectral photocurrent and incident light power density of (a) InSe on SiO_2, (b) InSe on BCB, and (c) InSe/DDAB on BCB obtained from wavelength scan from 300 nm to 690 nm at V_g=0V and V_{ds}=1V. The incident light power is adjusted to 34.3 mW/cm^2 for each wavelength. Wavelength dependence of (d) photocurrent and responsivity and (e) EQE% and detectivity of InSe on SiO_2, InSe on BCB and InSe/DDAB on BCB at V_g=0V and V_{ds}=1V. The power for each wavelength is fixed at 5μW/cm^2.

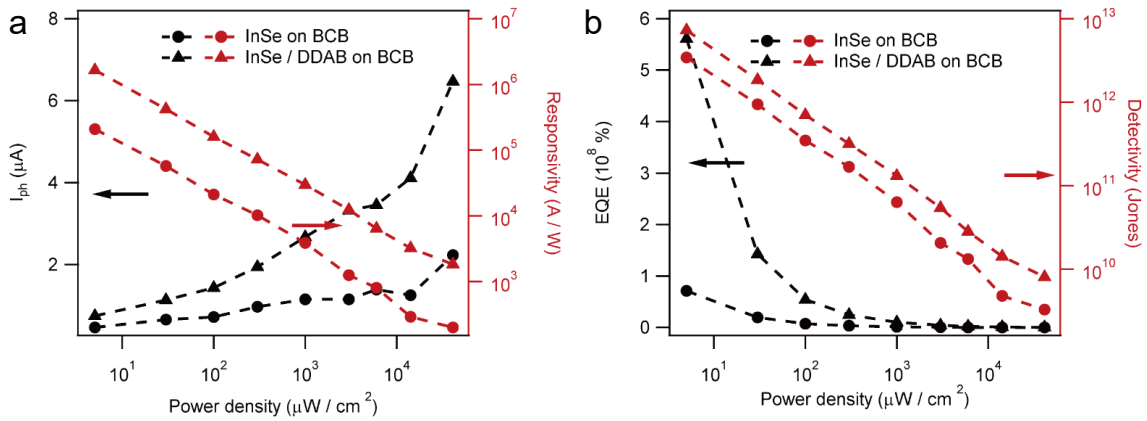

Figure 7.23: Power dependence of (a) photocurrent and responsivity and (b) EQE and detectivity of InSe on SiO_2, InSe on BCB and InSe/DDAB on BCB at V_g=0V and V_{ds}=1V illuminated with 365 nm light.

Figure 7.23 portrays the photoresponsive characteristics with respect to incident light power intensity (P) of 365 nm for InSe and InSe/DDAB. The photocurrent was found to scale linearity with light power density, complying $I_{ph} \propto P^{\alpha}$. The linearity factor α is calculated to be 0.448 for InSe and 0.658 for InSe/DDAB, implying a reduction of traps.[63] The time-dependent photoresponse at variable power density is displayed in **Figure 7.24**. In pristine InSe devices, the R and EQE in the low power region (5 μW/cm^2) have reached values of 2×10^5 A/W and 7×10^7 %, respectively, indicating an ultra-sensitive photodetection for low-power light. The DDAB functionalization enhances R up to 1×10^{6}A/W and EQE to 5×10^8 %.

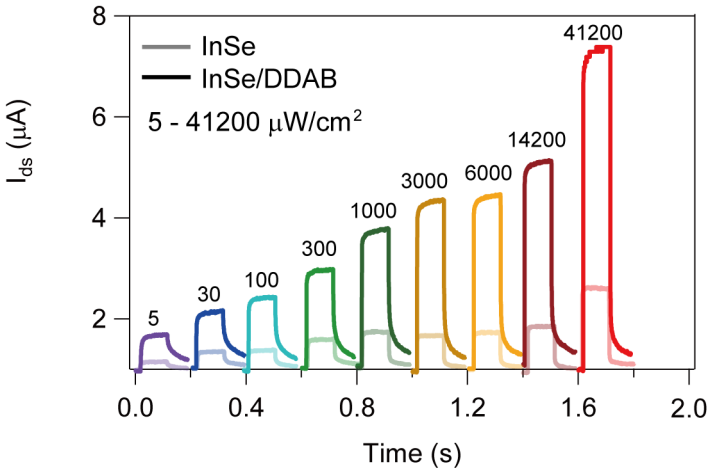

Figure 7.24: Time-dependent photoresponse of power density ranging from 5 μW/cm^2 to 41.2 mW/cm^2 of InSe and InSe/DDAB on BCB.

Secondly, D^* quantifies the signal to noise ratio of a given photodetection area. Power dependent detectivity of InSe and InSe/DDAB is plotted in **Figure 7.23b** ranging from 10^9 to 10^{12} for InSe. After functionalization with DDAB, the highest detectivity values reach ~10^{13} Jones for 5 μW irradiations. Overall, compared to previously reported 2D photodetectors, our molecularly functionalized phototransistors operating with ultra-low voltages (V_g=0V, V_{ds}=1V) have displayed extremely high responsivity up to 10^6 A/W, EQE approaching 10^8 %, and detectivity of 10^{13} Jones in the 300 to 690 nm wavelength region.

Photoresponse time of low-power incident light is also a critical factor to evaluate a photodetector. InSe and InSe/DDAB phototransistors have all exhibited ultra-fast time response for low-power (50μW/cm^2, **Figure 7.25**) illumination reaching a response time of 4.9 ms.

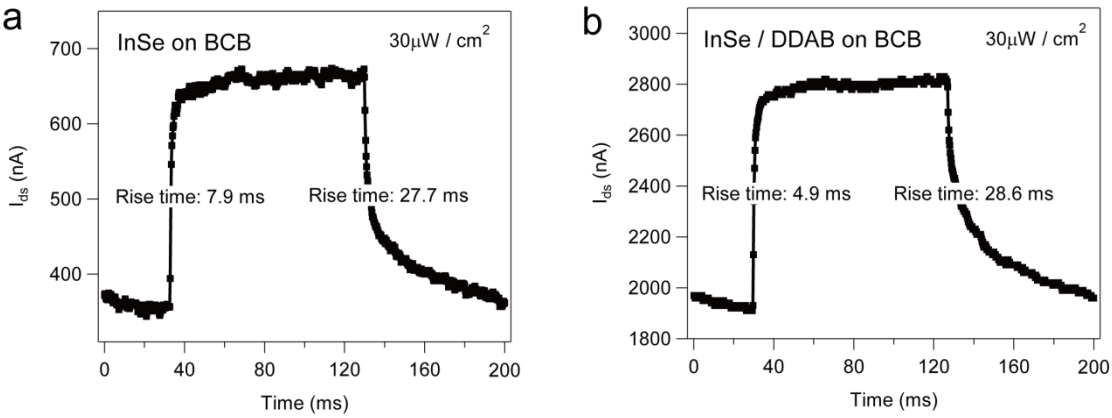

Figure 7.25: Time response of low-power light illumination. Photoresponse at 365 nm of (a) InSe on BCB, and (b) InSe/DDAB on BCB.

In order to explore the photogating effect, we have also calculated the photoconductive gain (G) which is expressed as

$$G = \frac{\tau_{life}}{\tau_{transit}}$$

where τ_{life} is the lifetime of photocarriers and $\tau_{transit}$ is the timescale of free carrier drifting in the photodetector channel. The τ_{life} is equivalent to the decay time of photocurrent and $\tau_{transit}$ is able to be calculated by

$$\tau_{transit} = \frac{{L_{ch}}^2}{\mu V_{ds}}$$

where L_{ch} is the channel length, μ is the carrier mobility at V_g = 0V and V_{ds} is the drain-source voltage. Here,for a specific device analysed, we take L_{ch} equals to 10 μm,20 μm and 10 μm for InSe on SiO_2, InSe on BCB, and InSe/DDAB on BCB respectively. The V_{ds} corresponds to 1V.

Wavelength (nm)	$\tau_{transit}$ **(ns)**			**Gain**		
	InSe on SiO_2	InSe on BCB	InSe/DDAB on BCB	InSe on SiO_2	InSe on BCB	InSe/DDAB on BCB
690	4038.77	27.45	2.58	1.11×10^5	6.10×10^5	6.27×10^6
600	2217.29	28.67	3.68	2.02×10^5	5.85×10^5	4.40×10^6
530	2235.14	36.26	4.56	2.00×10^5	4.62×10^5	3.55×10^6
440	1780.31	29.63	3.71	2.51×10^5	5.66×10^5	4.37×10^6
365	876.42	10.61	1.12	5.10×10^5	1.58×10^6	1.44×10^7

Table 7.2: Calculated $\tau_{transit}$ and gain for different wavelength.

The resulting gain values in **Table 7.2** are in agreement with experimental observations with EQE attaining 10^6 for InSe and 10^7 for InSe/DDAB, justifying a limited photogating effect which leads to much higher theoretical gain.[196,197]

7.3.4 Molecular functionalized InSe asymmetric Schottky junction

Photodetectors based on 2D lateral p-n junctions have been realized by either controlling the semiconducting channel region by selective doping, or by manipulating the electron/hole injection through the use of asymmetric metal contact.[75,98,139,198-200] Here we adopt both strategies to realize high performance lateral p-n junction based on multi-layer InSe by chemical doping with DDAB. The device structure is shown in **Figure 7.26**.

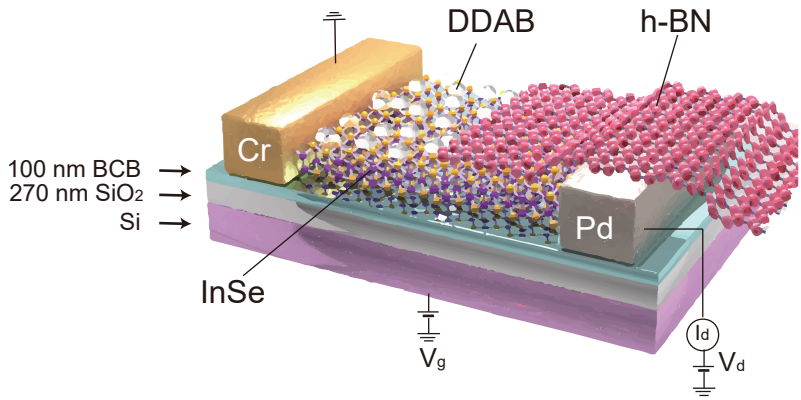

Figure 7.26: Illustration of device structure of lateral InSe asymmetric Schottky junction.

We have carefully chosen metals with high and low work functions (Pd: ~5.6 eV Cr: 4.4 eV) to form large Schottky barrier difference.[43,201] The metal-semiconductor contact is analysed in **Figure 7.27a** and **b**, revealing large Schottky barrier with Pd. Therefore, a depletion region is formed at the Pd-InSe interface thereby p-doping the contact region of InSe (**Figure 7.27c)**. While the n-doping by DDAB is uniform for InSe, the hole transport region is protected by few-layer of hexagonal boron nitride (h-BN) as displayed in the AFM image in **Figure 7.27d**.

The device showed a gate-dependent rectification where the rectification ratio amounts to 198 at V_g= 0V in dark (**Figure 7.28**). After doping with DDAB, the reverse bias current maintained in sub-nanoampere range with a 5-fold increase in the forward bias current, reaching a rectification ratio of 716.

The evaluation of diode could be deduced from the Shockley diode equation where

$$I_d = I_s\ [\exp\left(\frac{qV_d}{\eta kT}\right) - 1]$$

Where I_d is the diode current, I_s is the saturation current obtained from extrapolating the current from the log-linear plot to V= 0, q is elementary charge, V_d is the voltage across the diode, k and T is the Boltzmann constant and temperature respectively and η is the ideal factor which is linked to the slope of I-V curve. When η=1,the diode is operating in ideal performances while defects and interfacial traps could increase η up to 2. As is shown in **Figure 7.29**, the ideal factor drops from 1.52 to 1.02 for a typical device, indicating that the electrical performances of the lateral P-N junction are largely enhanced by molecular functionalization benefitting from the stable DDAB-InSe interaction with the defect sites.

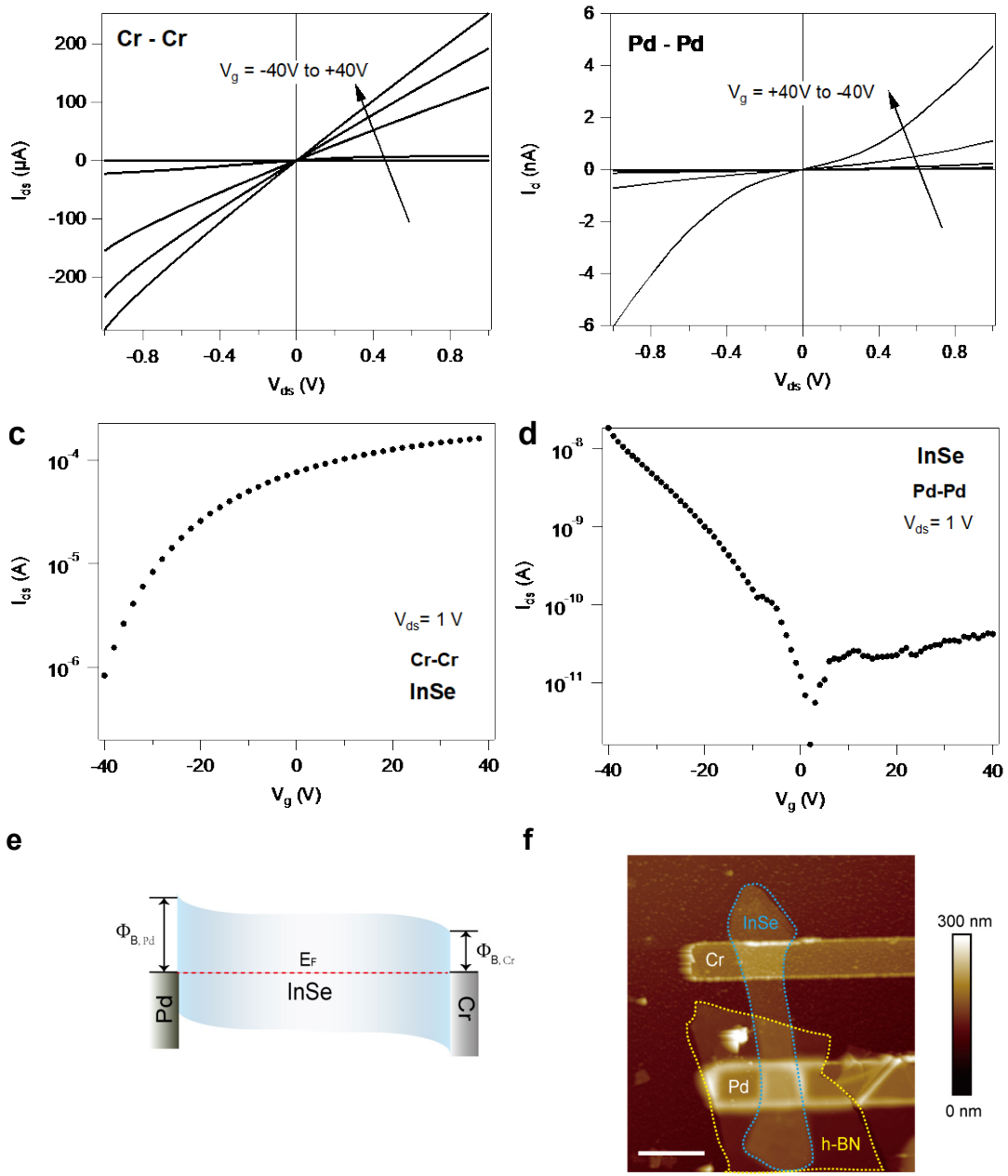

Figure 7.27: I-V characteristics of InSe with symmetric contacts. (a) (b) Output curve of InSe FET of (a) Cr-Cr and (b) Pd-Pd symmetric contact. (c) (d) Transfer curves of InSe FET of (c) Cr-Cr and (d) Pd-Pd symmetric contact. (c) Band alignment of InSe with Pd and Cr contacts. (d) AFM image of representative lateral InSe asymmetric Schottky junction partially covered with few-layer h-BN on top. The scale bar is 6 μm. (e) Band alignment of InSe with Pd and Cr contacts. Here, the Schottky barrier height (SBH) was estimated from Ref.[194] where the SBH is 280 meV and 560 meV for Cr and Pd respectively. c) AFM image of representative lateral InSe asymmetric Schottky junction partially covered with few-layer h-BN on top. The scale bar is 6 μm.

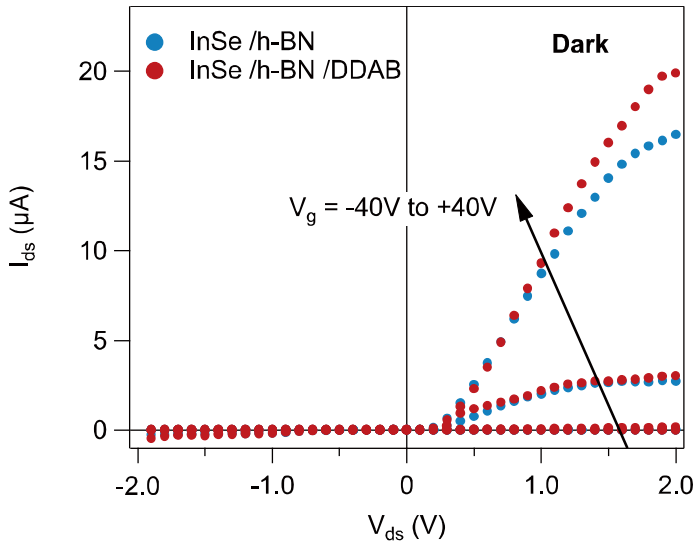

Figure 7.28: Gate-dependent I-V curves of InSe/h-BN before and after doping with DDAB in dark condition.

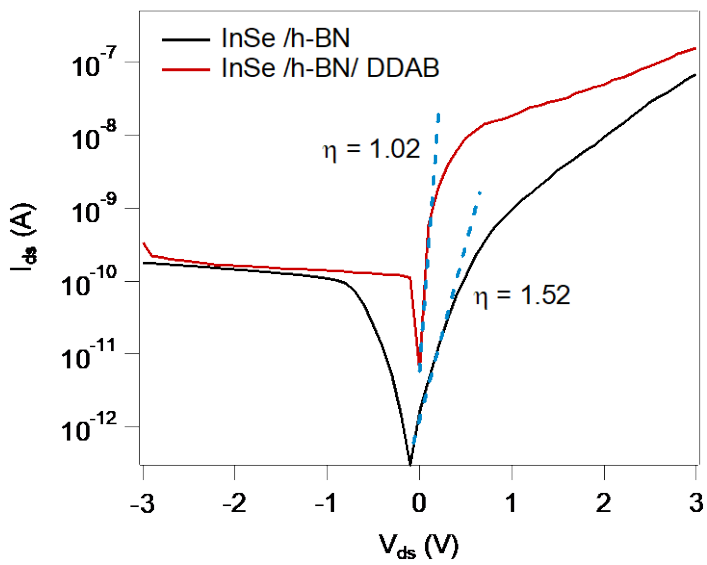

Figure 7.29: I-V characteristics and ideal factors of asymmetric Schottky junctions.

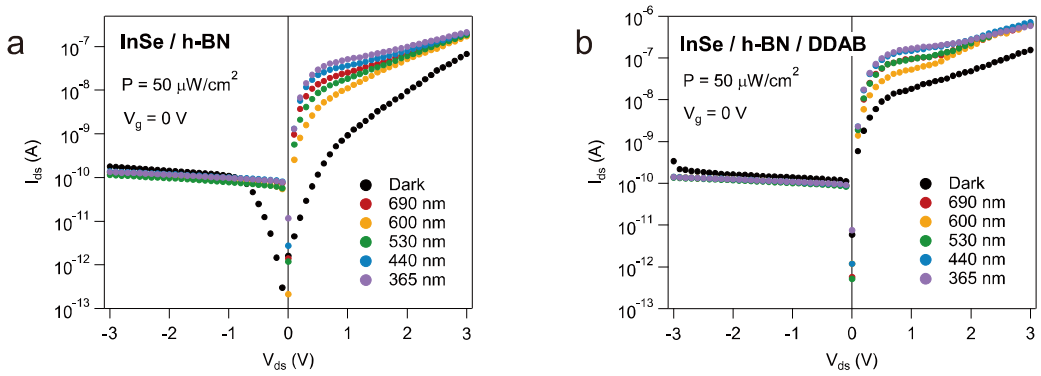

Figure 7.30: (a) Photodetection of lateral InSe asymmetric Schottky junction before doping with DDAB. (b) Photodetection of lateral InSe asymmetric Schottky junction after doping with DDAB.

The wavelength-dependent photodetective properties of such a p-n junction are evaluated in **Figure 7.30**. Similar to InSe phototransistor, the lateral p-n junction shows selective photoresponse for UV light (**Figure 7.31**). Additional photodetection test on 850 nm and 940 nm near infrared (NIR) light is presented in **Figure 7.32**.

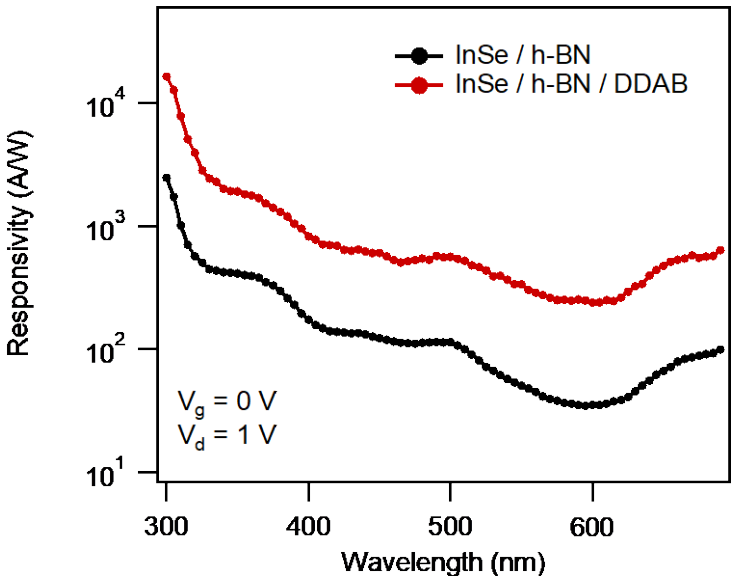

Figure 7.31: Calculated responsivity with of lateral InSe Schottky junction. Responsivity with wavelength scan from 300 nm to 690 nm. The interval of wavelength is 5 nm.

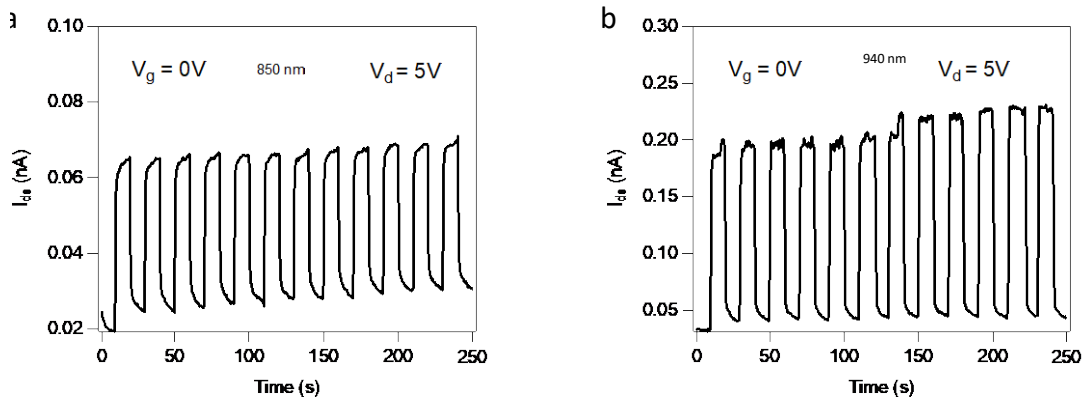

Figure 7.32. Photoresponse of lateral InSe Schottky junction illuminated at near-infrared (NIR) region. Time dependent photoresponse at V_d=5V and V_g=0V for illumination at (a) 850 nm and (b) 940 nm.

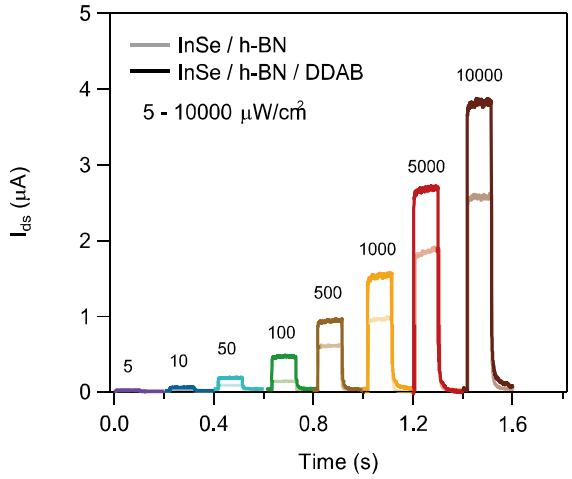

Figure 7.33: Time-dependent photoresponse of power density ranging from 5μW/cm² to 5000μW/cm² of InSe/h-BN and InSe/h-BN/DDAB.

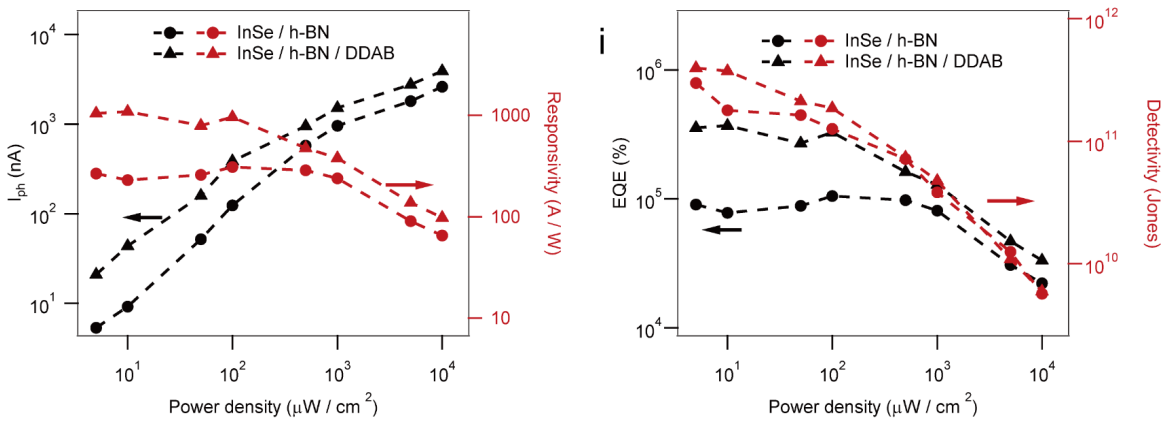

Figure 7.34: Power dependence of (a) photocurrent and responsivity and (b) EQE and *D** of InSe/h-BN InSe/h-BN/DDAB on BCB at V_g=0V and V_d=1V illuminated with 365 nm light.

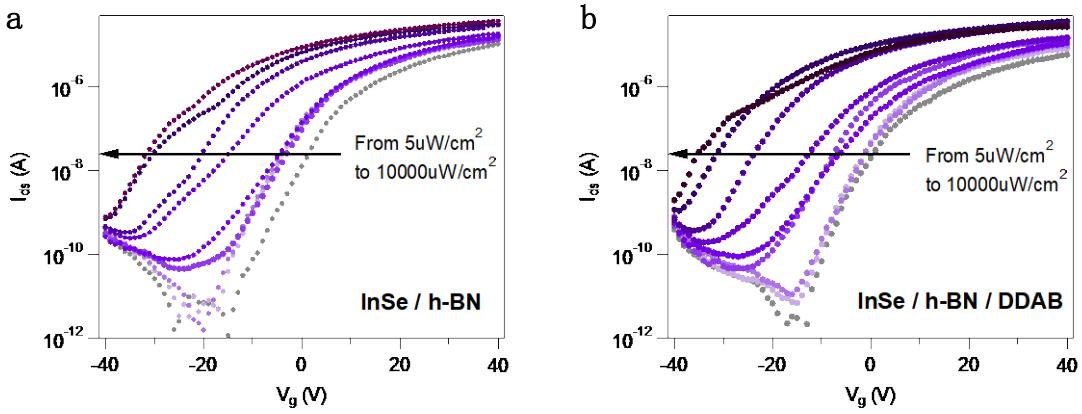

Figure 7.35: Gate dependent photoresponse illuminated by 365 nm light of InSe Schottky junction. Transfer curve (a) before, and (b) after doping with DDAB. with light power ranging from 5 μW/cm^2 to 10000 μW/cm^2.

The device displays strong power dependence (**Figure 7.33** to **Figure 7.35**). The linearity factor drops from 0.8440 for InSe/h-BN to 0.8065 for InSe/h-BN/DDAB, likely because of the inhomogeneity in the channel where the n-region is governed by the physisorbed organic molecules, while the p-region is screened by crystalline inorganic h-BN. Furthermore, by calculating R, EQE and D*, the lateral P-N junction reaches high R and EQE exceeding 10^3 A/W and 3×10^5 % upon 5μW/cm^2 illumination after DDAB functionalization, being 4 times greater than undoped junction. Simultaneously, *D** also shows 10-fold enhancement at low power illumination, reaching 4×10^{11} Jones. The photoresponse time of the lateral P-N junction is also found to be ultrafast for both unfunctionalized and functionalized samples, which all decreased below 1 ms (**Figure 7.36**). Compared to previously reported InSe lateral P-N junctions, our molecular functionalized device not only represents a novel device architecture that is highly suitable for exploring the photodetection of InSe, but also displayed record performance when operating at very low voltage inputs, demonstrating the power of molecular doping in InSe Schottky junctions.

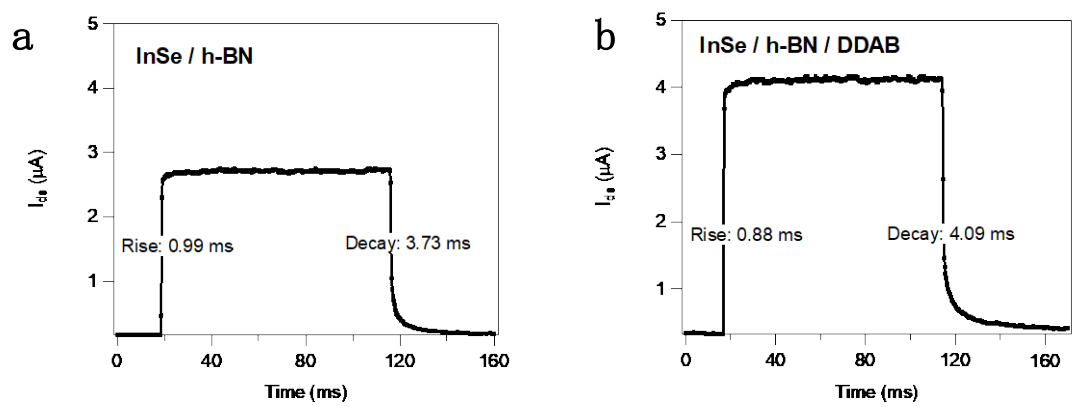

Figure 7.36: Time-resolved photoresponse of InSe Shottky junction. Time-resolved photoresponse of InSe Shottky junction (a) InSe/ h-BN, and (b) InSe/ h-BN/ DDAB at V_g=0V and V_{ds}=1V under the illumination of 365 nm. Light power is adjusted at 10 μW/cm^2.

7.3.5 Molecular functionalized BP-InSe van der Waals p-n heterostructures

Two-dimensional materials have been widely exploited as building blocks for vdW p-n heterostructures with tuneable bandgaps by varying the material composition and thicknesses. As an n-type semiconducting material, InSe could form type-Ⅱ band alignment with various p-type 2D semiconductors including the archetypical naturally p-doped 2D material is black phosphorus (BP), which possesses a small bandgap of ~ 0.3 eV. The band alignment of BP and InSe is demonstrated in **Figure 7.37**.

While the development of functional devices based on BP heterostructures with graphene, MoS_2, ReS_2, etc. have been widely reported in the literature, only two recent papers reported BP-based heterostructure with InSe which unfortunately did not demonstrate reliable high-performance photodetectors as other 2D materials.[202-206] This is achieved here, where we first focus on the dielectric engineering of the BP-InSe heterostructure showing evident performance enhancement of the P-N junction.

In BP-InSe heterostructure on SiO_2, large reverse bias leakage current on the same scale of forward bias current has been demonstrated.[202,203] Previous studies revealed that multi-scattering effects of amorphous state of SiO_2 is responsible for the leakage current of P-N junctions.[207] Therefore, we apply the dielectric modification strategy with BCB polymer, according to the device structure illustrated in **Figure 7.38**.

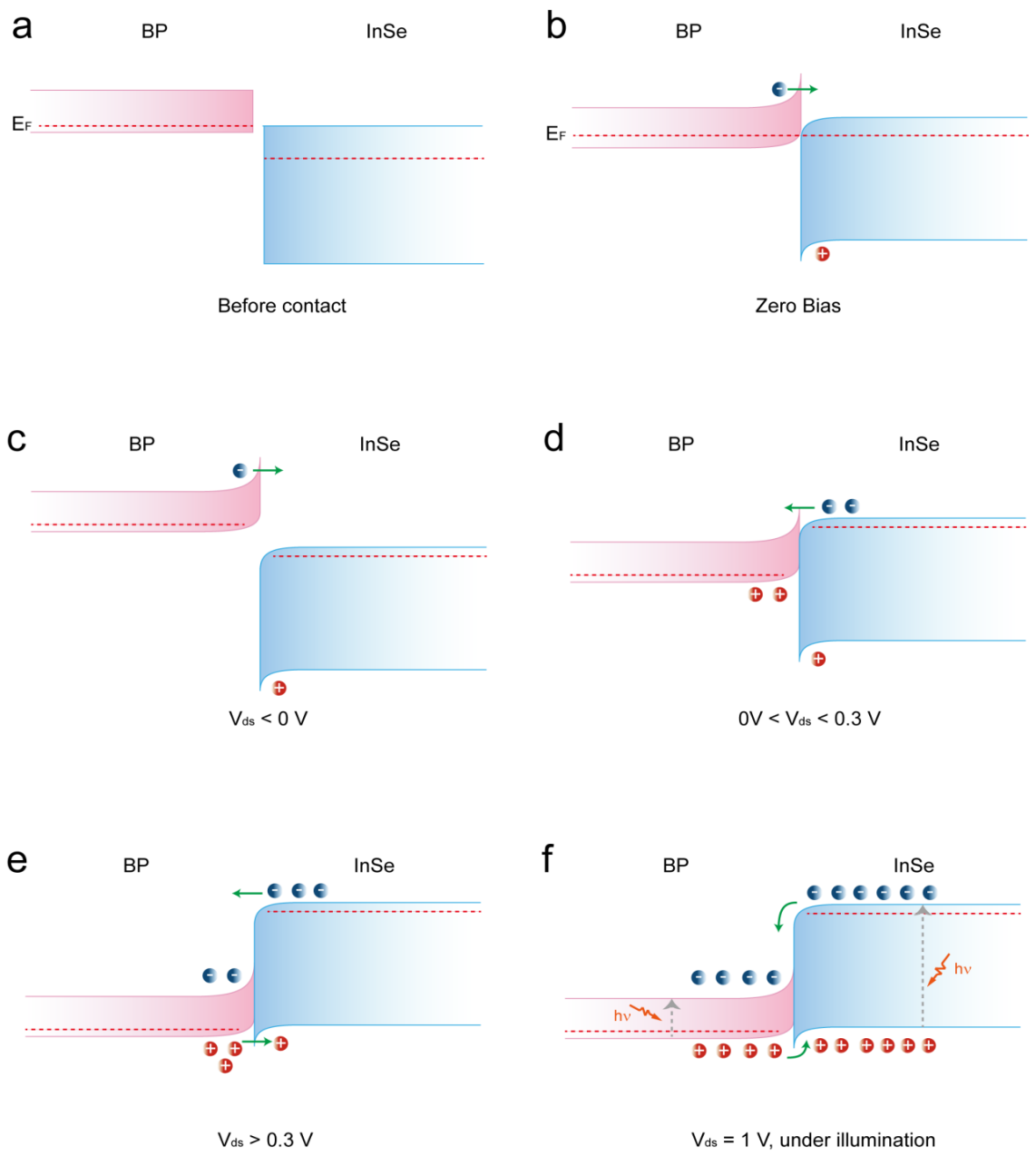

Figure 7.37: Band alignment of BP and InSe vdW heterostructure. (a) Before contact. The bandgap of BP is estimated to be 0.3 eV, and the bandgap of InSe is estimated to be 1.25-1.31 eV[203,208-210]; (b) After contact. The band bending occurs at the interface of BP and InSe as a result of Fermi level alignment; (c) Under reverse bias condition. The reverse bias enlarges the flat band energy difference of the PN junction, making it difficult for the tunneling of carriers; (d) Under small forward bias. When the forward bias voltage is below 0.3V, there is still a tunneling barrier for charges to flow within the junction given the small bandgap of BP; (e) Under larger forward bias. When the forward bias voltage is larger than 0.3 eV, the charge carriers in the heterostructure overcomes the potential barrier and result in enlargement diode current; (f) Under illumination. When external light is illuminated in the

heterostructure, the photoinduced excitons are separated by the built-in potential of the heterostructure and flow to the opposite side, which is electrons to p-side and holes to n-side.

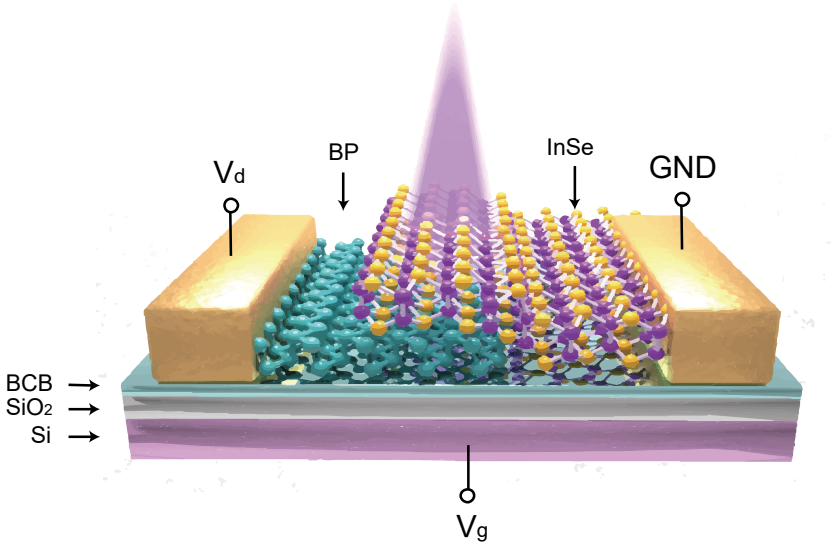

Figure 7.38: Illustration of device structure of BP-InSe vdW heterostructure. V_d, V_g and GND are drain electrode, gate electrode and ground electrode, respectively.

A few-layer thick InSe flake is stacked on the top of BP by dry transfer by exploiting a polydimethylsiloxane (PDMS) stamp. Raman and AFM characterizations are reported in **Figure 7.39**. They provide evidence for the successful formation of vdW heterostructure characterized by a flat surface.

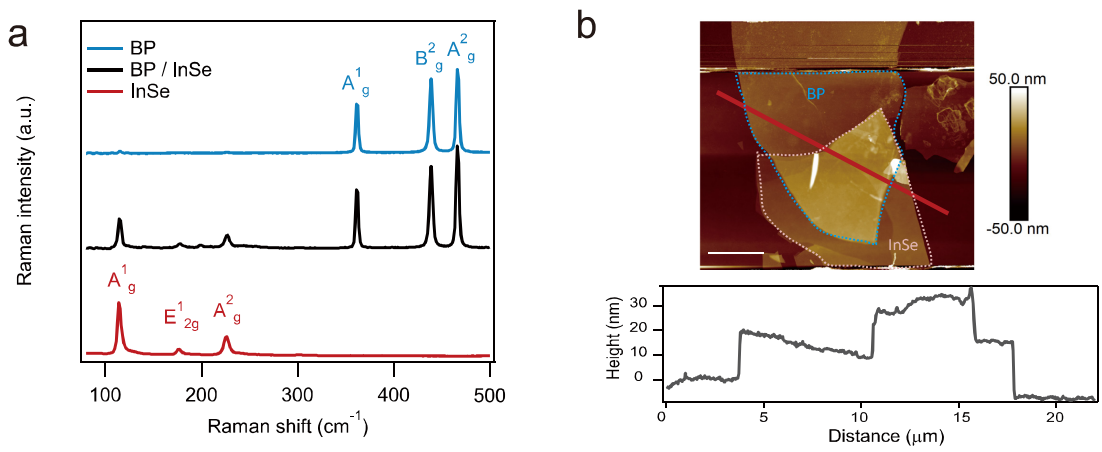

Figure 7.39: (a) Raman spectra and (b) AFM height image of as fabricated heterostructure.

After the deposition of Cr/Au electrode, the vertical P-N junction shows abrupt rectification behaviour when drain bias is applied. When comparing the output curve of the heterostructure on SiO_2 (**Figure 7.40a**) and on BCB (**Figure 7.40b**), two main enhancements can be observed. The first one is under dark, with the P-N heterostructure on SiO_2 requiring positive gate input to operate while on BCB a marked rectifying phenomenon appears at V_g=0 (**Figure 7.41**). This means that for heterostructure on SiO_2, an n-doping is needed to be applied to activate electron transport. The failure of operating the device at V_g=0V could be account of the slight p-doping of the silanol group of SiO_2.[211]

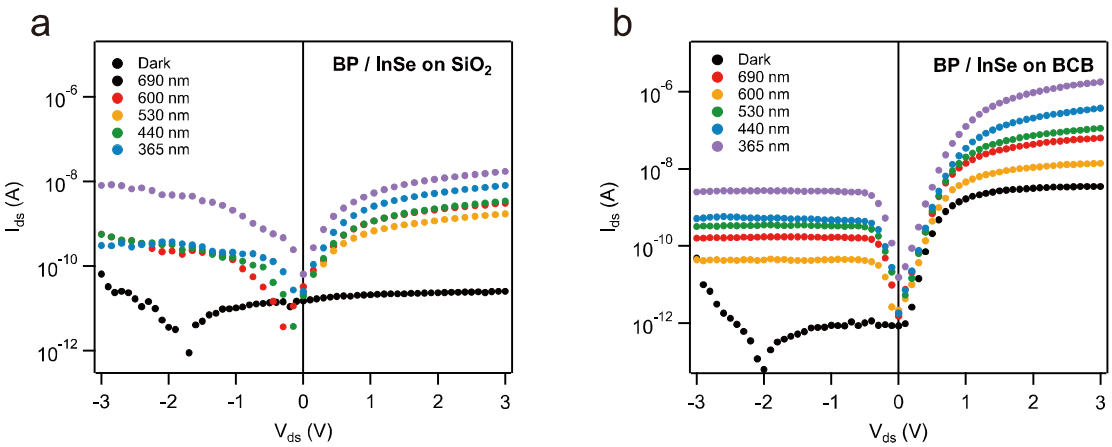

Figure 7.40: Output characteristic of BP-InSe heterostructure at V_g= 0V on dielectric material (a) SiO_2 and (b) BCB/SiO_2.

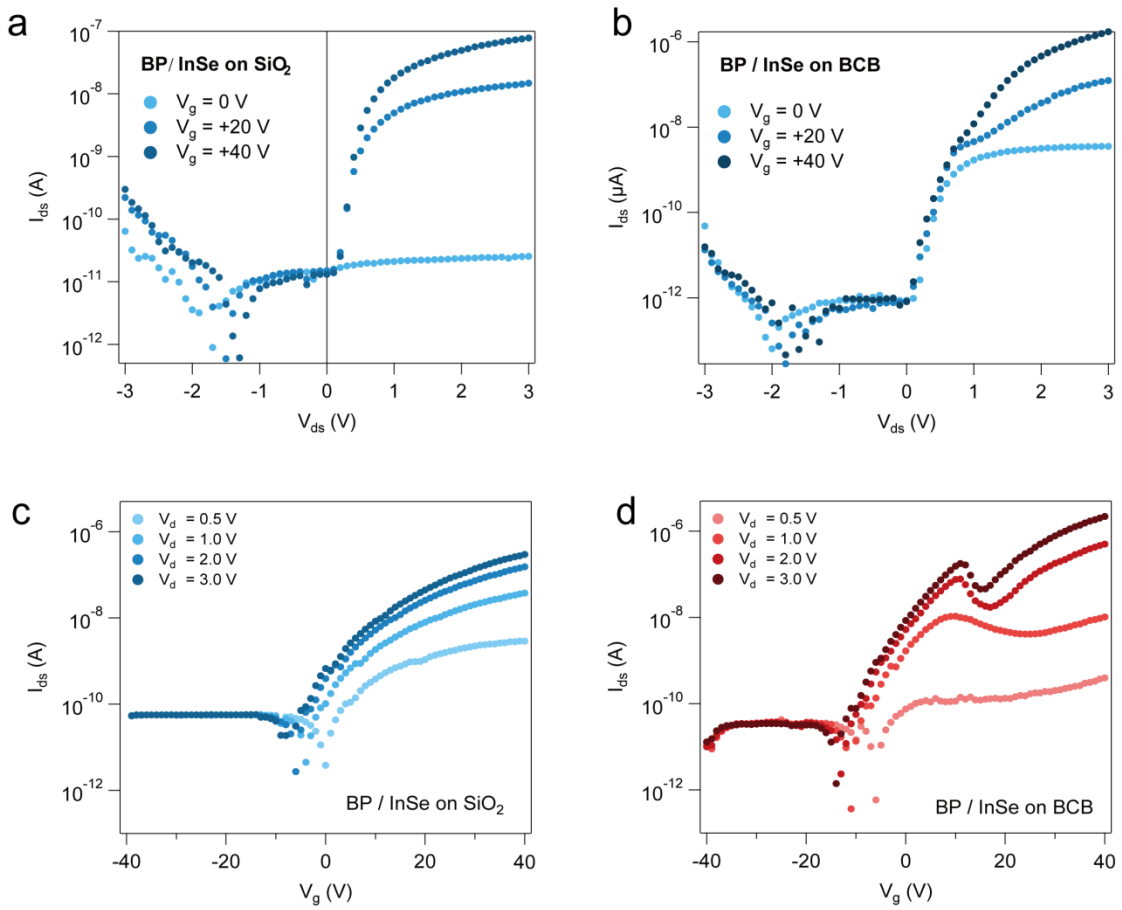

Figure 7.41: Detailed electrical performances of BP-InSe heterostructure on different substrates. Gate-dependent output characteristics (a) SiO_2 and (b) BCB. Drain-bias-dependent transfer curves of BP-InSe heterostructure on (c) SiO_2 and (d) BCB.

For both cases, as shown in the chart in **Figure 7.42**, the larger the positive gate, the higher is the rectification ratio, being a common phenomenon in 2D heterostructures.[212] A second observation is that under illumination, the reverse bias leakage current is on the nA scale, being comparable to the forward bias current. In contrast, the photocurrent at reverse bias conditions on BCB is much lower, leading to a rectification of 2 orders of magnitude higher than on SiO_2 for a broad range of wavelengths (**Figure 7.42**). This effect could be attributed to the enhanced tunnelling when a negative V_{ds} is applied on SiO_2 due to the heavier p-doping from the dielectric substrate. The shift of band structure in BP (which in close contact to the SiO_2 substrate) facilitates the electrons from the conduction band of InSe to tunnel through the depletion layer and flow to the valence band of BP, leading to an unsaturated of reverse bias photocurrent. Conversely, on BCB coated substrate, this effect is largely suppressed.

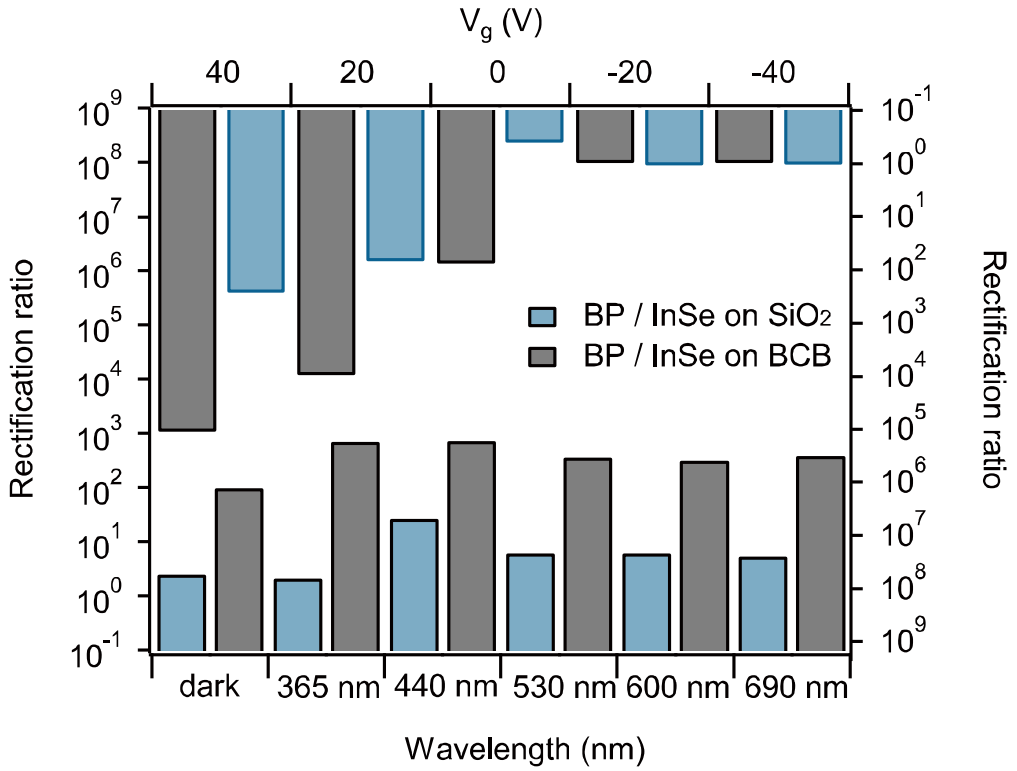

Figure 7.42: Comparison of rectification ratio in relation with gate voltage and incident light wavelength.

In analogy to InSe phototransistors, the photoresponsive time could be tremendously shortened after the dielectric modification with BCB, as demonstrated in **Figure 7.43**. Not only the photocurrent underwent a 10-fold increase, but also both the rise/decay time have reduced from 70 ms/55 ms to 2 ms/8 ms, thereby breaking the record among non-graphene contacted InSe heterostructures. The ultra-fast photoresponse with steady photocurrent with multiple illumination cycles under various wavelengths is observed with no fatigue (**Figure 7.44**). These findings validate the paramount importance of reducing charge trapping in dielectric layers also for vdW heterostructures.

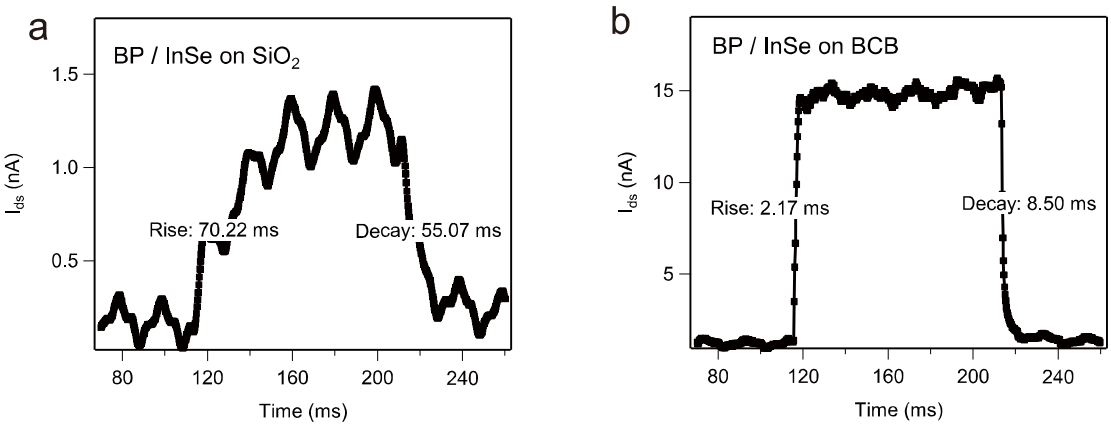

Figure 7.43: Time-resolved photoresponse of BP/ InSe on (a) SiO_2 and (b) BP/ InSe on BCB at V_g=0V and V_{ds}=1V under the illumination of 365 nm. Light power is adjusted at 8.32 mW/cm^2.

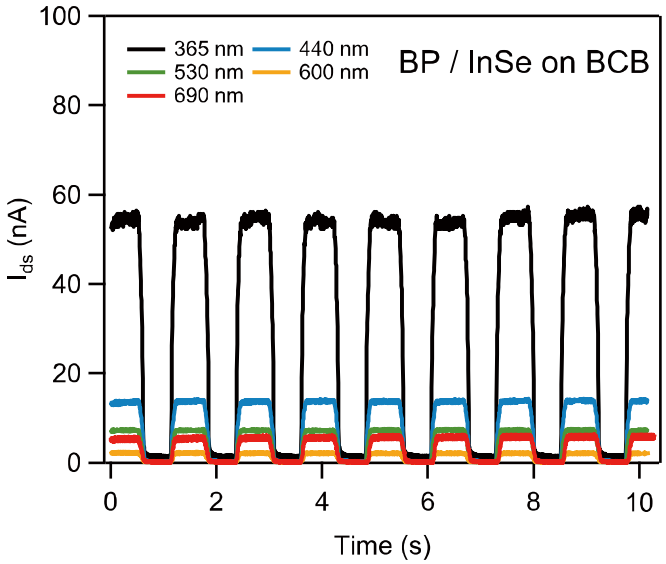

Figure 7.44: Time-resolved photoresponse cycles of BP/ InSe on BCB at V_g=0V and V_{ds}=1V under the illumination of 365 to 694 nm range (light power = 34.3 mW/cm^2).

Based on previous discussions, electron doping in the n-region is beneficial for enhancing the performances of P-N junctions. Therefore, it is reasonable to envisage a strong molecular n-dopant such as DDAB could easily promote the photodetection properties. In order to isolate BP from molecular doping, we partially passivated the BP flake with h-BN to prevent its exposure to molecules, as displayed in **Figure 7.44**. After functionalization with DDAB, a nearly 10-fold increase in the forward bias photocurrent has been recorded, while the reverse bias current retained the same magnitude (**Figure 7.45** and **Figure 7.46**).

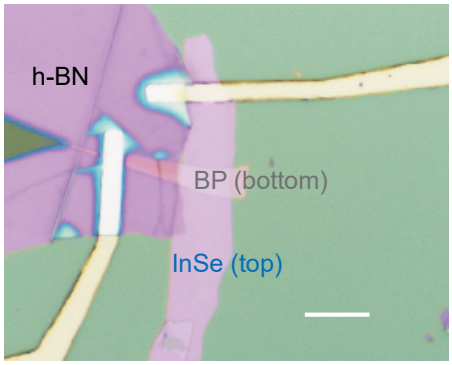

Figure 7.45: Optical image of BP/InSe heterostructure partially encapsulated by h-BN.

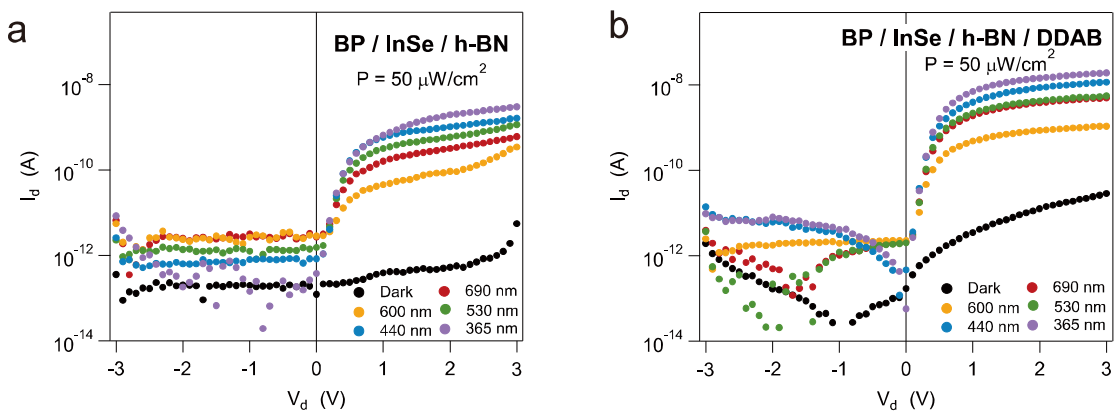

Figure 7.46: Output curves of BP/InSe/h-BN heterostructure (b) before and (c) after the functionalization of DDAB.

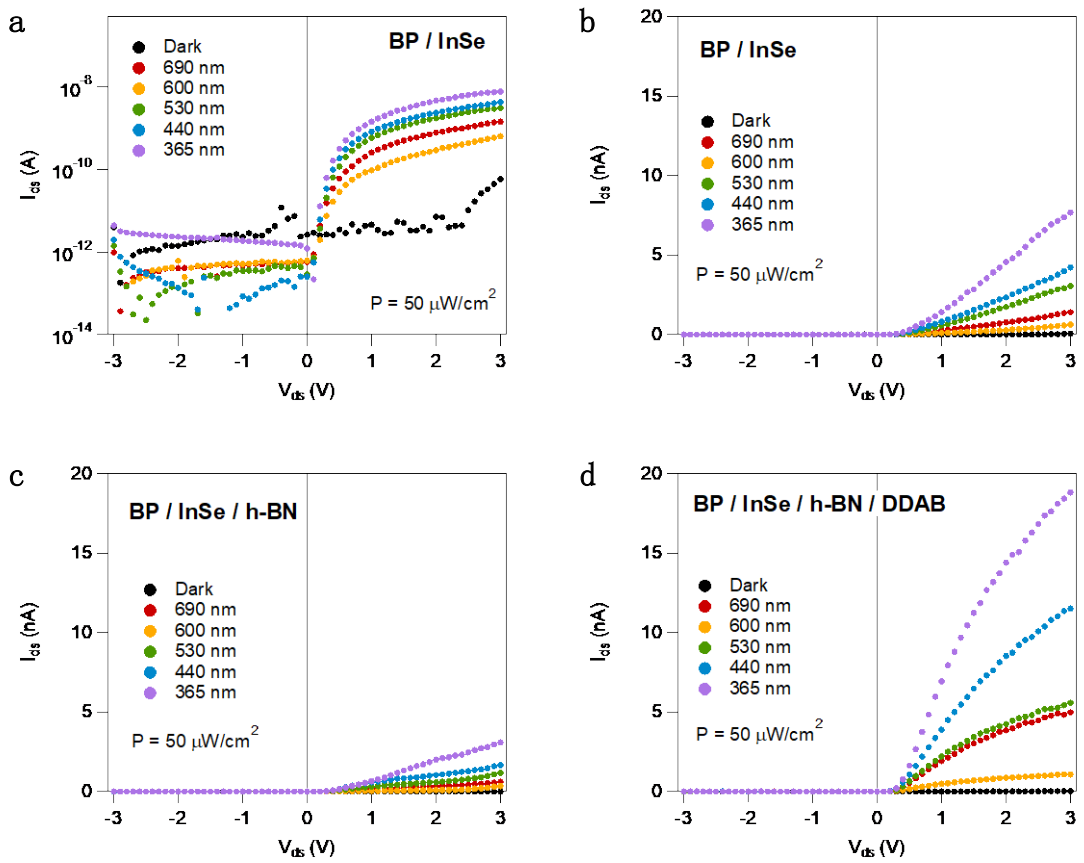

Figure 7.47: Other photoresponse characteristics of BP-InSe heterostructure. (a) Output curve of BP/InSe on BCB before encapsulation with h-BN of the specific device shown in Figure 7.4. Output curves of (b) BP/InSe (c) BP/InSe/h-BN (d) BP/InSe/h-BN/DDAB plotted in linear scale.

Such observations can be explained by the upshift of Fermi level in the n-InSe region, prompting a larger built-in potential in the depletion region. This allows photoinduced excitons to easily dissociate into photoelectrons (holes) across the heterostructure, assisted by an external drain bias of 1V. In this regard, the photoresponse time has also drastically decreased from 24.40/ 36.41ms to 0.96/ 2.97ms (**Figure 7.48**), which could be ascribed to a drifting of photocarriers (electrons to n-InSe and holes to p-BP) facilitated by the larger potential difference at the vdW interface as well as the molecular functionalization filling the defect states of InSe, thereby reducing the scattering of photocarriers that would notably slow down the photoresponse time. The enhancement of the functionalization is proved to be reproducible in different devices (**Figure 7.49**).

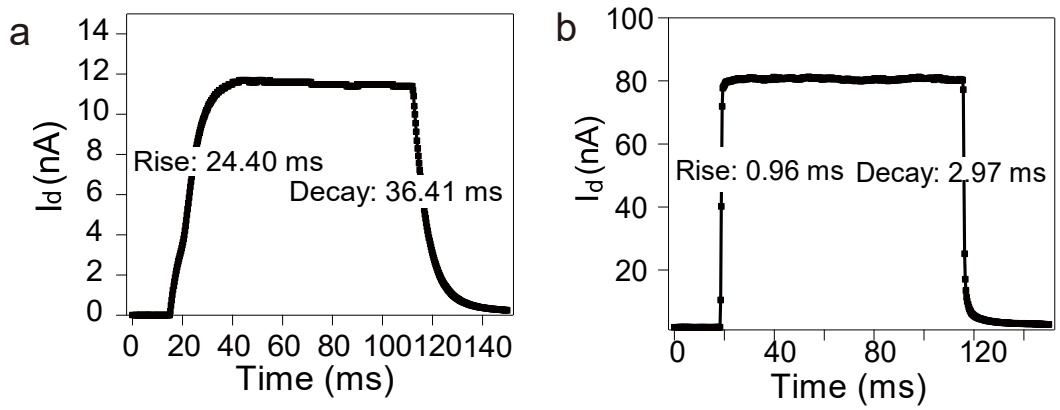

Figure 7.48: Time-resolved photoresponse of (a) BP/ InSe/ h-BN and (b) BP/ InSe/ h-BN/ DDAB at V_g=0V and V_d=1V under the illumination of 365 nm. Light power is adjusted at 4.12 mW/cm^2.

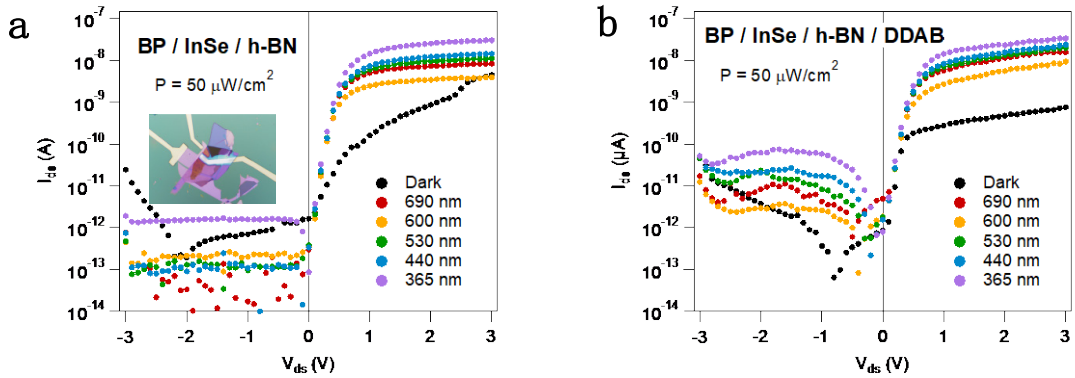

Figure 7.49: Light responsive output curves of another representative BP/InSe vdW P-N heterostructure. (a) Output curve before DDAB functionalization. (b) output curve after DDAB functionalization.

Compared to pure InSe with single absorption band (**Figure 7.31**), the spectral R of the heterostructure showed two additional absorption bands from 450 to 550 nm and from 600 to 690 nm (**Figure 7.50**). It is attributed to the presence of BP who possesses a much smaller bandgap, is able to generate larger photocurrent at the large wavelength region compared to pure InSe, contributing to the total photocurrent response, which is reflected as additional photocurrent absorption bands in the spectrum.

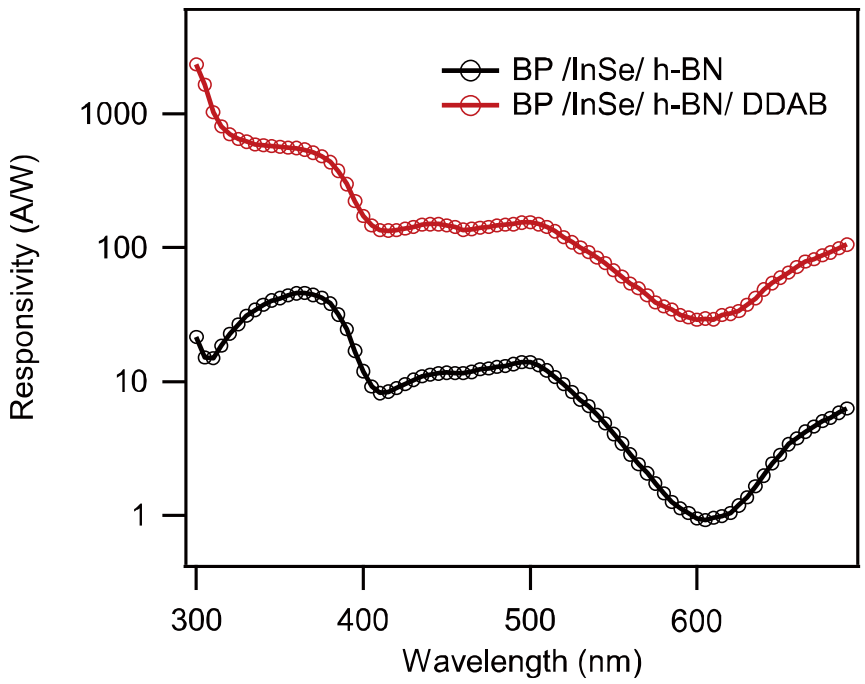

Figure 7.50: Spectral responsivity of wavelength scan from 300 nm to 690 nm at V_g=0V and V_{ds}=1V. The interval of wavelength is 5 nm.

The R value reaches a maximum value of 46 A/W and 537 A/W at 365 nm before and after the molecular functionalization, respectively. The ultrahigh responsivity reaches a record value among reported 2D-2D P-N heterostructures, especially, by operating the device with only 1V of voltage input. The power-dependent photodetection from 5μW/cm^2 to 4120μW/cm^2 before and after the DDAB doping in **Figure 7.51** to **Figure 7.52** indicates the photocurrent improvement to be universal for different power density. By calculating the linearity factor, we obtain α=0.44 for non-functionalized and α=0.48 for functionalized heterostructure, revealing a reduction of the amount of impurities (e.g.defects) in the P-N junction. The highest R and EQE exceeded 10^3 A/W and 3.5×10^5% after the functionalization, being almost 2 orders of magnitude larger than the unfunctionalized device while D^* remains on the same range of 10^{11} Jones. The successful realization of vdW BP-InSe P-N heterostructure and its performance improvement provides even stronger evidence of the high relevance of molecular functionalization of InSe to boost performances in a broad range of opto-electronic device types, and in particular for low-power ultra-responsive photodetectors.

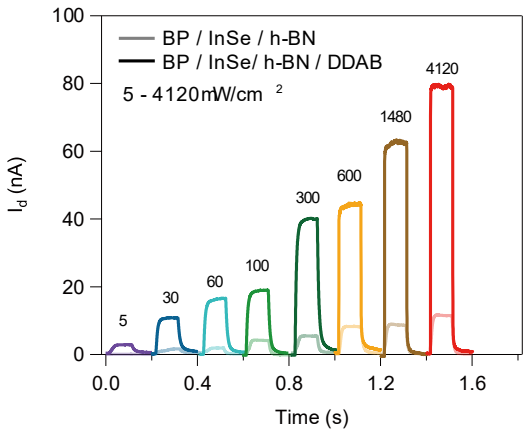

Figure 7.51: Photoresponse of power density ranging from 5μW/cm² to 4120μW/cm² of BP/ InSe/h-BN and BP/ InSe/h-BN/DDAB.

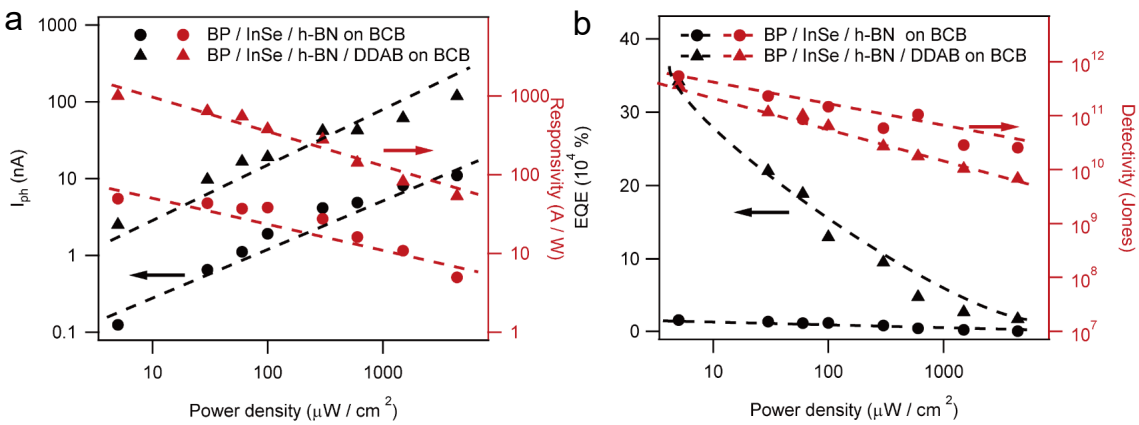

Figure 7.52: Power dependence of (a) photocurrent and responsivity and (b) EQE and *D** of BP/InSe/h-BN and InSe/h-BN/DDAB at V_g=V and V_d=1V illuminated with 365 nm light.

7.4 Conclusions

In summary, we have demonstrated novel strategies for markedly improve the performances of multifunctional opto-electronic devices based on few-layer InSe by means of dielectric engineering using trap-free polymer and molecular functionalization with DDAB. By combining experimental work with theoretical calculations, we showed that DDAB could form a stable physisorbed layer onto the surface of InSe by lowering the Fermi level and, at the same time, healing the defect states of InSe. The resulting transistors displayed field-effect mobilities exceeding 10^3 cm²/Vs with a high doping density of 10^{12}/cm². By further exploring molecular functionalized InSe as photodetectors, we successfully fabricated InSe devices in the form of

phototransistor, Schottky contact lateral P-N junction and vdW vertical P-N junction with ultra-high performances even when operated at very low bias input. The phototransisitor reaches ultra-high photoresponsivity of 10^6 A/W, meanwhile showing very fast photoresponse below 5 ms. The photoresponse time was efficiently decreased to sub-microsecond scale with molecular doped P-N junction, meanwhile the EQE was enhanced up to 10^5 %, thus outperforming previous reports of 2D P-N junctions (**Table 7.3**). The high photoresponsivity is reproducible among devices (**Figure 7.53**). This work provides distinct evidence of the full potential of molecular doping of InSe as viable platform for improving the functional complexity and ultimately fabricate high-performance 2D opto-electronic device. More generally, the employed chemical functionalization does not require sophisticated instruments; it is efficient, practical, up-scalable, and widely applicable to manipulate at will various physical properties of 2D semiconductors for large-area applications.

Material	R (A/W)	rise time (ms)	decay time (ms)	V_d (V)	V_g (V)	Reference
Phototransistors						
InSe/DDAB	1.6×10^6	16.88	16.19	1	0	this work
InSe/Ti_2CT_x	1×10^5	0.5	26	3	0	Ref.[74]
InSe	5×10^4	5	8	2	40	Ref.[68]
InSe/Graphene	9400	-	-	0.05	0	Ref.[172]
InSe	157	45	55	10	0	Ref.[69]
InSe/Graphene	60	0.1	0.1	10	80	Ref.[195]
Schottky junctions						
InSe/DDAB	1087	0.88	4.09	1	0	This work
InSe	853	0.047	0.061	2	10	Ref.[200]
InSe/AuNP	280	23	25	0	0	Ref.[199]
InSe/Graphene	3.65	0.00045	0.00024	0	0	Ref. [75]
vdW P-N heterostructures						
BP/InSe	1005	0.96	0.97	1	0	this work
BP/InSe	0.04	22	48	1	0	Ref.[203]

Table 7.3: Comparison of literature reported InSe-based photodetectors.

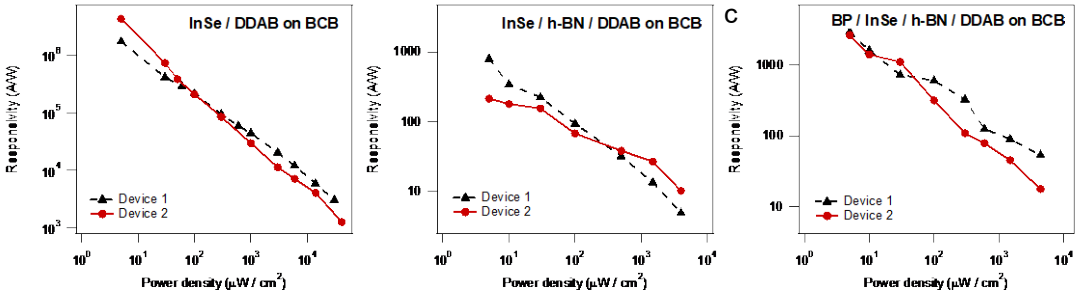

Figure 7.53: Statistical analysis of the photoresponsivity of additional devices. Plots of responsivity versus power density of DDAB functionalized devices of (a) InSe phototransistor, (b) InSe lateral Schottky diode, (c) BP/InSe vertical vdW PN heterojunction.

Chapter 8 Collective dipole-dominated doping of MoS_2 via the supramolecular approach

8.1 Introduction

Two-dimensional (2D) transition metal dichalcogenides (TMDs) have been the subject of intensive studies during the last decade because of their unique physico-chemical properties.[24,30,213,214] The most representative member of the family, MoS_2, is a semiconductor possessing a layer-dependent tunable bandgap (1.2 eV for bulk material and 1.9 eV for monolayer), high I_{on}/I_{off} ratio, large charge carrier mobility, and fast light response. Such unique features make MoS_2 a promising component for a variety of applications from (opto)electronics to valleytronics.[102,110,215] In particular, these properties open up a multitude of opportunities for the construction of high-performance ultra-thin heterojunction devices, e.g. p-n junctions and photodetectors.[7,216-219] Interestingly, the combination of organic molecules with TMDs was proven to be a versatile approach to tune the properties of the latter component via the 2D material's doping,[15,16,220-223] defect engineering,[224,225] device performance improvement,[32,188,226] etc..

Metal phthalocyanines (MPcs), an established family of symmetrical macrocycles comprising four iminoisoindoline units interacting with central metal ions, have been explored as molecular pigments for over a century. More recently, the applications of MPcs expanded to field-effect transistors, photovoltaic devices, phototherapies and catalysis by taking full advantage of the chemically modifiable structure which allows the tuning of many fundamental properties such as electron/hole conduction, light absorption and emission, etc.[227-230] The anionic aromatic ring tightly bonded with a cation center renders the conformationally planar MPcs highly stable against decomposition.[228] Moreover, most MPcs form type Ⅱ band alignment with monolayer and

few-layer MoS_2.[231] Thus, they are appropriate candidates to functionalize ultra-thin MoS_2 films, eventually via the formation of van der Waals organic-inorganic heterostructures. This type of heterostructures has been proved to feature charge transfer from the LUMO of MPc to the conduction band of MoS_2, resulting in doping in field-effect transistors (FETs), [232] Raman enhancement,[8] photoresponse improvement,[233,234] etc.

The combination of MPcs and MoS_2 has been the subject of previous studies, all of them focused on either the charge transfer mechanism or the influence of the type of metal core on the energy of LUMO ($2e_g$ orbital) in the complex.[8,92,231,232] Surprisingly, the exploration of axially functionalized MPcs has never been addressed. Coordination chemistry offers a broadest variety of functionalization solutions to decorate 2D materials beyond the two-dimensional space through the bonding of organic ligands to metal ions. Pyridine, being one among the most common ligands, enables a coordination involving the hybridization of its sp^2 electron lone pair to metal *d* orbitals, yielding a decrease of the 18-π aromaticity in MPcs, ultimately pulling the metal core out of the plane.[235] The axial pyridinic ligand is always standing perpendicular to the basal plane of the Pc ring. In fact, the four planar coordination sites in octahedral metal *d* orbitals are already occupied by four nitrogen atoms in the pyrrole rings, thus, the only possibilities for pyridine ligands to be coordinated are in the axial fifth and/or sixth sites. Previous works have shown that MPcs self-assemble on MoS_2 or graphite by forming supramolecular mono-molecular thick arrays with the Pc ring lying parallel to the basal plane of the substrate.[8,236-238] In this regard, one can consider that once axial ligands are coordinated onto self-assembled MPcs already coupled with MoS_2, they form ordered molecular arrays that are perpendicular to the MoS_2 /MPc heterojunction plane. When the axial ligands possess non-negligible dipole moments, these perpendicular molecular arrays could be translated as aligned molecular dipoles which are considered as a main factor to affect physical properties of MoS_2 in molecular doping.[15] In this framework, it is essential to exploit the chemical programmability of axial ligands under the context of atomic-thin heterostructures.

In this work, we propose a radically novel strategy to molecular doping of monolayer MoS_2 by using MPcs as self-assembled template to grow ligands featuring relatively large molecular dipoles oriented perpendicularly the basal plane of the 2D material. Our approach consists of two-step functionalization: 1) Growth from solution of an ultra-thin self-assembled MPcs onto monolayer MoS_2; 2) Coordination of functionalized pyridines (fPys) onto the MoS_2/MPc heterostructures (Scheme 1**a**) in the vapor phase. In particular, we use two prototypical MPcs, i.e. zinc phthalocyanine (ZnPc) and cobalt phthalocyanine (CoPc) with distinct d-electron fillings (Co: d^7

and Zn: d^{10}). For fPy, we have chosen fluorine and amine substituted pyridines in different positions of the aromatic ring to ensure marked variation of the dipole moment magnitude and orientation, namely 3,5-difluoropyridine (3,5-FP), 3-fluoropyridine (3-FP), 2-fluoropyridine (2-FP) and 4-aminopyridine (4-AP). The chemical structures of MPcs and fPys are depicted in **Scheme 8.1a** and 8.**1b**, respectively. Our approach holds three major advantages compared to the state-of-the-art: First, the low-temperature nature of the process of coordination of the central metal with the pyridine avoids occurrence of re-aggregation of the MPcs thereby guaranteeing their planar packing onto monolayer MoS_2;[8] second, the use of a vapour phase deposition of the substituted pyridines means that the MPcs are not subjected to re-dissolution, thus guaranteeing the largest amount of fPy to be coordinated; third, the orientation of the ligand dipole in the fPy-MPc complex is ruled by geometric control of coordination bond, in full absence of π-π packing between fPy ligand and adjacent Pc rings which typically takes place in solution phase processes. In our textbook experiment, we found that simple variation of the magnitude and the orientation of ligand dipoles can be attained by changing the type and position of substitution groups in pyridine rings resulting in a tuneable modulation of charge carrier density in monolayer MoS_2/MPc heterostructures either via p- or n-doping. Both experimental and theoretical results provided unambiguous evidence for the pronounced effect of molecular dipole generated by axially bonded ligand, paving the way for controllable molecular doping of 2D materials.

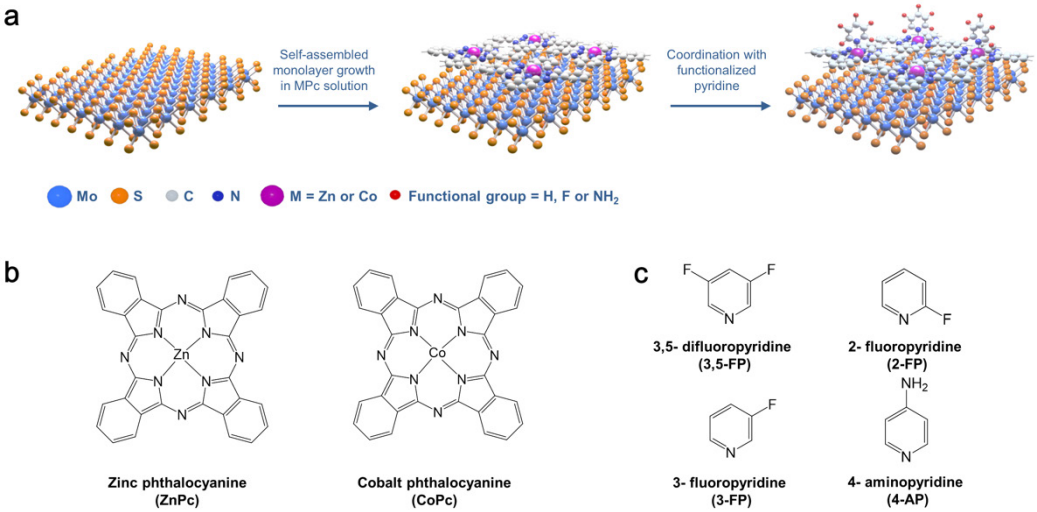

Scheme 8.1. (a) Illustration of two-step functionalization of ligand-coordinated MoS_2/MPc heterojunction. Chemical structure of (b) MPcs and (c) fPys used in this work.

8.2 Experimental methods

8.2.1 Sample preparation

Monolayer MoS_2 were mechanically exfoliated from commercially available molybdenite crystals (Furuchi, Japan) using the scotch tape method and transferred on thermally oxidized heavily *n*-doped silicon substrates (Fraunhofer Institute IPMS, $\rho_{Si} \sim 0.001$ Ω·cm, t_{ox} = 270 nm). Their thickness was monitored by optical microscope combined with Raman spectroscopy and Atomic Force Microscopy (AFM). The samples were thermally annealed at 200 °C inside a vacuum chamber to desorb atmospheric adsorbates. ZnPc and CoPc are purchased from Merck. The MoS_2/MPc hybrids were realized by immersing monolayer MoS_2 into 0.5 mM MPc in anhydrous solution, then rinsed vastly and thermally annealed in nitrogen to remove aggregates and evaporate solvents. To avoid the desorption of MPc on MoS_2 when reacting with ligands in solvent environment, the coordination of pyridinic ligand (TCI Chemicals) is reacted in vapor phase where 50 μL of pure pyridine was added in a 60 mL closed beaker containing the MoS_2/MPc heterostructure on Si/SiO_2 chip. The whole beaker is heated up to an ad hoc temperature (85 °C for 3,5-FP, 3-FP, 2-FP and 175 °C for 4-AP) to form pyridine vapours to enable the contact with MPc. The optimal functionalization time was defined by time-dependent study of the functionalization;

it amounts to 25 min for 3,5-FP, 3-FP, 4-AP, and 15 min for 2-FP. Subsequently, post thermal-annealing treatments (95 °C for 3,5-FP, 3-FP, 2FP and 200 °C for 4-AP) for 20 min is performed in order to remove physisorbed pyridines from the surface. The functionalized samples are measured after being cooled down to room temperature. All the reactions were done in a nitrogen-filled glovebox to exclude the effect from O_2 and H_2O in air.

8.2.2 Device fabrication and electrical characterization

As-exfoliated MoS_2 monolayer were coated with 2 layers of PMMA (Allresist, 600K/ 950K) immediately after exfoliation to avoid air exposure. Top-contact (80 nm Au) field-effect transistors were fabricated by standard E-beam lithography and lift-off in warm acetone in glovebox. All devices were annealed under vacuum at 200°C overnight to remove absorbents. The characterization of device performance was realized by Keithley 2636A under N_2 atmosphere.

8.2.3 Raman spectroscopy

Raman and Photoluminescence spectra were carried out in inert atmosphere (N_2) by Renishaw inVia spectrometer equipped with 532 nm laser in a nitrogen-filled sealed holder (Linkam). Samples were mounted in the glovebox and immediately measured after annealing or after molecule deposition to avoid exposure to contaminant chemicals. The excitation power was kept below 1 mW to avoid local heating damage effects. The wavenumber (energy) resolution was ~1 meV.

8.2.4 AFM measurement

AFM imaging was performed by means of a Bruker Dimension Icon set-up operating in air, in tapping mode, by using tip model TESPA-V2 (tip stiffness: k=42 N/m).

8.2.5 XPS measurements

Commercial CVD-grown triangle monolayer MoS_2 on Si/SiO_2 (6Carbon Technology (Shenzhen)) was employed to study the surface chemistry of MoS_2, MoS_2/MPc and MoS_2/MPc/fPy. XPS analyses were carried out with a Thermo Scientific K-Alpha X-ray photoelectron spectrometer with a basic chamber pressure of ~10^{-9} mbar and an Al anode as the X-ray source (x-ray radiation of 1486 eV).

Spot sizes of 400 μm and pass energies of 200.00 eV for wide energy scans and 10.00-20.00 eV for scans were used.

8.2.6 Photoelectron spectroscopy measurement in air

Commercial CVD-grown triangle monolayer MoS_2 on Si/SiO_2 (6Carbon Technology (Shenzhen)) was employed to measure the experimental work functions of MoS_2, MoS_2/MPc and MoS_2/MPc/fPy by PhotoElectron Yield counter operating in Ambient conditions (PEYA), using an AC-2 Photoelectron Spectrometer (Riken-Keiki Co.). The ambient photoelectron spectroscopy measurements were performed by sampling in each measurement an area of about 4 mm^2 (beam size) with an ultraviolet (UV) incident light power of 300 nW with a counting time of 10 seconds per point.

8.2.7 Computational details

All DFT calculations were performed with the projector-augmented wave (PAW) basis set, as implemented in the VASP code. [178,239] The exchange and correlation effects are treated with the Perdew–Burke–Ernzerhof (PBE) functional,[158] incorporating dipole moment correction along the 'c' axis (Z direction and perpendicular to the MoS_2 surface) and dispersion forces by Grimme correction (PBE+D2),[159] with a kinetic energy cutoff of 550 eV and using a Monkhorst-Pack mesh of 2×2×1 for the Brillouin zone (BZ) integration. All MPc/fPys were adsorbed on a 10×10 supercell of MoS_2 monolayer with the vacuum space was set to be 25 Å to avoid the interaction with periodic images. Geometries of MoS_2/MPc/fPy heterostructures were fully optimized prior to calculation of work functions. Work function (φ) of heterostructures is calculated as difference of Fermi energy (E_f) and the electrostatic potential at vacuum level (E_p). Fermi level (E_f) is set to the energy of valence band maximum for MoS_2/ZnPc/fPys and for MoS_2/CoPc/fPys, which are open shell systems, E_f is set to the maximum energy of the valence band with doubly occupied electrons ignoring the energy state of the unpaired electron localized on Co.

8.3 Results and discussions

To understand the electronic effect of axially functionalized MPc on MoS_2, we first gained

qualitative insight into the effects of axial ligands on the monolayer MoS_2. **Figure 8.1a** and **b** show the AFM images of monolayer MoS_2 before and after the formation of 4-AP axial ligand on ZnPc. The pristine monolayer MoS_2 was found to be 0.73 nm thick, in agreement with the literature.[98] After the functionalization, the average height of the adlayer increased significantly thereby reaching 2.07 nm. Such an increase in thickness resulted from the physisorption of ZnPc, the binding of 4-AP and the out-of-plane displacement of zinc atom after coordination. The interfacial distance between ZnPc and MoS_2 was previously reported being ~ 0.37 nm,[240] the ZnPc monolayer thickness amounting to ca. 0.40 nm, the height of 4-AP being ca. 0.50 nm, and the displacement of Zn atom consisting of 0.05 nm.[235] We found that the difference of vertical distance before and after the functionalization amounts to 1.34 nm (**Figure 8.1d**), thus matching perfectly with the expected molecular configuration in **Scheme 8.1a**. High-resolution AFM images, as those displayed in **Figure 8.1c**, revealed that the morphology of self-assembled ZnPc/4-AP on MoS_2 consists of long parallel stripes with a width ranging between 12 and 20 nm. Such result is in line with previous STM observations with MPcs physisorbed onto MoS_2 forming stripes of closely packed two or more molecular rows with a gap between the stripes of 0.78 nm.[237] The periodic structure also confirms that the coordination of ligands using our method does not destroy the self-assembled motif of ZnPc on MoS_2, enabling the edge-on packing of the pyridines. Raman spectroscopy also confirmed the successful functionalization of 4-AP ligand (**Figure 8.1e**). While a group of peaks appeared at high wavenumber as a result of the formation of MoS_2/ZnPc heterostructure, corresponding to the vibration mode from Pc ring,[241] after the coordination of 4-AP, these features were preserved and combined with intensity enhancement at ~1405 cm^{-1} and 1510 cm^{-1}. The latter two peaks can be ascribed to the amino group and pyridine, respectively.[242,243] In all the combination of MPcs and fPys, we have observed similar signatures. XPS spectra of N 1s (e.g. see **Figure 8.1f**) also validated the efficient ligand functionalization. The proportion of nitrogen linked with metal increased from 36.95% (approx. 3 out of 8 nitrogen atoms) to 39.19% (approx. 3.6 out of 9 nitrogen atoms) after the coordination with 4-AP, indicating a 88.17% functionalization yield. The Mo 3d and S 2p spectra have demonstrated evident shifts according to different fPy functionalization, which could be found in **Figure 8.2**.

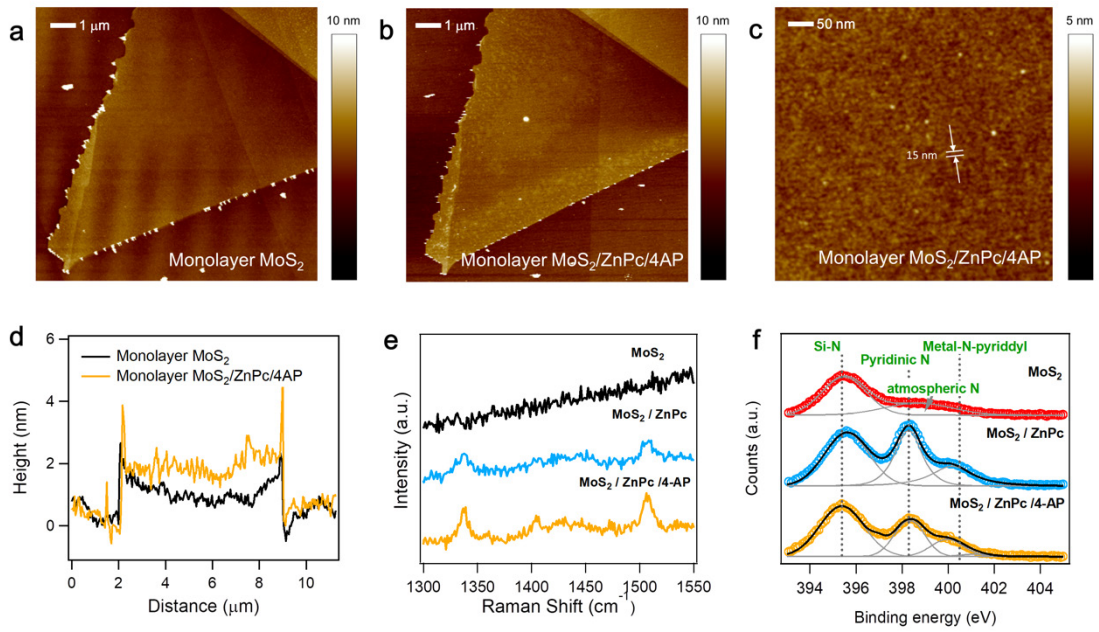

Figure 8.1: Surface characterizations of MoS_2/ZnPc/4-AP. Topographic AFM image of (a) pristine monolayer MoS_2 and (b) monolayer MoS_2/ZnPc/4-AP, (c) the latter also on the sub-µm scale. (d) Height profile of monolayer MoS_2 and monolayer MoS_2/ZnPc/4-AP. (e) Raman spectra of monolayer MoS_2, monolayer MoS_2/ZnPc, and monolayer MoS_2/ZnPc/4-AP in high wavenumber range. (f) XPS spectra of N 1s of monolayer MoS_2, monolayer MoS_2/ZnPc, and monolayer MoS_2/ZnPc/4-AP.

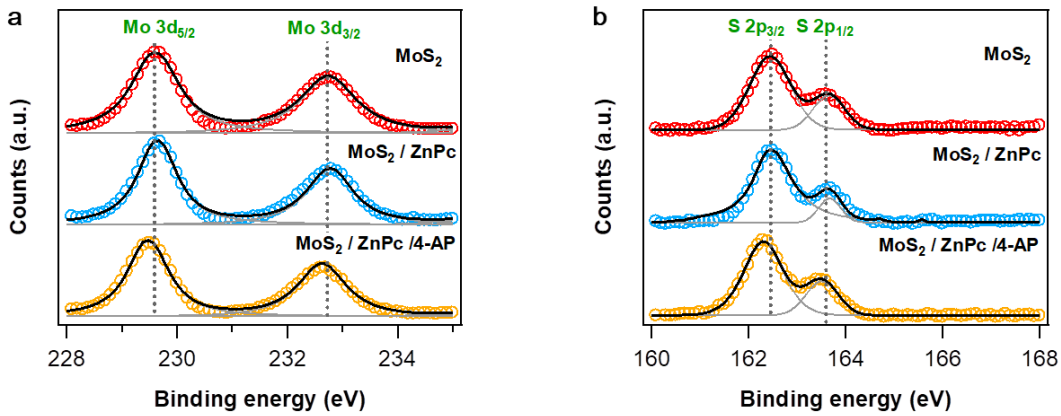

Figure 8.2: XPS (a) Mo 3d and (b) S 2p spectra of MoS_2/ ZnPc hybrid functionalized with 4-AP.

After confirming the effective functionalization, we explored how the axial ligands approach influences the electronic properties of MoS_2. We have fabricated back-gate, top-contact FETs with monolayer MoS_2 as channel material, as portrayed in **Figure 8.3**. After the formation of self-assembled MPcs, we have observed a large shift of transfer curve (I_{ds}-V_g) to the positive direction (**Figure 8.4a** and **b**). Such evidence can be attributed to the formation of p-n junctions, in

agreement with previous studies.[232,234] By further coordinating the fPys, we have observed shifts in two opposite directions: for 3,5-FP and 3-FP, the I_{ds}-V_g curves shift to positive voltages while for 2-FP and 4-AP, the curves shift to the negative direction.

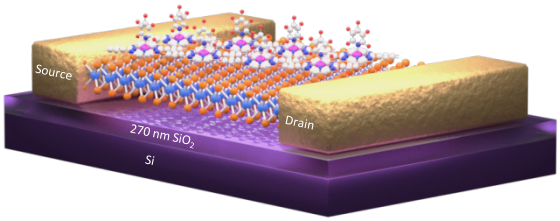

Figure 8.3: Device structure of monolayer MoS_2 functionalized with MPc/fPy.

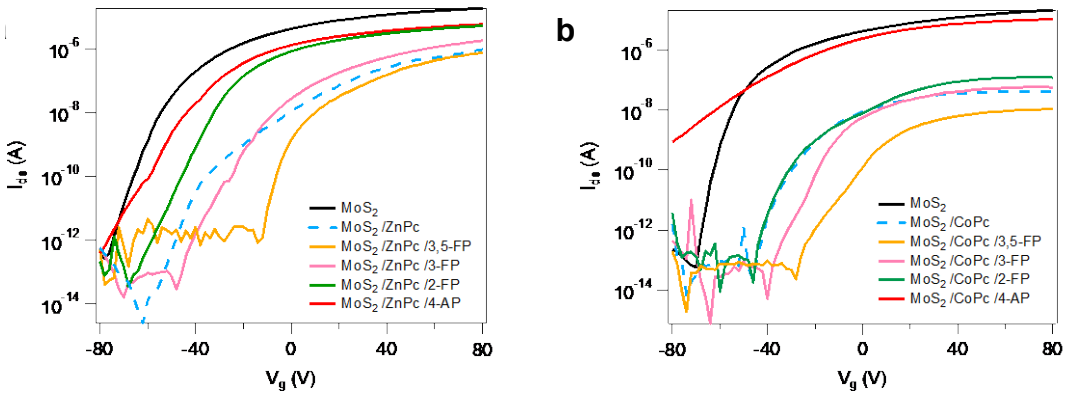

Figure 8.4: (a) Comparison of transfer curves of MoS_2/ZnPc heterojuction coordinated with ligands. (b) Comparison of transfer curves of MoS_2/CoPc heterojuction coordinated with ligands.

The shift could be quantified by calculating the threshold voltage change (ΔV_{th}) in the transfer curve,as shown in **Figure 8.5**. This value is known to correlate linearly with the charge carrier density change Δn by molecular doping in a semiconducting material, which could be solved with the following equation:

$$\Delta n = \frac{C_{ox}\,\Delta V_{th}}{e} = \frac{\varepsilon_{ox}\,\Delta V_{th}}{t_{ox}\,e}$$

where Δn is the change in electron (negative charge) density, C_{ox} is the capacitance per unit area of 270 nm SiO_2, e is the elementary charge, and ε_{ox} is the dielectric constant of SiO_2, ΔV_{th} is the change of threshold voltage and t_{ox} is the thickness of SiO_2.

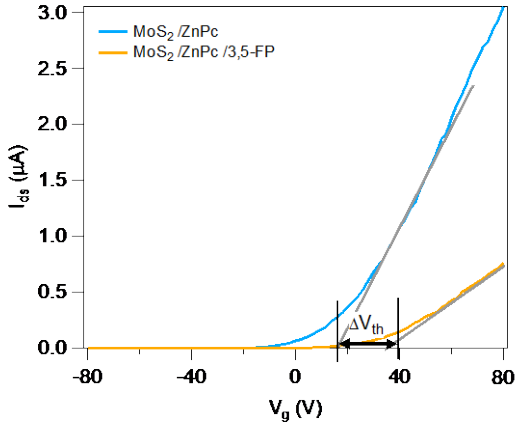

Figure 8.5: Typical transfer curve of MoS_2/ZnPc and MoS_2/ZnPc/3,5-FP showing the calculation of ΔV_{th} before and after ligand functionalization.

The calculated results are presented in **Figure 8.6** in solid circles. We found that for MoS_2/ZnPc, ligand functionalization enables to modulate the carrier density in MoS_2 from -3.0×10^{12}/cm^2 in 3-FP to 1.8×10^{12}/cm^2 in 4-AP, while for MoS_2/CoPc, the modulation ranges from -3.5×10^{12}/cm^2 in 3-FP to 5.32×10^{11}/cm^2 in 4-AP, with respect to the reference case of MoS_2/MPc. The magnitude of the changes is surprisingly high, being comparable to the doping of ZnPc and CoPc on MoS_2 which amounts 1.8×10^{12}/cm^2 and 2.1×10^{12}/cm^2, respectively. Considering that the major charge carriers in MoS_2 are electrons, it is then obvious to conclude that 3,5-FP and 3-FP decrease in electron density in MoS_2/MPc, inducing p-doping, whereas 2-FP and 4-AP increase the electron density, inducing n-doping. The overall doping has also been observed to be dependent on the time of the fPys coordination.

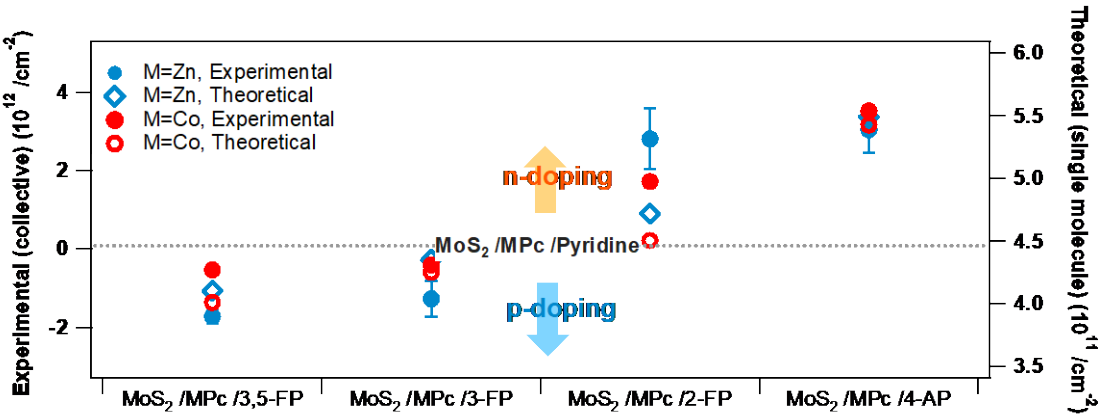

Figure 8.6: Charge carrier density shift in monolayer MoS_2 after ligand functionalization of fPys on MPc obtained from FET measurements with comparison to the theoretical results calculated from work function analysis.

This time-dependent study also enables us to define the optimal functional time for each ligand to achieve the maximum doping effect on the MoS_2/MPc heterostructure. Little is known on the complexation kinetics of MPc and the fPys that we have chosen in our study. Although the various fPys display similar structures, their side groups featuring distinct electronegativity could strongly affect the reaction kinetics. Therefore, it is necessary to carry out an-depth kinetic study of the complexation of these fPys onto MPcs in order to find out the optimal reaction times. The kinetic process of fPy coordination with ZnPc could be monitored by recording the electrical characteristics of the hybrid system in field-effect transistor devices. With the increasing time of functionalization, the molecular dipole density increases, and the doping caused by ligand dipole is enhanced, due to its collective nature. We have observed, that in **Figure 8.7a-d**, the threshold voltage shift increases with time. We have noticed that with 3,5-FP, the coordination quickly reaches a plateau after 5 min of functionalization, while for 3-FP, it takes 20 min to stabilize. Yet, we have not observed a plateau in 2-FP and 4-AP. Interestingly in 2-FP, n-doping is shown in first 15 min of functionalization. After that, a weakened n-doping (or relative p-doping) is observed. This might be explained with the coordination saturating with the first 15 min, followed by a physisorption of additional and 2-FP molecules onto MoS_2 or MoS_2/ZnPc surface. Since the fluorine atom in 2-FP is very electronegative, it tends to attract electrons from MoS_2 or MoS_2/ZnPc, inducing a p-doping. Based on these results, we chose 25 min of functionalization time for 3,5-FP, 3-FP and 4-AP, and 15 min for 2-FP in our study to maximize the doping of the ligands, in the meantime excluding the effects of unexpected physisorption of ligands on MoS_2/MPc.

Despite the V_{th} shift (**Figure 8.7e**), the field-effect mobility μ is also varied by the functionalization of time, which could be derived via

$$\mu = \frac{L}{WC_{ox}V_{ds}}\frac{dI_{ds}}{dV_g}$$

where L and W are channel length and channel width, respectively. $\frac{dI_{ds}}{dV_g}$ is the maximum slope extracted from the linear region of the transfer curve.

The results is shown in **Figure 8.7f**, in which the n-doping induced an increase in the electron mobility in MoS_2 whereas the p-doping yielded a decrease in the electron mobility.

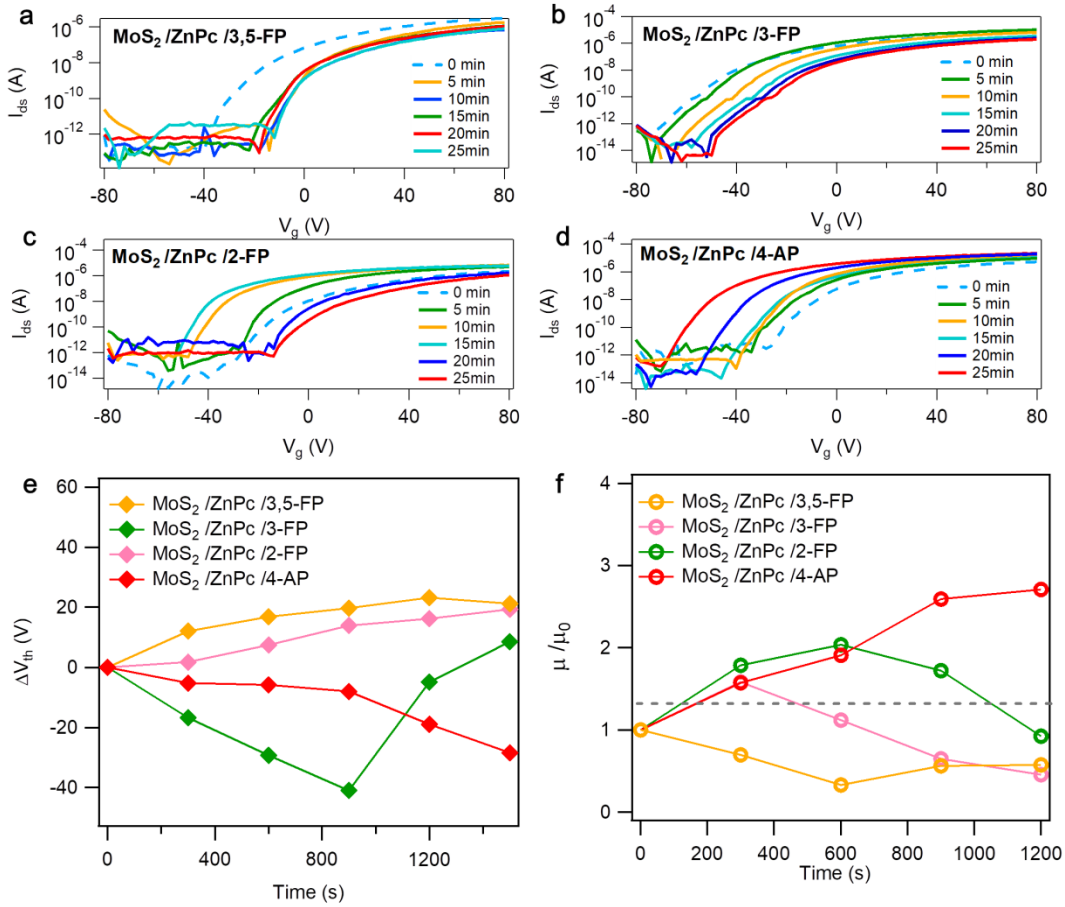

Figure 8.7. Kinetic analysis of MoS_2/ZnPc coordinated with ligands. (a)-(d) Transfer curve of FET with different functionalization time of fPys. (e) The threshold voltage change of each functionalization time. (f) Charge carrier mobility change of MoS_2/ZnPc functionalized by different fPys.

The tuneable either p- or n-type doping exhibits considerable changes in carrier densities in MoS_2/ZnPc which are comparable to effective molecular doping reported in the literature, being of the same orders of magnitude.[232,244] The combination effect of ZnPc and 3,5-FP could decrease the electron density by $3.5\times10^{12}/cm^2$,whereas the combination of CoPc and 4-AP could yield to an increase the electron density by $1.5\times10^{12}/cm^2$. The largest difference in electron density achieved with different binding ligands, namely 3,5-FP and 4-AP, reaches values as high as $4.8\times10^{12}/cm^2$ for ZnPc and $4.1\times10^{12}/cm^2$ for CoPc. These values are markedly larger than the values attained by using unsubstituted MPcs as dopants of monolayer MoS_2.[232-234] Blank experiments carried out by interfacing fPys directly on MoS_2 via physisorption, in absence of the MPcs templating layer, revealed a much weaker effect after thermal annealing (at 95 °C for 3,5-FP,3-FP,2-FP and 200 °C for 4-AP) as a result of molecular desorption (**Figure 8.8**).Moreover, all fPys showed mild n-doping effect with Vth shift by 3 to 4 V ($\Delta n=2.4\times10^{11}/cm^2$ to $3.2\times10^{11}/cm^2$), in stark contrast to our observations in the n- and p-type doping in the MoS_2/MPc/fPy hybrid

heterostructure, especially when 3,5-FP and 3-FP are used as ligands. Thereby, the observed doping, which is strongly affected by the orientation of the dipoles, should be ascribed to the effect of the MPc-fPy coordination, in contrast to the random physisorption of fPys on MoS_2.

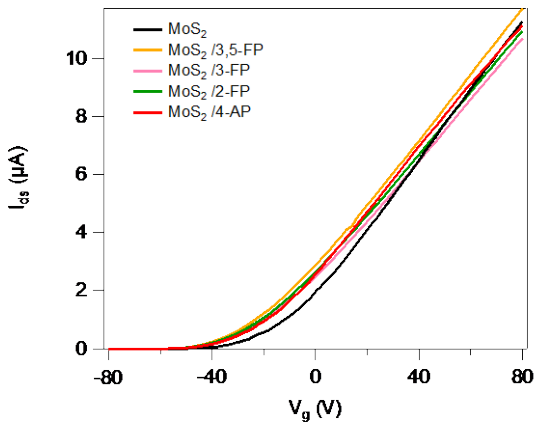

Figure 8.8: Control experiment of FET measurement of monolayer MoS_2 only with fPys functionalization step, indicating that without MPcs serving as templating layer for the ligands, the fPys interact weakly via physisorption with MoS_2, and upon thermal annealing the pyridines desorb thereby yielding a negligible doping effect.

In order to investigate the role of ligand functionalized MPcs in modulating the charge carrier density, we have carried out density functional theory (DFT) calculations. It is indeed notorious that the component of molecular electric dipoles perpendicular to the surface of 2D materials exert a polarization capable of shifting the surface work function, hence inducing a local doping.[82] Accordingly, we have calculated the theoretical work function (φ_{th}) of MoS_2/MPc/fPy heterostructures in conjunction to the axial dipole moment of these heterostructures and the dipole induced electrostatic potential of isolated molecules at vacuum level (Ep) in order to trace the relative changes in φ_{th} of MPc/fPys. All MPc/fPys form type II heterostructures with MoS_2, irrespective of the type of axial ligands, as emphasized in previous works, [16,17] wherein the HOMO of MPc/fPys is located within the band gap of MoS_2 monolayer (see **Figures 8.9-Figure 8.11**).

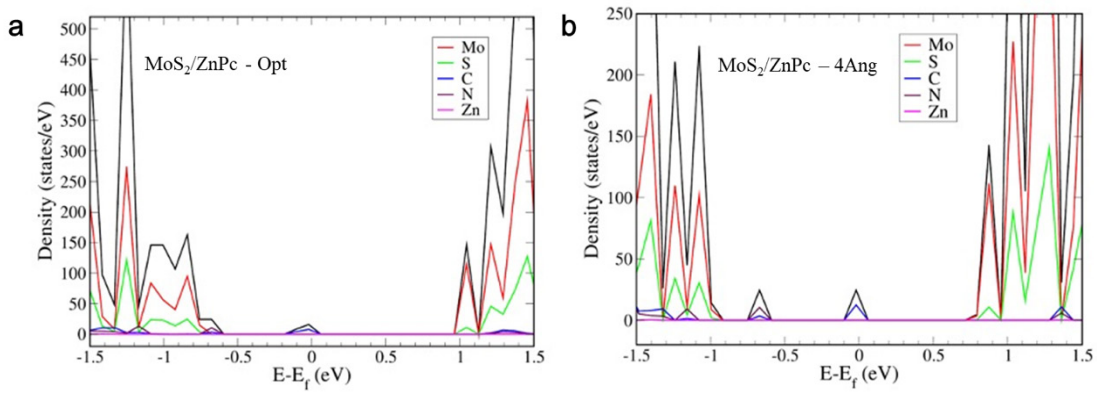

Figure 8.9: Density of states of MoS_2/ZnPc heterostructures. (a) ZnPc molecule as at optimum distance from MoS_2 surface in the DFT optimized geometry, and (b) when ZnPc molecule is axially lifted by an additional 4 Å from the MoS_2 surface (with respect to equilibrium distance) to simulate a non-interacting case. MoS_2/ZnPc form Type -II heterostructures with HOMO of the molecule (indicated at $E-E_f = 0$ eV) forming the valence band and MoS_2 surface forming the conduction band.

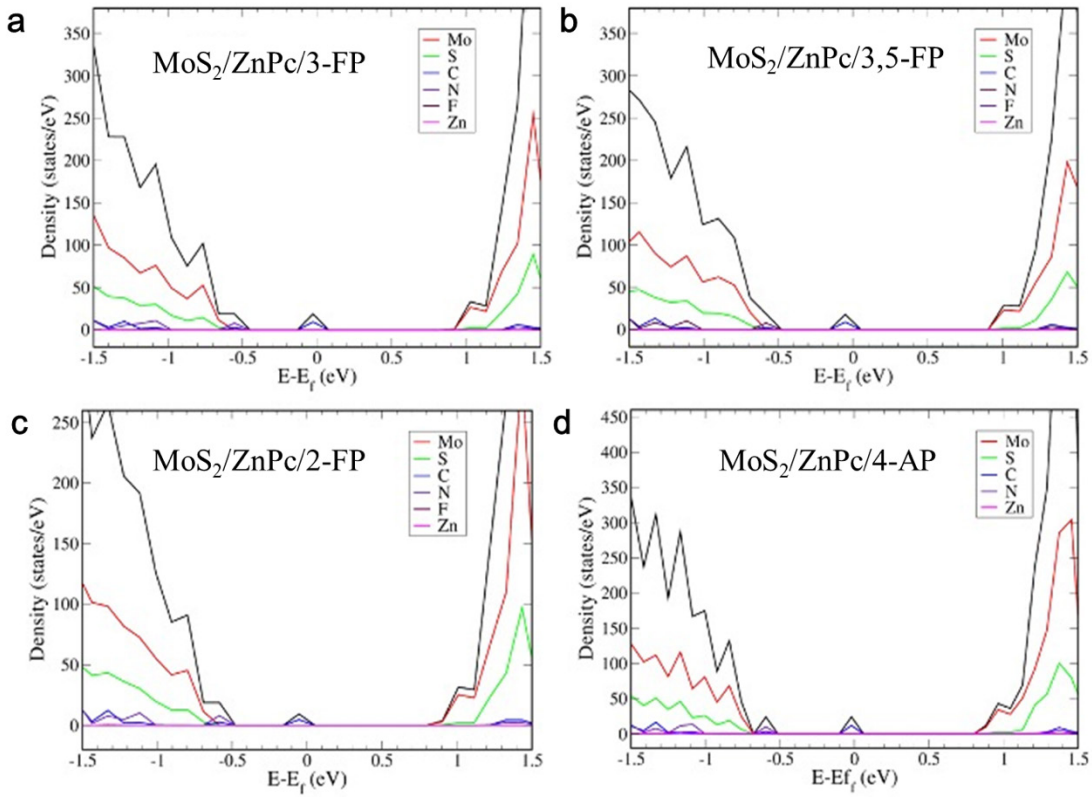

Figure 8.10: Density of states of MoS_2/ZnPc/fPys with (a) 3-FP, (b) 3,5-FP, (c) 2-FP, and (d) 4-AP functional groups. All MoS_2/ZnPc/fPy systems form Type II heterostructures with HOMO of the molecule (indicated at $E-E_f = 0$ eV) forming the valence band and MoS_2 surface forming the conduction band. When fPys are varied, small changes in the position of conduction band with respect to HOMO of the molecule were observed.

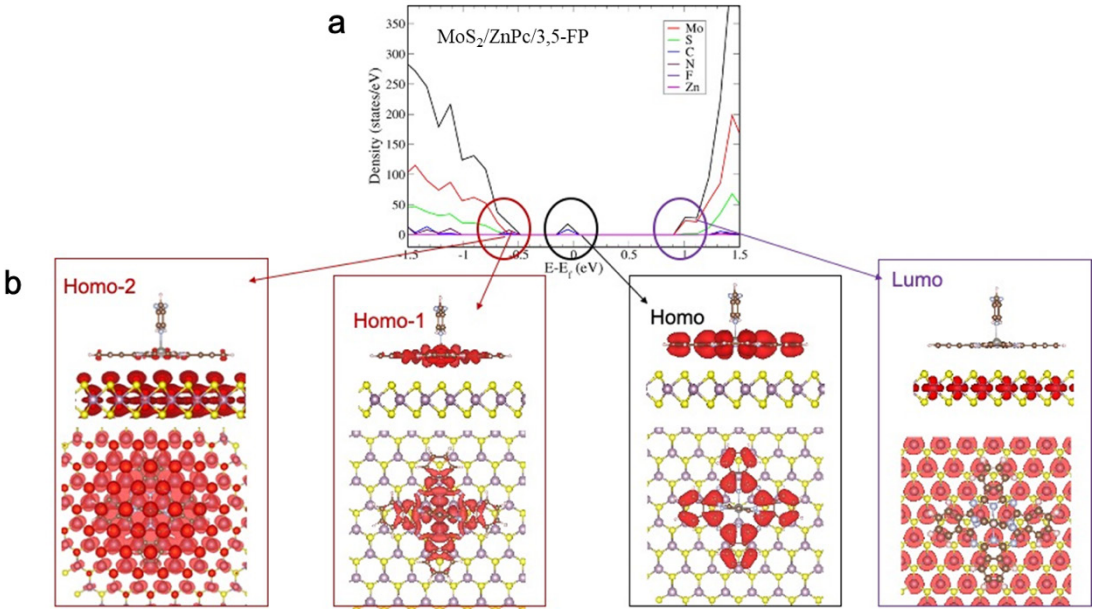

Figure 8.11: (a) Density of states, and (b) electron wavefunction plots of MoS_2/ZnPc/3,5-FP at Γ-point. While MoS_2 surface contributes to the conduction band (indicated by wavefunction plot at LUMO), the localization of wave function on the ZnPc/3,5-FP molecules close to the Fermi energy (indicated at $E-E_f = 0$ eV) could be observed.

Theoretical values for the work function (φ_{th}) of MoS_2/ZnPc and MoS_2/CoPc are found to be 5.13 eV and 5.18 eV respectively, in close agreement with the experimental observations (see **Figure 8.12** and **Table 8.1**). Upon addition of the axial 'un-functionalized' pyridine (Py) ligand to MPc, the work function was found to increase. This is because MoS_2/MPc/Py features an axial dipole moment (perpendicular to and directed towards the basal plane of MoS_2 surface, note as dipole 1) originating from the ligand induced metal-N coordination bonding. When the axial pyridine ligand has functional groups on the aromatic ring, additional changes in the work function can be predicted: MoS_2/MPc/3,5-FP and MoS_2/MPc/3-FP showed relatively higher φ_{th} values than MoS_2/MPc/Py, whereas MoS_2/MPc/2-FP and MoS_2/MPc/4-AP displayed comparatively lower φ_{th} values. These relative changes in work function of MoS_2/MPc/fPys with respect to MoS_2/MPc/Py follow the variation in the net dipole moment (axial component, note as dipole 2) of the functionalized molecules. To comprehend the relative variation in net dipole moment due to pyridine functionalization and its subsequent impact on the observed work function changes, we define dipole 2 as the difference between the net dipole moments of functionalized pyridine molecules (MoS_2/MPc/fPys) and dipole 1, which is the net dipole moment of un-functionalized pyridine (MoS_2/MPc/Py). Dipole 2 therefore quantifies the contribution of functional groups present on the pyridine ligand to the net dipole moment of MoS_2/MPc/fPys, wherein a positive (negative) value of dipole 2 partially cancels (add to) the contribution of dipole 1. The net dipole moments of MoS_2/MPc/3,5-FP and MoS_2/MPc/3-FP are lower than that of MoS_2/MPc/Py, as the relative positioning of fluorine atoms in 3,5-FP and 3-FP generates a dipole electric field that is directed away from the MoS_2 surface (positive dipole 2), thereby partially cancelling the field induced by the metal-N coordination. In contrast, the net dipole moments of MoS_2/MPc/2-FP and MoS_2/MPc/4-AP were found being higher compared to MoS_2/MPc/Py, because the normal component of the dipole carried by the functional groups adds in phase to the metal-N coordination dipole, both being directed towards the surface. As is shown in **Figure 8.13**). MPc/3-FP and MPc/3,5-FP induce a p-doing relative to MPc/Py, whereas MPc/2-FP and MPc-4AP induce a relative n-doing. This relative variation in doping with respect to MPc/Py can be traced back to the dipole induced by the functionalization of the pyridine ligand, which is quantified as dipole 2. Dipole, as reported in Fig S7, is computed by taking the difference between the total dipole moment of MoS_2/MPc/Py (un-functionalized pyridine) and the total dipole moment of MoS_2/MPc/fPys (functionalized pyridine), while dipole 1 is the total dipole moment of MoS_2/MPc/Py. Furthermore, as presented in **Figure 8.12**, the variation in the dipole moment of MoS_2/MPc/fPy heterostructures and the associated work function changes are proportional to the dipole induced electrostatic potential of isolated molecules at their vacuum level (E_p). Because of

the atomic thickness of monolayer MoS_2, the electric field generated by aligned molecular dipole could result in a large charge carrier modulation and thus promote doping, analogously to a local electric gate.[16] Hence, with reference to MoS_2/MPc/Py, a relative p-doping could be predicted for MoS_2/MPc/3,5-FP and MoS_2/MPc/3-FP that showed a reduced normal dipole moment, while a relative n-doping would be expected for MoS_2/MPc/2-FP and MoS_2/MPc/4-AP yielding an increased dipole moment. Photoelectron spectroscopy measurements in air (PEYA) in **Figure 8.14** confirmed that experimentally, the work function values shift with the same trends observed in DFT calculations, with 4-AP reducing the work function value to 5.11 eV and 3,5-FP increasing the work function up to 5.30 eV. The great modulation of work function revealed that the Fermi level of monolayer MoS_2 is largely influenced by the ligand functionalization with much more important contribution coming from the molecular dipole.

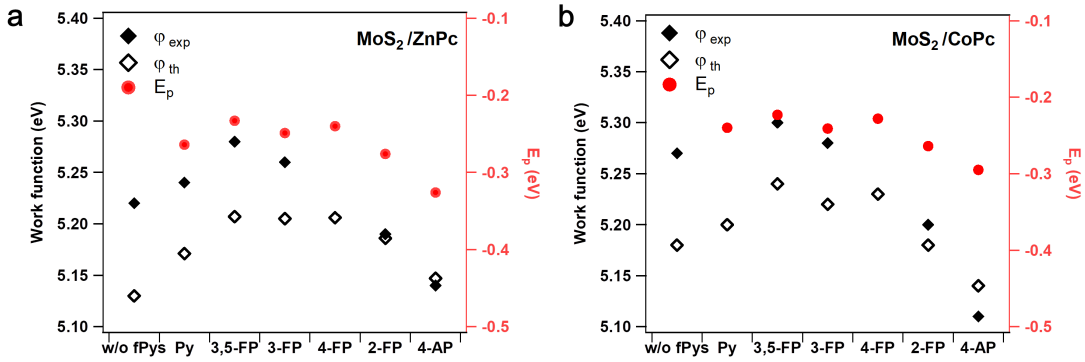

Figure 8.12: Calculated work function of MoS_2/MPc/fPys for (a) M=Zn, and (b) M=Co. The φ_{exp} stands for experimental work function values measured by PhotoElectron Yield counter operating in Ambient conditions (PEYA) which are presented in **Figure S8**. The work function trends follow the computed dipole induced electrostatic potential (E_p) of the isolated molecules at vacuum level.

Molecule	φ_{exp} (eV)	φ_{th} (eV)	D_{total} (D)	E_p (eV)
MoS_2/ZnPc/fPys				
MoS_2/ZnPc	5.22	5.130	-1.333	-0.136
MoS_2/ZnPc/Py	5.24	5.171	-7.465	-0.264

MoS_2/ZnPc/3,5-FP	5.28	5.207	-5.431	-0.233
MoS_2/ZnPc/3-FP	5.26	5.205	-6.455	-0.249
MoS_2/ZnPc/4-FP	--	5.206	-5.767	-0.240
MoS_2/ZnPc/2-FP	5.19	5.186	-7.924	-0.276
MoS_2/ZnPc/4-AP	5.14	5.147	-10.661	-0.326
MoS_2/CoPc/fPys				
MoS_2/CoPc	5.27	5.18	-1.522	-0.129
MoS_2/CoPc/Py	--	5.20	-6.679	0.240
MoS_2/CoPc/3,5-FP	5.30	5.24	-4.957	-0.223
MoS_2/CoPc/3-FP	5.28	5.22	-6.006	-0.241
MoS_2/CoPc/4-FP	--	5.23	-5.109	-0.228
MoS_2/CoPc/2-FP	5.20	5.18	-7.218	-0.264
MoS_2/CoPc/4-AP	5.11	5.14	-9.985	-0.295

Table 8.1: Work function and dipole moment of MoS_2/MPc/fPy systems. φ_{th}: work function of MoS2 monolayer functionalized with MPc/fPys. φ_{exp} : work function values measured by PhotoElectron Yield counter operating in Ambient conditions (PEYA) which are presented in **Figure S8**. D_{total}: total dipole moment of MoS_2/MPc/fPy in Debye, negative sign indicates dipole moment directed towards basal plane of MoS_2 surface. E_p: Dipole induced electrostatic potential (in eV) of isolated ligand at vacuum level. Additional calculations were performed on MoS_2/MPc/4-fluoropyridine (4-FP) for consistency in φ - Dipole moment trends.

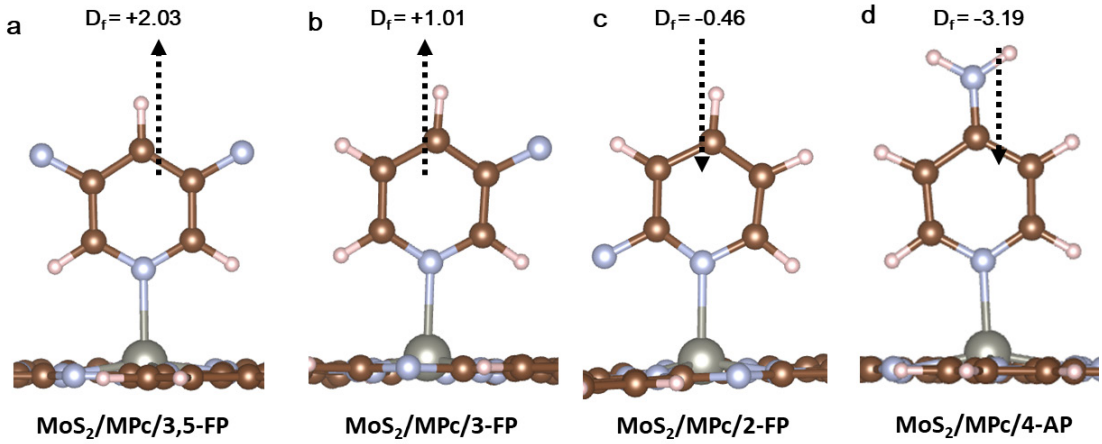

Figure 8.13: Calculated (relative) dipole moment generated by functional groups in fPys. (a) 3,5-FP, (b) 3-FP, (c) 2-FP, and (d) 4-AP. The net dipole moment in MoS_2/MPc/fPys heterostructures can be decomposed into two components. Dipole 1 resulting from metal-N coordination directed towards the surface (D_{Py}), and dipole 2 induced by the functional groups on pyridine ligand (D_f).The dipole moment induced by functional groups (D_f, in the unit of Debye), are calculated as D_{fPy}-D_{Py}, D_{fPy} is the total dipole moment of respective 'functionalized' pyridine ligands (MoS_2/M_{PC}/fPys) and D_{Py} is the total dipole moment of 'unfunctionalized' pyridine (MoS_2/MPc/Py). Positive (negative) D_f indicate a decrease (increase) in net dipole moment due to pyridine functionalization.

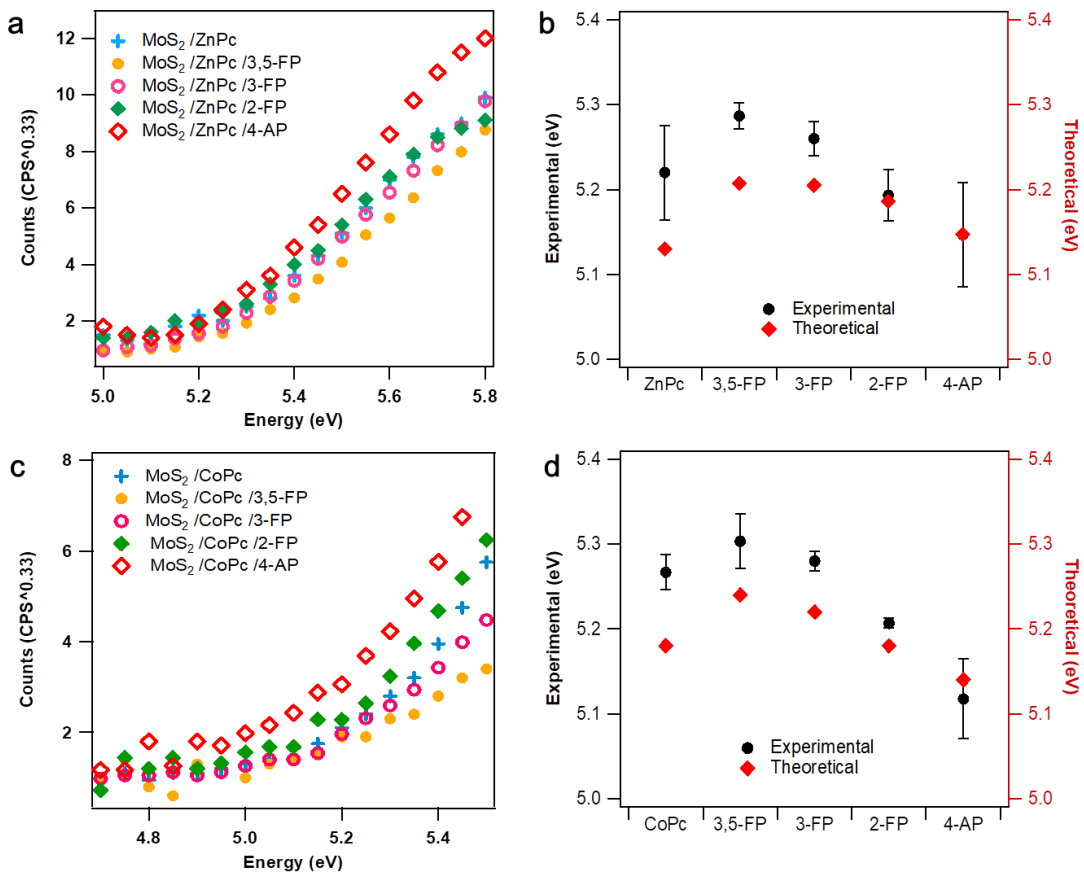

Figure 8.14: Work function plots of (a) MoS_2/ZnPc/fPys and (c) MoS_2/MPc/fPys measured by PhotoElectron Yield counter operating in Ambient conditions (PEYA). For the sake of comparison, work function values of (b) MoS_2/ZnPc/fPys, and (d) MoS_2/MPc/fPys computed by DFT calculations are also depicted.

Not only the electrical properties in MoS_2 are strongly influenced by ligand-induced dipoles, but also the optical properties are greatly affected. The direct bandgap at K point enables strong

photoluminescence (PL) emission in monolayer MoS_2. Typical PL spectra of monolayer MoS_2 can be found in **Figure 8.15**. We could find two major peaks originated from spin-orbit splitting of transition metal, one at lower energy, denoting A exciton peak, and the other, the B exciton peak, at higher energy. Referring to the literature,[35,122,187,245] A exciton peak could be split into two components after Lorentzian fitting, which are noted as X^- at around 1.83 eV, and X at around 1.87 eV. The ability of binding an extra electron to neutral exciton X (one electron binds with one hole) gives rise to the negative trion X^- with binding energy of around 40 meV in room temperature, when the charge carrier density in monolayer MoS_2 is in excess of electrons. Hence, the switching of intensity of trion and exciton mirrors the balance between electrons and hole in MoS_2 sheets, in other words, the doping level in MoS_2. We are able to quantify the trion weight γ by

$$\gamma = \frac{I_{X^-}}{I_{total}} = \frac{I_{X^-}}{I_{X^-} + I_X}$$

As is demonstrated in the left panel in **Figure 8.15a**, the electronic coupling of ZnPc on MoS_2 caused decrease in trion from 0.71 to 0.31, implying compensating of excessive negative charges in pristine MoS_2, inducing p-dope decreasing the electron. After coordinating fPys, 3,5-FP and 3-FP yielded a further decrease of trion weight (middle panel in **Figure 8.15a**), whereas 2-FP and 4-AP brought back the recombination of trion (right panel in **Figure 8.15a**). The quantified values of trion weight are plotted in **Figure 8.15b**. Unfunctionalized pyridine whose dipole moment induced by the functional groups is considered to be 0 showed trion weight between 3-FP and 2-FP after coordinating with ZnPc, indicating that the inversion of sign of dipole 2 could alternatively influence the regulation of trion weight. Similarly, in **Figure 8.15c** and **8.15d**, despite the severe suppression of the formation of trions after doping with CoPc, the coordination of fPys led to a similar trend observed for ZnPc, but in a smaller value range.

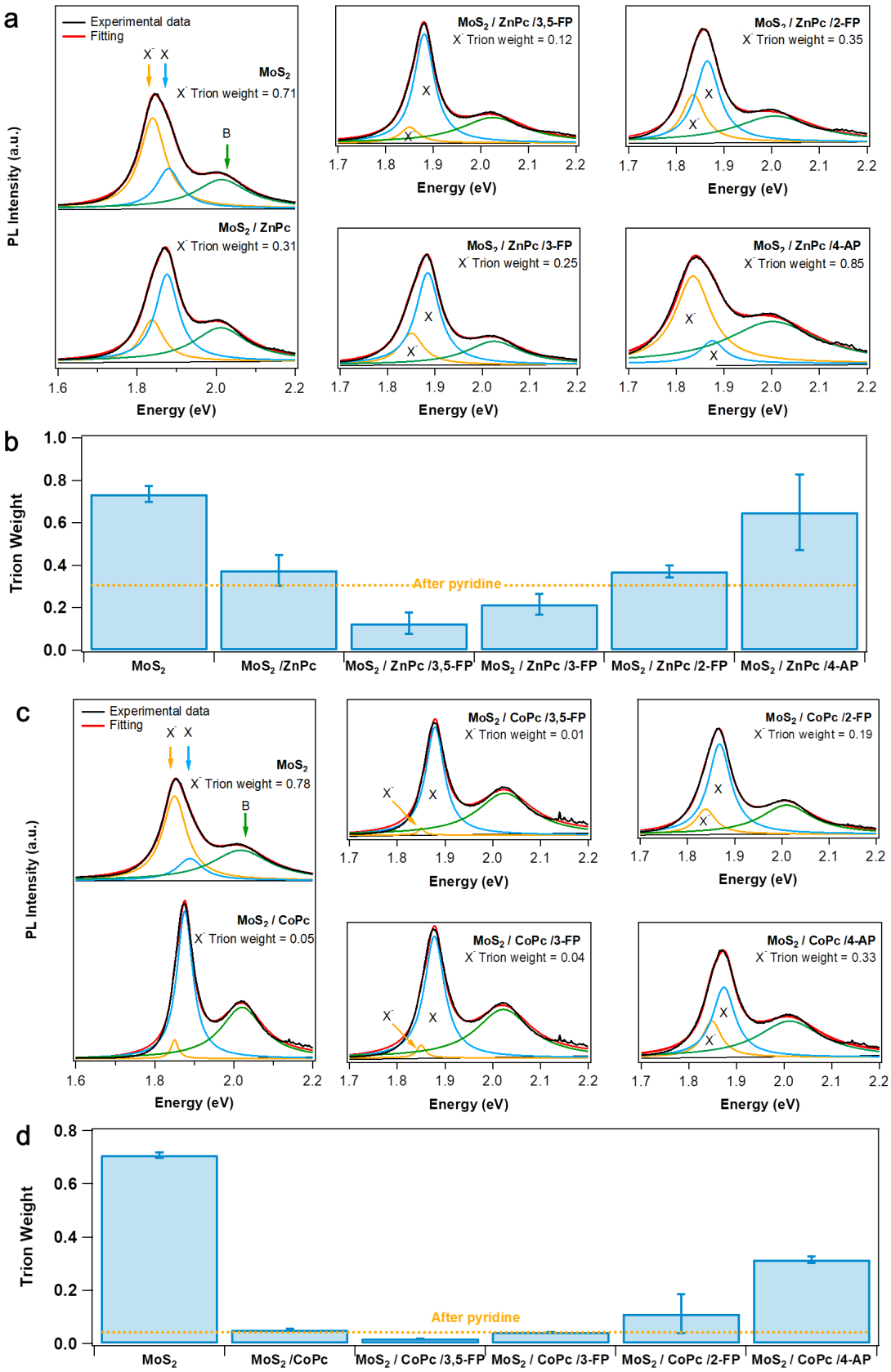

Figure 8.14: Photoluminescence spectra of (a) MoS_2/ZnPc and (c) MoS_2/CoPc coordinated with fPys. (b) and (d) average trion weight of each ligand coordinated heterojunction with ZnPc and CoPc, respectively.

To exclude the doping originated from physisorption of pyridines and solvents, we performed control experiments without MPcs with the same experimental procedures whose results are portrayed in **Figure 8.16**. In particular, similar results were found when doing blank tests with MoS_2 based FETs coated by fPys, in absence of templating MPcs. Upon thermal annealing treatments, the fPys were found to desorb leading to negligible doping effects of the MoS_2. The only small amount of fPys remained on the surface possess a random geometrical configuration without alignment of molecular dipoles, thus eliminating the molecular gating effect induced by a collective process. The trion weight can be translated to charge carrier density by means of the mass action model. The correlation of $\Delta\gamma^-$ and charge transfer value can be estimated by:

$$\frac{N_X n_{el}}{N_{X^-}} = \left(\frac{4m_X m_e}{\pi\hbar^2 m_{X^-}}\right) k_B T exp\left(-\frac{E_b}{k_B T}\right) \quad (4)$$

where N_X and N_{X^-} are the population of excitons (X) and trions (X^-). n_{el} is the electron density and E_b is the binding energy of trion (~20 meV). T is the temperature (78 K). m_X , m_{X^-} and m_e are effective masses of exciton, trion and electron respectively. Considering $m_e \approx 0.35m_0$ and $m_h \approx 0.45m_0$, , m_X and m_{X^-} can be calculated as $m_X = m_e + m_h = 0.8m_0$, and $m_{X^-} = 2m_e + m_h = 1.15m_0$. Hence, the trion weight can be expressed as

$$\frac{I_{X^-}}{I_{total}} = \frac{\frac{\gamma_{tr}}{\gamma_{ex}}\frac{N_{X^-}}{N_X}}{1 + \frac{\gamma_{tr}}{\gamma_{ex}}\frac{N_{X^-}}{N_X}} \approx \frac{1.5 * 10^{-15} n_{el}}{1 + 1.5 * 10^{-15} n_{el}}$$

where γ_{tr} and γ_{ex} are radiative decay rates of trion and exciton, respectively.

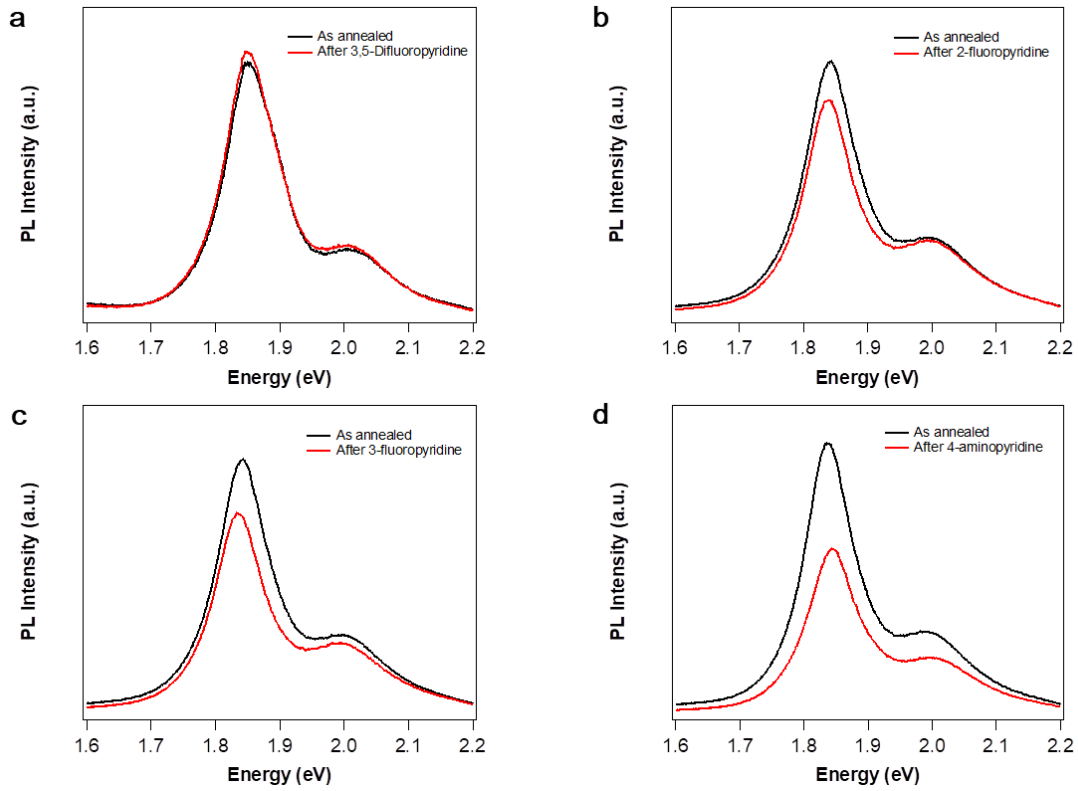

Figure 8.16: Control experiment of PL measurements of monolayer MoS_2 on which fPys has been physisorbed without MPcs serving as supporting layer for the ligands. For each case, the PL spectra has been recorded just after molecular physisorption and subsequently to a thermal annealing process aimed at desorbing the weakly tethered molecules. Such desorption turned out to be successful as evidenced by the negligible doping effect which is observed. Molecules physisorbed: (a) 3,5-FP, (b) 2-FP, (c) 3-FP, and (d) 4-AP.

	MoS_2/ZnPc	**MoS_2/CoPc**
3,5-FP	-5.81	-0.83
3-FP	-3.37	-0.25
2-FP	1.14	1.55
4-AP	10.34	7.22

Table 8.2: Charge carrier density change of MoS_2/MPc heterostructures tuned by fPys calculated from PL measurement. The unit is in $10^{12}/cm^2$.

We found approximate values as in FET analysis (shown in **Table 8.2**), confirming that molecular dipole induced doping by fPys is very little affected by the optical properties of MPcs.

Furthermore, Raman vibrations of monolayer MoS_2 were also found to be sensitive to the coordination of fPys. Two main Raman modes of undoped MoS_2 were measured, i.e. the out-of-plane E^1_{2g} mode at ~386 cm^{-1} and the in-plane A_{1g} mode at 405 cm^{-1}. Compared to the bare MoS_2, the addition of MPc resulted in small blueshift in A_{1g} peak and nearly no change in E^1_{2g} peak (**Figure 8.17**). It is reported in the literature that doping could affect the A_{1g} mode in higher extent than E^1_{2g} mode, thus yielding shifts in peak position. The redshift corresponds to the increase in electron concentration which softens the Raman vibration, and the blueshift corresponds to decrease of electron concentration which hardens the vibration.[244] The ligands, accordingly, led to non-negligible shift in A_{1g} modes. As shown in **Figure 8.18a**, 3,5-FP and 3-FP blueshifted the A_{1g} peak for 0.402 cm^{-1} and 0.120 cm^{-1} respectively, indicating p-doping. 2-FP and 4-AP induce redshift of 0.213 cm^{-1} and 0.564 cm^{-1}, reflecting n-doping. The observed effect is in perfect agreement with FET analysis, DFT calculation and PL measurements providing an unambiguous evidence that MPcs p-dopes the pristine MoS_2. The average Raman shift of A_{1g} peak between different fPy ligands could be as much as 0.966 cm^{-1}, while the E_{2g} peak remained constant under the influence of molecular dipoles. (**Figure 8.18b**). The full width at half maximum (FWHM) of A_{1g} peak was also found to be broadened by n-doping and sharpened by p-doping, demonstrated in **Figure 8.18b**. This could be explained by enhanced electron-phonon coupling of A_{1g} mode by increasing the electron density in MoS_2. The variation of FWHM could attain ~1 cm^{-1} by changing the functionalized ligand.

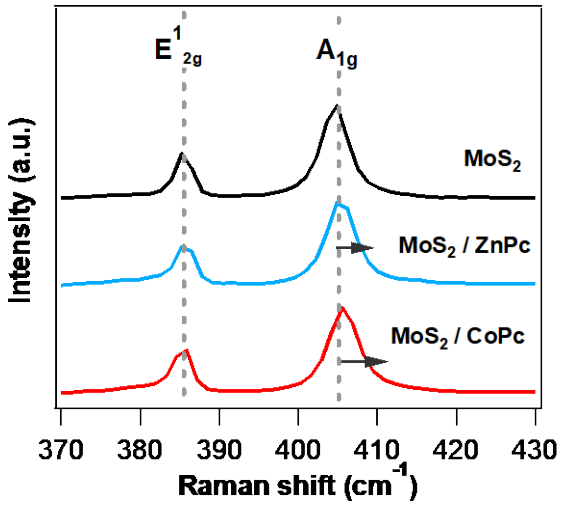

Figure 8.17: Raman spectra of MoS_2/ZnPc and MoS_2/CoPc compared with bare MoS_2 showing a slight blueshift in A_{1g} peak and no shift in E^1_{2g} peak.

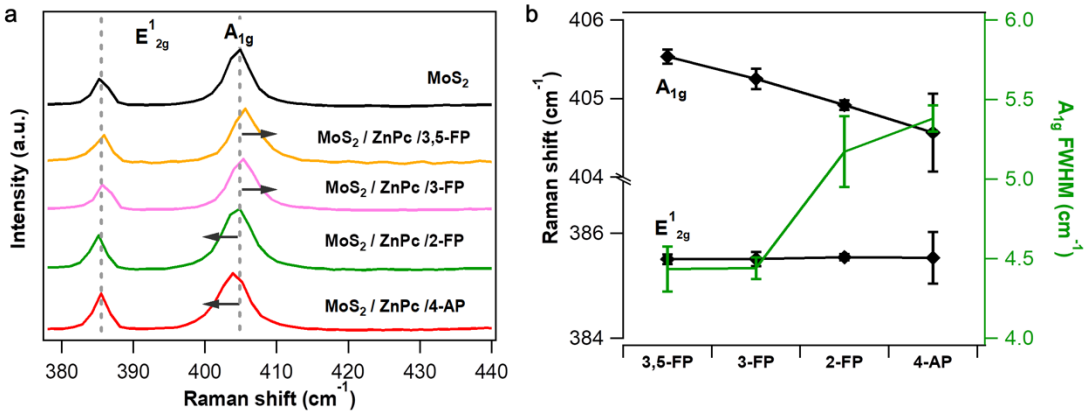

Figure 8.18: (a) Raman spectra of pristine MoS_2 and functionalized with ZnPc/fPys. (b) Plot of the shift in E^1_{2g} mode and A_{1g} mode, and the variation of full width of half maximum (FWHM) of A_{1g} peak upon the functionalization by different fPy ligands.

8.4 Conclusions

In summary, we have demonstrated a new strategy for doping 2D semiconductors by combining supramolecular self-assembly at surfaces, coordination chemistry and molecularly driven electrical gating. Aligned molecular dipoles having a precise orientation with respect to the basal plane of the MoS_2 surface were generated by taking advantage of the versatile functionalization of pyridine molecules and the geometry-controlled ligand binding direction in zinc and cobalt phthalocyanines. Electrical analysis, spectroscopic measurements and DFT calculations confirmed that not only charge transfer between axially functionalized MPc and monolayer MoS_2 participate in the tuning of properties, but also that the aligned dipole moments generated by pyridinic ligands play a much more important role in controlling the either n- or p-type doping of MoS_2 by modulating the charge carrier density up to $4.8 \times 10^{12}/cm^2$. Optical properties, such as exciton/trion switching and Raman features were found to be largely influenced by the molecular dipoles. Our results revealed how the variation of molecular dipole could strongly affect both the electrical and optical properties of underneath substrate material. A brand-new concept in realizing the controllable doping by organic molecules without the need of cumbersome synthesis or functionalization with complex chemical reactions has been proposed. The large magnitude of this doping effect is guaranteed by the collective nature of the dipole effect induced by the simultaneous alignment of a huge number of molecules yielding a nonlocal macroscopic effect. Our approach of molecularly tuned dipole induced doping is highly modulable and generally applicable to other 2D materials, thereby opening new avenues for enhancing the performances of 2D materials for applications in opto-electronics.

Chapter 9 Dynamic programmable 2D logic devices by self-assembled on-surface photoswitchable complex

9.1 Introduction

Nowadays, the vastly increasing demand of data manipulation requires tremendous numbers of computer units to fulfil efficient data processing and storage. The prevailing von Neumann architecture in computers reaches the bottleneck where the computing and memory units are physically separated rising the concerns for energy efficiency. Therefore, the in-memory computing, especially logic computing has also become highly demanding to adequately fit the requirements.[5,13,246] The construction concept of logic-in-memory (LIM) devices resides on incorporating non-volatile memory units, e.g. floating gate and ferroelectric gate on metal-oxide-semiconductor field-effect transistor (MOSFET) based logic gates.[247,248] In these devices, either by charging-discharging or by electrical polarization, the memory of logic is stored by electrically manipulating the control gate thereby influencing the current values in the channel. While the electrical control for endorsing memory in logic gates is efficient, other approaches of memory writing and reading, such as optical manipulation, are also necessary to add functionalities of the logic-in-memory computing, in particular, in extreme circumstances where optoelectronic memory is more facile to access.

One of the best candidate to achieve such goal is to establish optically controllable memory using photochromic molecular switches.[249-254] The light-induced photochromic changes could not only amplify the functionality of materials in work function tuning and reversible doping, but are also active elements in memory manipulation.[253,255-258] Common photochromic molecules include azobenzene, diarylethenes, stilbene, spiropyrans and their derivatives. The simple chemical structures of the molecules make them convenient to be blended or chemically grafted on organic semiconductors and polymers, ensuring the stability of the functionalization. Two-

dimensional (2D) materials are a better "partner" for the molecular switches, in view of their extraordinary physical and chemical properties. [259,260] Among them, transition metal dichalcogenides (TMDs) are most studied semiconducting 2D materials with layer-dependent bandgap, high field-effect mobility and I_{on}/I_{off} ratio. The variety of electronic properties of the TMD family makes it viable to build up N-MOSFET, P-MOSFET which are key components of binary logic devices. A number of organic molecules could be stably physisorbed on the atomically-thick, ultra-flat surface 2D TMDs by π–π stacking therefore inducing striking influences such as doping, forming van der Waals (vdW) heterostructures, etc.[191,261] The most representative photochromic molecule, azobenzene, have been used to functionalize graphene and MoS_2 leading to improved exfoliation, enhanced photoresponse and light-controlled doping, emission tuning, etc.[97,98,262-265] Especially, the reversible dipole-induced doping effect of azobenzene photoswitches which modulates the threshold voltages and channel current dynamically by light stimuli, makes it ideal to establish optoelectronic memory on 2D logic devices.

Azobenzene molecules have been tethered to the surface of 2D materials either covalently or non-covalently. In the former case it rises a concern of the low functionalization yield of azobenzene given the limited reactivity of 2D materials with organic species. In the latter case, the azobenzenes are closely packed lying flat on the 2D surface. As a result, the magnitude of dipolar change is not enough to ensure a large optoelectronic memory window on the 2D devices. An alternative strategy consists in the use of platform introduced in **Chapter 8** as a base and enchoring point to control the patterning, thus positioning, of azobenzenes by placing them at ca. 1 nm far apart adopting an upstanding conformation. More precisely, the distance of azobenzenes is governed by the distance of the target center, which is always much larger than the cross-section occupied by an up-standing azobenzene, thus the motion of azobenzenes is not hindered by the adjacent molecules and photoswithing could take place with a relatively great yield. Furthermore, the photoswitching can give rise to a collective effect given that the vertical azobenzenes are all aligned among each other, forming periodic structures, to maximize the influence on the electronic properties of 2D materials underneath. Several previous works show that triazatriangulenium (TATA) ions on surface could be an appropriate platform to bind azobenzene with ethinyl or phenyl spacers where the photoisomerization of freestanding azobenzene is observed by scanning tunnelling microscopy (STM).[95,266,267] Recently, this class of molecule has been proved to enhance Raman signals and modulate the work functions on 2D materials.[268,269] However, production of the TATA platform requires a multistep cumbersome synthesis, whereas a molecular assembly approach would be more convenient. Metal porphyrins and phthalocyanines, could also provide such functionality for growing axially-bonded azobenzene ligands in a more versatile

manner. Based on our previous work reported in **Chapter 8**, axial coordination of metal and functional pyridines is able to generate vertical electrical field to monolayer MoS_2 induced by different orientations and magnitudes of molecular dipoles taking advantage of the confinement of crystal field of octahedral transition metal *d*-orbital of zinc and cobalt phthalocyanine.[191] The method is also proved not long ago for stable growth of larger p-conjugated pyridinic ligands.[270] Our previous observations revealed that the dipole-induced doping of axially -coordinated pyridines could attain $10^{12}/cm^2$ of charge carrier density change to MoS_2, being comparable to traditional electron donor/acceptor molecules, ensuring a memory window of more than 20V on SiO_2 dielectric. Azobenzene molecules whose molecular dipole could easily be tuned by photoisomerization, is the best candidate in achieving collective dynamic doping on 2D materials. Therefore, in this work, we target at the design of a novel molecular switch in which the azobenzene ligand is oriented perpendicular to the 2D surface. The molecular platform is used to template the azobenezene growth enabling the precise construction of optoelectronic memory of 2D logic devices by collective molecular dipoles that are controlled by light.

9.2 Experimental methods

9.2.1 Sample preparation

Monolayer MoS_2, few-layer WSe_2 and graphene were mechanically exfoliated from commercially available crystals (Furuchi, Japan for MoS_2; HQ graphene for WSe_2; Materials Quartz, Inc for HOPG) using the scotch tape method and transferred on thermally oxidized heavily n-doped silicon substrates (Fraunhofer Institute IPMS, ρSi ~ 0.001 Ω·cm, tox = 270 nm). Their thickness was monitored by optical microscope combined with Raman spectroscopy and Atomic Force Microscopy (AFM). The samples were thermally annealed at 200 °C inside a vacuum chamber to desorb atmospheric adsorbates. CoPc are purchased from Merck. The MX_2/CoPc hybrids were realized by immersing monolayer MoS_2 into 0.5 mM CoPc in DMSO solution, then rinsed vastly with chloroform, acetone and IPA and thermally annealed in nitrogen to remove aggregates and evaporate solvents. To avoid the desorption of MPc on MX_2 when reacting with ligands in solvent environment, chloroform (which do not dissolve CoPc) was chosen to be the solvent for azopyridinic ligand. The MX_2/MPc heterostructures on Si/SiO_2 substrate were directly immersed into ligand solution at 40 °C for 12h followed by rinsing vastly with chloroform, acetone and IPA and thermal annealing in nitrogen. The functionalized samples are measured after being cooled down to room temperature.

4-(4-((4-(trifluoromethyl)phenyl)diazenyl)phenyl)pyridine (TFAP) is synthesized with the following steps. 4-(trifluoromethyl)aniline (400 mg, 2.48 mmol) were dissolved in CH_2Cl_2 (10 ml), a solution of Oxone® (1.525 g, 4.96 mmol) in water (5 ml) was added. The mixture was stirred at room temperature overnight. After that, the organic phase was washed with brine (3 x 25 ml). The solvent was evaporated under vacuum affording 1-nitroso-4-(trifluoromethyl)benzene as a greenish solid that was used without further purification. The crude was then suspended in acetic acid (20 ml) and 4-(pyridin-4-yl)aniline (337 mg, 1.98 mmol) were added and the reaction was stirred at room temperature under inert atmosphere for 24 h. The crude was basified with KOH (6 M) and extracted with ethyl acetate (3 x 25 ml) and the combined organic phases were washed with brine (2 x 50 ml). The solvent was eliminated under vacuum and the product was purified by column chromatography in hexane/ethyl acetate (10/6) obtaining the desired product as an orange powder (350 mg, 6 %).

9.2.2 UV-Vis spectroscopy

UV-Vis spectra in solution were recorded on JASCO V-670 spectrophotometer in 1 cm path quartz cuvettes. All the experiments were done using spectroscopic grade solvents. UV and visible light irradiation was done with an optical fiber-coupled LEDs (ThorLabs): for UV light λ_{max} = 367 nm, FWHM = 9 nm, for Vis light λ_{max} = 451 nm, FWHM = 20 nm. UV-Vis spectra on film are measured with CVD-grown monolayer triangle MX_2 film on double-polished sapphire (6carbon, China) without any further transfer process.

9.2.3 UPLC measurement

Chromatograms were recorded on an UPLC Ultimate3000 hyphenated to an HRMS (ESI+ Orbitrap) Executive Plus EMR system from Thermo Fisher Scientific. UPLC was run during 3.21 min using a gradient mode, starting with 98% of H_2O (0,05 % fromic acid) and 2 % and CAN (0,05% fromic acid) with an RP-C18 Hyper Gold Sil from Thermo Fisher at 1.15mL min^{-1}. The quantification of the different isomers was done by integration of all the ionic species generated by each compound. The fraction of the corresponding isomer was calculated as the area of the isomer divided by the area of the sum of both components and was expressed in %. (HRMS (ESI+): *m/z* calculated for $[TFAP]^+$ 328.1061 found 328.1056.)

9.2.4 Device fabrication

All electronic devices were patterned by photolithography (AZ1505 photoresist and MIF726 developer, Micro Chemicals) using laser writer LW405B from Microtech. For MoS_2 FET, 60 nm of gold were thermally evaporated with Plassys MEB 300 following a lift-off process in warm acetone to obtain the final source and drain electrodes. For WSe_2 FET, the electrodes were patterned with laser writer and 60 nm Pd was deposited with Egun evaporator Plassys ME300, after lift-off in warm acetone,. For MX_2 inverter, the NMOS were first fabricated by patterning the electrode and depositing 60 nm Au. The PMOS were then fabricated with the deposition of 60 nm Pd as electrode metal. The devices were rinsed with acetone and 2-propanol to remove resist residues. All devices were annealed under vacuum at 100°C to remove absorbents.

9.2.5 Electrical characterizations

The characterization of device performance was realized by Keithley 2636A and 2635A under N_2 atmosphere. The in-situ photoswitching is performed by a Polychrome V system (Thermo Fisher) used as monochromatic light source. The output power has been calibrated by a PM100A Power Meter (Thorlabs) where the 365 nm UV light to be 13.5 mW/cm^2 and 680 nm Vis light to be 15.5 mW/cm^2. All the electrical measurements were done in dark to exclude the photoconductive effect of 2D materials.

9.2.6 Raman and photoluminescence spectroscopy

Raman and photoluminescence spectra were carried out by Renishaw inVia spectrometer equipped with 532 nm laser. The excitation power was kept below 1 mW to avoid local heating damage effects. The wavenumber (energy) resolution was ~1 meV.

9.2.6 AFM measurement

AFM imaging was performed by means of a Bruker Dimension Icon set-up operating in air, in tapping mode, by using tip model TESPA-V2 (tip stiffness: k=42 N/m).

9.2.7 XPS measurements

CVD-grown monolayer triangle MX_2 film on Si/SiO_2 (6carbon, China) were applied for XPS measurement without any further transfer process. XPS analyses were carried out with a Thermo Scientific K-Alpha X-ray photoelectron spectrometer with a basic chamber pressure of ~10^{-9} mbar and an Al anode as the X-ray source (x-ray radiation of 1486 eV). Spot sizes of 400 μm and pass energies of 200.00 eV for wide energy scans and 10.00-20.00 eV for scans were used.

9.3 Results and discussions

Our designed molecular switch is composed of a macromolecular complex, cobalt phthalocyanine, and a pyridinic ligand containing azobenzene (4-(4-((4-(trifluoromethyl)phenyl)diazenyl)phenyl)pyridine, denoted as TFAP, as molecular switch motion unit (**Figure 9.1a**). The ^{1}H NMR and ^{13}C NMR spectrum of TFAP are shown in **Annex 2**. The UV-Vis absorption spectrum in chloroform shows the expected features for azobenzene derivatives with an intense band at 355 nm and broad low intensity band at 455 nm attributed to the π-π* and *n*-π*, respectively (**Figure 9.2a)**. Ultra-performance liquid chromatography coupled to high resolution mass spectrometry (UPLC-HRMS) measurement confirmed that the departing isomer is 100% *trans*-TFAP (**Figure 9.2b**). The *trans* to *cis* photoisomerization of TFAP was studied upon irradiation of a diluted solution with a UV led lamp (λ_{max} = 367 nm, 2.4 mW cm^{-2}). **Figure 9.2a** shows the variations of the light absorption due to the gradual transformation of the *trans* into the *cis* isomer. Notably, the band at 355 nm decreases while the band at 455 nm increases. Under the explored experimental conditions, the photo-stationary (UV-PSS) was reached after 12 min of irradiation (**Figure 9.2c-d**). Then, the back isomerization to the *trans* isomer was fully achieved upon irradiation with a visible led lamp (λ_{max} = 367 nm, 2.4 mW cm^{-2}). The photoswitching behaviour of the axial coordinated complex of TFAP ligand and CoPc (denoted as CoPc-TFAP) is displayed in **Figure 9.1b** where both the Q (630-700 nm) band B band (300-400 nm) of CoPc, and the π-π* band TFAP (350 nm) are presented. Similar to the photoswitching of TFAP, the π-π* band decreases and n-π* (455 nm) increases upon UV irradiation, and the absorption is recovered upon irradiation with visible light. Due to the overlap of the B band of CoPc and the π-π* band of TFAP (in accordance with literature [271,272]), even at photostationary state, a weak absorption at 300-400 nm is observed. The Q band is not affected by the photoisomerization of TFAP, indicating the absence of electronic coupling between the two choromophores.[271,273] The complex photoswitch at *trans* conformation intrinsically possess large molecular dipole moment by

bridging the strong electron-withdrawing property of the -CF_3 group far at the end of TFAP ligand. The photoisomerization of the complex triggers the rotation/inversion of N=N-C bond. The -CF_3 group is therefore driven closer to the 2D surface and yielding a shift of the molecular dipole. (**Figure 9.1c**). The modulation of the functional group distance and orientation brings to a distinct and collective change of collective molecular dipole from +3.55 Debye (pointing out of the basal plane of MX_2) to -1.40 Debye (pointing towards the basal plane of MX_2) for MoS_2 and from +3.42 Debye to -1.58 Debye for WSe_2, as is shown in **Figure 9.1c**. Such large molecular dipoles act as a local electrical gate to atomically-thin 2D material, introducing a decrease of the work function of MX_2 from 5.31 eV to 5.07 eV for MoS_2, and from 4.66 eV to 4.27 eV for WSe_2. The shift of work function could directly influence the drain-source current (I_{ds}) of the MOSFETs based on 2D MX_2 hence realizing program-read-erase process of the memory cell dynamically by external light stimuli. Here in this work, we demonstrate how the motion of molecular switches on the surface of 2D semiconductors could establish memorized electrical readout of field-effect transistors (FETs) of both N-MOSFET and P-MOSFET of 2D TMDs, and be applied in light-programmable logic-in-memory NOR gate based on these 2D MOSFET, thus realizing dynamic electrical switch without complex circuit fabrication.

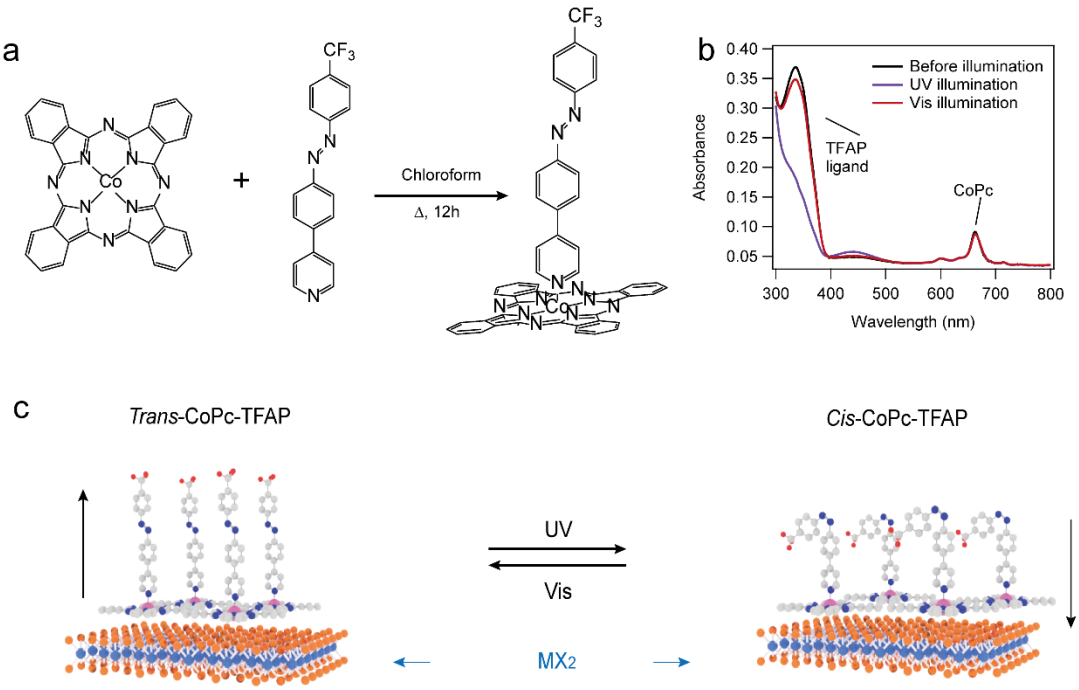

Figure 9.1: Light-induced motion of molecular switch on 2D surface. (a) Coordination of CoPc and photoswitchable TFAP ligand. (b) UV-Vis spectra of the switching of CoPc-TFAP complex in chloroform. (c) Scheme of the *trans* state and cis state molecular switch on MX_2 (M=Mo, W and X=S, Se) surface

controlled by light.

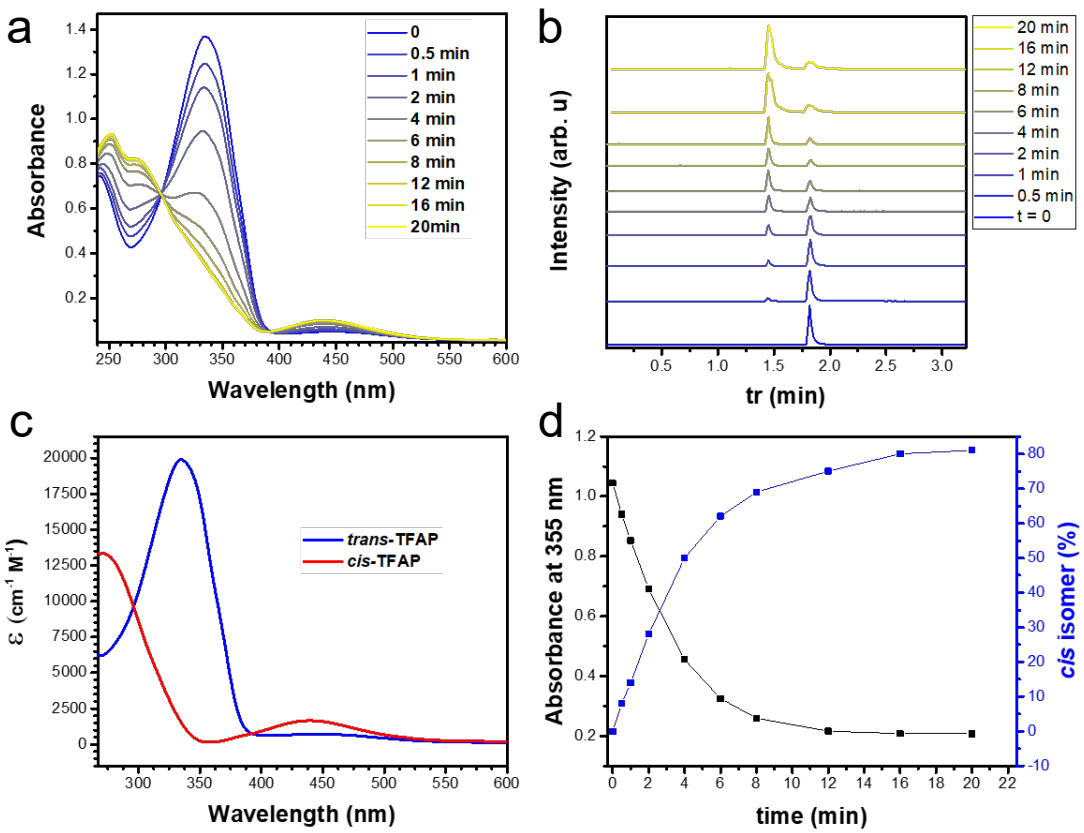

Figure 9.2: Trans to cis isomerization of TFAP. (a) UV-Vis absorption spectra of the TFAP ligand in DCM solution with irradiation of different time of 365 nm UV light. (b) UPLC spectra of TFAP irradiated with different time of 365 nm UV light. (c) Photostationary state (PSS) of UV-Vis spectra indicating composition of 19 % *trans* and 81 % *cis* under the studied conditions. (d) Plot of absorbance of 355 nm band and cis% at different irradiation time.

Before elucidating how molecular switches could serve as optoelectronic memory units of binary inverters, we first evaluate the influence on the building blocks of binary inverters: n- and p-type MOS (NMOS and PMOS). Here we use monolayer MoS_2 and few-layer WSe_2 as NFET and PFET. Previous works from our group showed that light-tunable molecular dipole could achieve the reversible doping by remote control of light.[80-82,98] Inspired by these findings, we manipulate our molecular switch as a dynamic doping controller for MoS_2 and WSe_2 transistor. We adopt the two-step on-surface axial ligand growth strategy from our previous work, as is shown in **Figure 9.3a**.[191] Unlike traditional approaches in functionalization of azobenzene switches on 2D

materials which suffers from the incomplete photoswitching due to the dense packing on surface, the TFAP ligand in the complex is freestanding with large conformational degree of freedom for switching from *trans* to *cis* conformation thanks to the large planar molecular area and spacing of CoPc self-assembly.[95,274-276] The metal phthalocyanines are able to self-assemble on 2D surfaces with the phthalocyanine ring parallel to the basal plane of 2D materials, as shown in **Figure 9.4**.[8,237,277] The pristine WSe_2 shows clean surface with roughness of 0.14 nm. The adsorption with CoPc platform indicates quasi-continuous film in small measure range, with the roughness mounting to 1.5 nm. Finally, the azobenzene-based assembly grown in such a molecular approach shows features of grain-like aggregates on surface. The islands were found by AFM imaging to have a periodic height profile ranging from 1.5 to 2 nm, corresponding well with the height of the molecular switch (**Figure 9.4**). XPS spectra show clear appearance of cobalt and fluorine after the functionalization (**Figure 9.5**).

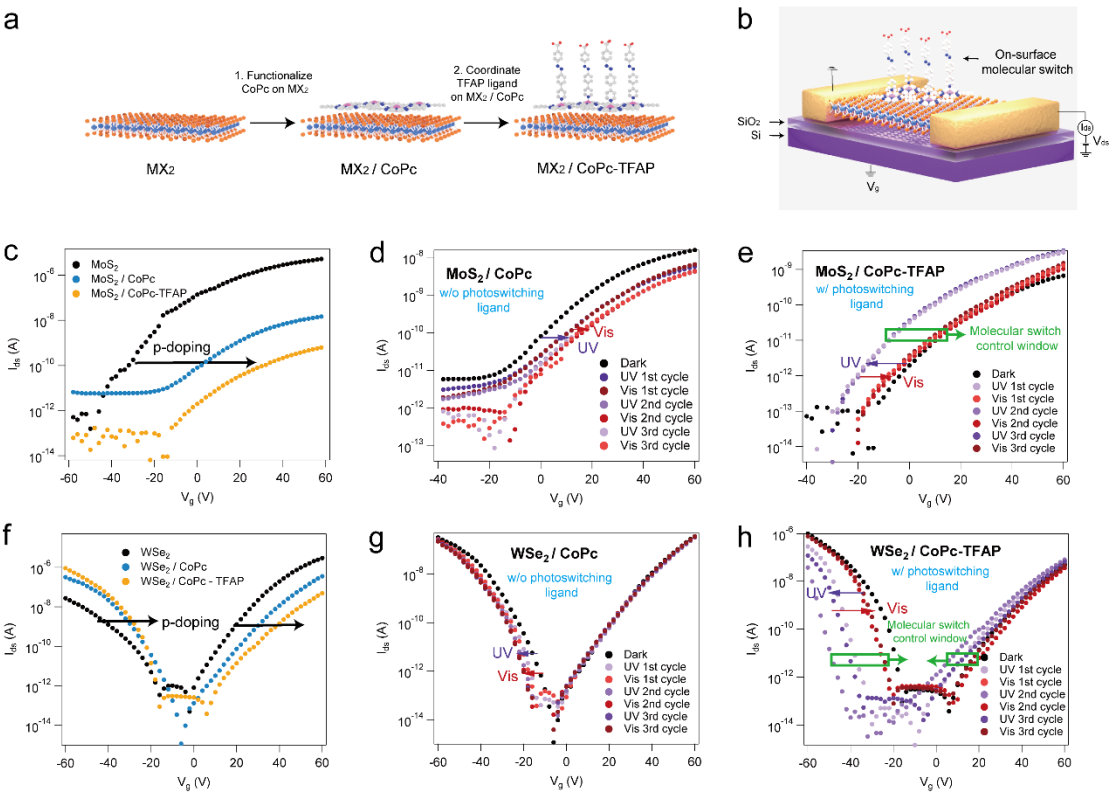

Figure 9.3: Molecular switch control over dynamic doping of MX_2 MOSFET. (a) On-surface growth of molecular switch. (b) Device structure of MX_2 MOSFET controlled by molecular switch. (c) I_d-V_g curve of MoS_2 MOSFET before and after each step of molecular switch growth. (d)-(e) Photoswitching of the molecular switch on MoS_2 (d)before and (e) after the coordination with TFAP ligand. (f) Id-Vg curve of WSe_2 MOSFET before and after each step of molecular switch growth. (g)-(h) Photoswitching of the molecular switch on WSe_2 (g) before and (h) after the coordination with TFAP ligand.

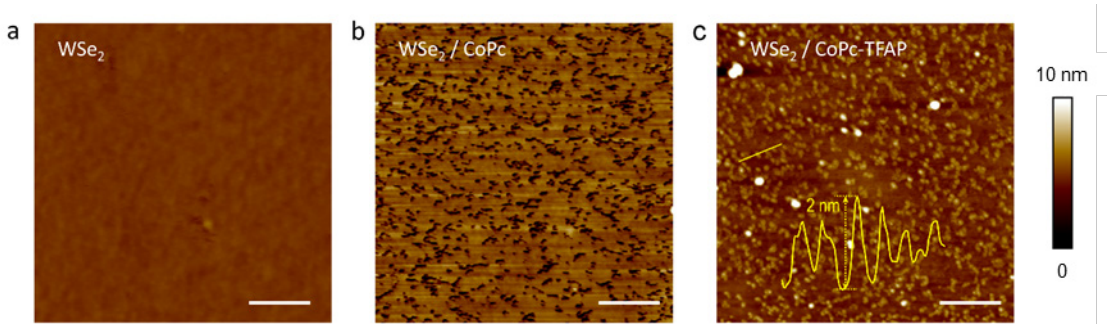

Figure 9.4: Surface morphology of molecular switch on the surface of WSe_2. High resolution AFM image of (a) pristine WSe_2, (b) WSe_2/CoPc and (c) WSe_2/CoPc-TFAP. The lateral scale bar is 200 nm.

The resulting molecular-switch-functionalized MX_2 MOSFET is depicted in **Figure 9.3b**. A distinct p-doping effect is observed after each step of functionalization with a final charge carrier density shift of 4.38× 1012/cm2 for MoS2 and 7.76 $\times 10^{11}/cm^2$ for WSe_2 (**Figure 9.3c** and **f**). In order to distinguish the doping caused by the light-induced charge transfer between CoPc and MX_2, and the one resulting the photoswitching of two states the molecular switch, we conducted UV and Vis switching cycles for both the MX_2/CoPc heterostructure with and without the TFAP ligand. As demonstrated in **Figure 9.3d**, the illumination by UV light induces a slight p-doping to MoS_2, corresponding to electron transfer from the conduction band of MoS_2 (4.1 eV) to the first reduction potential of CoPc (4.31 eV), while by illuminating with Vis light, the electron transfer is not recovered through the cycles. While for WSe_2, the major charge carrier being hole, we observe a slight irreversible photoinduced hole transfer from the valence band of WSe_2 (4.8 eV) to the first oxidation state of CoPc (5.5 eV) (**Figure 9.3g** and **Figure 9.6**).

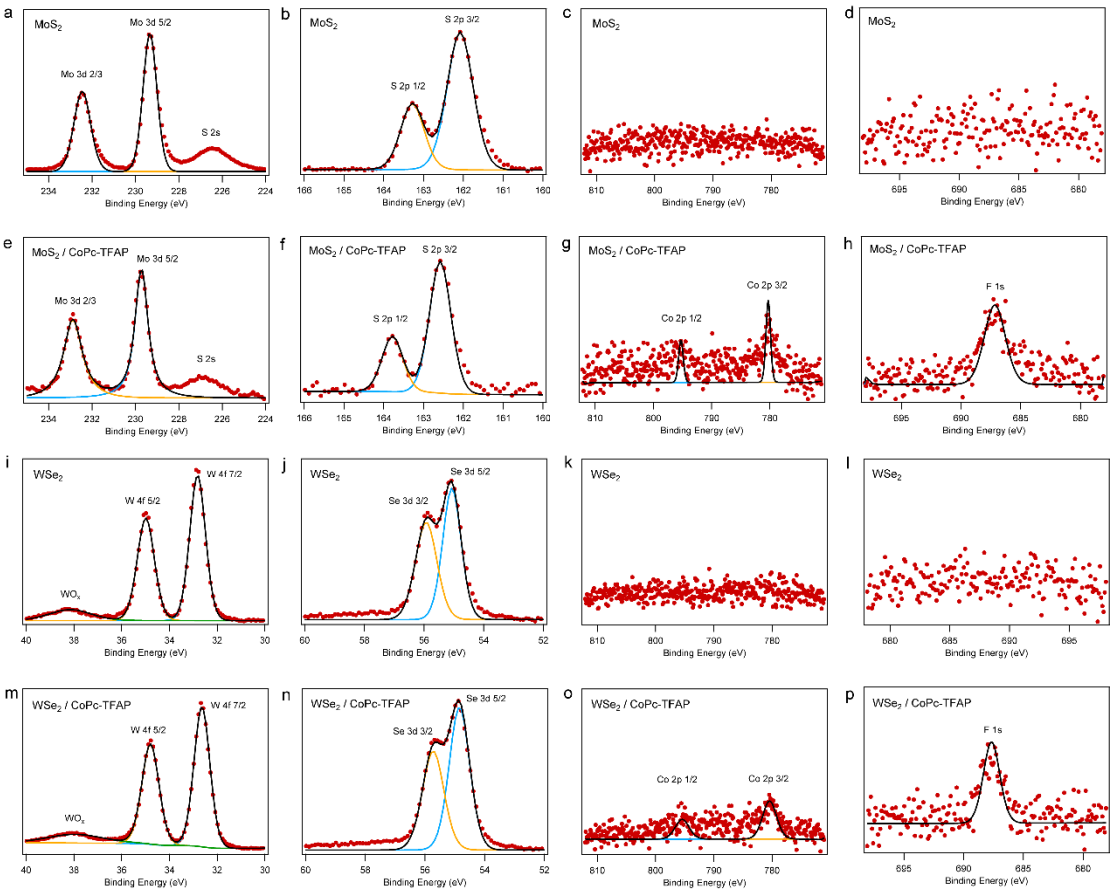

Figure 9.5: XPS spectra of pristine MX_2 and MX_2/CoPc-TFAP. (a)- (d) High-resolution XPS spectra of (a) Mo 3d, (b) S 2p, (c) Co 2p, (d) F 1s of pristine MoS_2. (e)- (h) High-resolution XPS spectra of (e) Mo 3d, (f) S 2p, (g) Co 2p, (h) F 1s of MoS_2 with CoPc-TFAP molecular switch on top. (i)- (l) High-resolution XPS spectra of (i) Mo 3d, (j) S 2p, (k) Co 2p, (l) F 1s of pristine WSe_2. (m)- (p) High-resolution XPS spectra of (m) Mo 3d, (n) S 2p, (o) Co 2p, (p) F 1s of WSe_2 with CoPc-TFAP molecular switch on top.

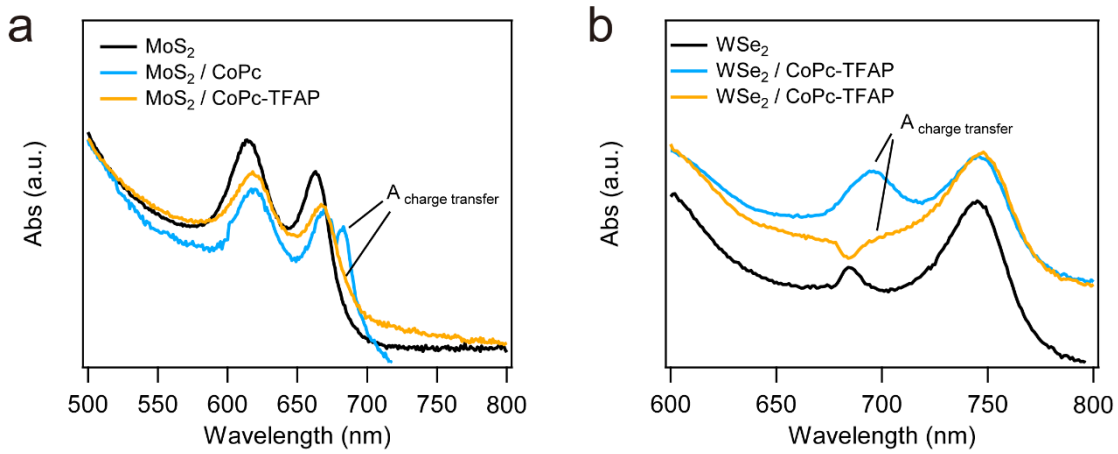

Figure 9.6: UV-Vis spectra of molecular switch on MX_2 on sapphire. (a) UV-Vis absorption of CoPc and CoPc-TFAP on CVD monolayer MoS_2. (b) UV-Vis absorption of CoPc and CoPc-TFAP on CVD monolayer WSe_2. Additional charge transfer peak appears at 680 nm and 700 nm between CoPc complex and MoS_2, and WSe_2, respectively.

After adding the photoswitching ligand TFAP on MX_2/CoPc, as shown in **Figure 9.3e** and **h**, the light induced state transition of on-surface molecular switches creates a dynamic doping control window of averagely $(1.18 \pm 0.79) \times 1012/cm2$ for MoS2 and $(4.37 \pm 0.48) \times 10^{11}/cm^2$ for WSe_2 (statistical analysis see **Figure 9.7**).

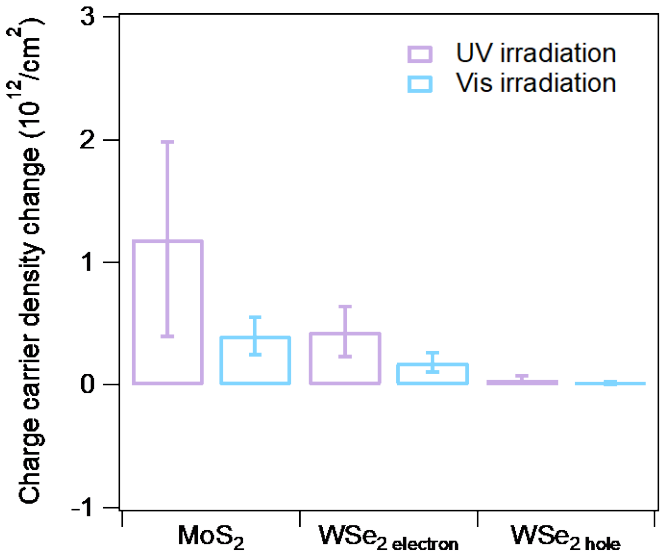

Figure 9.7: Statistical analysis of charge carrier density modulation of MX_2/CoPc-TFAP by UV and Vis irradiation.

The direction change of dipole moment from *trans* state to *cis* state creates a collective effect which is reflected on the threshold voltage (V_{th}) shift with light manipulation. The photoconductive and the persistent photocurrent effect of MX_2 on SiO_2 dielectric is excluded in our experiments, as is shown in the control experiment with graphene MOSFET which has no photoconductive effect due to its zero bandgap (**Figure 9.8-9.9**).

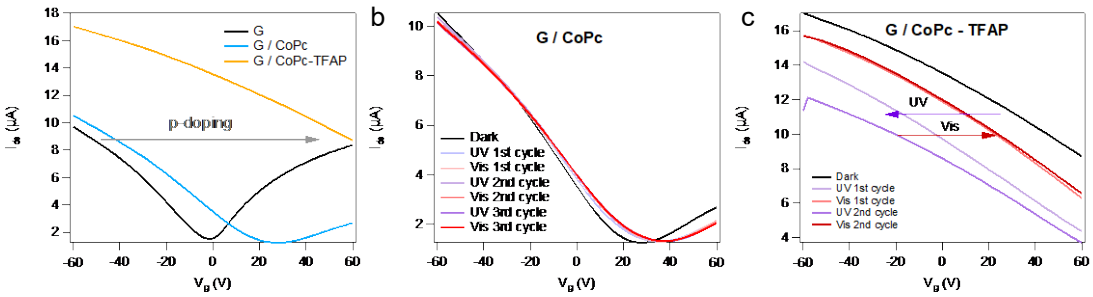

Figure 9.8: Control experiment of the molecular switch photoswitching on graphene FET. (a) I_d-V_g curve of graphene FET before and after each step of molecular switch growth. (b)-(c) Photoswitching cycles of the molecular switch on graphene (b)before and (c) after the coordination with TFAP ligand.

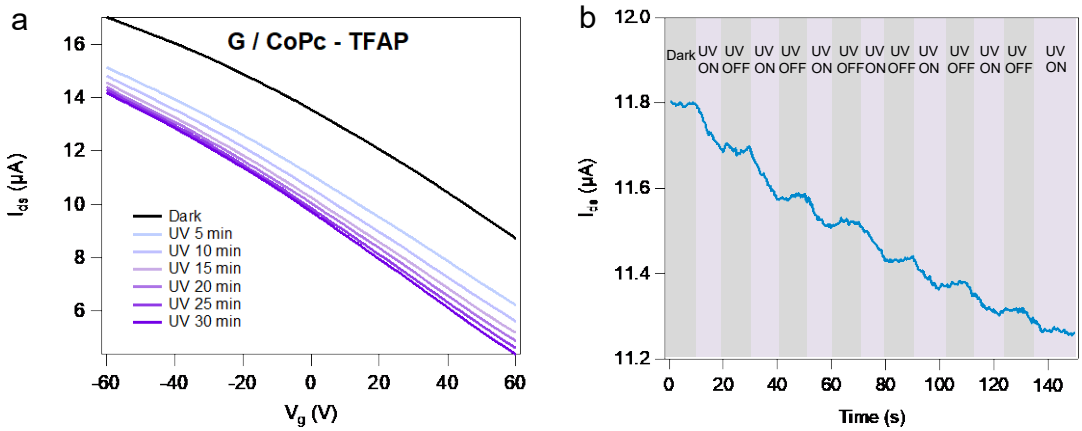

Figure 9.9: Time-dependent doping of graphene by molecular switch. (a) Transfer curve of G/ CoPc-TFAP FET of different UV illumination time. (b) Time-dependence Ids at V_g=0 V with 10s UV pulse cycles of G/ CoPc-TFAP FET.

Furthermore, we have observed an opposite V_{th} shift with pure TFAP ligand randomly physisorbed on the surface without any special confinement (**Figure 9.10**). The molecular switch controlled dynamic doping is also reflected in the optical properties of MoS_2, as is displayed in **Figure 9.11**.

In essence, by controlling the movement of the molecular switches remotely by light, one can achieve transistors with dynamic threshold voltage control, which is beneficial for its use in smart electronics.

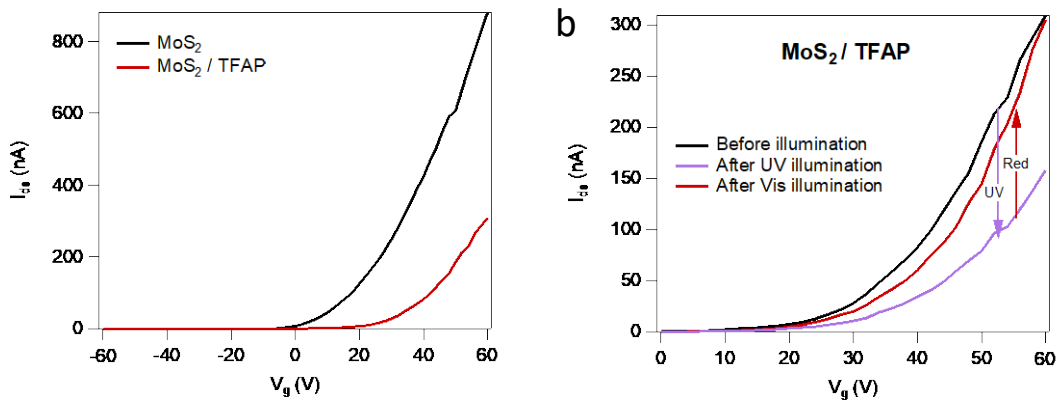

Figure 9.10: Control experiment of the photoswitching properties only with TFAP. (a) Transfer curve of pristine MoS_2 and MoS_2 only with physisorbed TFAP. An obvious p-doping is observed from the presence of $-CF_3$ group in TFAP (b) Transfer curve of MoS_2/ TFAP illuminated with UV and Vis light. The opposite doping direction compared to MoS_2/CoPc-TFAP indicates that the aromatic sector in TFAP results in a π-stacking on 2D surfaces without the direction confinement of metal-pyridine bond, therefore, with the rotation of N=N bond with response to UV light, there is an increase of dipole moment pointing out of the basal plane of MoS_2, inducing the decrease of work function.

The direct bandgap in monolayer MX_2 results in strong photoluminescence at room temperature. The intense PL peak corresponds to the A exciton in the monolayer, as is shown in the orange and blue line in **Figure 9.9**. By fitting the A exciton peak with Lorentzian, two distinct peaks, namely neutral exciton (X^0) at 1.88 eV and trion (X^-) at 1.84 eV are presented. The intensity of these two peaks depends largely on the doping level in the monolayer.[30,191,223] The trion (X^-) weight could be calculated as follows:

$$X^- \text{ weight} = \frac{I_{X^-}}{I_{total}} = \frac{I_{X^-}}{I_{X^-} + I_{X^0}}$$

The correlation of trion weight change and charge carrier density can be estimated by *mass action model:*

$$\frac{N_X n_{el}}{N_{X^-}} = \left(\frac{4m_X m_e}{\pi\hbar^2 m_{X^-}}\right) k_B T exp\left(-\frac{E_b}{k_B T}\right)$$

where N_X and N_{X^-} are the population of excitons (X) and trions (X^-). n_{el} is the electron

density and E_b is the binding energy of trion (~20 meV). T is the temperature (298 K). m_X , m_{X^-} and m_e are effective masses of exciton, trion and electron, respectively. Considering $m_e \approx 0.35m_0$ and $m_h \approx 0.45m_0$, m_X and m_{X^-} can be calculated as $m_X = m_e + m_h = 0.8m_0$,and $m_{X^-} = 2m_e + m_h = 1.15m_0$. Hence, the trion weight can be expressed as

$$\frac{I_{X^-}}{I_{total}} = \frac{\frac{\gamma_{tr}}{\gamma_{ex}}\frac{N_{X^-}}{N_X}}{1 + \frac{\gamma_{tr}}{\gamma_{ex}}\frac{N_{X^-}}{N_X}} \approx \frac{1.5 * 10^{-15} n_{el}}{1 + 1.5 * 10^{-15} n_{el}}$$

Therefore, a charge carrier density change in MoS_2 modulated by the molecular machine is estimated to be $6.08\times10^{11}/cm^2$, being similar to the value obtained with electrical measurements.

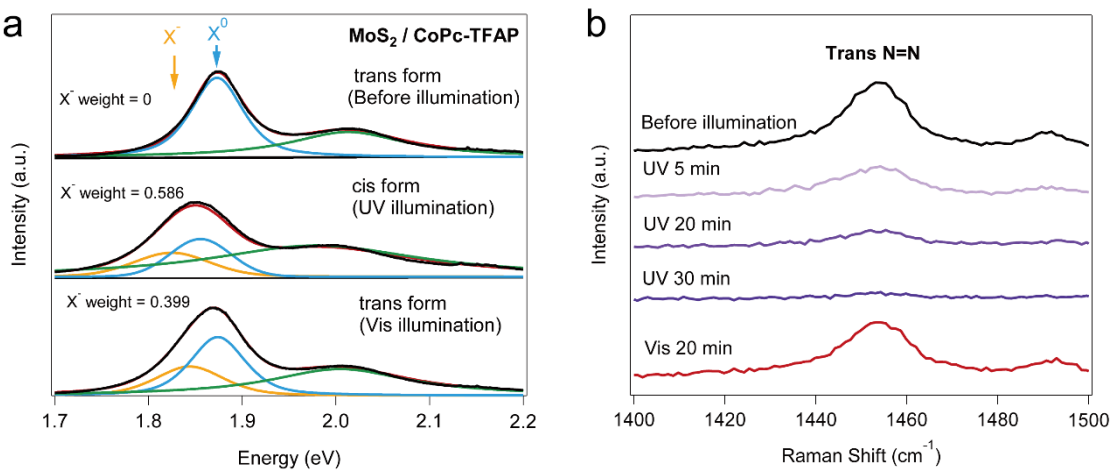

Figure 9.11: Optical properties of MoS_2 controlled by molecular switch. (a) Photoluminescence (PL) spectra of molecular switch on monolayer MoS_2 modulated by light illumination. (b) High wavenumber range of Raman spectra of molecular machine on monolayer MoS_2 modulated by light illumination. The trans-azo feature is present at 1450 cm^{-1}, the peak disappeared progressively by UV illumination and recovers by the Vis illumination.

In a word, by controlling the movement of molecular switch remotely with light, one can achieve transistors with dynamic threshold voltage control, which is beneficial for the use of smart electronics.

Based on previous discussions, our on-surface molecular switches could achieve dynamic control of threshold voltages by building optoelectronic memory window both on transistors of MoS_2 and WSe_2. It is essential to explore how they perform when these molecular-switch-controlled devices participate in electronic circuits. While a great demand of data storage and simultaneous fast

computing rised recently, logic-in-memory devices counts as an important element for semiconductor industry. Therefore, we build up a binary logic inverter (NOR gate) in which the MoS_2 and WSe_2 MOSFETs are in series in order to demonstrate for the first time a logic-in-memory device realized by molecular switches. The structure and the electrical circuit, and the optical microscope image of the inverter are demonstrated in **Figure 9.12a** and **Figure 9.13a**. Each MOSFET (NMOS being MoS_2 channel and PMOS being WSe_2 channel) shows unipolar transfer characteristics with $I_{on}/I_{off} > 10^5$ (**Figure 9.12b**) and both of their V_{th} shifts negatively at *cis* state compared to *trans* state. Note that only when WSe_2 under the thickness of 5 nm with high work function Pd contacts acts as p-type unipolar transistor in our experimental conditions. The V_{out} versus V_{in} of the inverter is presented in **Figure 9.12c** together with the gain shown in **Figure 9.13b**.

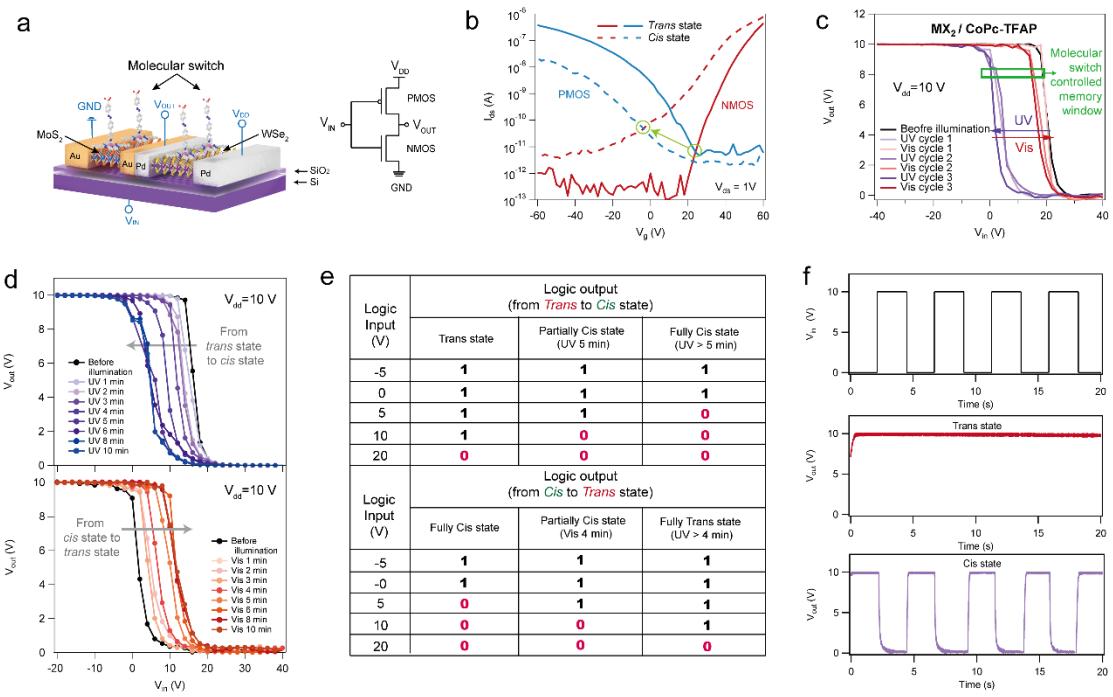

Logic Input (V)	Logic output (from *Trans* to *Cis* state)		
	Trans state	Partially Cis state (UV 5 min)	Fully Cis state (UV > 5 min)
-5	1	1	1
0	1	1	1
5	1	1	0
10	1	0	0
20	0	0	0

Logic Input (V)	Logic output (from *Cis* to *Trans* state)		
	Fully Cis state	Partially Cis state (Vis 4 min)	Fully Trans state (UV > 4 min)
-5	1	1	1
-0	1	1	1
5	0	1	1
10	0	0	1
20	0	0	0

Figure 9.12: Molecular switch enabled light-programmable logic-in-memory device. (a) Schematic representation and the circuit of molecular switch controlled MoS_2-WSe_2 binary inverter. (b) Transfer characteristics of the N- and P- MOSFET with the molecular switch on both trans state and cis state. (c) V_{out}-V_{in} of the inverter and the dynamic cycles controlled by the molecular switch. The green circle indicates two distinctive transition point from different switch states. (d) V_{out}-V_{in} of the programmable dynamic switching point transition of the inverter controlled by illumination time on molecular switch. (e) Summary of the programmable dynamic logic output states by manipulating the molecular switch motion with UV and Vis illumination time. The measurement is done at V_{dd}=10 V. The logic output "1" corresponds to V_{out}=10V and logic output "0" corresponds to V_{out}=0V. (f) Time-dependent V_{out} of the inverter with Vin pulse cycles at trans and cis state of

molecular switch showing distinct output signals in the two states. The cis state (metastable state) of molecular switch shows stability over gate electrical field.

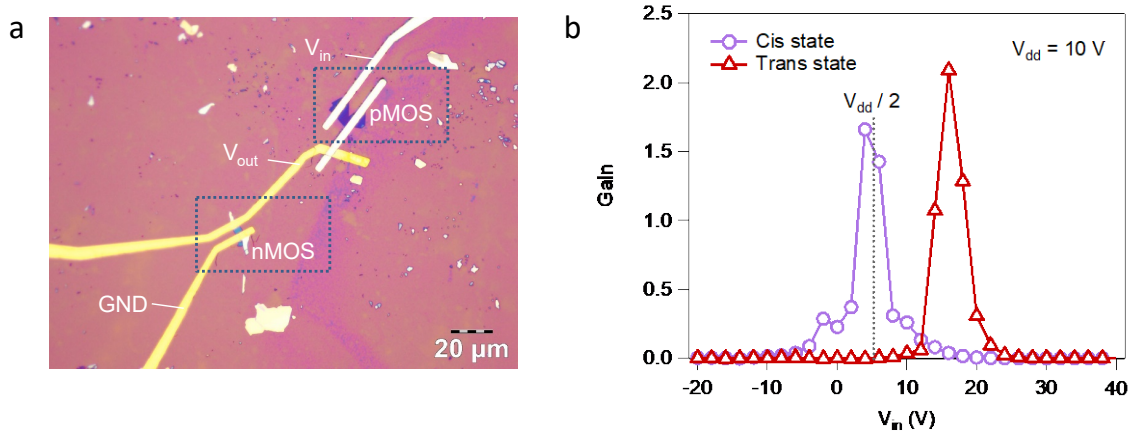

Figure 9.13: (a) Optical microscope image of MoS_2-WSe_2 inverter. (b) Voltage gain of the molecular controlled inverter at unfolded state and folded state of the molecular switch. The overall gain is smaller than in previously reported work because of the use of relatively low-k dielectric material (SiO_2).

The large dipolar doping from the *trans* conformation of molecular switch give rise to the transition point appearing in the range of +18 V to +20 V, showing high-skewed inverter characteristics. While by manipulating the motion of molecular switch to *cis* conformation, we could successfully adjust the transition point at V_{dd} / 2 (5V), reaching the critical performance of an ideal inverter. This shift of the inverter transition point is fully reversible through UV-Vis illumination cycles, creating a memory window of 20V. Here, the molecular switch could be considered as a light-programmable "molecular switch gate" in which the readout of the inverter underneath could be programmed and erased with different wavelengths of light. The existence of the memory window of the inverter is only attributed to the motion of azobenzene unit on the TFAP ligand in the molecular switch. While without the foldable ligand, the inverter shows static transition point even with long illumination time (**Figure 9.14**).

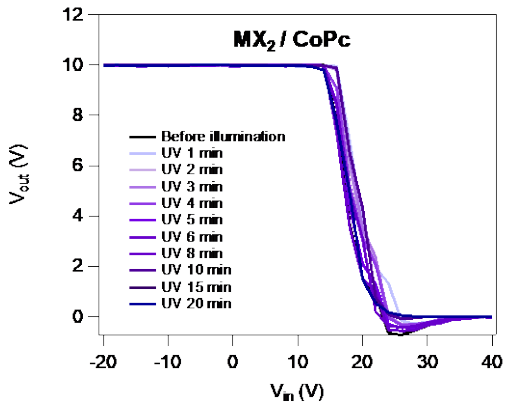

Figure 9.14: Vout-Vin of the inverter (MX_2/ CoPc) without the TFAP ligand. The inverter did not show distinct transition point shift with light illumination, indicating that the dynamic modulation is merely caused by the motion of TFAP ligand.

The shift is also time-dependent, according to the molecular kinetics of the TFAP ligand. As demonstrated in **Figure 9.12d**, the illumination time on the molecular switch is critical to the logic output that for the same V_{in}, V_{out} could be different according to the configuration of the molecular switch on surface. In this case, we realize a novel programmable logic device prototype by modulating the motion state of molecular switch, hence achieving dynamic logic output by UV-Vis illumination, other than the traditional floating gate technology. Taking advantage of the molecular switch motion dynamics, we could define three programmable memory states of the inverter where the molecular switch is at 1) *trans* state, (2) *partially cis* state, and (3) *fully cis* state. The logic output results are listed in **Figure 9.12e** where the molecular switch states programming generate different logic output values for the same input voltage, meanwhile reversible by changing the illumination wavelength. Furthermore, the programmable dynamic logic output could be maintained through input pulse cycles (**Figure 9.12f**) in long timescale and is reproducible among different devices (**Figure 9.15**), hence realizing the logic-in-memory manipulation in. whereas our fabrication process is less complex and costless and more tunable according to the large availability variation of molecular structures of molecular switches.[247,278]

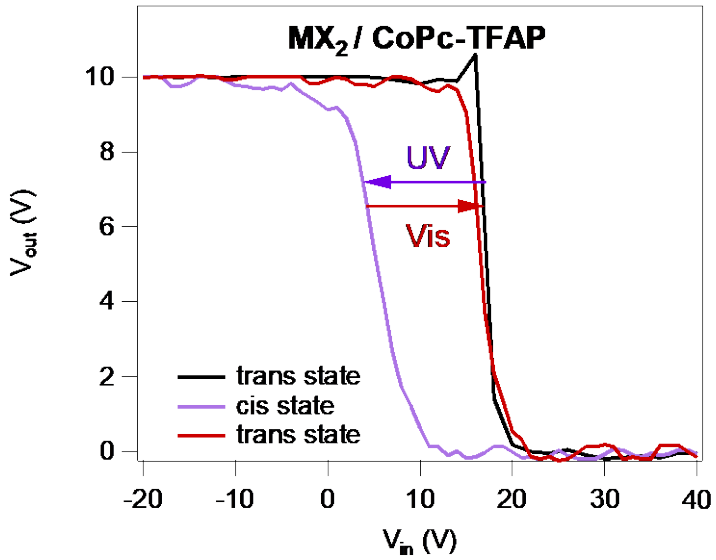

Figure 9.15: Molecular switch controllable dynamic binary inverter. Another device example of programmable dynamic logic output controlled by molecular switch.

9.4 Conclusions

In summary, we have demonstrated an innovative and revolutionary concept of functioning the on-surface molecular switch which is composed of metal phthalocyanine as self-assembly platform and a photoswitching azobenzene axial ligand to tune the properties two-dimensional semiconducting materials. The dynamic motion of our designed molecular switch could provide strong reversible doping to 2D semiconductors which is critical to field-effect transistors. Finally, the integration of molecular switch in logic circuits exhibits light-programmable dynamic logic output simply by modulating the light illumination. This work shows the first examples on the use of the versatility of molecular switch in logic-in-memory, which offers offering new solutions for the next-generation smart control of nano-devices.

Chapter 10 Conclusion and Outlooks

In this thesis, hybrid functional systems of organic molecules and two-dimensional (2D) semiconducting materials have been developed. A wide selection of 2D materials have been exploited as semiconducting platforms including monolayer transition metal dichalcogenides (MoS_2, WSe_2) to few-layer black phosphorus (BP) and indium selenide (InSe), carrying distinct electronic and optical properties. On the other hand, different organic molecules, have been chosen based on their unique properties that can be tailored via chemical synthesis. The choices of organic molecules varied from simple aromatic molecules, ionic alkyl chain (surfactants), to large complexes of metal phthalocyanine. The majority of these molecules are able to self-assemble onto the surface of 2D materials forming ordered architectures that can be used to explore collective characteristics to magnify the impact on the change of properties of the 2D semiconductor platform. Specifically:

- Optical and electronic properties of monolayer transition metal dichalcogenides could be tuned by the charge transfer between the 2D materials and aromatic solvent molecules. These physisorbed simple benzene derivatives bearing electron-withdrawing ($-CF_3$) or electron-donating ($-CH_3$) functional groups are able to shift the Fermi level of MoS_2 and WSe_2, which could only be observed by low-temperature photoluminescence (PL) spectra. The inversion of trion and exciton peak signals the quantification of the charge carrier density change in the material that induced by molecular doping. Not only did we revealed the power of molecules in tuning the electronic and optical properties of the 2D material, we have also defined the exciton, positive trion and negative trion peak position of monolayer WSe_2 at 78K for the first time, providing text-book results of studies. (**Chapter 5. Tuning the optical and electronic properties of monolayer transition metal dichalcogenides**)

- Electronic properties of few-layer black phosphorus (BP) could be largely influenced by common organic solvents. These daily-used solvent for cleaning, functionalization and nanofabrication are often neglected in evaluating an electronic device based on 2D materials, yet they could be stably physisorbed onto the 2D material giving great impact in doping. The solvents are found to be grouped in two classes: 1) small dipole moment molecules where the

doping direction, whether p- or n- doping, is stable within small variation. This include m-xylene, p-xylene, benzene, hexane and toluene; 2) large dipole moment molecules where the doping fluctuates among p- or n- doping, given the random distribution of the molecular dipole during the deposition. This include acetone, chloroform, ethanol and isopropanol. The doping is obviously observed in field-effect transistors (FET) which affects its functions in electronic circuits. This study provides referential results for related works in materials science and electronics. (**Chapter 6. Studying the solvent effect on few-layer black phosphorus**)

- Self-assembled ionic surfactants physisorbed on 2D surfaces are capable to induce electron doping to few-layer indium selenide (InSe) and to boost the field-effect mobility up to ~3000 cm^2/Vs. The molecular functionalization is extended to photodetectors based on InSe including prototypes of phototransistor, lateral asymmetric P-N Schottky diode, and vertical van der Waals (vdW) P-N junction based formed with BP and InSe. The photoresponse has witnessed exponential improvement attaining 10^6 A/W of responsivity (R) and photoresponse time down to < 1 ms. The functionalization by molecules to InSe is the first demonstration in literature for such highly beneficial result yet obtained by taking use of a simple solution-processable methods. By fabricating ultra-high-performance devices, we demonstrated that molecule-2D material hybrids could achieve similar or even better properties compared to sophisticated technologies, yet without expensive vacuum system and programmable logic controller (PLC) to modify fundamental changes. (**Chapter 7. Molecular-functionalized few-layer indium selenide for ultra-high-performance photodetectors**)

- Axially coordinated metal phthalocyanine complexes enables the alignment of molecular dipoles on 2D surfaces, in particular monolayer materials. The exerted electrical field is perpendicular to the basal plane of monolayer MoS_2 and considerably affect the electronic band structure of MoS_2, shifting the Fermi energy and induce doping in MoS_2 in different directions. Both p-doping and n-doping could be achieved by varying the magnitude and directions of the functional groups in the pyridine ligands where 4-aminopyridine and 3-fluoropyridine induce n-doping with negative molecular dipole, and 3-fluoropyridine and 3,5-difluoropyridine induces p-doping with positive molecular dipole. The findings show for the first time the combination of supramolecular complex chemistry with 2D materials electronics, creating a spatial influences at the z-axis on the flatland. (**Chapter 8. Collective dipole-dominated doping of MoS_2 via the supramolecular approach**)

- The molecular dipole doping could also be programmed to be dynamic, by exploiting the axial ligand with photoswitching units bonded to the metal atom in phthalocyanine ring. Conformational change of azobenzene with strong electron-withdrawing group results in opposite directions of molecular dipole compared to the 2D surfaces which induce doping in the opposite directions. The process is totally reversible by illumination with light. Both n-type MoS_2 and p-type WSe_2 FET are proved to be effectively dynamically doped under the photoswitchable ligand change. The dynamic process of doping enables us to design a light-controlled logic-in-memory device by connecting MoS_2 and WSe_2 FET in series. The optoelectronic memory of azobenzene ligand could create a memory window as large as 20V, acting as a light-triggered molecular floating gate. This indicates that without complicated techniques for fabricating of dielectric-metal-dielectric inorganic floating gate, the photoswitchable molecules are able to augment functionalities to traditional binary inverters in equal dimension. (**Chapter 9. Dynamic programmable 2D logic devices by self-assembled on-surface photoswitchable complex**)

With these exemples we have proven the great versatility and immense power of molecules and assemblies thereof to induce major modulations of the physical properties of 2D semiconductors, also in a dynamic manner, which is instrumental for sophisticated applications in smart opto-electronics. On the short-term, to cast even further light onto the hybrid systems studied in this thesis, some additional investigations can be performed, for exploring even further the funcdamenntal characteristics. This may for example include step forward starting from the project presented in Chapter 9, including:

- elucidating the mechanism of dipole doping by CoPc-TFAP molecular switch on MoS_2 and WSe_2.
- studying the novel dual-Schottky diode of WSe_2 in detail by measuring the Schottky barrier height of both Pd-WSe_2 and Ag-WSe_2 contacts.

On the long-term, on the topic of this thesis work there are still a great number of challenges and problems to be tackled, including both those concerning fundamental properties and some others which are more application-oriented ones.

In the past years, researchers have made two-dimensional materials again rising stars as the hosts of a bunch of new physical phenomenon after the isolation of graphene in 2004 by Manchester

researchers. This time, more sophisticated yet exciting findings in condensed matter physics, in the field of twisted graphene led by Y. Cao.[18,279,280] In 2D/molecule hybrids, there is a huge void of such fundamental studies in physics/physical chemistry since most of the works shift to application point of view due to the sophisticated behaviors of molecules on 2D materials that cannot be easily and directly visualized by the existing techniques.[281]In most previous works of 2D material/molecule hybrids, the focus is usually 2D materials and the molecules are always playing a supporting role to functionalize 2D materials. The integrated hybrid material or using 2D materials to functionalize molecules are seldom being discussed. A great chance of studying the exotic fundamental phenomenon of 2D material/molecule hybrids is foreseen in the future.

Not only 2D materials enable to unravel numerous unknown physical principles, but they are also attracting more attention for applications in nanoelectronics, energy storage, catalysis, etc. Yet there are still many obstacles in these applied fields which must be tackled.

- the major concern is the large-scale fabrication of high-quality mono-to-few layer 2D materials which is key for application in electronics. Though high quality graphene, MoS_2, WS_2 have been utilized in fabricating device arrays using CVD grown materials, few works have made them possible to make electronic circuits out of 2D materials possible. The expensive growth costs by CVD method and the poor performances could not guarantee these 2D materials to take over silicon. The additional gate dielectric deposition adds to the cost of fabrication. Moreover, as some high-performance 2D semiconductors, such as BP and InSe demonstrated in the thesis, suffer from the high reactivity with oxygen, large-scale growth becomes more difficult. Though laboratory-research have shown magnificent performances of 2D materials functionalized by molecules that are superior to almost all the other types of semiconductors in the world, the problems discussed above all hinder the way for 2D electronics to step into the market although almost 20 years have passed since the emergence of this field.

- Another issue of the future development of the field is to solve the stability of the 2D materials against air degradation. Encapsulation approaches have been attempted in previous years by oxide (e.g. Al_2O_3) and polymers (e.g. PMMA) or insulating 2D materials (e.g. h-BN). Molecular approaches are also a large branch for preventing the interactions with oxygen and water in air. However, the long-term stability of both chemical and physical properties of 2D materials encapsulated by the molecules is still problematic. Since molecules are able to add functionalities to 2D materials without complex systems, the direction to solve the instability

problem of 2D materials with molecular approach would be a breakthrough for this field.

The combination of molecules and 2D materials are far from being fully exploited. As soon as new molecules, new materials, or new physical properties out of the traditional tool-box are discovered, new phenomenon of molecule-material hybrid systems at the atomic scale emerge.

Annex

1. Light intensity adjustment of monochromator

area: 0.01 cm2	10%	100%	20	30	40	50	60	70	80	90
fixed distance (9 mm)	uW	uW	uW	uW	uW	uW	uW	uW	uW	uW
300	0.38	2.37	0.73	1.08	1.39	1.65	1.85	2.05	2.2	2.31
305	0.5	3.67								
310	1.18	8.2								
315	2.82	18								
320	5.32	33	11	16.5	21.2	24.9	27.6	29.9	31.5	32.5
325	8.3	50.9								
330	11.2	69.4								
335	13.9	86.4								
340	16.2	101.9								
345	18.4	116								
350	20.2	128.6	41.7	62.7	80.7	95.2	105.7	115	121.5	125.8
355	22	140.6								
360	23.4	150.4								
365	24.9	160.2								
370	26.7	172.7								
375	28.3	182.4								
380	30.5	196.6								
385	32.8	210.3								
390	35.2	225.5								
395	37.5	241.5								
400	39.4	255	81.2	122.1	157.6	186.6	207.9	227.2	240.5	249.5
405	41.1	266.2								
410	42.7	276.8								
415	44.5	288.6								

420	45.8	297.1								
425	46.7	303.1								
430	47.4	307.8								
435	47.7	312.6								
440	48.7	322.5								
445	51.7	336.3								
450	53.5	350.7	110.2	165.6	214.1	253.9	284.1	310.2	329.9	342.9
455	56.8	370.8								
460	61.2	397.5								
465	65.6	419.7								
470	63.7	418.2								
475	61.4	404.5								
480	57.5	386.4								
485	58	378								
490	55.6	369.4								
495	54.5	358.5								
500	52.3	346.5	107.9	162.4	210.8	250.3	280.1	307.2	325.6	338.6
505	51.3	338.3								
510	50.6	334.2								
515	50.1	329.2								
520	49.2	324.5								
525	48.4	319.6								
530	47.4	312.4								
535	46.6	307.4								
540	46	303.6								
545	45.3	297.7								
550	44.5	293.8	91.9	138.4	179	212.2	236.9	259.3	275.7	287.6
555	43.7	288.2	--	--	--	--	--	--	--	--
560	43.1	283.1	--	--	--	--	--	--	--	--
565	42.1	277.4	--	--	--	--	--	--	--	--
570	41.2	272.2	84.8	127.8	165.4	196.3	219.7	241.1	256.2	266.2
575	40.4	268.1	--	--	--	--	--	--	--	--
580	39.9	262.5	--	--	--	--	--	--	--	--
585	39.1	257.8	--	--	--	--	--	--	--	--

590	38.5	254.2	--	--	--	--	--	--	--	--
595	38	251.3	--	--	--	--	--	--	--	--
600	37.7	248.7	77.8	116.9	151	179.3	200.8	220	233.7	243.3
605	37.4	246.4		--	--	--	--	--	--	--
610	37	243.5	--	--	--	--	--	--	--	--
615	36.4	239	--	--	--	--	--	--	--	--
620	35.3	233.3	--	--	--	--	--	--	--	--
625	34.1	224.7	--	--	--	--	--	--	--	--
630	32.7	216.2	--	--	--	--	--	--	--	--
635	31.5	208.2	--	--	--	--	--	--	--	--
640	30.5	201.2	--	--	--	--	--	--	--	--
645	29.7	195.4	--	--	--	--	--	--	--	--
650	28.7	190	59	88.8	114.8	136.5	152.9	167.5	178.2	185.2
655	27.9	183.6	--	--	--	--	--	--	--	--
660	27.1	178	--	--	--	--	--	--	--	--
665	26.5	173.8	--	--	--	--	--	--	--	--
670	26	171.2	--	--	--	--	--	--	--	--
675	25.9	169.9	--	--	--	--	--	--	--	--
680	25.7	168.6	--	--	--	--	--	--	--	--
685	25	163.8	--	--	--	--	--	--	--	--
690	23.5	156.5	48.5	73	94.7	112.6	126.1	138.1	146.9	153

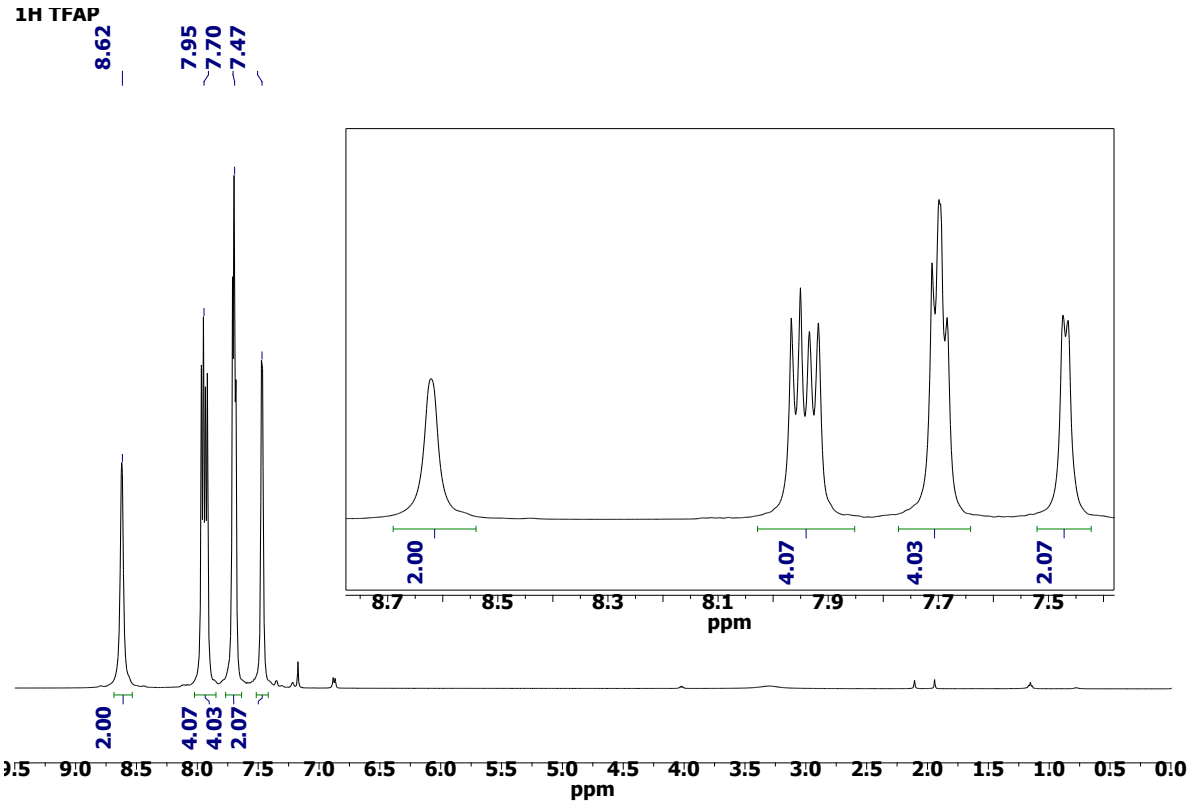

^{1}H NMR spectrum of TFAP in $CDCl_3$.

^{1}H-NMR (500 MHz, $CDCl_3$): δ (ppm) δ 8.62 (s, 2H), 7.94 (dd, J = 16.3, 8.2 Hz, 4H), 7.76 – 7.63 (m, 2H), 7.47 (d, J = 4.5 Hz, 4H).

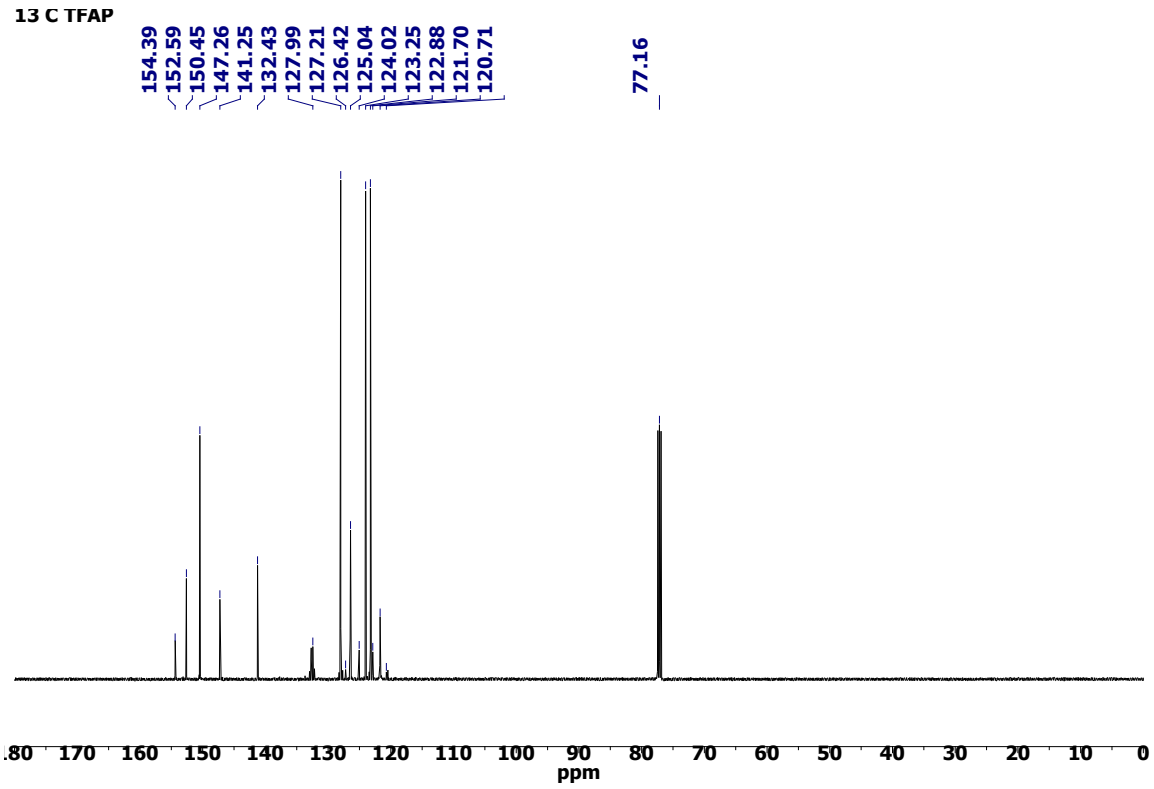

^{13}C NMR spectrum of TFAP in $CDCl_3$.

^{13}C-NMR (125.8 MHz, $CDCl_3$): δ (ppm) 154.39, 152.59, 150.45, 147.26, 141.25, 132.43, 127.99, 127.21, 126.42, 125.04, 124.02, 123.25, 122.88, 121.70, 120.71, 77.16.

Bibliography

1 Geim, A. K. & Novoselov, K. S. The Rise of Graphene. *Nat. Mater.* **6**, 183-191 (2007).
2 Novoselov, K. S. *et al.* Electric Field Effect in Atomically Thin Carbon Films. *Science* **306**, 666-669 (2004).
3 Mak, K. F. & Shan, J. Photonics and optoelectronics of 2D semiconductor transition metal dichalcogenides. *Nat. Photonics* **10**, 216 (2016).
4 Li, L. *et al.* Black phosphorus field-effect transistors. *Nat. Nanotechnol.* **9**, 372 (2014).
5 Waldrop, M. M. More than Moore. *Nature* **530**, 144-147 (2016).
6 Wang, Y. *et al.* Van der Waals contacts between three-dimensional metals and two-dimensional semiconductors. *Nature* **568**, 70-74 (2019).
7 Geim, A. K. & Grigorieva, I. V. Van der waals heterostructures. *Nature* **499**, 419 (2013).
8 Amsterdam, S. H. *et al.* Electronic Coupling in Metallophthalocyanine–Transition Metal Dichalcogenide Mixed-Dimensional Heterojunctions. *ACS Nano* **13**, 4183-4190 (2019).
9 Ryder, C. R., Wood, J. D., Wells, S. A. & Hersam, M. C. Chemically tailoring semiconducting two-dimensional transition metal dichalcogenides and black phosphorus. *ACS Nano* **10**, 3900-3917 (2016).
10 Lin, Y. *et al.* Dielectric screening of excitons and trions in single-layer MoS_2. *Nano Lett.* **14**, 5569-5576 (2014).
11 Yu, L. *et al.* High-Performance WSe2 Complementary Metal Oxide Semiconductor Technology and Integrated Circuits. *Nano Lett.* **15**, 4928-4934 (2015).
12 Kang, D.-H. *et al.* Controllable nondegenerate p-type doping of tungsten diselenide by octadecyltrichlorosilane. *ACS Nano* **9**, 1099-1107 (2015).
13 Khan, H. N., Hounshell, D. A. & Fuchs, E. R. Science and research policy at the end of Moore's law. *Nat. Electron.* **1**, 14-21 (2018).
14 Choi, W. *et al.* Recent development of two-dimensional transition metal dichalcogenides and their applications. *Mater. Today* **20**, 116-130 (2017).
15 Gobbi, M., Orgiu, E. & Samorì, P. When 2D materials meet molecules: opportunities and challenges of hybrid organic/inorganic van der Waals heterostructures. *Adv. Mater.* **30**, 1706103 (2018).
16 Bertolazzi, S., Gobbi, M., Zhao, Y., Backes, C. & Samorì, P. Molecular chemistry approaches for tuning the properties of two-dimensional transition metal dichalcogenides. *Chem. Soc. Rev.* **47**, 6845-6888 (2018).
17 Unuchek, D. *et al.* Room-temperature electrical control of exciton flux in a van der Waals heterostructure. *Nature* **560**, 340-344 (2018).
18 Cao, Y. *et al.* Unconventional superconductivity in magic-angle graphene superlattices. *Nature* **556**, 43-50 (2018).
19 Hao, Z. *et al.* Electric field–tunable superconductivity in alternating-twist magic-angle trilayer graphene. *Science* **371**, 1133-1138 (2021).
20 Castellanos-Gomez, A. Why all the fuss about 2D semiconductors? *Nat. Photonics* **10**, 202-204 (2016).
21 Huang, Y. *et al.* Universal mechanical exfoliation of large-area 2D crystals. *Nat. Comm.* **11**, 1-9 (2020).
22 Liu, F. *et al.* Disassembling 2D van der Waals crystals into macroscopic monolayers and reassembling into artificial lattices. *Science* **367**, 903-906 (2020).
23 Li, Z. & Wong, S. L. Functionalization of 2D transition metal dichalcogenides for biomedical applications. *Materials Science and Engineering: C* **70**, 1095-1106 (2017).
24 Manzeli, S., Ovchinnikov, D., Pasquier, D., Yazyev, O. V. & Kis, A. 2D transition metal dichalcogenides. *Nat. Rev. Mater.* **2**, 17033 (2017).
25 Kang, J., Tongay, S., Zhou, J., Li, J. & Wu, J. Band offsets and heterostructures of two-dimensional semiconductors. *Appl. Phys. Lett.* **102**, 012111 (2013).
26 Gao, G. *et al.* Charge mediated semiconducting-to-metallic phase transition in molybdenum disulfide monolayer and hydrogen evolution reaction in new $1T'$ phase. *J. Phys. Chem. C* **119**, 13124-13128 (2015).
27 Mueller, T. & Malic, E. Exciton physics and device application of two-dimensional transition metal dichalcogenide semiconductors. *npj 2D Mater. Appl.* **2**, 1-12 (2018).
28 Barbone, M. *et al.* Charge-tuneable biexciton complexes in monolayer WSe_2. *Nat. Comm.* **9**, 1-6 (2018).

29 Chernikov, A. *et al.* Exciton binding energy and nonhydrogenic Rydberg series in monolayer WS_2. *Phys. Rev. Lett.* **113**, 076802 (2014).

30 Mak, K. F. *et al.* Tightly bound trions in monolayer MoS2. *Nat. Mater.* **12**, 207-211 (2013).

31 Jones, A. M. *et al.* Optical generation of excitonic valley coherence in monolayer WSe_2. *Nat. Nanotechnol.* **8**, 634 (2013).

32 Mouri, S., Miyauchi, Y. & Matsuda, K. Tunable photoluminescence of monolayer MoS_2 via chemical doping. *Nano Lett.* **13**, 5944-5948 (2013).

33 Kim, H., Lien, D.-H., Amani, M., Ager, J. W. & Javey, A. Highly stable near-unity photoluminescence yield in monolayer MoS_2 by fluoropolymer encapsulation and superacid treatment. *ACS Nano* **11**, 5179-5185 (2017).

34 Nan, H. Y. *et al.* Strong Photoluminescence Enhancement of MoS_2 through Defect Engineering and Oxygen Bonding. *ACS Nano* **8**, 5738-5745 (2014).

35 Mak, K. F. *et al.* Tightly bound trions in monolayer MoS_2. *Nat. Mater.* **12**, 207 (2013).

36 Kim, H., Lien, D. H., Amani, M., Ager, J. W. & Javey, A. Highly Stable Near-Unity Photoluminescence Yield in Monolayer MoS_2 by Fluoropolymer Encapsulation and Superacid Treatment. *ACS Nano* **11**, 5179-5185 (2017).

37 Wang, Z. *et al.* Giant photoluminescence enhancement in tungsten-diselenide–gold plasmonic hybrid structures. *Nat. Comm.* **7**, 1-8 (2016).

38 Lin, S., Chui, Y., Li, Y. & Lau, S. P. Liquid-phase exfoliation of black phosphorus and its applications. *FlatChem* **2**, 15-37 (2017).

39 Castellanos-Gomez, A. Black phosphorus: narrow gap, wide applications. *J. Phys. Chem. Lett.* **6**, 4280-4291 (2015).

40 Park, C. M. & Sohn, H. J. Black phosphorus and its composite for lithium rechargeable batteries. *Adv. Mater.* **19**, 2465-2468 (2007).

41 Xia, F., Wang, H. & Jia, Y. Rediscovering black phosphorus as an anisotropic layered material for optoelectronics and electronics. *Nat. Comm.* **5**, 4458 (2014).

42 Ling, X., Wang, H., Huang, S., Xia, F. & Dresselhaus, M. S. The renaissance of black phosphorus. *Proc. Natl. Acad. Sci.* **112**, 4523-4530 (2015).

43 Perello, D. J., Chae, S. H., Song, S. & Lee, Y. H. High-performance n-type black phosphorus transistors with type control via thickness and contact-metal engineering. *Nat. Comm.* **6**, 1-10 (2015).

44 Avsar, A. *et al.* van der Waals bonded Co/h-BN contacts to ultrathin black phosphorus devices. *Nano Lett.* **17**, 5361-5367 (2017).

45 Castellanos-Gomez, A. *et al.* Isolation and characterization of few-layer black phosphorus. *2D Mater.* **1**, 025001 (2014).

46 Wang, X. *et al.* Highly anisotropic and robust excitons in monolayer black phosphorus. *Nat. Nanotechnol.* **10**, 517 (2015).

47 An, J. *et al.* Research development of 2D materials based photodetectors towards mid - infrared regime. *Nano Select* **2**, 527-540 (2021).

48 Guo, Q. *et al.* Black phosphorus mid-infrared photodetectors with high gain. *Nano Lett.* **16**, 4648-4655 (2016).

49 Yuan, H. *et al.* Polarization-sensitive broadband photodetector using a black phosphorus vertical p–n junction. *Nat. Nanotechnol.* **10**, 707-713 (2015).

50 Luo, W. *et al.* Surface chemistry of black phosphorus under a controlled oxidative environment. *Nanotechnology* **27**, 434002 (2016).

51 Zhang, T. *et al.* Degradation chemistry and stabilization of exfoliated few-layer black phosphorus in water. *J. Am. Chem. Soc.* **140**, 7561-7567 (2018).

52 Birowska, M. *et al.* The impact of hexagonal boron nitride encapsulation on the structural and vibrational properties of few layer black phosphorus. *Nanotechnology* **30**, 195201 (2019).

53 Constantinescu, G. C. & Hine, N. D. Multipurpose black-phosphorus/hBN heterostructures. *Nano Lett.* **16**, 2586-2594 (2016).

54 Liu, X. *et al.* Regulating the reactivity of black phosphorus via protective chemistry. *Sci. Adv.* **6**, eabb4359 (2020).

55 Zhao, Y. *et al.* Surface coordination of black phosphorus for robust air and water stability. *Angew. Chem. Int. Ed.* **55**, 5003-5007 (2016).

56 Illarionov, Y. Y. *et al.* Highly-stable black phosphorus field-effect transistors with low density of oxide traps. *npj 2D Mater. Appl.* **1**, 1-7 (2017).

57 Artel, V. *et al.* Protective molecular passivation of black phosphorus. *npj 2D Mater. Appl.* **1**, 1-5 (2017).

58 Grimaldi, I. *et al.* Structural investigation of InSe layered semiconductors. *Solid State Commun.* **311**, 113855 (2020).

59 Mudd, G. *et al.* The direct-to-indirect band gap crossover in two-dimensional van der Waals Indium Selenide crystals. *Sci. Rep.* **6**, 1-10 (2016).

60 Bandurin, D. A. *et al.* High electron mobility, quantum Hall effect and anomalous optical response in atomically thin InSe. *Nat. Nanotechnol.* **12**, 223-227 (2017).

61 Wei, T.-R. *et al.* Exceptional plasticity in the bulk single-crystalline van der Waals semiconductor InSe. *Science* **369**, 542-545 (2020).

62 Ho, P.-H. *et al.* High-mobility InSe transistors: the role of surface oxides. *ACS Nano* **11**, 7362-7370 (2017).

63 Zhao, Q. *et al.* The role of traps in the photocurrent generation mechanism in thin InSe photodetectors. *Mater. Horiz.* **7**, 252-262 (2020).

64 Sucharitakul, S. *et al.* Intrinsic electron mobility exceeding 10^3 $cm^2/(V\ s)$ in multilayer InSe FETs. *Nano Lett.* **15**, 3815-3819 (2015).

65 Li, M. *et al.* High Mobilities in Layered InSe Transistors with Indium - Encapsulation - Induced Surface Charge Doping. *Adv. Mater.* **30**, 1803690 (2018).

66 Jiang, J. *et al.* Stable InSe transistors with high-field effect mobility for reliable nerve signal sensing. *npj 2D Mater. Appl.* **3**, 1-8 (2019).

67 Buscema, M. *et al.* Photocurrent generation with two-dimensional van der Waals semiconductors. *Chem. Soc. Rev.* **44**, 3691-3718 (2015).

68 Feng, W. *et al.* Ultrahigh photo-responsivity and detectivity in multilayer InSe nanosheets phototransistors with broadband response. *J. Mater. Chem. C* **3**, 7022-7028 (2015).

69 Tamalampudi, S. R. *et al.* High performance and bendable few-layered InSe photodetectors with broad spectral response. *Nano Lett.* **14**, 2800-2806 (2014).

70 Lopez-Sanchez, O., Lembke, D., Kayci, M., Radenovic, A. & Kis, A. Ultrasensitive Photodetectors Based on Monolayer MoS_2. *Nat. Nanotechnol.* **8**, 497-501 (2013).

71 Zhang, W. *et al.* Role of metal contacts in high-performance phototransistors based on WSe_2 monolayers. *ACS Nano* **8**, 8653-8661 (2014).

72 Jang, H. *et al.* High - Performance Near - Infrared Photodetectors Based on Surface - Doped InSe. *Adv. Funct. Mater.* **31**, 2006788 (2021).

73 Liu, L. *et al.* Ferroelectric-Gated InSe Photodetectors with High On/Off Ratios and Photoresponsivity. *Nano Lett.* **20**, 6666-6673 (2020).

74 Yang, Y. *et al.* Plasmonic transition metal carbide electrodes for high-performance InSe photodetectors. *ACS Nano* **13**, 8804-8810 (2019).

75 Dai, M. *et al.* Ultrafast and Sensitive Self-Powered Photodetector Featuring Self-Limited Depletion Region and Fully Depleted Channel with van der Waals Contacts. *ACS Nano* **14**, 9098-9106 (2020).

76 Lee, C.-H. *et al.* Atomically thin p–n junctions with van der Waals heterointerfaces. *Nat. Nanotechnol.* **9**, 676 (2014).

77 Massicotte, M. *et al.* Picosecond photoresponse in van der Waals heterostructures. *Nat. Nanotechnol.* **11**, 42-46 (2016).

78 Urbaszek, B. & Srivastava, A. Materials in flatland twist and shine. (Nature Publishing Group 2019).

79 Novoselov, K. S., Mishchenko, A., Carvalho, A. & Castro Neto, A. H. 2d materials and van der waals heterostructures. *Science* **353**, aac9439 (2016).

80 Gobbi, M. *et al.* Periodic potentials in hybrid van der waals heterostructures formed by supramolecular lattices on graphene. *Nat. Comm.* **8**, 14767, doi:10.1038/ncomms14767 (2017).

81 Gobbi, M. *et al.* Graphene transistors for real-time monitoring molecular self-assembly dynamics. *Nat. Comm.* **11**, 1-8 (2020).

82 Gobbi, M. *et al.* Collective molecular switching in hybrid superlattices for light-modulated two-dimensional electronics. *Nat. Comm.* **9**, 1-9 (2018).

83 Jariwala, D. *et al.* Hybrid, gate-tunable, van der Waals p–n heterojunctions from pentacene and MoS_2. *Nano Lett.* **16**, 497-503 (2016).

84 Bettis Homan, S. *et al.* Ultrafast exciton dissociation and long-lived charge separation in a photovoltaic pentacene–MoS_2 van der Waals heterojunction. *Nano Lett.* **17**, 164-169 (2017).

85 McQuarrie, D. A., Rock, P. A. & Gallogly, E. B. *General chemistry*. (WH Freeman New York, 1984).

86 Nicolosi, V., Chhowalla, M., Kanatzidis, M. G., Strano, M. S. & Coleman, J. N. Liquid exfoliation of layered materials. *Science* **340** (2013).

87 Barrett, P., Frye, D. & Linstead, R. 213. Phthalocyanines and associated compounds. Part XIV. Further investigations of metallic derivatives. *J. Chem. Soc.*, 1157-1163 (1938).

88 Barrett, P., Dent, C. & Linstead, R. 382. Phthalocyanines. Part VII. Phthalocyanine as a co-ordinating group. A general investigation of the metallic derivatives. *J. Chem. Soc.*, 1719-1736 (1936).

89 Linstead, R. 212. Phthalocyanines. Part I. A new type of synthetic colouring matters. *J. Chem. Soc.*, 1016-1017 (1934).

90 Steed, J. W. & Atwood, J. L. *Supramolecular chemistry.* (John Wiley & Sons, 2013).

91 Kettle, S. F. A. *Physical inorganic chemistry: a coordination chemistry approach.* (Springer, 2013).

92 Liao, M.-S. & Scheiner, S. Electronic structure and bonding in metal phthalocyanines, metal= Fe, Co, Ni, Cu, Zn, Mg. *J. Chem. Phys.* **114**, 9780-9791 (2001).

93 Nakatani, K., Piard, J., Yu, P. & Métivier, R. Introduction: organic photochromic molecules. *Photochromic materials: preparation, properties and applications*, 1-45 (2016).

94 Fu, L.-N., Leng, B., Li, Y.-S. & Gao, X.-K. Photoresponsive organic field-effect transistors involving photochromic molecules. *Chin. Chem. Lett.* **27**, 1319-1329 (2016).

95 Rusch, T. R. *et al.* Observation of collective photoswitching in free‐standing TATA‐based azobenzenes on Au (111). *Angew. Chem.* **132**, 17345-17349 (2020).

96 Margapoti, E. *et al.* A 2D semiconductor-self-assembled monolayer photoswitchable diode. *Adv. Mater.* **27**, 1426-1431 (2015).

97 Li, J. *et al.* Tuning the optical emission of MoS_2 nanosheets using proximal photoswitchable azobenzene molecules. *Appl. Phys. Lett.* **105**, 241116-241116 (2014).

98 Zhao, Y., Bertolazzi, S. & Samorì, P. A Universal Approach toward Light-Responsive Two-Dimensional Electronics: Chemically Tailored Hybrid van der Waals Heterostructures. *ACS Nano* **13**, 4814-4825 (2019).

99 Tkalya, E. E., Ghislandi, M., de With, G. & Koning, C. E. The use of surfactants for dispersing carbon nanotubes and graphene to make conductive nanocomposites. *Curr. Opin. Colloid. Interface. Sci.* **17**, 225-232 (2012).

100 Boussaad, S. & Tao, N. Electron transfer and adsorption of myoglobin on self-assembled surfactant films: an electrochemical tapping-mode AFM study. *J. Am. Chem. Soc.* **121**, 4510-4515 (1999).

101 Ahmadi, M. A. & Sheng, J. Performance improvement of ionic surfactant flooding in carbonate rock samples by use of nanoparticles. *Pet. Sci.* **13**, 725-736 (2016).

102 Radisavljevic, B., Radenovic, A., Brivio, J., Giacometti, V. & Kis, A. Single-Layer MoS_2 Transistors. *Nat. Nanotechnol.* **6**, 147-150 (2011).

103 Mali, K. S., Pearce, N., De Feyter, S. & Champness, N. R. Frontiers of supramolecular chemistry at solid surfaces. *Chem. Soc. Rev.* **46**, 2520-2542 (2017).

104 Sze, S. M., Li, Y. & Ng, K. K. *Physics of semiconductor devices.* (John wiley & sons, 2021).

105 刘恩科, 朱秉升 & 罗晋生. *半导体物理学.* (电子工业出版社, 2008).

106 Bhushan, B. *Encyclopedia of nanotechnology.* (Springer Dordrecht, Netherlands, 2012).

107 Akinwande, D., Petrone, N. & Hone, J. Two-dimensional flexible nanoelectronics. *Nature Communications* **5**, 5678, doi:10.1038/ncomms6678 (2014).

108 Fiori, G. *et al.* Electronics Based on Two-Dimensional Materials. *Nat. Nanotechnol.* **9**, 768-779 (2014).

109 Hu, Y. *et al.* Two-dimensional transition metal dichalcogenide nanomaterials for biosensing applications. *Mater. Chem. Front.* **1**, 24-36 (2017).

110 Li, S.-L., Tsukagoshi, K., Orgiu, E. & Samorì, P. Charge transport and mobility engineering in two-dimensional transition metal chalcogenide semiconductors. *Chem. Soc. Rev.* **45**, 118-151, doi:10.1039/C5CS00517E (2016).

111 Yan, W. *et al.* A two-dimensional spin field-effect switch. *Nat. Comm.* **7**, 13372 (2016).

112 Anichini, C. *et al.* Chemical sensing with 2D materials. *Chem. Soc. Rev.* (2018).

113 Bertolazzi, S., Gobbi, M., Zhao, Y., Backes, C. & Samorì, P. Molecular chemistry approaches for tuning the properties of two-dimensional transition metal dichalcogenides. *Chem. Soc. Rev.* (2018).

114 Lee, I. *et al.* Non-degenerate n-type doping by hydrazine treatment in metal work function engineered WSe2 field-effect transistor. *Nanotechnology* **26**, 455203 (2015).

115 Kiriya, D., Tosun, M., Zhao, P., Kang, J. S. & Javey, A. Air-stable surface charge transfer doping of MoS2 by benzyl viologen. *J. Am. Chem. Soc.* **136**, 7853-7856 (2014).

116 Splendiani, A. *et al.* Emerging Photoluminescence in Monolayer MoS_2. *Nano Lett.* **10**, 1271-1275 (2010).

117 Mak, K. F., Lee, C., Hone, J., Shan, J. & Heinz, T. F. Atomically Thin MoS_2: A New Direct-Gap Semiconductor. *Phys. Rev. Lett.* **105**(2010).

118 Ross, J. S. *et al.* Electrical control of neutral and charged excitons in a monolayer semiconductor. *Nat. Comm.* **4**, 1474 (2013).

119 Tongay, S. *et al.* Broad-range modulation of light emission in two-dimensional semiconductors by molecular physisorption gating. *Nano Lett.* **13**, 2831-2836, doi:10.1021/nl4011172 (2013).

120 Gobbi, M., Orgiu, E. & Samorì, P. "When 2D Materials Meet Molecules: Opportunities and Challenges of Hybrid Organic/Inorganic van der Waals Heterostructures *Adv. Mater.* **30**, 1706103 (2018).

121 Jing, Y., Tan, X., Zhou, Z. & Shen, P. W. Tuning electronic and optical properties of MoS_2 monolayer via molecular charge transfer. *J. Mater. Chem. A* **2**, 16892-16897 (2014).

122 Han, H. V. *et al.* Photoluminescence enhancement and structure repairing of monolayer $MoSe_2$ by hydrohalic acid treatment. *ACS Nano* **10**, 1454-1461 (2016).

123 de la Rosa, C. J. L. *et al.* Molecular doping of MoS_2 transistors by self-assembled oleylamine networks. *Appl. Phys. Lett.* **109**, 253112 (2016).

124 Kang, D. H. *et al.* Ultra-low Doping on Two-Dimensional Transition Metal Dichalcogenides using DNA Nanostructure Doped by a Combination of Lanthanide and Metal Ions. *Sci. Rep.* **6**, 20333, (2016).

125 Fang, H. *et al.* High-performance single layered WSe_2 p-FETs with chemically doped contacts. *Nano Lett.* **12**, 3788-3792 (2012).

126 Fisher, A. & Blöchl, P. Adsorption and scanning-tunneling-microscope imaging of benzene on graphite and MoS 2. *Phys. Rev. Lett.* **70**, 3263 (1993).

127 Dong, X. *et al.* Doping single ‐ layer graphene with aromatic molecules. *Small* **5**, 1422-1426 (2009).

128 Kresse, G. & Furthmüller, J. Efficient iterative schemes for ab initio total-energy calculations using a plane-wave basis set. *Phys. Rev. B* **54**, 11169 (1996).

129 Kresse, G. G. Kresse and D. Joubert, Phys. Rev. B 59, 1758 (1999). *Phys. Rev. B* **59**, 1758 (1999).

130 Perdew, J. P., Burke, K. & Ernzerhof, M. Generalized gradient approximation made simple. *Phys Rev Lett* **77**, 3865 (1996).

131 Grimme, S. Semiempirical GGA ‐ type density functional constructed with a long ‐ range dispersion correction. *J. Comput. Chem.* **27**, 1787-1799 (2006).

132 Monkhorst, H. J. & Pack, J. D. Special points for Brillouin-zone integrations. *Phys. Rev. B* **13**, 5188 (1976).

133 Korn, T., Heydrich, S., Hirmer, M., Schmutzler, J. & Schüller, C. Low-temperature photocarrier dynamics in monolayer MoS_2. *Appl. Phys. Lett.* **99**, 102109 (2011).

134 Lanzillo, N. A. *et al.* Temperature-dependent phonon shifts in monolayer MoS_2. *Appl. Phys. Lett.* **103**, 093102 (2013).

135 Crispin, X. *et al.* Characterization of the interface dipole at organic/metal interfaces. *J. Am. Chem. Soc.* **124**, 8131-8141 (2002).

136 Pearson, R. G. The electronic chemical potential and chemical hardness. *J. Mol. Struct.: THEOCHEM* **255**, 261-270 (1992).

137 Tang, W., Sanville, E. & Henkelman, G. A grid-based Bader analysis algorithm without lattice bias. *J. Phys. Cond. Matter.* **21**, 084204 (2009).

138 Choi, J., Zhang, H., Du, H. & Choi, J. H. Understanding solvent effects on the properties of two-dimensional transition metal dichalcogenides. *ACS Appl. Mater. Interfaces* **8**, 8864-8869 (2016).

139 Ross, J. S. *et al.* Electrically tunable excitonic light-emitting diodes based on monolayer WSe_2 p–n junctions. *Nat. Nanotechnol.* **9**, 268 (2014).

140 You, Y. *et al.* Observation of biexcitons in monolayer WSe_2. *Nat. Phys.* **11**, 477 (2015).

141 Buscema, M., Steele, G. A., van der Zant, H. S. J. & Castellanos-Gomez, A. The effect of the substrate on the raman and photoluminescence emission of single-layer mos2. *Nano Research* **7**, 1-11 (2014).

142 Long, M. *et al.* Broadband photovoltaic detectors based on an atomically thin heterostructure. *Nano Lett.* **16**, 2254-2259 (2016).

143 Kou, L., Frauenheim, T. & Chen, C. Phosphorene as a superior gas sensor: Selective adsorption and distinct I–V response. *J. Phys. Chem. Lett.* **5**, 2675-2681 (2014).

144 Miao, J. *et al.* Air-stable humidity sensor using few-layer black phosphorus. *ACS Appl. Mater. Interfaces* **9**, 10019-10026 (2017).

145 Cho, S. Y. *et al.* Superior chemical sensing performance of black phosphorus: Comparison with MoS_2 and graphene. *Adv. Mater.* **28**, 7020-7028 (2016).

146 Abellán, G. *et al.* Noncovalent functionalization of black phosphorus. *Angew. Chem.* **128**, 14777-14782 (2016).

147 Du, Y., Yang, L., Zhou, H. & Peide, D. Y. Performance enhancement of black phosphorus field-effect transistors by chemical doping. *IEEE Electron Device Lett.* **37**, 429-432 (2016).

148 Jing, Y., Tang, Q., He, P., Zhou, Z. & Shen, P. Small molecules make big differences: molecular doping effects on electronic and optical properties of phosphorene. *Nanotechnology* **26**, 095201 (2015).

149 Wang, C. *et al.* Charge Transfer at the PTCDA/Black Phosphorus Interface. *J. Phys. Chem. C* **121**, 18084-18094 (2017).

150 Abellán, G. *et al.* Noncovalent functionalization and charge transfer in antimonene. *Angew. Chem.* **129**, 14581-14586 (2017).

151 Korolkov, V. V. *et al.* Supramolecular networks stabilise and functionalise black phosphorus. *Nat. Comm.* **8**, 1385 (2017).

152 Abbas, A. N. *et al.* Black phosphorus gas sensors. *ACS Nano* **9**, 5618-5624 (2015).

153 Mayorga - Martinez, C. C., Sofer, Z. & Pumera, M. Layered black phosphorus as a selective vapor sensor. *Angew. Chem. Int. Ed.* **54**, 14317-14320 (2015).

154 Liu, G., Rumyantsev, S., Jiang, C., Shur, M. & Balandin, A. Selective Gas Sensing With $ h $-BN Capped MoS2 Heterostructure Thin-Film Transistors. *IEEE Electron Device Lett.* **36**, 1202-1204 (2015).

155 Mao, N., Chen, Y., Liu, D., Zhang, J. & Xie, L. Solvatochromic effect on the photoluminescence of MoS2 monolayers. *Small* **9**, 1312-1315 (2013).

156 Lei, W., Liu, G., Zhang, J. & Liu, M. Black phosphorus nanostructures: recent advances in hybridization, doping and functionalization. *Chem. Soc. Rev.* **46**, 3492-3509 (2017).

157 Xiang, D. *et al.* Surface transfer doping induced effective modulation on ambipolar characteristics of few-layer black phosphorus. *Nat. Comm.* **6**, 6485 (2015).

158 Perdew, J. P., Burke, K. & Ernzerhof, M. Generalized gradient approximation made simple. *Phys. Rev. Lett.* **77**, 3865 (1996).

159 Grimme, S. Semiempirical GGA - type density functional constructed with a long - range dispersion correction. *J. Comput. Chem.* **27**, 1787-1799 (2006).

160 Monkhorst, H. J. & Pack, J. D. Special points for Brillouin-zone integrations. *Phys. Rev. B* **13**, 5188 (1976).

161 Wang, Y. *et al.* Doping of monolayer transition-metal dichalcogenides via physisorption of aromatic solvent molecules. *J. Phys. Chem. Lett.* **10**, 540-547 (2019).

162 Crivillers, N. *et al.* Large work function shift of gold induced by a novel perfluorinated azobenzene-based self-assembled monolayer. *Adv. Mater.* **25**, 432-436 (2013).

163 Del Rio Castillo, A. E. *et al.* Exfoliation of few-layer black phosphorus in low-boiling-point solvents and its application in Li-ion batteries. *Chem. Mater.* **30**, 506-516 (2018).

164 Kim, S., Lee, G. & Kim, J. Chemical Doping Effects of Gas Molecules on Black Phosphorus Field-Effect Transistors. *ECS J. Solid State Sci. Technol.* **7**, Q3065-Q3069 (2018).

165 Han, C. *et al.* Surface functionalization of black phosphorus via potassium toward high-performance complementary devices. *Nano Lett.* **17**, 4122-4129 (2017).

166 Yang, J. *et al.* Optical tuning of exciton and trion emissions in monolayer phosphorene. *Light Sci. Appl.* **4**, e312 (2015).

167 Kang, D.-H. *et al.* Self-Assembled Layer (SAL)-Based Doping on Black Phosphorus (BP) Transistor and Photodetector. *ACS Photonics* **4**, 1822-1830 (2017).

168 Long, M., Wang, P., Fang, H. & Hu, W. Progress, challenges, and opportunities for 2D material based photodetectors. *Adv. Funct. Mater.* **29**, 1803807 (2019).

169 Sang, L., Liao, M. & Sumiya, M. A comprehensive review of semiconductor ultraviolet photodetectors: from thin film to one-dimensional nanostructures. *Sensors* **13**, 10482-10518 (2013).

170 Natali, D. & Caironi, M. in *Photodetectors* 195-254 (Elsevier, 2016).

171 Wu, Y. L., Fukuda, K., Yokota, T. & Someya, T. A Highly Responsive Organic Image Sensor Based on a Two - Terminal Organic Photodetector with Photomultiplication. *Adv. Mater.* **31**, 1903687 (2019).

172 Chen, Z., Biscaras, J. & Shukla, A. A high performance graphene/few-layer InSe photo-detector. *Nanoscale* **7**, 5981-5986 (2015).

173 Heo, J. *et al.* Reconfigurable van der Waals heterostructured devices with metal–insulator transition. *Nano Lett.* **16**, 6746-6754 (2016).

174 Lv, Q., Yan, F., Wei, X. & Wang, K. High - performance, self - driven photodetector based on graphene sandwiched GaSe/WS_2 heterojunction. *Adv. Opt. Mater.* **6**, 1700490 (2018).

175 Zhou, X. *et al.* Highly anisotropic GeSe nanosheets for phototransistors with ultrahigh photoresponsivity. *Adv. Sci.* **5**, 1800478 (2018).

176 Nguyen, D. A. *et al.* Highly enhanced photoresponsivity of a monolayer WSe_2 photodetector with nitrogen-doped graphene quantum dots. *ACS Appl. Mater. Interfaces* **10**, 10322-10329 (2018).

177 Hansen, W. N. & Hansen, G. J. Standard reference surfaces for work function measurements in air. *Surf. Sci.* **481**, 172-184 (2001).

178 Kresse, G. & Furthmüller, J. Efficient iterative schemes for ab initio total-energy calculations using a plane-wave basis set. *Phys. Rev. B* **54**, 11169 (1996).

179 Kresse, G. & Joubert, D. From ultrasoft pseudopotentials to the projector augmented-wave method. *Phys. Rev. B* **59**, 1758 (1999).

180 Chamlagain, B. *et al.* Mobility improvement and temperature dependence in $MoSe_2$ field-effect transistors on parylene-c substrate. *ACS Nano* **8**, 5079-5088 (2014).

181 Dolui, K., Rungger, I. & Sanvito, S. Origin of the n-type and p-type conductivity of MoS_2 monolayers on a SiO2 substrate. *Phys. Rev. B* **87**, 165402 (2013).

182 Yu, Z. *et al.* Analyzing the Carrier Mobility in Transition - Metal Dichalcogenide MoS_2 Field - Effect Transistors. *Adv. Funct. Mater.* **27**, 1604093 (2017).

183 Edwards, A. H. in *The Physics and Chemistry of SiO_2 and the Si-SiO_2 Interface* 271-283 (Springer, 1988).

184 Poindexter, E. H., Caplan, P. J. & Gerardi, G. J. in *The Physics and Chemistry of SiO_2 and the Si-SiO_2 Interface* 299-308 (Springer, 1988).

185 Guo, Y. *et al.* Charge trapping at the MoS2-SiO_2 interface and its effects on the characteristics of MoS2 metal-oxide-semiconductor field effect transistors. *Appl. Phys. Lett.* **106**, 103109 (2015).

186 Du, Y. C., Liu, H., Neal, A. T., Si, M. W. & Ye, P. D. Molecular Doping of Multilayer MoS2 Field-Effect Transistors: Reduction in Sheet and Contact Resistances. *IEEE Electron Device Lett.* **34** (2013).

187 Wang, Y. *et al.* Doping of Monolayer Transition Metal Dichalcogenides via Physisorption of Aromatic Solvent Molecules. *J. Phys. Chem. Lett.* (2019).

188 Stoeckel, M.-A. *et al.* Boosting and Balancing Electron and Hole Mobility in Single-and Bilayer WSe_2 Devices via Tailored Molecular Functionalization. *ACS Nano* **13**, 11613-11622 (2019).

189 Yang, F.-S. *et al.* Oxidation-boosted charge trapping in ultra-sensitive van der Waals materials for artificial synaptic features. *Nat. Comm.* **11**, 1-11 (2020).

190 Tsai, T.-H. *et al.* High-Mobility InSe transistors: the nature of charge transport. *ACS Appl. Mater. Interfaces* **11**, 35969-35976 (2019).

191 Wang, Y., Gali, S. M., Slassi, A., Beljonne, D. & Samorì, P. Collective Dipole - Dominated Doping of Monolayer MoS2: Orientation and Magnitude Control via the Supramolecular Approach. *Adv. Funct. Mater.* **30**, 2002846 (2020).

192 Rai, A. *et al.* Air stable doping and intrinsic mobility enhancement in monolayer molybdenum disulfide by amorphous titanium suboxide encapsulation. *Nano Lett.* **15**, 4329-4336 (2015).

193 Ahmad, I. *et al.* Self-assembly and wetting properties of gold nanorod–CTAB molecules on HOPG. *Beilstein J. Nanotechnol.* **10**, 696-705 (2019).

194 Chen, Y.-H. *et al.* Oxidized-monolayer tunneling barrier for strong Fermi-level depinning in layered InSe transistors. *npj 2D Mater. Appl.* **3**, 1-7 (2019).

195 Luo, W. *et al.* Gate Tuning of High - Performance InSe - Based Photodetectors Using Graphene Electrodes. *Adv. Opt. Mater.* **3**, 1418-1423 (2015).

196 Tsai, T.-H. *et al.* Photogating WS_2 Photodetectors Using Embedded WSe2 Charge Puddles. *ACS Nano* **14**, 4559-4566 (2020).

197 Shen, C. *et al.* Tellurene Photodetector with High Gain and Wide Bandwidth. *ACS Nano* **14**, 303-310 (2019).

198 Choi, M. S. *et al.* Lateral MoS2 p–n junction formed by chemical doping for use in high-performance optoelectronics. *ACS Nano* **8**, 9332-9340 (2014).

199 Dai, M. *et al.* A dual-band multilayer InSe self-powered photodetector with high performance induced by surface plasmon resonance and asymmetric Schottky junction. *ACS Nano* **12**, 8739-8747 (2018).

200 Hu, S. *et al.* Au–InSe van der Waals Schottky junctions with ultralow reverse current and high photosensitivity. *Nanoscale* **12**, 4094-4100 (2020).

201 Kim, C. *et al.* Fermi level pinning at electrical metal contacts of monolayer molybdenum dichalcogenides. *ACS Nano* **11**, 1588-1596 (2017).

202 Cao, R. *et al.* Black Phosphorous/Indium Selenide Photoconductive Detector for Visible and Near - Infrared Light with High Sensitivity. *Adv. Opt. Mater.* **7**, 1900020 (2019).

203 Zhao, S. *et al.* Highly Polarized and Fast Photoresponse of Black Phosphorus - InSe Vertical p – n Heterojunctions. *Adv. Funct. Mater.* **28**, 1802011 (2018).

204 Deng, Y. *et al.* Black phosphorus–monolayer MoS2 van der Waals heterojunction p–n diode. *ACS Nano* **8**, 8292-8299 (2014).

205 Cao, S. *et al.* Ultrahigh-photoresponsive UV photodetector based on a BP/ReS_2 heterostructure p–n diode. *Nanoscale* **10**, 16805-16811 (2018).

206 Li, X. K. *et al.* Polarization - Dependent Photocurrent of Black Phosphorus/Rhenium Disulfide Heterojunctions. *Adv. Mater. Interfaces* **5**, 1800960 (2018).

207 Nagano, S., Tsukiji, M., Ando, K., Hasegawa, E. & Ishitani, A. Mechanism of leakage current through the nanoscale SiO2 layer. *J. Appl. Phys.* **75**, 3530-3535 (1994).

208 Huang, M. *et al.* Multifunctional high-performance van der Waals heterostructures. *Nat. Nanotechnol.* **12**, 1148-1154 (2017).

209 Xiong, X. *et al.* Reconfigurable Logic - in - Memory and Multilingual Artificial Synapses Based on 2D Heterostructures. *Adv. Funct. Mater.* **30**, 1909645 (2020).

210 Gnatenko, Y. P. & Zhirko, Y. I. About an increase of exciton binding energy in layered InSe. *Phys. Status Solidi B* **180**, 147-153 (1993).

211 Wehling, T. O., Lichtenstein, A. I. & Katsnelson, M. I. First-principles studies of water adsorption on graphene: The role of the substrate. *Appl. Phys. Lett.* **93**, 5143 (2008).

212 Vélez, S. *et al.* Gate-tunable diode and photovoltaic effect in an organic–2D layered material p–n junction. *Nanoscale* **7**, 15442-15449 (2015).

213 Zhao, Y. D. *et al.* Doping, Contact and Interface Engineering of Two-Dimensional Layered Transition Metal Dichalcogenides Transistors. *Adv. Funct. Mater.* **27**, 1603484 (2017).

214 Chhowalla, M. *et al.* The chemistry of two-dimensional layered transition metal dichalcogenide nanosheets. *Nature Chemistry* **5**, 263-275 (2013).

215 Wang, Q. H., Kalantar-Zadeh, K., Kis, A., Coleman, J. N. & Strano, M. S. Electronics and optoelectronics of two-dimensional transition metal dichalcogenides. *Nat. Nanotechnol.* **7**, 699-712 (2012).

216 Britnell, L. *et al.* Strong Light-Matter Interactions in Heterostructures of Atomically Thin Films. *Science* **340**, 1311-1314 (2013).

217 Jariwala, D., Sangwan, V. K., Lauhon, L. J., Marks, T. J. & Hersam, M. C. Emerging Device Applications for Semiconducting Two-Dimensional Transition Metal Dichalcogenides. *ACS Nano* **8**, 1102-1120 (2014).

218 Wang, X. & Xia, F. Van der Waals heterostructures: Stacked 2D materials shed light. *Nat. Mater.* **14**, 264-265 (2015).

219 Jariwala, D., Marks, T. J. & Hersam, M. C. Mixed-dimensional van der Waals heterostructures. *Nat. Mater.* **16**, 170-181 (2017).

220 Zhao, P. D. *et al.* Air Stable p-Doping of WSe_2 by Covalent Functionalization. *ACS Nano* **8**, 10808-10814 (2014).

221 Yang, L. *et al.* Chloride molecular doping technique on 2D materials: WS_2 and MoS_2. *Nano Lett.* **14**, 6275-6280 (2014).

222 Tarasov, A. *et al.* Controlled doping of large - area trilayer MoS_2 with molecular reductants and oxidants. *Adv. Mater.* **27**, 1175-1181 (2015).

223 Wang, Y., Slassi, A., Cornil, J., Beljonne, D. & Samorì, P. Tuning the Optical and Electrical Properties of Few - Layer Black Phosphorus via Physisorption of Small Solvent Molecules. *Small* **15**, 1903432 (2019).

224 Bertolazzi, S. *et al.* Engineering Chemically Active Defects in Monolayer MoS_2 Transistors *via* Ion-Beam Irradiation and Their Healing via Vapor Deposition of Alkanethiols. *Adv. Mater.* **29** (2017).

225 McDonnell, S., Addou, R., Buie, C., Wallace, R. M. & Hinkle, C. L. Defect-Dominated Doping and Contact Resistance in MoS2. *ACS Nano* **8** (2014).

226 Jo, S.-H. *et al.* A High-Performance WSe2/h-BN Photodetector using a Triphenylphosphine (PPh3)-Based n-Doping Technique. *Adv. Mater.* **28**, 4824-4831 (2016).

227 Bonnett, R. Photosensitizers of the porphyrin and phthalocyanine series for photodynamic therapy. *Chem. Soc. Rev.* **24**, 19-33 (1995).

228 McKeown, N. B. *Phthalocyanine materials: synthesis, structure and function.* (Cambridge University Press, 1998).

229 Sorokin, A. B. Phthalocyanine metal complexes in catalysis. *Chem. Rev.* **113**, 8152-8191 (2013).

230 Thomas, A. L. *Phthalocyanine research and applications.* (CRC Press, 1990).

231 Choi, J., Zhang, H. & Choi, J. H. Modulating optoelectronic properties of two-dimensional transition metal dichalcogenide semiconductors by photoinduced charge transfer. *ACS Nano* **10**, 1671-1680 (2016).

232 Benjamin, C. J., Zhang, S. & Chen, Z. Controlled doping of transition metal dichalcogenides by metal work function tuning in phthalocyanine compounds. *Nanoscale* **10**, 5148-5153 (2018).

233 Huang, Y. *et al.* Van der Waals coupled organic molecules with monolayer MoS_2 for fast response photodetectors with gate-tunable responsivity. *ACS Nano* **12**, 4062-4073 (2018).

234 Pak, J. *et al.* Enhancement of photodetection characteristics of MoS_2 field effect transistors using surface treatment with copper phthalocyanine. *Nanoscale* **7**, 18780-18788 (2015).

235 Przybył, B. & Janczak, J. 4+ 1 Complexes of zinc phthalocyanine with pyridine derivative ligands. *Dyes Pigm.* **118**, 102-109 (2015).

236 Naitoh, Y., Matsumoto, T., Sugiura, K.-i., Sakata, Y. & Kawai, T. Self-assembled stripe structure of zinc–phthalocyanine on graphite surfaces. *Surf. Sci.* **487**, L534-L540 (2001).

237 Strohmaier, R., Ludwig, C., Petersen, J., Gompf, B. & Eisenmenger, W. Scanning tunneling microscope investigations of lead–phthalocyanine on MoS_2. *J. Vac. Sci. Technol B* **14**, 1079-1082 (1996).

238 Choudhury, P., Ravavarapu, L., Dekle, R. & Chowdhury, S. Modulating Electronic and Optical Properties of Monolayer MoS2 Using Nonbonded Phthalocyanine Molecules. *J. Phys. Chem. C* **121**, 2959-2967 (2017).

239 Kresse, G., Marsman, M. & Furthmüller, J. (VASP, 2012).

240 Kafle, T. R. *et al.* Effect of the Interfacial Energy Landscape on Photo-induced Charge Generation at the ZnPc-MoS2 Interface. *J. Am. Chem. Soc.* (2019).

241 Tackley, D. R., Dent, G. & Smith, W. E. IR and Raman assignments for zinc phthalocyanine from DFT calculations. *PCCP* **2**, 3949-3955 (2000).

242 Chen, L. *et al.* Nonresonant chemical mechanism in surface-enhanced Raman scattering of pyridine on M@ Au 12 clusters. *Nanoscale* **8**, 4086-4093 (2016).

243 Wojciechowski, P. M., Zierkiewicz, W., Michalska, D. & Hobza, P. Electronic structures, vibrational spectra, and revised assignment of aniline and its radical cation: Theoretical study. *J. Chem. Phys.* **118**, 10900-10911 (2003).

244 Li, Y., Xu, C.-Y., Hu, P. & Zhen, L. Carrier Control of MoS_2 Nanoflakes by Functional Self-Assembled Monolayers. *ACS Nano* **7**, 7795-7804 (2013).

245 Su, W., Dou, H., Huo, D., Dai, N. & Yang, L. Enhancing photoluminescence of trion in single-layer MoS_2 using p-type aromatic molecules. *Chem. Phys. Lett.* **635**, 40-44 (2015).

246 Liu, C. *et al.* Two-dimensional materials for next-generation computing technologies. *Nat. Nanotechnol.* **15**, 545-557 (2020).

247 Marega, G. M. *et al.* Logic-in-memory based on an atomically thin semiconductor. *Nature* **587**, 72-77 (2020).

248 Breyer, E. T. & Slesazeck, S. in *Ferroelectricity in Doped Hafnium Oxide: Materials, Properties and Devices* 495-513 (Elsevier, 2019).

249 Ashwell, G. J. Photochromic memory devices. *Nature* **347**, 617-617 (1990).

250 Orgiu, E. & Samorì, P. 25th Anniversary Article: Organic Electronics Marries Photochromism: Generation of Multifunctional Interfaces, Materials, and Devices. *Adv. Mater.* **26**, 1827-1845, doi:10.1002/adma.201304695 (2014).

251 Mosciatti, T. *et al.* A multifunctional polymer-graphene thin-film transistor with tunable transport regimes. *ACS Nano* **9**, 2357-2367 (2015).

252 Zhang, X., Hou, L. & Samorì, P. Coupling carbon nanomaterials with photochromic molecules for the generation of optically responsive materials. *Nat. Comm.* **7** (2016).

253 Leydecker, T. *et al.* Flexible non-volatile optical memory thin-film transistor device with over 256 distinct levels based on an organic bicomponent blend. *Nat. Nanotechnol.* **11**, 769-775 (2016).

254 Zhao, Y., Ippolito, S. & Samorì, P. Functionalization of 2D Materials with Photosensitive Molecules: From Light - Responsive Hybrid Systems to Multifunctional Devices. *Adv. Opt. Mater.* **7**, 1900286 (2019).

255 Crivillers, N., Orgiu, E., Reinders, F., Mayor, M. & Samorì, P. Optical modulation of the charge injection in an organic field - effect transistor based on photochromic self - assembled - monolayer - functionalized electrodes. *Adv. Mater.* **23**, 1447-1452 (2011).

256 El Gemayel, M. *et al.* Optically switchable transistors by simple incorporation of photochromic systems into small-molecule semiconducting matrices. *Nat. Comm.* **6**, 1-8 (2015).

257 Orgiu, E. *et al.* Optically switchable transistor via energy-level phototuning in a bicomponent organic semiconductor. *Nat. Chem.* **4**, 675 (2012).

258 Carroli, M. *et al.* Multiresponsive Nonvolatile Memories Based on Optically Switchable Ferroelectric Organic Field - Effect Transistors. *Adv. Mater.*, 2007965 (2021).

259 Lemme, M. C. in *Beyond-CMOS Nanodevices 2* (ed Francis Balestra) Ch. 3, 97-116 (ISTE Ltd, London, John Wiley & Sons Inc., Hoboken, New Jersey, 2014).

260 Lembke, D., Bertolazzi, S. & Kis, A. Single-Layer MoS_2 Electronics. *Acc. Chem. Res.* **48**, 100-110 (2015).

261 Wang, Y., Slassi, A., Cornil, J., Beljonne, D. & Samorì, P. Tuning the Optical and Electrical Properties of Few - Layer Black Phosphorus via Physisorption of Small Solvent Molecules. *Small*, 1903432.

262 Lu, J., Lipatov, A., Vorobeva, N. S., Muratov, D. S. & Sinitskii, A. Photoswitchable monolayer and bilayer graphene devices enabled by in situ covalent functionalization. *Adv. Electron. Mater.* **4**, 1800021 (2018).

263 Tang, Z. *et al.* Optically triggered control of the charge carrier density in chemically functionalized graphene field effect transistors. *Chem. Eur. J.* **26**, 6473-6478 (2020).

264 Feng, W., Luo, W. & Feng, Y. Photo-responsive carbon nanomaterials functionalized by azobenzene moieties: structures, properties and application. *Nanoscale* **4**, 6118-6134 (2012).

265 Döbbelin, M. *et al.* Light-enhanced liquid-phase exfoliation and current photoswitching in graphene–azobenzene composites. *Nat. Comm.* **7**, 1-10 (2016).

266 Rusch, T. R., Hammerich, M., Herges, R. & Magnussen, O. M. Molecular platforms as versatile building blocks for multifunctional photoswitchable surfaces. *Chem. Commun.* **55**, 9511-9514 (2019).

267 Baisch, B. *et al.* Mounting freestanding molecular functions onto surfaces: The platform approach. *J. Am. Chem. Soc.* **131**, 442-443 (2009).

268 Brill, A. R., Biswas, S., Caspary Toroker, M., de Ruiter, G. & Koren, E. Dipole-Induced Raman Enhancement Using Noncovalent Azobenzene-Functionalized Self-Assembled Monolayers on Graphene Terraces. *ACS Appl. Mater. Interfaces* **13**, 10271-10278 (2021).

269 Brill, A. R., Kuntumalla, M. K., de Ruiter, G. & Koren, E. Formation of Highly Ordered Self-Assembled Monolayers on Two-Dimensional Materials via Noncovalent Functionalization. *ACS Appl. Mater. Interfaces* **12**, 33941-33949 (2020).

270 Orbelli Biroli, A. *et al.* Out - Of - Plane Metal Coordination for a True Solvent - Free Building with Molecular Bricks: Dodging the Surface Ligand Effect for On - Surface Vacuum Self - Assembly. *Adv. Funct. Mater.*, 2011008 (2021).

271 Rodríguez-Redondo, J. L. *et al.* Phthalocyanine-modulated isomerization behaviour of an azo-based photoswitch. *Chem. Commun.*, 1265-1267 (2006).

272 Gao, Y., Walter, V., Ferguson, M. J. & Tykwinski, R. R. Hierarchical Synthesis, Structure, and Photophysical Properties of Gallium - and Ruthenium - Porphyrins with Axially Bonded Azo Ligands. *Chem. Eur. J.* (2020).

273 Reddy, D. R. & Maiya, B. G. A molecular photoswitch based on an 'axial-bonding'type phosphorus (V) porphyrin. *Chem. Commun.*, 117-118 (2001).

274 Li, J. *et al.* Tuning the optical emission of MoS2 nanosheets using proximal photoswitchable azobenzene molecules. *Appl. Phys. Lett.* **105**, 241116 (2014).

275 Kim, M., Safron, N. S., Huang, C., Arnold, M. S. & Gopalan, P. Light-driven reversible modulation of doping in graphene. *Nano Lett.* **12**, 182-187 (2012).

276 Zhang, M., Yu, J., He, J. & Huang, C. Adjusting Fermi Level of Graphene by Controlling the Linker Lengths of Dipolar Molecules. *Langmuir* **35**, 5448-5454 (2019).

277 Padgaonkar, S. *et al.* Molecular-orientation-dependent interfacial charge transfer in phthalocyanine/MoS_2 mixed-dimensional heterojunctions. *J. Phys. Chem. C* **123**, 13337-13343 (2019).

278 Lee, S.-J. *et al.* Programmable devices based on reversible solid-state doping of two-dimensional semiconductors with superionic silver iodide. *Nat. Electron.* **3**, 630-637 (2020).

279 Park, J. M., Cao, Y., Watanabe, K., Taniguchi, T. & Jarillo-Herrero, P. Flavour Hund's coupling, Chern gaps and charge diffusivity in moiré graphene. *Nature* **592**, 43-48 (2021).

280 Rozen, A. *et al.* Entropic evidence for a Pomeranchuk effect in magic-angle graphene. *Nature* **592**, 214-219 (2021).

281 Tsai, H.-Z. *et al.* A molecular shift register made using tunable charge patterns in one-dimensional molecular arrays on graphene. *Nat. Electron.* **3**, 598-603 (2020).

Statement of Work

All the experimental and data analysis work in the thesis were carried out by myself except for the following:

In Chapter 5 and 6, the DFT simulations were made by Dr. Amine Slassi under the supervision of Prof. David Beljonne from Mons University, Belgium.

In Chapter 7, 8 and 9, the DFT simulations were carried out by Dr. Sai Manoj Gali under the supervision of Prof. David Beljonne from Mons University, Belgium.

In Chapter 9, the synthesis of TFAP ligand were carried out by Dr. Daniel Iglesias from University of Strasbourg, France.

Dr. Marc-Antoine Stoeckel and Dr. Simone Bertolazzi offered help and discussions in the work of Chapter 5 and 6. Dr. Hanlin Wang, Dr. Yifan Yao, Dr. Can Wang and Yusheng Chen participated in discussions and establishment of experimental setup in the work presented in Chapter 9.

Acknowledgements

My favourite scientific theory is the Dunning-Kruger effect (**Figure 1**, unfortunately it is not related to chemistry, physics and nanoscience) as it follows exactly what I have psychologically gone through during my 4 years of PhD life. Entering the Nanochemistry lab as a Master 2 intern, I was at the *"Peak of Mount Stupid"* and regarded scientific research as easy as the exams. The days and nights of experiments brought be down to the hill. After the four years happiness, success, achievement blended with sorrow, failure and criticism, I believe that I am stepping out of the *"Valley of Despair"*, thanks to the effort from everyone who has helped to shape my academic character.

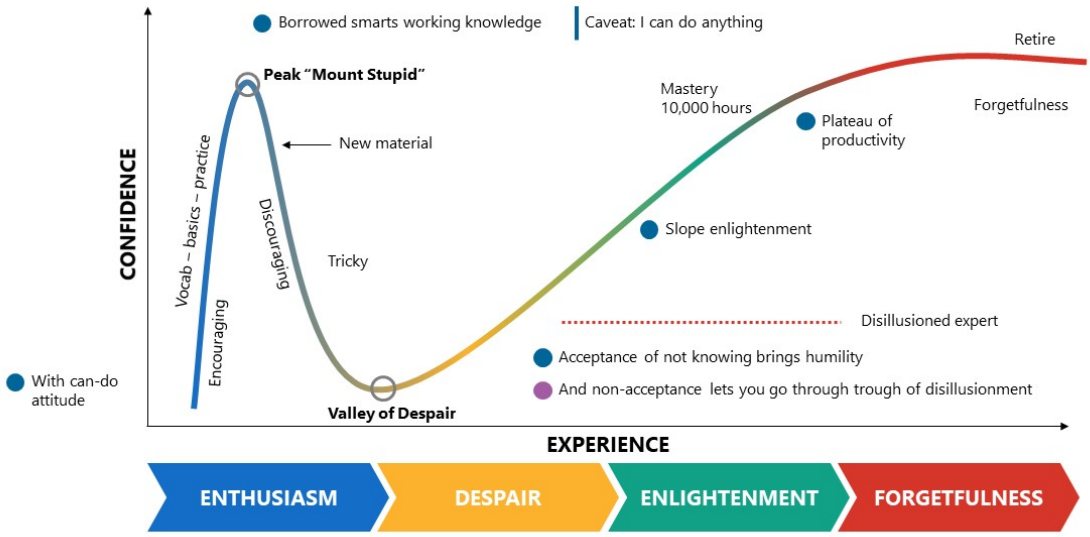

Figure 1: The Dunning-Kruger effect curve.

(source: https://slidemodel.com/templates/dunning-kruger-effect-powerpoint-template/)

I would like to firstly express my highest gratefulness to my PhD supervisor, Prof. Paolo Samorì. I appreciate that he could give me the opportunity to work in such outstanding research environment. Through the abundant discussions, he showed me how a successful scientist should be. His curiosity of science, rich knowledge, efficiency and hard-working attitude indeed build who I am in research now. His guidance helped me to grow independent-thinking and critical thinking. His generosity and open-mind to ideas are extremely encouraging for me as a young PhD student.

I would also like to thank Dr. Simone Bertolazzi, who have been my mentor of lab during my master internship and the 1st year of PhD study. He led me to the two-dimensional materials world, taught me almost all the experimental techniques that he knows, and showed me how to work in a series and responsible way. I am grateful for having inherited his skills that formed the basis of my experimental works during my four years of PhD study.

Another great appreciation goes to my collaborators in Mons University, Belgium. Prof. David Beljonne, Dr. Manoj Sai Gali and Dr. Amine Slassi are all high-level theoreticians that helped me to understand the mechanisms behind my experimental observations. Without them, I would not have been able to publish my works in those high-impact journals. Also our former colleague Dr. Marco Gobbi in CIC nanoGUNE, Spain, and Prof. Andrea Liscio in Italian National Research Council, Italy for current and future collaborations.

Very special thanks to Dr. Hanlin Wang, Dr. Yifan Yao, Dr. Marc-Antoine Stoeckel, Dr. Yuda Zhao and Dr. Can Wang for many of the fruitful discussions, collaborations and patiently answering my questions. Interacting with them broadens my eyes and stimulates my novel ideas. They are my models of excellent young researchers.

My in-lab collaborators, Dr. Daniel Iglesias, Dr. Verónica Montes Garcia, Prof. Stefano Casalini, Dr. Stefano Del Buffa and Nicholas Turetta, thank you for sharing your experimental expertise to me. Collaborating with them is a great pleasure and exchanging knowledge helped me to progress faster.

Besides, Dr. Changbo Huang, Dr. Lili Hou, Dr. Xiaoyan Zhang, Dr. Lei Zhang, Dr. Chun Ma, Dr. Zhaoyang Liu, Dr. Haipeng Guo, Haixin Qiu, Haijun Peng, Bin Han and Yusheng Chen, the Chinese team in Nanochemistry lab. With many of the endless working days and nights and weekends in the lab, their presence and accompany made my tedious experiments much more colorful.

Administrative members in the lab, Dr. Fanny Richard, Corinne Ledger, Dr. Artur Ciesielski and Dr. Nicolas Wiebel are all the largest helpers in the lab. I would strongly thank to Corinne who helped me in every aspect of lab chores. It is also a pleasure to work with Fanny for the maintenance of glovebox and solving the problems of XPS.

To all my previous office mates in Nanochemistry lab, Stefano Ippolito, Dr. Mathilde Eredia, Irene

Buraioli, Luca Cusin, Pietro Livio, Dr. Francesca Urban, Dr. Samanta Witomska, Iwona Janica. You helped me to discover my language talent and trained me how to speak Italian. The intercultural exchanges broke the stereotypes and made our lab more and more international.

I have also received strong support from members from outside Nanochemistry lab. I would specially thank to Dr. Eloïse Devaux from Ebbesen group at ISIS for enduring my vast demand of Ebeam evaporation, and to Dr. Hicham Majjad, Romain Bernard, Sabine Siegwald from at eFab, IPCMS for establishing the Ebeam lithography process. Other colleagues and friends in the ISIS who brought conversations and friendship, Dr. Sayali Shevate, Dr. Kuidong Wang, Dr. Yibo Wang… Just to name a few.

Outside the lab, the city of Strasbourg has become the place that I stayed for the longest period of time besides my hometown. What makes me feel like home is the Ruhlmann family, Manon, Tao and Laurent. They always treated me like family and welcome me with wonderful Chinese food and unforgettable happy moments. Especially, thank to Prof. Laurent Ruhlmann who have brought me to the Faculty of Chemistry of University of Strasbourg for my Master study. It is truly a turning-point of my life.

At last, thanks to my parents, who have always been my best friends of life, who treasure each step of my progress, who encourage me to go outside to see the wonderful world, and who guide me where to head to when I hesitate. Despite the geographical distance, our family are always tied with love.

Ye WANG

王也

List of Publications

1. **Y. Wang**, H. Wang, S. M. Gali, N. Turetta, Y. Yao, C. Wang, Y. Chen, D. Beljonne, P. Samorì, "Molecular Doping of 2D Indium Selenide for Ultrahigh Performance and Low-Power Consumption Broadband Photodetectors", *Adv. Funct. Mater.*, 2021, 2103353.
   DOI: 10.1002/adfm.202103353

2. H. Wang, **Y. Wang**, Z. Ni, N. Turetta, S. M. Gali, H. Peng, Y. Yao, Y. Chen, I. Janica, D. Beljonne, W. Hu, A. Ciesielski, P. Samorì, "2D MXene-Molecular Hybrid Additive for High-Performance Ambipolar Polymer Field-Effect Transistors and Logic Gates", *Adv. Mater.*, 2021, 2008215.
   DOI: 10.1002/adma.202008215

3. **Y. Wang**, S. M. Gali, A. Slassi, D. Beljonne, P. Samorì, "Collective dipole-dominated doping of monolayer MoS_2: orientation and magnitude control via the supramolecular approach", Adv. Funct. Mater., 2020, 30 (36), 2002846.
   DOI: 10.1002/adfm.202002846

4. V. Montes-García, R. Furlan de Oliveira, **Y. Wang**, A. Berezin, P. Fanjul-Bolado, M. B. González García, T. M. Hermans, D. Bonifazi, S. Casalini, P. Samorì, "Harnessing Selectivity and Sensitivity in Ion Sensing via Supramolecular Recognition: A 3D Hybrid Gold Nanoparticle Network Chemiresistor", Adv. Funct. Mater., 2020, 2008554.
   DOI: 10.1002/adfm.202008554

5. **Y. Wang**, A. Slassi, J. Cornil, D. Beljonne, P. Samorì, "Tuning the Optical and Electrical Properties of Few - Layer Black Phosphorus via Physisorption of Small Solvent Molecules", Small, 2019, 15 (47), 1903432.
   DOI: 10.1002/smll.201903432

6. M.-A. Stoeckel, M. Gobbi, T. Leydecker, **Y, Wang**, M. Eredia, S. Bonacchi, R. Verucchi, M. Timpel, M. V. Nardi, E. Orgiu, P. Samorì, "Boosting and Balancing Electron and Hole Mobility in Single- and Bilayer WSe_2 Devices via Tailored Molecular Functionalization", ACS Nano, 2019, 13 (10), 11613-11622.
   DOI: 10.1021/acsnano.9b05423

7. **Y. Wang**, A. Slassi, M.-A. Stoeckel, S. Bertolazzi, J. Cornil, D. Beljonne, P. Samorì, "Doping of Monolayer Transition-Metal Dichalcogenides via Physisorption of Aromatic Solvent Molecules", J. Phys. Chem. Lett., 2019, 10 (3), 540–547.
   DOI: 10.1021/acs.jpclett.8b03697

8. Y.X.Huang, Y.Lu, Q.He, **Y.Wang**, W.Fang, X.J.Liu, J.P.Jia, C.P.Wang " Thermodynamic assessment of the Be–Pu and Cd–Pu systems ". Calphad, 2016, 52, 120-124.
   DOI: 10.1016/j.calphad.2015.12.004

List of Presentations

1. Ye Wang, Amine Slassi, David Beljonne, Paolo Samorì, Chem2Dmat 2019, Dresde, Allemagne, 03-06 Septembre 2019. Poster

2. Ye Wang, Amine Slassi, Jérôme Cornil, David Beljonne, Simone Bertolazzi, Paolo Samorì, Optoelectronics on 2D materials (Ecole d'été), Davos, Suisse, 22 Août 2018. Poster

3. Ye Wang, Amine Slassi, Jérôme Cornil, David Beljonne, Simone Bertolazzi, Paolo Samorì, European Materials Research Society (EMRS) Spring Meeting 2018, Session J.06.22, Strasbourg, France, 19 Juin 2018. Poster

Awards

Best poster prize, Chem2Dmat 2019, Dresde, Allemagne, 03-06 Septembre 201

Ye WANG

Science moléculaire et matériaux bi-dimensionnels : Système hybride pour opto-électroniques

Résumé

Cette thèse étudie principalement le mécanisme des interactions entre les molécules et les matériaux semi-conducteurs bidimensionnels (2D) avec leurs applications associées en électronique. Les travaux de recherche commencent par l'étude de l'effet des solvants organiques sur les propriétés optiques et électroniques des dichalcogénures de métaux de transition (TMD) 2D et du phosphore noir, suivant par la fonctionnalisation du séléniure d'indium (InSe) 2D avec des molécules tensioactifs ioniques et les applications dans les photodétecteurs. La recherche se termine par la création de potentiels périodiques à l'aide de ligands pyridiniques fonctionnalisés axialement sur des phtalocyanines métalliques physisorbées sur des TMD 2D. Ces ligands comprennent les pyridines simplement fonctionnalisées et les pyridines avec de l'azobenzène photochromique pour induire un dopage sur des matériaux 2D.

Les projets interdisciplinaires concernent la chimie physique, la physique du solide, la chimie supramoléculaire, la science des matériaux, la nanoélectronique, la chimie computationnelle et la photochimie.

Mots clés: matériaux bidimensionnels, fonctionnalisation moléculaire, transistor à effet de champ, photodétecteur, chimie supramoléculaire

Résumé en anglais

This thesis mainly studies the mechanism of interactions between molecules and two-dimensional (2D) semiconducting materials, and the related applications in electronics. The research works begin with studying the effect of organic solvents on the optical and electronic properties of 2D transition metal dichalcogenides (TMDs) and black phosphorus, followed by functionalizing 2D indium selenide (InSe) with ionic surfactant molecules and the applications in photodetectors. The research is ended with creating periodic potentials using axially functionalized pyridinic ligands on metal phthalocyanines that are physisorbed onto 2D TMDs. These ligands include simply functionalized pyridine and the pyridines with photochromic azobenzene to induce doping on 2D materials.

The interdisciplinary projects involves physical chemistry, solid state physics, supramolecular chemistry, materials science, nanoelectronics, computational chemistry and photochemistry.

Keywords: two-dimensional materials, molecular functionalization, field-effect transistor, photodetector, supramolecular chemistry